UNIVERSITÀ DEGLI STUDI DI PADOVA

UNIVERSITÀ DEGLI STUDI DI PADOVA
CENTRO INTERDIPARTIMENTALE *"Centro Ricerche Fusione"*

UNIVERSIDADE TÉCNICA DE LISBOA
INSTITUTO SUPERIOR TÉCNICO

JOINT RESEARCH DOCTORATE IN FUSION SCIENCE AND ENGINEERING

CYCLE XXV

Three dimensional magnetohydrodynamics of fusion plasmas

Coordinator: Ch.mo Prof. Piero Martin

Supervisor: Ch.mo Prof. Antonio Buffa

Supervisor: Dott.ssa Susanna Cappello

Doctoral student: Marco Veranda

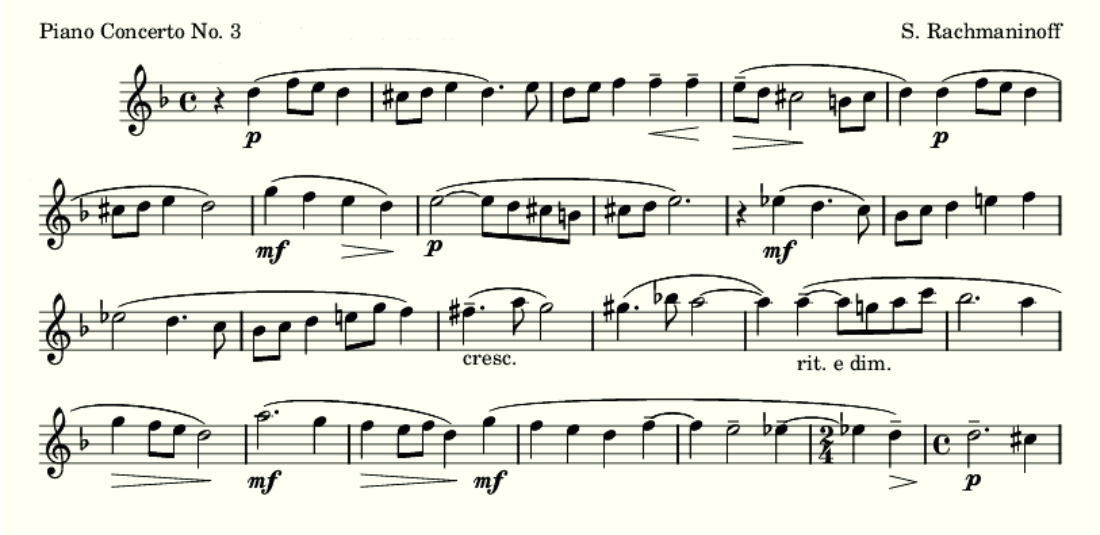

http://www.youtube.com/watch?v=WNlfAdF4pQ8

http://vimeo.com/58252598

A good recording: Kissin-Ozawa, Audio CD, RCA, 13 July 1993 EAN: 0090266154821

Abstract

The primary aim of the research on nuclear fusion is to obtain a new energy source to help satisfying a growing and sustainable consumption. This objective has to be reached through scientific research, both from the physics point of view and through the demonstration of the technological feasibility of a nuclear fusion reactor.
The option on which the major efforts of the international community are focused is to obtain controlled nuclear fusion using a magnetic field to confine a plasma formed by deuterium and tritium, in a vacuum chamber of toroidal shape. The most promising magnetic configuration is the so called tokamak configuration. The scientific community aims at addressing the remaining problems connected with physics performing the experiment ITER (International Thermonuclear Experimental Reactor) and to verify the technological feasibility of a nuclear fusion reactor with the DEMO experiment.
An important part of the scientific efforts is addressed to the study of configurations alternative to the tokamak, like the stellarator and the reversed-field pinch (RFP). These configurations achieve three dimensional helical states: in the RFP a global helical state is obtained spontaneously, due to the presence of a strong current flowing in the plasma, while currents flowing in external helically shaped coils generate a global helical state in the stellarator. Helical states can be obtained also in the tokamak configuration, for instance due to the presence of external magnetic field perturbations.
The research activity of my PhD focuses on the study of the 3D nonlinear magnetohydrodynamics model applied to the numerical study of the RFP and tokamak helical configurations.
The main aim of my research is the characterization, under three different aspects later described, of the three dimensional helical states. These states are presently believed to provide possible scenarios for reducing dangerous MHD activity for both RFP (magnetic chaos transport reduction) and tokamak (sawtooth mitigation, disruption avoidance).
The research activity included the development and the exploitation of advanced numerical tools to deal with the numerical solution of the 3D nonlinear MHD model, while the interaction with the experimental environment provided the opportunity to develop tools for model-experiment comparison (validation) and benchmarking of numerical

tools (verification).
The results obtained during my PhD provide a further step towards a predictive capability of the employed modelling tools. In fact, the boundary conditions are proved to be a key ingredient in bringing the comparison of MHD simulations with the experiment at a quantitative level. Moreover it recently inspired a successfull and promising experimental activity in RFX-mod, the biggest RFP experiment in the world, located in Padova.

My PhD research activity and results can be divided into three main areas. The first is the dynamical simulation of a magnetically confined plasma through numerical solution of the 3D nonlinear visco-resistive MHD model. The second area of research consists in the topological study of the magnetic field configurations obtained from MHD simulations. The third area is the study of transport due to magnetic stochasticity in both tokamak and RFP states, with data coming from MHD simulations, gyrokinetics simulations and experimental results.
The *first area of research* deals with the simulation of the dynamical properties of a magnetically confined plasma, performed using the 3D nonlinear MHD codes SPECYL and PIXIE3D. The most important achievement is represented by the level of agreement between MHD simulation and experimental dynamics of the RFP, a degree of agreement obtained in simulations where, for the first time, a helical boundary condition is applied. It is also demonstrated that by imposing a finite helical radial magnetic field at the edge it is possible to induce a global helical regime with the chosen helicity. As for the tokamak configuration the study of helical boundary conditions shows that they can favour a steady helical equilibrium, thus mitigating the sawtooth dynamics typically detrimental for the confinement.
This area of research leads to a unifying vision for the RFP and the tokamak, as the use of helical bondary condition for the magnetic field seems to allow the easier establishment of a helical equilibrium in both configurations, with interesting properties for the configurations.
The *second area of research* is centred on the topological study of the magnetic configurations obtained from the MHD simulations of the RFP. The separatrix expulsion of the dominant helical mode has been studied analyzing the magnetic field topology with the field line tracing code NEMATO. Two so-called paradigmatic cases, characterized by a simplified MHD dynamics, have been analyzed. In the first one it was shown that the dominant mode separatrix expulsion can reduce the level of magnetic field lines stochasticity remarkably, in the second case an "exotic" (before these studies) dynamics was considered, i.e. the development of a helical equilibrium from a non-resonant mode. These results confirmed older studies that placed separatrix expulsion in di-

rect connection with helical RFP states obtained in RFX-mod, which develop internal transport barriers observed as electronic temperature steep gradients. Furthermore it showed that the helical equilibrium based on a non-resonant mode can result in particularly strong magnetic order. The favourable properties found led to the proposal to experimentally drive QSH states built upon non-resonant MHD modes in the RFX-mod experiment: these states were successfully produced in the experiment, and the study of thermal properties is presently ongoing.
Topological studies on more realistic cases coming from MHD simulations that show a quantitative agreements with the standard operation of the RFX-mod experiment are also tackled in this thesis. The results obtained underline the importance of the spectrum of secondary perturbations to the helical equilibrium.
The *third area of research* focuses on the consequences of transport produced by the presence of magnetic stochasticity. Two specific cases relevant for the RFP and the tokamak are considered: the magnetic chaos produced by microtearing activity at the electron internal transport barrier in the RFP, and the case of edge magnetic stochasticity due to the action of edge helical magnetic perturbations in the tokamak. The tools to study transport were developed and used to calculate the energy diffusion coefficient and other meaningful quantities. Such tools are now available for further and more general applications.
On a *numerical ground* two important activities were performed during the PhD. The parallelization of the field line tracing code NEMATO, during one month mobility at Oak Ridge National Laboratory, was fundamental for the speeding up of the research activity. The numerical verification of NEMATO and ORBIT was also performed. The verification gave a positive result, showing a satisfactory agreement, both qualitative and quantitative, on the features of the magnetic field topology in the RFP configuration.

The thesis is organized in five parts.
The first part, named prologue, is an introduction to nuclear fusion and magnetic confinement. The second part gives a description of the modelling and numerical tools employed. The third part tackles MHD dynamics and magnetic field topology: in this part the main results are presented. The fourth part confronts the activity related to the experimental area and the magnetic stochasticity related transport. An outline and a local summary of the results are placed respectively at the beginning and at the end of each chapter contained in these two last parts. In the fifth part, named epilogue, more general conclusions are drawn. Technical aspects are included in the appendixes.

1 - Prologue: where the main concepts, needed to define the area of study of this thesis, are introduced.
The *first chapter* discusses the nuclear fusion reaction and the main confinement methods. The focus will be on magnetic confinement, with the introduction of the tokamak and stellarator configurations. The *second chapter* deals with the RFP magnetic confinement configuration from the theoretical, numerical and experimental point of view.

2 - Modelling tools: the theoretical models and the numerical tools used during my PhD are presented.
The *third chapter* presents the MHD model to describe the macroscopic behaviour of a magnetically confined plasma, described as a conductive quasi-neutral fluid in a magnetic field. The MHD equilibrium states and stability properties will be explored. The *fourth chapter* describes the numerical codes SPECYL and PIXIE3D, that solve the MHD model in a cylindrical (the former) or arbitrary (the latter) 3D geometry. The *fifth chapter* describes the NEMATO code for magnetic field lines tracing. This code is fundamental for the analysis of the magnetic field topology, as its numerical features make it particularly suitable for the RFP configurations.

3 - Modelling results: the research on the helical states is described.
The *sixth chapter* deals with the chaos healing effect due to the separatrix expulsion process. The *seventh chapter* begins to explore RFP configuration in helicities different from the ones spontaneously observed in the experiment (that is usually associated with the first resonant mode with respect to the safety factor profile). The *eighth chapter* deals with helical states in the RFP configuration stimulated through the use of external magnetic perturbations. The *ninth chapter* studies the topological properties of the set of simulations performed in the previous chapter.

4 - Application to experimental activity: The *tenth chapter* describes how the idea of stimulating helical states in the RFP have been applied to the RFX-mod experiment. The *eleventh chapter* explores theoretical features of the transport associated with the magnetic field line stochasticity. Two applications, one on the RFP and the other on the tokamak configuration, will be described.

5 - Epilogue: some conclusions are drawn and a vision on the actual state of research on RFP helical states will be proposed together with the future perspectives that can be traced.

Appendixes: where the numerical works will be described more in detail and further

information on the RFX-mod experiment will be given.
In *appendix A* the numerical verification of NEMATO and ORBIT codes will be described. The ORBIT code, one of the most used numerical tools for magnetic field line tracing, will be described.
In *appendix B* the parallelization of NEMATO will be described.
Appendix C describes the RFX-mod experiment, operating in Padova, Italy.

Prefazione

L'obiettivo principale della ricerca sulla fusione nucleare è l'ottenimento di una fonte di energia in grado di contribuire a soddisfare una domanda crescente. Tale obiettivo deve essere raggiunto attraverso la ricerca scientifica, sia dal punto di vista della fisica che attraverso la dimostrazione della fattibilità tecnologica di un reattore a fusione nucleare.
L'opzione sulla quale si sono concentrati i maggiori sforzi economici della comunità internazionale è l'ottenimento della fusione nucleare controllata usando un campo magnetico per confinare un plasma formato da deuterio e trizio in una camera da vuoto di forma toroidale. La configurazione magnetica più promettente è quella chiamata tokamak. La comunità scientifica prevede di risolvere i rimamenti problemi legati alla fisica attraverso l'esperimento ITER (International Thermonuclear Experimental Reactor) e di verificare la fattibilità tecnologica di un reattore a fusione nucleare con l'esperimento DEMO.
Una parte importante degli sforzi scientifici è rivolta allo studio di configurazioni alternative al tokamak, come lo stellarator e il reversed-field pinch (RFP). Queste configurazioni raggiungono stati elicoidali tridimensionali: nel RFP uno stato elicoidale globale è ottenuto spontaneamente, a causa della presenza di una forte corrente che circola nel plasma, mentre correnti che circolano in bobine elicoidali esterne producono uno stato elicoidale globale nello stellarator. Stati elicoidali possono essere ottenuti anche nella configurazione tokamak, ad esempio a causa della presenza di perturbazioni esterne al campo magnetico.
L'attività di ricerca del mio dottorato si concentra sullo studio del modello magnetoidrodinamico (MHD) 3D nonlineare applicato allo studio numerico delle configurazioni elicoidali nel RFP e nel tokamak.
L'obbiettivo principale della mia ricerca è la caratterizzazione, sotto tre diversi aspetti descritti nel seguito, degli stati elicoidali tridimensionali. Si ritiene che questi stati possano rappresentare una possibile via per ridurre la dannosa attività MHD sia nel RFP (riduzione del trasporto collegato al comportamento caotico del campo magnetico) che nel tokamak (mitigazione dell'instabilità sawtooth, prevenzione delle instabilità).
L'attività di ricerca ha compreso lo sviluppo e l'uso di strumenti numerici avanzati per

risolvere il modello MHD 3D nonlineare, mentre l'interazione con l'ambiente sperimentale ha permesso di avere una opportunità di sviluppare strumenti per il confronto tra modello ed esperimento (validazione) e di confronto tra strumenti numerici (verificazione).
I risultati ottenuti durante il mio PhD costituiscono un ulteriore passo verso la capacità predittiva degli strumenti numerici utilizzati. Infatti le condizioni al contorno sul campo magnetico si sono dimostrate un ingrediente fondamentale per portare il confronto tra le simulazioni MHD e l'esperimento ad un livello quantitativo. In più ha recentemente ispirato una promettente attività sperimentale in RFX-mod che ha confermato i risultati teorici ottenuti. RFX-mod è il più grande esperimento RFP nel mondo, ed è situato a Padova.

La mia attività di ricerca durante il PhD e i risultati che ho ottenuto possono essere divisi in tre principali aree. La prima area consiste nella simulazione dinamica di un plasma confinato magneticamente attraverso la soluzione numerica del modello MHD viscoresistivo 3D nonlineare. La seconda area di ricerca consiste nello studio topologico di configurazioni di campo magnetico ottenute da simulazioni MHD. La terza area consiste nello studio del trasporto dovuto alla presenza di un campo magnetico stocastico sia nel tokamak che nel RFP, utilizzando dati provenienti da simulazioni MHD, simulazioni girocinetiche e risultati sperimentali.
La prima area di ricerca tratta la simulazione delle proprietà dinamiche di un plasma confinato magneticamente, simulazione svolta utilizzando i codici MHD 3D nonlineare SPECYL e PIXIE3D. Il più importante risultato è rappresentato dal livello di accordo tra simulazioni MHD e la dinamica sperimentale del RFP, un grado di accordo ottenuto in simulazioni dove, per la prima volta, sono state applicate condizioni al contorno elicoidali sul campo magnetico. Si è anche dimostrato che imponendo un valore finito di campo magnetico elicoidale in direzione radiale al bordo è possibile indurre un regime elicoidale globale con l'elicità scelta. Per quanto riguarda la configurazione tokamak lo studio delle condizioni al contorno elicoidali mostra che queste possono favorire un equilibrio elicoidale stazionario, mitigando la dinamica sawtooth che è tipicamente dannosa per il confinamento.
Questa area di ricerca porta ad una visione unificante per il RFP e per il tokamak, poiché l'uso di condizioni al contorno elicoidali per il campo magnetico sembra permettere una più semplice formazione di un equilibrio elicoidale in entrambe le configurazioni, con interessanti proprietà per quel che riguarda tali configurazioni.
La seconda area di ricerca si concentra sullo studio topologico di configurazioni di campo magnetico ottenute da simulazioni MHD del RFP. L'espulsione della separatrice del modo elicoidale dominante è stata studiata analizzando la topologia del campo mag-

netico con il codice di calcolo delle linee di campo magnetico NEMATO. Due cosiddetti casi paradigmatici, caratterizzati da una dinamica MHD semplificata, sono stati analizzati. Nel primo si è mostrato che l'espulsione della separatrice del modo dominante può ridurre il livello di stocasticità delle linee di campo magnetico in maniera evidente, mentre nel secondo caso una dinamica "esotica" (prima di questi studi) è stata considerata, cioè lo sviluppo di un equilibrio elicoidale costruito su un modo non-risonante. Questi risultati hanno confermato studi precedenti che mettevano l'espulsione della separatrice in connessione diretta con l'ottenimento in RFX-mod di stati elicoidali, stati che sviluppano barriere di trasporto interne osservate come alti gradienti della temperatura elettronica. In più ha mostrato che l'equilibrio elicoidale costruito su un modo non-risonante può portare ad un ordine magnetico particolarmente accentuato. Queste proprietà favorevoli hanno portato alla proposta di ottenere sperimentalmente stati QSH costruiti su modi non-risonanti in RFX-mod: questi stati sono stati prodotti con successo nell'esperimento, e lo studio delle loro proprietà termiche è in corso.
Studi topologici su casi più realistici provenienti da simulazioni MHD che mostrano un accordo quantitativo con le tipiche operazioni su RFX-mod sono mostrati in questa tesi. I risultati ottenuti sottolineano l'importanza dello spettro di perturbazioni secondarie all'equilibrio elicoidale.
La terza area di ricerca si concentra sulle conseguenze del trasporto dovuto alla presenza di stocasticità del campo magnetico. Due casi rilevanti per il RFP e per il tokamak sono considerati: il chaos magnetico prodotto da attività di tipo microtearing alla barriera di trasporto interna nel RFP e il caso di stocasticità a bordo plasma dovuta all'azione di perturbazioni elicoidali di bordo al campo magnetico nel tokamak. Sono stati sviluppati degli strumenti per studiare il trasporto e sono stati utilizzati per calcolare il coefficiente di diffusione dell'energia e altre quantità significative. Questi strumenti sono ora disponibili per ulteriori e più generali applicazioni.
Per quanto rigurda *l'aspetto numerico* due importanti attività sono state svolte durante il PhD. La parallelizzazione del codice NEMATO per il calcolo delle linee di campo magnetico, svolta durante un mese di mobility presso l'Oak Ridge National Laboratory, è risultata fondamentale per la velocizzazione dell'attività di ricerca. La verifica numerica dei codici NEMATO e ORBIT è stata svolta, con risultati positivi: un accordo soddisfacente sulle caratteristiche della topologia magnetica nel RFP è stato evidenziato, sia qualitativamente che quantitativamente.

La tesi è organizzata in cinque parti.
La prima parte contiene un'introduzione alla fusione nucleare e al confinamento magnetico. La seconda parte descrive i modelli e gli strumenti numerici utilizzati. La terza parte affronta la dinamica MHD e la topologia del campo magnetico: in questa

parte sono presentati i risultati principali. La quarta parte descrive l'attività collegata all'esperimento e al trasporto dovuto ad un campo magnetico stocastico. Un'introduzione e un riassunto locale dei risultati sono posti all'inizio e alla fine di ciascuna capitolo delle parti tre e quattro. La quinta parte contiene delle conclusioni generali. Nelle appendici sono contenuti aspetti tecnici.

1 - Prologo: in cui si introdurranno i concetti fondamentali necessari per definire l'ambito degli studi presentati in questa tesi.
Il *capitolo primo* discuterà la reazione di fusione nucleare e i principali metodi di confinamento. Il capitolo sarà concentrato sul confinamento magnetico introducendo le configurazioni tokamak e stellarator. Il *capitolo secondo* tratterà la configurazione di confinamento magnetico RFP dal punto di vista teorico, numerico, sperimentale.

2 - Strumenti per la modellizzazione: si descriveranno i modelli teorici e i corrispondenti strumenti numerici utilizzati per gli studi presentati in questa tesi.
Il *capitolo terzo* descriverà il modello MHD che studia il comportamento macroscopico di un plasma confinato magneticamente, descritto come un fluido conduttore quasi-neutro in un campo magnetico. Verranno esplorate le configurazioni MHD di equilibrio e le loro proprietà di stabilità. Il *capitolo quarto* descrive i codici SPECYL e PIXIE3D, che risolvono il modello MHD in una geometria rispettivamente cilindrica o arbitraria 3D. Il *capitolo quinto* descrive invece il codice di calcolo delle linee di campo magnetico NEMATO. Il codice è risultato fondamentale per l'analisi della topologia del campo magnetico in quanto le sue caratteristiche numeriche lo rendono adatto allo studio del RFP.

3 - Risultati: viene descritta la ricerca sugli stati elicoidali.
Il *capitolo sesto* descrive il lenimento del caos magnetico a seguito del fenomeno di espulsione della separatrice. Il *capitolo settimo* inizierà ad esplorare la topologia magnetica di configurazioni RFP con elicità diversa da quella spontaneamente osservata nell'esperimento (usualmente associata al primo modo risonante rispetto al profilo del fattore di sicurezza). Il *capitolo ottavo* tratta gli stati elicoidali nel RFP ottenuti a partire da perturbazioni magnetiche esterne. Il *capitolo nono* studia le proprietà topologiche dell'insieme di simulazioni presentate nel capitolo precedente.

4 - Applicazione all'attività sperimentale: Il *capitolo decimo* descrive come l'idea di stimolare stati elicoidali nel RFP è stata applicata all'esperimento RFX-mod. Il *capitolo undicesimo* esplora le caratteristiche teoriche del trasporto associato ad un campo magnetico stocastico. Due applicazioni, una sul RFP l'altra sul tokamak, saranno descritte.

5 - Epilogo: le conclusioni sono tratte e una visione dello stato attuale della ricerca sugli stati elicoidali nel RFP sarà proposta, assieme alle prospettive future che possono essere individuate.

Appendici: in cui verrà descritto più in dettaglio il lavoro numerico e verranno date maggiori informazioni sull'esperimento RFX-mod.
Nell'*appendice A* verrà descritto il lavoro di verifica numerica tra i codici NEMATO e ORBIT. Il codice ORBIT, uno degli strumenti più usati per tracciare le linee di campo magnetico, verrà descritto. Nell'*appendice B* verrà descritto il lavoro di parallelizzazione del codice NEMATO. L'*appendice C* descrive l'esperimento RFX-mod che opera a Padova, in Italia.

Contents

I

Prologue

1

Fusion energy and plasma confinement

The improvement of the standard of living of a growing world population implies a significant increase in the energy consumption. This is one of the most difficult challenges that the international community has to face at the beginning of the millennium. The solution is represented by the combined use of different energy sources, to overcome the intrinsic limitations that each of them presents (reserves, toxic emissions, availability, CO_2 production and the climate change it implies).
Energy from nuclear fusion will likely play an important role in the forthcoming energetic scenario, given its virtually unlimited fuel reserves and low environmental impact.
This chapter deals with the basic principles of nuclear fusion and fusion energy production. The definition of plasma will also be given, as this is the state of matter at the high temperatures required to have a significant number of nuclear reactions. The main plasma confinement approaches will be discussed, notably the magnetic and the inertial ones.
Outline of the chapter. The chapter deals with the nuclear fusion and with the methods used to produce and confine fusion plasmas.
Section 1.1 will discuss the nuclear fusion reaction. To achieve nuclear fusion matter has to be in the plasma state, defined in section 1.2, and plasma has to be confined magnetically (the basic principles are tackled in section 1.3). The two main configurations for the magnetic confinement of fusion plasma, namely the tokamak (section 1.4) and the stellarator (section 1.5), will be then described.

1.1 Thermonuclear fusion

Nuclear fusion is the reaction between two light nuclei that fuse into a heavier one, releasing energetic reaction products. Fusion reactions are known to provide the huge energy production in stars.
Studies about the nuclear properties of light nuclei show that there are three main reactions exploitable in laboratory to produce energy. These reactions, that are different from those active in the sun, involve deuterium (^{2}H), tritium (^{3}H) and helium-3 (^{3}He). The main need for fusion to occur is the overcoming of the coulombian barrier existing between charged particles: fusion achievement thus excludes the use of heavier nuclei (with higher electric charge and thus higher coulombian barrier, that scales as the squared effective nuclear charge, Z^2). The controlled reaction that uses the particles' thermal energy to overcome the coulombian barrier is called *thermonuclear controlled fusion*.
The main reactions are:

$$
\begin{aligned}
{}^2_1\mathrm{D} + {}^2_1\mathrm{D} &\rightarrow {}^3_1\mathrm{T}(1.0\ \mathrm{MeV}) + p(3.0\ \mathrm{MeV}) \\
{}^2_1\mathrm{D} + {}^2_1\mathrm{D} &\rightarrow {}^3_2\mathrm{He}(0.8\ \mathrm{MeV}) + n(2.5\ \mathrm{MeV}) \\
{}^2_1\mathrm{D} + {}^3_1\mathrm{T} &\rightarrow {}^4_2\mathrm{He}(3.5\ \mathrm{MeV}) + n(14.1\ \mathrm{MeV}) \\
{}^2_1\mathrm{D} + {}^3_2\mathrm{He} &\rightarrow {}^4_2\mathrm{He}(3.6\ \mathrm{MeV}) + p(14.7\ \mathrm{MeV})
\end{aligned}
$$

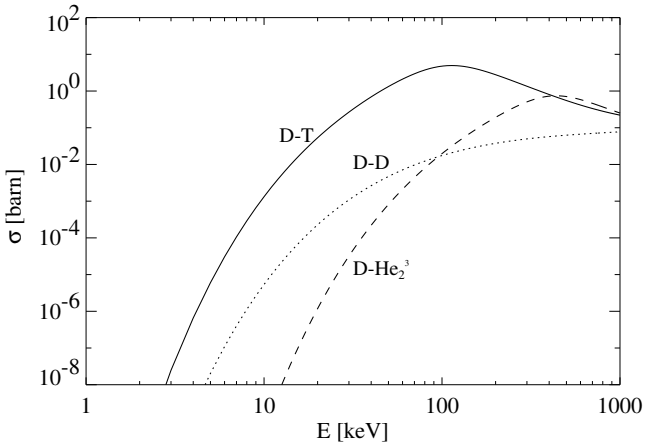

Figure 1.1: Cross section of the tipical fusion reactions:(D-T), (D-D) (D-^{3}He). It mimics the reaction probability as a function of reactant energy. $1\ \mathrm{barn} = 10^{-28}\ \mathrm{m}^2$.

The coulombian barrier is more easily overcome at precise value of energy of the reactants, as it can be noticed looking at figure 1.1 where the reactions' cross sections are

plotted against reactant kinetic energy. The most promising reaction is the D-T one, which has the highest reaction's cross section at a temperature of $\sim$15 keV, where matter is in the *plasma* state.
The tecnological-scientifical problem connected with the achievement and the maintenance of the temperature and of the density conditions leading to a sufficient number of thermonuclear fusion reactions is called *plasma confinement*.

1.2 Fusion plasmas

A plasma is a quasi-neutral ionized gas that possesses a high electrical conductivity and whose behaviour is dominated by collective effects. Two criterions must be satisfied for an ionized gas to be considered a plasma.
The first criterion involves the role of the high electrical conductivity, that results in the ability to shield electrical fields. It is shown [Freidberg, 2007] that the maximum spatial dimension over which charge unhomogeneity can appear is given by the *Debye length*, defined as:

$$\lambda_D = \sqrt{\frac{\varepsilon_0 T_e}{n_e e^2}}, \tag{1.1}$$

where T_e and n_e are the electron temperature and density.
Plasma behaviour requires $\lambda_D \ll L$, where L represents the typical macroscopic length of the plasma. Charge inhomogeneities are shielded in a time scale given by the *plasma frequency*:

$$\omega_p = \sqrt{\frac{n_e e^2}{m_e \varepsilon_0}}. \tag{1.2}$$

The second criterion defines the role of collective effects. In order for collective effects to dominate the number of particles that must be present in a sphere whose radius is equal to λ_D (this quantity is denoted by Λ_D) must be much greater than one. Low collisionality (that means low level of local coulombian interaction and long range collective effects dominating) implies:

$$\Lambda_D = \frac{4\pi}{3} \frac{\varepsilon_0^{3/2}}{e^3} \frac{T_e^{3/2}}{n_e^{1/2}} \gg 1. \tag{1.3}$$

1.3 Plasma magnetic confinement

Plasma can be confined gravitationally, inertially or magnetically.
Stars confine the plasma by the only action of gravitational interaction. The thermonuclear reactions provide the energy that prevent the stars from collapsing under the action of their own gravitational attraction.

Inertial confinement fusion relies on the heating and compression of a target of deuterium and tritium using laser light. For more information the reader is referred to [Pfalzner, 2006].
The magnetic confinement concept is based on the behaviour of a charged particle in an electromagnetic field. The Lorentz force on a charged particle is given by:

$$\mathbf{F} = q(\mathbf{v} \times \mathbf{B} + \mathbf{E}) \tag{1.4}$$

Under the action of this force a particle girates around the magnetic field lines with a radius and a frequency called *Larmor radius* and *cyclotron frequency*, defined as:

$$r_L = \frac{mv_\perp}{q|B|} \qquad\qquad \omega_c \equiv \frac{q|B|}{m}, \tag{1.5}$$

where $v_\perp$ is the velocity perpendicular to the $\mathbf{B}$ vector.
Thus a plasma can be confined by magnetic fields. The best topological configuration to avoid particle losses is the toroidal one. In particular magnetic field lines need to be twisted to avoid the drift motions, like the outward $\mathbf{E} \times \mathbf{B}$ drift (see [Freidberg, 2007]) that would cause large particle losses in a purely toroidal magnetic field. Three main configurations for twisting the magnetic field lines have been invented in the 50's and in the 60's: the tokamak, the stellarator, and the Reversed-Field Pinch (RFP).

1.3.1 Magnetic field-related parameters

In this section a list of three important parameters related to the magnetic field and to the energy confinement will be defined.
The magnetic field lines' twist is a fundamental quantity to deal with the problem of the stability of the plasma column. It is quantified by the safety factor q, that describes the number of toroidal turns that a magnetic field line performs while making one poloidal turn around a magnetic axis. In cylindrical approximation a form of the safety factor is given by:

$$q(r) = \frac{rB_\phi}{R_0 B_\theta}, \tag{1.6}$$

where R_0 represents the major radius of the torus. B_ϕ and B_θ represent the toroidal and poloidal magnetic field components, while r is a radial coordinate.
The pinch parameter Θ, defined as:

$$\Theta = \frac{B_\theta(a)}{\langle B_\phi \rangle} = \frac{\mu_0 a I_P}{2\Phi}, \tag{1.7}$$

is proportional to the ratio between plasma current I_P and the toroidal flux Φ; $\langle\bullet\rangle$ represents the average over a fixed poloidal section, a the minor radius of the torus.
The quantity β is a measure of how effectively the applied magnetic fields confine plasma pressure. It can be defined as the ratio between kinetic and magnetic pressure:

$$\beta = \frac{2\mu_0\langle p\rangle}{B_{\phi a}^2 + B_{\theta a}^2}. \tag{1.8}$$

Usually the normalized beta (or Troyon factor) β_N is used as an operational parameter to indicate how close the system is to strongly destabilizing MHD activity (that will be described in chapter 3). Its definition is:

$$\beta_N = \beta\frac{aB_0}{I_P}, \tag{1.9}$$

with B_0 representing the on-axis magnetic field. Typically the maximum reached β_N values are around 4.

1.4 The tokamak

The tokamak configuration was invented in 1952 and in the present days represents the most promising toroidal axisymmetric configuration for fusion plasmas confinement.
The plasma is created by the action of a central solenoid that produces a time varying poloidal magnetic flux which induces a toroidal loop voltage. Together with the low but finite plasma resistivity this creates a toroidal current.
The toroidal magnetic field is provided by magnets. The poloidal component of the magnetic field, typically a factor of ten weaker, is generated by the plasma current itself, providing the fundamental ingredient for the field lines' twist. In a tokamak $\Theta < 1$, meaning that the magnetic field produced by the plasma itself is much weaker than the one produced by the external coils.
Plasma pressure and the expansion force of a closed current loop would tend to create a force directed outward that is balanced by a set of so called *vertical field coils*.
The performance of tokamak fusion experiments, measured by the fusion triple product $nT\tau_E$ [Freidberg, 2007], has grown exponentially in the last decades, representing one of the main successes of this configuration. In the formula n represents plasma density, T the plasma temperature and τ_E the energy confinement time (that measures the scale on which thermal energy from the plasma can be confined). The values in time of this important parameters are shown in figure 1.2. The empirical scaling law for the energy confinement time τ_E is shown in figure 1.3, where its dependence on some important plasma quantities is also described.

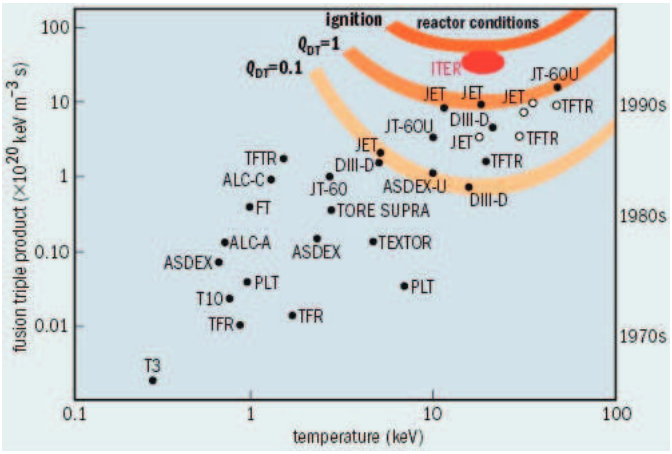

Figure 1.2: Behaviour of the fusion triple product $nT\tau_E$ with respect to time (right axis) and core temperature of the selected devices (x-axis). Note that ITER construction should be completed, as is planned at the beginning of 2013, in 2020.

The main tokamak under construction is ITER (International Thermonuclear Experimental Reactor). It is an international project involving worldwide cooperation and an investment of billions of euro. The aim of the scientifical community is the demonstration of scientific possibility of obtaining power from fusion. After this step the problem of its technological and economical feasibility will be faced with the DEMO experiment. A picture of ITER, with some technical data, can be found in figure 1.4.

1.5 The stellarator

The stellarator configuration was proposed in 1951 in Princeton plasma physics laboratory [`http://www.pppl.gov/about/history`]. The main feature of this configuration is that the field lines' twist is created solely by the action of an external coil system. This condition, that can not be satisfied by axisymmetric device, makes the stellarator intrinsecally 3D and represents a source of complexity both from the physical and the technological point of view.

The first advantage of the stellarator is that its operations are not limited by the magnetic induction effect of the central solenoid, like in tokamaks and RFPs. A second advantage is represented by the low plasma current (a pressure driven current component, due to toroidal effects, is present despite the original stellarator concept is free from plasma current) that avoids the *disruption* process: a disruption is a sudden loss of thermal energy followed by a fast termination of the discharge. This can cause strong thermal and mechanical stresses on the machine's components, being one of the major causes of concern for the next generation of tokamaks experiments.

The main physical problems of this configuration are the high level of neoclassical

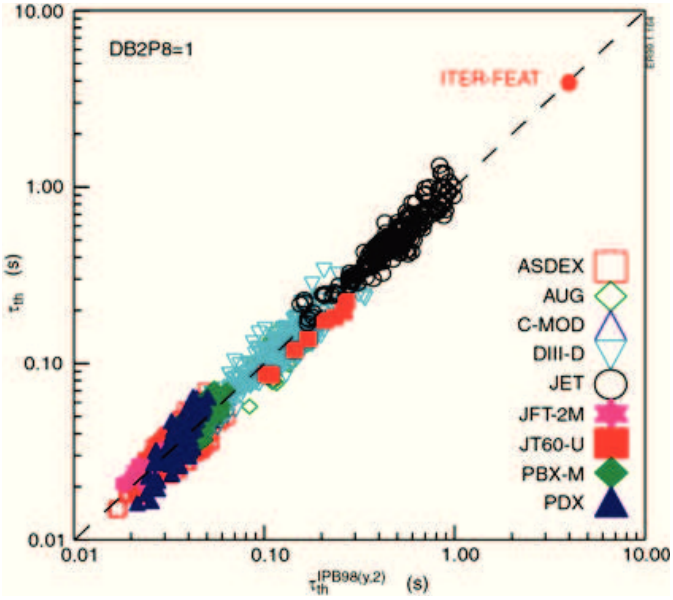

Figure 1.3: Empirical energy confinement time scalings for the biggest tokamak experiments in the world: one important information is the linear increase of τ_E with the plasma current I_P, that can be appreciated by the formula $\tau_E \approx H I_P^{0.93} P_{heat}^{-0.63} B_\phi^{0.15}$, with H measuring the quality of confinement relatively to the scaling law.

transport: this requires an elaborate optimization to achieve the necessary confinement. This optimization process has to deal with a large set of issues: it has to sufficiently confine thermal plasma and fast ions, to allow reliable operations at high plasma densities and pressure, to take into account the role of wall materials and the effect of impurities. This process has been performed, in particular for the construction of the W7-X (see figure 1.5) stellarator in Germany [Wolf, 2008]: this device should allow operations and MHD stability up to $\beta \approx 5\%$ and a small level of neoclassical transport.

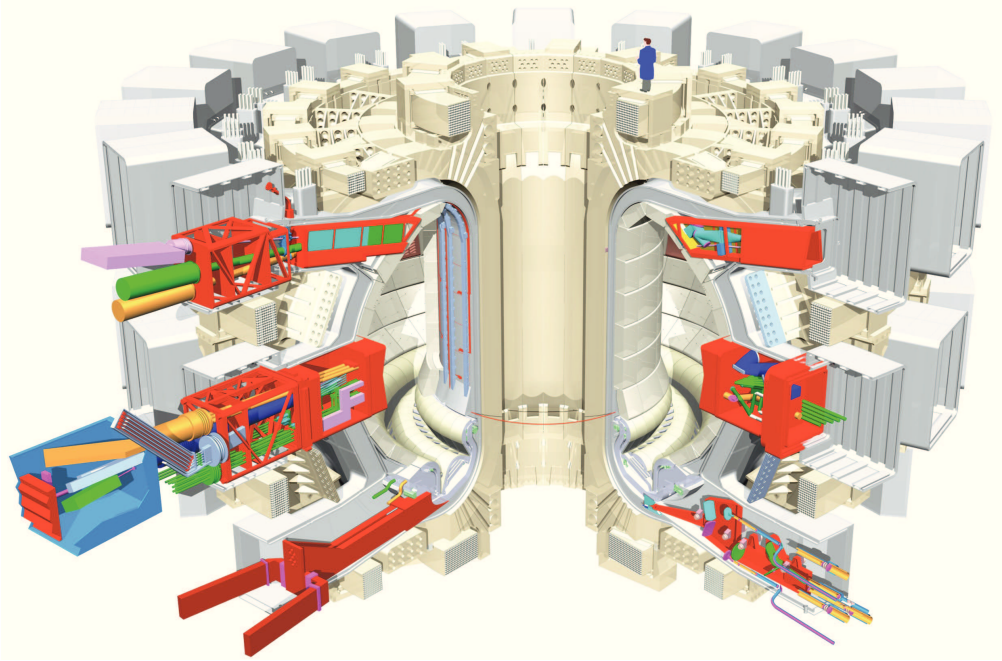

Figure 1.4: A picture of the ITER experiment that is being built in the south of France. Some technical data: main radius 6.2 m, minor plasma radius 2.0 m, magnetic field at R_0 will be 5.3 T, maximum plasma current 17 MA, total weight 23000 tons, discharge time 400 s, average electron temperature 8.8 keV, fusion power 400 MW.

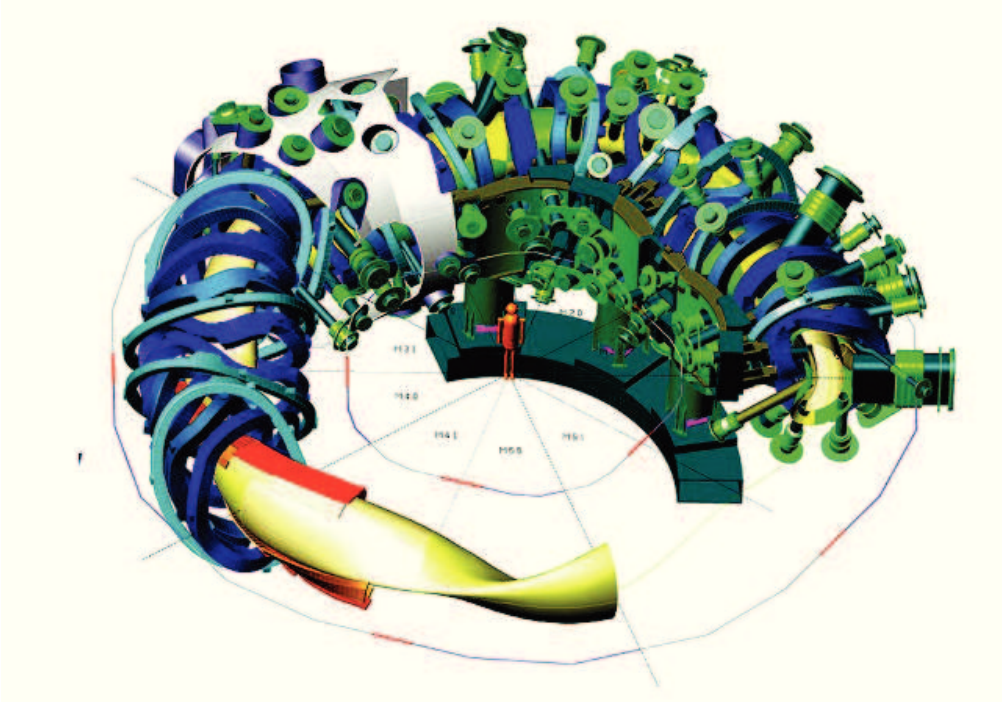

Figure 1.5: A picture of the Wendelstein 7-X experiment that is being built in Greifswald. Some technical data: diameter of the device will be 16 m, main radius 5 m, minor plasma radius 0.53 m, magnetic field 3 T, total weight 725 tons, discharge time 30 mins.

2

The reversed-field pinch configuration

The Reversed-Field Pinch (RFP) is a toroidal pinch configuration (nominally axisymmetric) for the magnetic confinement of fusion plasmas [Ortolani and Schnack, 1993]. The RFP is similar to the tokamak as both the configurations exploit the pinch effect, i.e. the self-confinement effect obtained driving a toroidal electrical current on a plasma embedded in a toroidal magnetic field.
A new paradigm, supported by theoretical, numerical and experimental evidences describes the configuration as a self-organized state based on the saturation of a single resistive-kink tearing mode which leads to a regime of reduced chaotic transport [Escande et al., 2000a]. This paradigm outdates a previous picture of the RFP as a device prone to a heavy turbulent MHD activity due to the relatively higher current driven in this configuration. Depending on the ability to further reduce transport, the configuration would have several positive features. For example, with the same on-axis toroidal field the configuration has a much higher value of plasma current, which results in the possibility of heating the plasma through ohmic dissipation without employing additional heating systems. Furthermore the weaker edge toroidal field implies that a less expensive technology is required to build the reactor's magnets. From the theoretical point of view, see [Freidberg, 1987], the favourable MHD stability properties for pressure driven modes leads to the possibility of operating the configuration at a β value higher than the one found in tokamaks. In this chapter an introduction to the RFP configuration will be given, focusing on theoretical, numerical and experimental results.
Outline of the chapter. This chapter deals with the RFP configuration for the magnetic confinement of fusion plasma.
After a general introduction to the RFP in section 2.1, the study of the magnetic configuration is developed from the theoretical (section 2.2), numerical (section 2.3) and

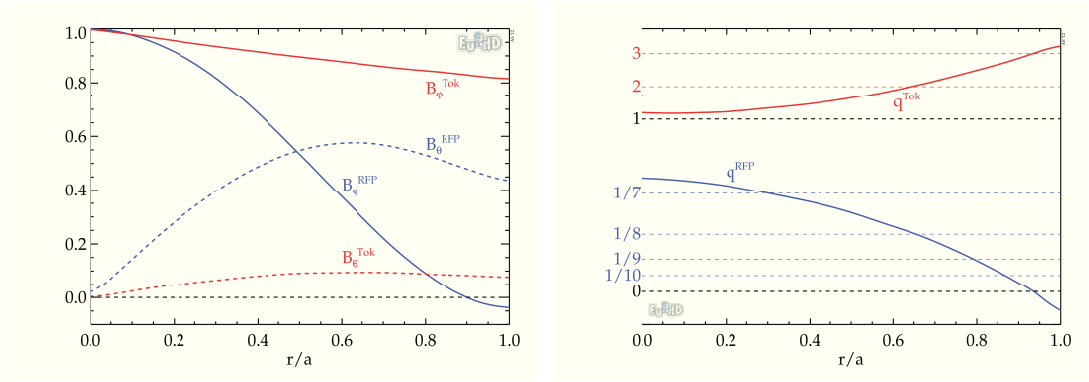

(a) **(b)**

Figure 2.1: a) Radial profiles of the toroidal and poloidal magnetic field for a RFP configuration. **b)** Radial profile of the safety factor.

experimental (section 2.4) point of view.

2.1 The Reversed Field Pinch

The RFP is a toroidal configuration for the magnetic confinement of fusion plasmas whose main feature is that the toroidal component of the field has the same order of magnitude as the poloidal one (in fact the RFP has a pinch parameter $\Theta > 1$, see equation 1.7 for the definition of Θ). A picture of the mean axis symmetric field is given in figure 2.1a. A second feature is the reversal of the toroidal component of the magnetic field next to the plasma edge. The small edge value of the toroidal component indicates that the external coils produce a little part of the magnetic field only: this is the signature that magnetic fields in the RFP configuration are produced by the plasma current itself through a process of self-organization, which will be intuitively explained later in this chapter.
A parameter, called *reversal parameter*, describes the depth of the reversal of the field at the edge:

$$F = \frac{B_\varphi(a)}{\langle B_\varphi \rangle}. \tag{2.1}$$

The RFP is often described showing the relation between the Θ and F parameters, that can be observed in figure 2.2 (see [Cappello, 2004]).

2.2 Theory

This section aims at giving a description of the RFP from a theoretical point of view. This description will be given first using two intuitive descriptions of why the axial

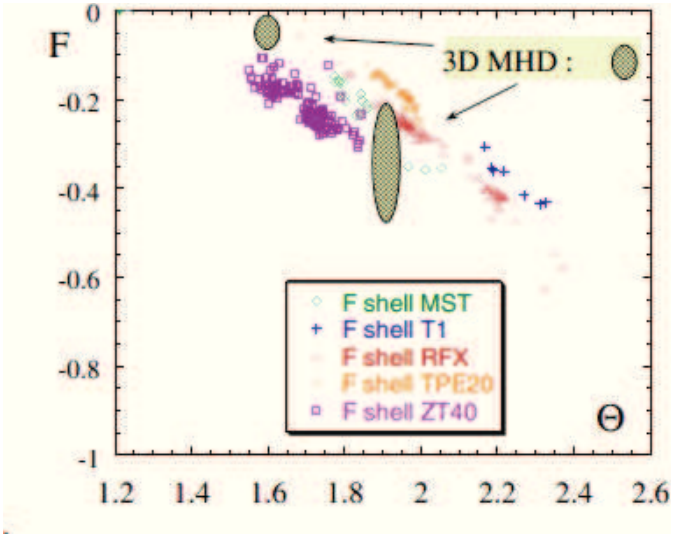

Figure 2.2: Diagram showing the relation between the pinch parameter Θ and the reversal parameters F in several experiments and nonlinear 3D MHD simulations. Note the reversal of the toroidal field for $\Theta > 1.4$.

component of the magnetic field reverses and of why an helical deformation of the plasma column is necessary to obtain the reversal (no axis-symmetric RFP exists).
In the second part of this section the first steps towards an analytical description of the Single Helicity (SH) ohmic RFP equilibrium configuration will be described.

2.2.1 Intuitive description of the RFP

Two intuitive descriptions of why the magnetic field reverses and of why an axis-symmetric RFP ohmic equilibrium can not exist will be proposed in this section. First the wire model will be proposed to explain why the axial component of the magnetic field reverses. This model also provides a first hint to a vision of the RFP as a device subject to a helical deformation supplied by the nonlinear saturation of a resistive kink instability. This vision is supported by numerical simulations, see section 2.3.
Then a theorem stating that no axis-symmetric ohmic RFP can exist will be demonstrated.

The wire model

Consider a wire placed in the axis of a hollow cylinder with conductive walls, which therefore conserves magnetic flux [Escande et al., 2000a]. The presence of poloidal currents on the cylindrical shell ($I_{\theta shell}$) maintains an initial axial magnetic field that can interact with the current flowing on the wire (I_{wire}): the equilibrium is an unstable one.

In fact a small kink perturbation can create a poloidal component of the wire current that attracts it towards the shell (if $I_{\theta,wire}$ has the same direction of $I_{\theta shell}$) and increases its distortion. This implies that $I_{\theta,wire}$ and the $\mathbf{B}$ inside the wire raises and that I_{shell} diminishes, as the magnetic flux has to be conserved. As different portions of the helical wire carry currents in opposite directions the instability can not come to an end and the growth of the magnetic flux inside the wire forces the outside magnetic field and I_{shell} to reverse. Then the instability saturates due to the opposite currents in the shell and in the wire.

Cowling theorem for the RFP

The possibility of an axis-symmetric pinch configuration with a reversal of the axial component of the magnetic field at the edge is ruled out by a *Cowling theorem for the RFP*.
The original version of the Cowling theorem, used in the astrophysical field, states that an axis-symmetric magnetic configuration can not be maintained by axis-symmetric dynamo velocity fields.
A *Cowling theorem for the RFP* can be stated in the framework of the cylindrical MHD resistive force-free model (that is introduced in chapter 3).

Theorem 1 (Cowling's theorem for the RFP) *No axis-symmetric dynamo can maintain an axis-symmetric RFP magnetic field.*

Proof, as given in [Escande et al., 2000a]: The theorem can be proved by absurd. Consider the resistive MHD equilibrium equations, given by:

$$\nabla \cdot \mathbf{B} = 0 \tag{2.2a}$$

$$\mathbf{J} \times \mathbf{B} = 0 \tag{2.2b}$$

$$\nabla \times \mathbf{B} = \mathbf{J} \tag{2.2c}$$

$$\mathbf{E} + \mathbf{v} \times \mathbf{B} = \eta \mathbf{J}. \tag{2.2d}$$

$\mathbf{J}$ and $\mathbf{B}$ represent the current and the magnetic field, $\mathbf{v}$ the fluid velocity and $\mathbf{E} = E_0 \hat{\mathbf{z}}$ an externally imposed electric field .
Equation 2.2b, describing the force-free condition, states that $\mathbf{J} = \mu \mathbf{B}$. Taking the parallel component of 2.2d gives $E_0 B_z = \eta \mu B^2$: this means that if B_z reverses so does μ.
From 2.2c and 2.2b and keeping in mind that the system is axis-symmetric one obtains $J_\theta = -\frac{\partial B_z}{\partial r} = \mu B_\theta$. This means that when μ reverses J_θ must be zero (B_θ is always positive, being produced by an inductively driven toroidal current) and so must be $\frac{\partial B_z}{\partial r}$. This is absurd, as B_z can not be minimum at its reversal. Thus the axis-symmetry has to be broken to obtain a RFP.

2.2.2 Analytical description of the RFP

In this section the actual state in the research towards an analytical theory of the single helicity (SH) ohmic RFP configuration is presented. The helical Grad-Shafranov equation and the parallel Ohm's law are considered. This analytical calculations represent the attempt to go beyond Taylor relaxation theory [Taylor, 1986], that was considered a reference for the RFP description but that is now falsified by a series of experimental and theoretical results. A criticism of Taylor theory is presented in section 7 of [Cappello et al., 2008], where the advantages of the new paradigm here presented are also listed.

Helical Grad-Shafranov equation

A complete derivation of the helical Grad-Shafranov equation, that sums up the equilibrium described by equations 2.2, can be found in [Bonfiglio et al., 2011] and [Finn et al., 1992]. The essential step will be proposed here, using the resistive MHD model in cylindrical geometry (r, θ, z) in the force-free limit, $p = 0$.
The SH state is defined by the mode poloidal and toroidal mode number m and n: all the quantities depend on r and on $u = m\theta + kz$, $k = -n/R$ and $2\pi R$ is the axial periodicity. Considering a $A_r = 0$ gauge the magnetic field can be written as:

$$\mathbf{B} = \nabla\Psi \times \nabla z + \nabla\Phi \times \nabla\theta. \tag{2.3}$$

Ψ and Φ represent respectively the poloidal and toroidal flux functions. In term of the helical flux $\chi = m\Psi - k\Phi$ the magnetic field can be written as:

$$\mathbf{B} = \nabla\chi \times \mathbf{h} + g\mathbf{h}. \tag{2.4}$$

Here g represents a *helical magnetic field* $g = r\mathbf{B} \cdot \boldsymbol{\sigma} = r\mathbf{B} \cdot (\nabla r \times \nabla u)$.
The vector h is given by $h = f(r)\boldsymbol{\sigma} = r/(m^2 + k^2 r^2)\boldsymbol{\sigma}$. From this definition is comes that $\mathbf{B} \cdot \nabla\chi = 0$, meaning that χ is constant on magnetic field lines that lie on constant χ flux surfaces labelled as S_χ. Using the Maxwell's equation $\mathbf{J} = \nabla \times \mathbf{B}$ the force free equation $\mathbf{J} \times \mathbf{B} = 0$ can be rewritten to obtain the *helical Grad-Shafranov equation* just by taking its component parallel to the vector $\mathbf{h}$.
The essential definition needed are: λ defined by $\mathbf{J} = \lambda\mathbf{B}$ and the derivative
$\triangle_h = f^{-1}(\partial_r(f\partial_r\chi) + r^{-1}\partial_u^2\chi)$.
The helical Grad-Shafranov equation is given by [Biskamp, 1992]:

$$\triangle_h\chi = g\beta - g\, dg/d\chi, \tag{2.5}$$

with $\beta = -2mk/(m^2 + r^2k^2)$. If one considers the tokamak-like axis-symmetric case $m = 1, n = 0$ the Grad-Lüst-Rubin-Schlüter-Shafranov equation [Lüst and Schlüter, 1957; Shafranov, 1958; Grad and Rubin, 1958] is recovered.

Definition of the helical q-profile and of $\mathbf{q_h}$

The helical q profile $q(\chi)$ gives the number of toroidal turns that field lines (lying on the magnetic surface S_χ) perform for one poloidal turn around the helical axis. It represents the first attempt to account for the actual three-dimensional nature of the magnetic flux surfaces. A general definition is given by [Freidberg, 1987; D'haeseleer et al., 1991]:

$$q(\chi) = \frac{d\Phi(\chi)}{d\Psi(\chi)}, \tag{2.6}$$

with Φ and Ψ are respectively the toroidal and poloidal flux across the surface S_χ.
The case of a SH magnetic field can be treated introducing flux coordinates or, in an hamiltonian description of the magnetic field, introducing action-angle variables corresponding to the integrable dynamics defined by the helical flux function $\chi(\Phi, u)$. The introduction of the new coordinates results in the unique dependence of the helical flux function on the quantity Φ_h, that represents the toroidal flux inside a flux surface S_χ. In formulae:

$$\chi = \chi(\Phi_h) \tag{2.7}$$

As in the hamiltonian vision Φ_h is a constant of the motion, it is possible to define the helical rotational transform $\iota_h = \partial\chi/\partial\Phi_h$ and then the q_h quantity:

$$q_h = \iota_h^{-1} = \frac{\partial\Phi_h}{\partial\chi}. \tag{2.8}$$

Parallel Ohm's law

The use of Ohm's law allows to complete the analytical definition of the SH *ohmic* RFP state. The generalized Ohm's law (described in 3.2.2) is given by:

$$\mathbf{E} + \mathbf{v} \times \mathbf{B} = \eta\mathbf{J} + \frac{\mathbf{J} \times \mathbf{B} - \nabla p_e}{ne} \tag{2.9}$$

The basic assumptions in treating Ohm's law is that the electronic pressure is constant along magnetic field lines ($\nabla p_e \cdot \mathbf{B} = 0$) and that the electric field is stationary, $\mathbf{E} = E_0\hat{\mathbf{e}}_z - \nabla\phi$.
The *parallel Ohm's law* is obtained calculating the Ohm's law equation in the magnetic field direction:

$$\mathbf{B} \cdot \nabla\phi = E_0\mathbf{B} \cdot \hat{\mathbf{e}}_z - \eta\mathbf{B} \cdot \mathbf{J}. \tag{2.10}$$

A more interesting form can be obtained averaging the parallel Ohm's law over the S_χ helical flux surfaces obtaining the *average parallel Ohm's law*:

$$0 = \langle \mathbf{B} \cdot \nabla \phi \rangle_\chi = E_0 \langle \mathbf{B} \cdot \hat{\mathbf{e}}_z \rangle_\chi - \langle \eta \mathbf{B} \cdot \mathbf{J} \rangle_\chi, \tag{2.11}$$

where the first equality comes from the fact that the average is over the flux surfaces [1]. The average is defined as:

$$\langle K \rangle_\chi = \frac{\int_{D(\chi)} K dV}{\int_{D(\chi)} dV}, \tag{2.12}$$

with $D(\chi)$ representing the volume inside the flux surface labelled S_χ. Using the force-free condition the average parallel Ohm's law becomes:

$$E_0 \langle \mathbf{B} \cdot \hat{\mathbf{e}}_z \rangle_\chi = \lambda \langle \eta \mathbf{B}^2 \rangle_\chi. \tag{2.13}$$

It was used the fact that λ is a flux function, as it can be shown taking the divergence of equation $\mathbf{J} = \lambda \mathbf{B}$ and considering that both $\mathbf{J}$ and $\mathbf{B}$ are solenoidal fields.
At this point the next step is the perturbations of the SH ohmic RFP equations (2.13) and (2.5), but the mathematical complexities rapidly rise. A recently developed path, well described in [Bonfiglio et al., 2011], is the derivation of an equation valid only for the averaged axial component of the magnetic field, $\langle B_z \rangle_\chi$, called *pinch-stellarator equation*:

$$\frac{d}{d\chi} \langle B_z \rangle_\chi = \frac{E_0}{\langle \eta \mathbf{B}^2 \rangle_\chi} \langle B_z \rangle_\chi + S(\chi) \tag{2.14}$$

Two important consequences of this equation can be stated here. The first is that if an axially symmetric pinch is considered it can be shown that the stellarator term $S(\chi)$ is equal to zero: thus the equation implies the impossibility of a reversal of the quantity $\langle B_z \rangle_\chi$, confirming Cowling's theorem for the RFP. The second consequence is that if $S(\chi)$ is positive in a finite edge radial domain in χ the quantity $\langle B_z \rangle_\chi$ can reverse in that domain.

2.3 Numerical studies

The RFP can be simulated numerically by using the nonlinear MHD model, which will be introduced and widely explained in chapter 3.
A most used approximation is the visco-resistive MHD model, in the force-free or low β limit [Cappello and Biskamp, 1996; Stephens et al., 2010; Sovinec et al., 2003; Schnack et al., 1987]. The model equations are given in dimensionless form by:

[1] The relation $\langle \mathbf{B} \cdot \nabla \phi \rangle_\chi = 0$ comes from the divergence theorem: $\int_{D(\chi)} \mathbf{B} \cdot \nabla \phi dV = \int_{S_\chi} \phi \mathbf{B} \cdot \mathbf{d\Sigma} = 0$, because on a flux surface $\mathbf{B} \cdot \mathbf{d\Sigma} = 0$.

$$\frac{d\mathbf{v}}{dt} = \mathbf{J} \times \mathbf{B} + \nu \nabla^2 \mathbf{v} \tag{2.15a}$$

$$\frac{\partial \mathbf{B}}{\partial t} = \nabla \times (\mathbf{v} \times \mathbf{B} - \eta \mathbf{J}) \tag{2.15b}$$

$$\mathbf{J} = \nabla \times \mathbf{B} \tag{2.15c}$$

$$0 = \nabla \cdot \mathbf{B} \tag{2.15d}$$

In these equations resistive dissipation is described by η, the inverse Lundquist number, and viscosity by ν, the inverse magnetic Reynolds number. It turns out from extensive numerical studies that dissipation rules the numerical transition between two different RFP's dynamics [Cappello, 2004], also experimentally observed, namely the Single Helicity (SH) and the Multiple Helicity (MH) states.

2.3.1 Single Helicity states

The RFP's Single Helicity state is obtained when a single resistive kink/tearing perturbation saturates and a helical, stationary stable RFP configuration is obtained. This state represents a fluid upgrade of the lumped element model provided by the wire model presented in section 2.2.1.
The possibility of having a RFP plasma in such an equilibrium was found in the '80s through two dimensional numerical simulations. Later SH, states were also found in 3D numerical simulations in which no helicity was imposed [Cappello and Paccagnella, 1992]. Under the condition of high visco-resistive dissipation the MHD model foresees the onset of numerical SH states: the signature of these states can be found analysing the Fourier spectrum of the magnetic field and looking for states in which only the $(m = 1, n = h)$ mode and its harmonics $(n = hm)$ are present; in cylindrical and toroidal geometry m represents the poloidal wave number and n the axial or toroidal one.

2.3.2 Multiple Helicity states

As dissipation is decreased other modes can become unstable and the system enters in a non-stationary MH regime characterized by a broad spectrum of Fourier modes with $m = 1$ and different n values. The nonlinearity of 2.15 also produce a wide spectrum of $m \neq 1$ modes.
The MH character of the magnetic field results in the production of a series of magnetic islands corresponding to resistive kink/tearing modes resonating at rational values of the q profile (see section 3.6.2). The interaction between these magnetic structures

makes the dynamic of the field line chaotic, with detrimental effect on the confinement of energy and particles.

2.3.3 Numerical transition between MH and SH states

It has been found that the RFP dynamic is ruled, when the inertial terms in 2.15 are negligible, by a parameter called *Hartmann number* $H = (\eta\nu)^{-1/2}$ [Cappello and Escande, 2000].

At high H, as can be seen in the figure 2.3, the Fourier spectrum of the magnetic field

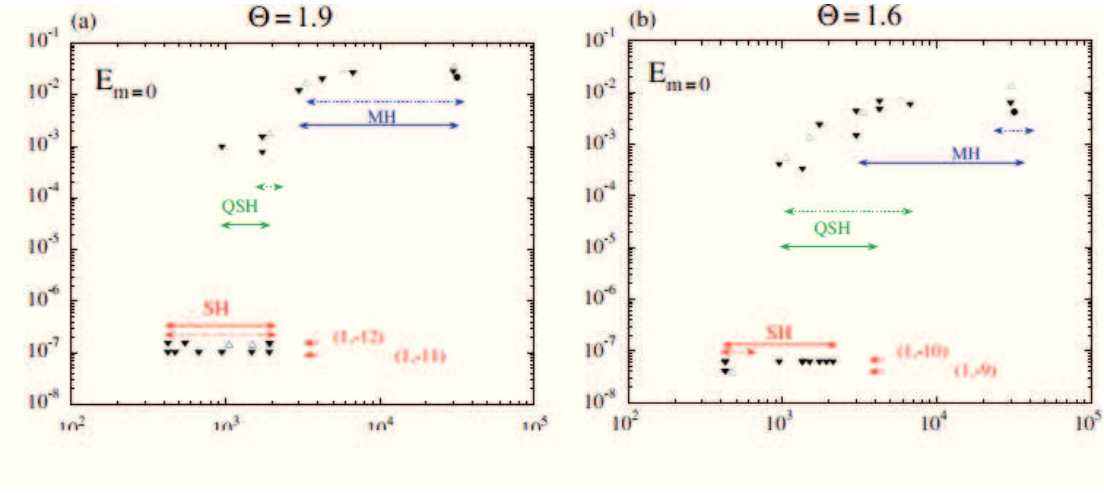

Figure 2.3: Time averaged magnetic energy of the spectral component $m = 0$ as a function of the Hartmann number H. Simulations are performed with the SPECYLcode. See [Cappello, 2004].

is characterized by a high energy of the $m = 0$ modes that nonlinearly couple the wide spectrum of $m = 1$ modes. As H decreases (dissipation raises) the energy of the $m = 0$ modes exponentially decreases and the system sets on a SH state.

When H decreases the transition from MH to SH states turns out to be continuous. In the medium H region the so-called Quasi Single Helicity (QSH) states are found. The transition details are also seen to depend on the pinch parameter Θ.

The results I present in this thesis show that QSH states can be obtained also at high H by imposing helical boundary conditions at the edge of the simulation domain. This is in agreement with the observation from RFP experiments. In fact QSH states are found at high current/temperature, i.e. at low resistivity (no experimental indication on the value of viscosity is available), and a remnant edge radial magnetic field persists.

2.4 Experimental results

The first decades of experimental study of the RFP configuration contributed to give a picture of the RFP as a system characterized by a very high level of magnetic turbulence and poor energy confinement time due to chaotic magnetic field lines and high plasma-wall interaction. The features of these experimental states are the same that can be found in the numerical simulation of MH states.
After 2000 plasmas in various RFP devices around the world were observed more often in quasi helical regimes, the so called Quasi Single Helicity (QSH) states: these states are found in various RFP experiment [Bartiromo et al., 1999; Escande et al., 2000b; Martin et al., 2003; Chapman et al., 2012; Sarff et al., 2013]. They are qualitatively similar to the previously described SH numerical regimes [Cappello and Paccagnella, 1992; Cappello and Biskamp, 1996; Cappello and Escande, 2000]. The expectation of better confinement properties due to chaos healing effects [Escande et al., 2000c] are still under development: a significant confirmation was achieved with the emergence of internal transport barriers, detected in terms of strong local gradients of the electron temperature profiles in phases of achieved helical equilibrium [Lorenzini et al., 2009].
In the next subsections the experimental features of MH and QSH states will be briefly presented.

2.4.1 Experimental MH states

The experimental MH states are characterized by a high level of MHD activity: a broad spectrum of magnetic modes, in particular many $m = 0$ and $m = 1$ modes with comparable amplitude, are measured. The magnetic islands they form overlap each other, destroying the magnetic surfaces. This allows magnetic field lines to move rapidly from the plasma core to the plasma edge, with detrimental effects on confinement.
The experimental measurements highlight a quasi-periodical oscillation of various physical quantities, which can be interpreted as dynamo relaxation events (that group together the whole magnetic activity that leads the system to a state characterized by a lower energetic content). Images of the plasma core obtained through soft X-ray (SXR) tomography display a poloidally symmetric emissivity. This is in agreement with the existence of a chaotic magnetic field which transports energy in the whole plasma volume.

2.4.2 Experimental QSH states

The experimental QSH states are characterized by the presence of a dominant MHD mode with $m = 1$ whose amplitude is several times that of the other MHD modes. The

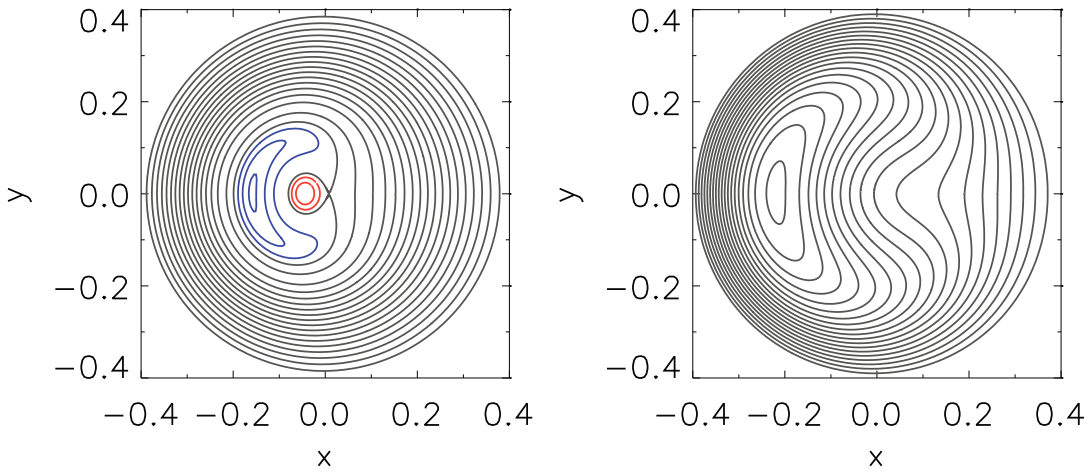

(a) **(b)**

Figure 2.4: a) Magnetic surfaces topology (on a $z = cost$ plane) in a DAx case. **b)** On a SHAx case.

presence of such a dominant helical mode is seen in the measurements by many different diagnostics as soft-X-ray emission tomography, magnetic measurements, Thomson scattering in many RFP devices [Martin et al., 2003]. All these diagnostic show the presence of a hot 'bean-like' structure consistent with the helical shape of the magnetic flux surfaces that can be traced considering the helical flux function of numerical SH states. The RFP plasma self-organizes into a helical state [Lorenzini et al., 2009] that corresponds to two bifurcations: the first is represented by the transition from MH to QSH states and the second changes the magnetic field topology. The original topological state corresponds to a situation in which two magnetic axis are present (Double Axis, DAx, see figure 2.4a), one corresponding to the equilibrium field and the other to the magnetic island associated with the dominant MHD mode; these axis are separated by a separatrix magnetic surface. The final state is called Single Helical Axis (SHAx) state and is obtained when the magnetic separatrix merges with the main magnetic axis and a plasma column with a single helical axis is obtained, see figure 2.4b. This process is called *dominant mode separatrix expulsion*.

The transport properties of such QSH states are improved with respect to the MH states, as can be seen in figure 2.5, where the electron temperature profiles measured in RFX-mod is shown (RFX-mod will be described in chapter C). The presence of an internal transport barrier [Puiatti et al., 2011; Martin et al., 2011] can be seen in figure 2.5d.

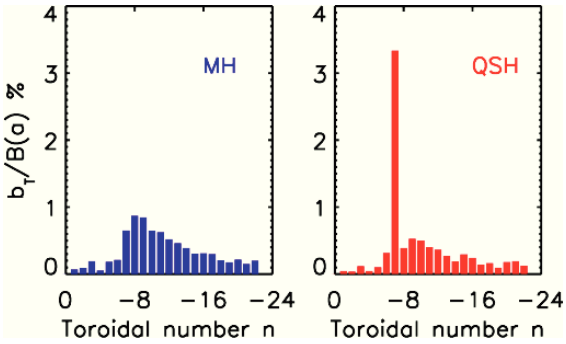

(a) MHD modes spectrum in MH-QSH(DAx) states

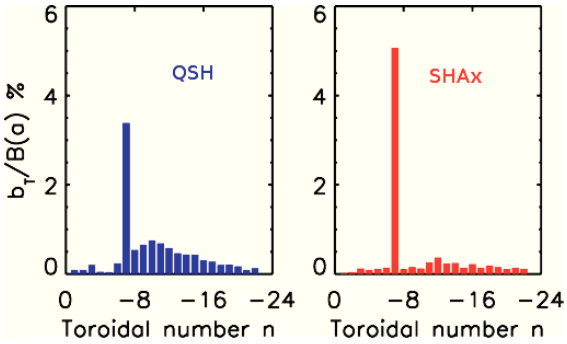

(b) MHD modes spectrum QSH(DAx)-QSH(SHAx) states

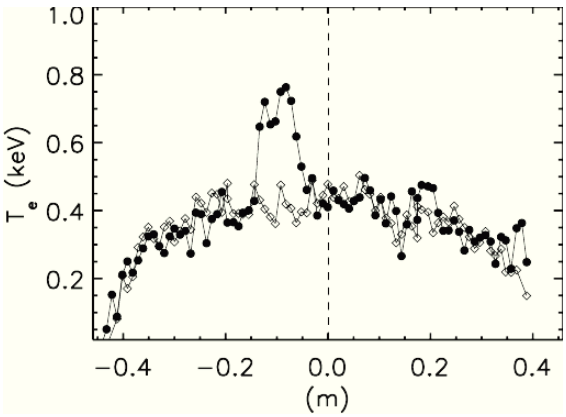

(c) Electronic temperature in MH states (white circles) and QSH(DAx) (black circles)

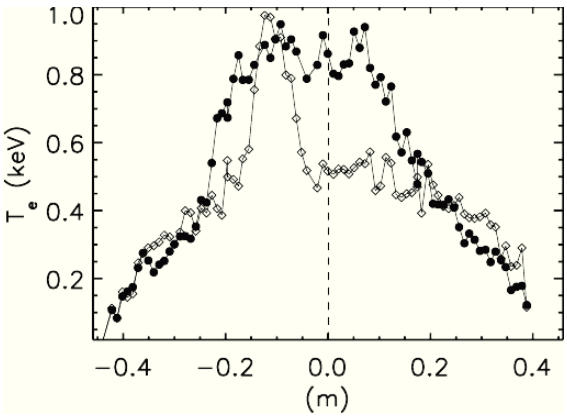

(d) Electronic temperature in QSH(DAx) states (white circles) and QSH(SHAx) (black circles)

Figure 2.5: Comparison between the MHD modes spectrum and the radial profile of the electronic temperature in the MH con QSH(DAx) configurations, figures **a)-c)**. Comparison between the MHD modes spectrum and the radial profile of the electronic temperature in the QSH(DAx) and QSH(SHAx) configurations, figures **b)-d)**. Note the progressive amplification of the high temperature region as the dominant mode becomes bigger in intensity.

II

Modelling tools

3

The magnetohydrodynamic model

First-principle models are of fundamental importance to obtain a physical understanding of the forces that rule the behaviour of a magnetized plasma. Such models describe how the current and charge density generated by the particles forming the plasma affect the electric and magnetic fields originally applied to magnetically confine a plasma and vice-versa, in a self-consistent way.

The first and most complete level of development of a self-consistent model is represented by the kinetic theory, whose aim is the determination of the plasma particles' distribution function.

The second level involves the derivation of *fluid models* for the different particles species present in the plasma (i.e. electrons and ions), macroscopically averaging the kinetic equations. Two requirements have to be fulfiled for a fluid model to be valid. First, the system has to be maintained close to the thermodynamical equilibrium by a (generalized) form of collisions between its components. In the case of fusion plasmas, usually characterized by a low collisionality, the magnetic field contributes to maintain a fluid-like behaviour of the species in its perpendicular direction.

Second, the average of the kinetic equations have to be performed into a sufficiently small element not to lose spatial resolution and sufficiently big to give a statistical sense to the averages.

The third level consists in a reduction of the *two fluid model* to a *single fluid* one, focusing on the relevant spatial and temporal scales for the study of the plasma macroscopic behaviour. An extended form of the magneto-hydro dynamic (MHD) model can be obtained after this process. Further assumptions lead to the derivation of the visco-resistive MHD model.

Outline of the chapter. This chapter deals with the MHD model for treating plasmas as a single fluid in an electromagnetic field.
Section 3.1 introduces the Boltzmann's equation in the framework of kinetic theory and the derivation of the dynamical model (fluid equations) for a two species hydrogen plasma through an averaging procedure. In section 3.2 the main assumptions that lead from a two-fluid to a single-fluid dynamical model (MHD) are described and the four main equation are analyzed. The meaning of viscosity and resistivity of a plasma is also discussed. In section 3.3 the extended MHD model equations are listed, while in section 3.4 the visco-resistive MHD model is introduced. In section 3.5 the equilibrium states that can be described by the MHD model are analyzed, while in section 3.6 the main instabilities that can arise from the equations are studied.

3.1 Fluid model

The most rigorous way to construct a self-consistent two-fluid model for a plasma is the derivation of a dynamical theory from the kinetic equations. The aim of this derivation, performed for example in [Bittencourt, 2004] and not shown here, is the calculation of macroscopic fluid variables like the *number density* n_α, the *flow velocity* v_α and the *temperature* T_α and of their dynamical evolution ($\alpha = i$ for ions and $\alpha = e$ for electrons). The differential equations governing the temporal and spatial evolution of these macroscopic variables can be obtained starting from the Boltzmann equation:

$$\frac{\partial f_\alpha}{\partial t} + \mathbf{u}\cdot\nabla f_\alpha + \mathbf{a}\cdot\nabla_u f_\alpha = \left(\frac{\delta f_\alpha}{\delta t}\right)_{coll}, \tag{3.1}$$

where $\mathbf{u}$ represent the velocity of the particles and $f_\alpha = f_\alpha(\mathbf{x},\mathbf{u},t)$ is the distribution function for the particles of species α. The quantity $\left(\frac{\delta f_\alpha}{\delta t}\right)_{coll}$ represents the rate of change of f_α due to collisions. The explicit dependence of f_α with $(\mathbf{x},\mathbf{u},t)$ will not be indicated anymore.
Fluid equations are moments of the Boltzmann equation. To obtain the fluid equations the momenta of order k of equation (3.1) have to be calculated. The momentum of order k applied to equation (3.1) is given by:

$$\int d\mathbf{u}\frac{m_\alpha}{k!}u_j^k\left(\frac{\partial f_\alpha}{\partial t} + \mathbf{u}\cdot\nabla f_\alpha + \mathbf{a}\cdot\nabla_u f_\alpha\right) = \int d\mathbf{u}\frac{m_\alpha}{k!}u_j^k\left(\frac{\delta f_\alpha}{\delta t}\right)_{coll}, \tag{3.2}$$

where m_α represents the mass of the particle of species α. Calculating the moments of order $k=0$, $k=1$ and $k=2$ and defining:

$$\mathbf{v}_\alpha = \langle\mathbf{u}_\alpha\rangle = \frac{1}{n_\alpha}\int d\mathbf{u}\mathbf{u}f_\alpha \tag{3.3}$$

the following set of equations can be obtained ($\alpha = i, e$):

$$\frac{\partial \rho_\alpha}{\partial t} + \nabla \cdot (\rho_\alpha \mathbf{v}_\alpha) = 0, \tag{3.4a}$$

$$\rho_\alpha \left(\frac{\partial \mathbf{v}_\alpha}{\partial t} + \mathbf{v}_\alpha \cdot \nabla \mathbf{v}_\alpha \right) = n_\alpha q_\alpha (\mathbf{E} + \mathbf{v}_\alpha \times \mathbf{B}) + \rho_\alpha \mathbf{g} - \nabla \cdot \mathcal{P}_\alpha - \rho_\alpha \sum_\tau \nu_{\alpha\tau} (\mathbf{v}_\alpha - \mathbf{v}_\tau), \tag{3.4b}$$

$$\frac{3}{2} n_\alpha \left(\frac{\partial T_\alpha}{\partial t} + \mathbf{v}_\alpha \cdot \nabla T_\alpha \right) + \mathcal{P}_\alpha : \nabla \mathbf{v}_\alpha + \nabla \cdot \mathbf{q}_\alpha = Q_\alpha. \tag{3.4c}$$

The operation : is defined as $\mathcal{P}_\alpha : \nabla \mathbf{v}_\alpha = \mathcal{P}_{\alpha,ij} \frac{\partial v_{\alpha j}}{\partial x_i}$.
In the above equations ρ_α represents the mass density of the fluid. The quantity $\mathbf{v}_\alpha$ represents the *flow velocity* of the species α. $\mathbf{E}$ and $\mathbf{B}$ represent the electric and magnetic field.
$\mathcal{P}_\alpha$ represents the *pressure tensor*, defined as $\mathcal{P}_\alpha = \rho_\alpha \langle \mathbf{c}_\alpha \mathbf{c}_\alpha \rangle$, where $\mathbf{c}_\alpha = \mathbf{u} - \mathbf{v}_\alpha$ is called *random velocity* and represents the velocity of a particle of type α relative to the average velocity $\mathbf{v}_\alpha$. The term $\nu_{\alpha\tau}$ is called *collision frequency for momentum transfer* between the particles of type α and those of type τ; note that, for momentum conservation during a collision, $\rho_\alpha \nu_{\alpha\tau} = \rho_\tau \nu_{\tau\alpha}$. The quantity T_α represents the *absolute temperature* of the random particle. It is defined as $p_\alpha = n_\alpha T_\alpha = \rho_\alpha \langle c_{\alpha i}^2 \rangle$, with $c_{\alpha i} = c_\alpha^2/3$. The quantity $\mathbf{q}_\alpha = \frac{1}{2} \rho \alpha \langle c_\alpha^2 \mathbf{c}_\alpha \rangle$ represents the heat flow vector, while Q_α groups together all the sources and sinks of energy. It has to be stressed that the expression for the pressure tensor $\mathcal{P}$ and for the heat flux vector $\mathbf{q}$ depend on the forms of the collision operator in equation (3.1).
It can be also useful to introduce the lagrangian derivative for a scalar function f:

$$\frac{df}{dt} = \frac{\partial f}{\partial t} + \mathbf{v} \cdot \nabla f. \tag{3.5}$$

3.2 Single-fluid extended magnetohydrodynamic model

3.2.1 Basic assumptions

The two fluid equations (3.4) contain many terms that describe a wide range of physical phenomena happening in a fluid embedded in an electromagnetic field.
To describe a plasma within a fluid model some fundamental approximations have to be made.
Quasi neutrality: This approximation results from the fact that the characteristic scale length of MHD a satisfies $a \gg \lambda_D$ (λ_D is defined in (1.1)) leading to the possibility to neglect the $\nabla \cdot \mathbf{E}$ term in Poisson's equation. It results $n_i \approx n_e \approx n$, a relation that

substitutes the $\nabla \cdot \mathbf{E} = 0$ equation. This assumption allows to discard the electric force from the momentum equation and the displacement term from Maxwell equations.
To describe a magnetically confined fusion plasma a further assumption has to be performed.
Small larmor radius approximation: $\frac{\rho_{i,e}}{L} \ll 1$, with L representing the macroscopic length of the system and $\rho_{i,e} = \frac{m_{i,e} v_{i,e}}{eB} = \frac{v_{i,e}}{\omega_{c\,i,e}}$. $\omega_{c\,i,e}$ represents the cyclotron frequency. This corresponds to a particle performing several gyrations before leaving the plasma. This spatial condition can be turned into a temporal condition if we define a macroscopic transit time $\omega_T^{-1} = \frac{L}{v}$. It is found that $\omega_T \ll \omega_{ci} \ll \omega_{ce}$.
This assumptions allow an ordering procedure between the terms in the fluid equations that helps deciding which terms have to be kept and which have to be discarded in the investigation of a particular phenomena.

3.2.2 Equations

Consider a hydrogen plasma, so $q_\alpha = \pm e$. The single-fluid model here described treats the plasma as a single fluid characterized by the following macroscopic physical quantities:

$$\text{mass density} \qquad \rho = n_i m_i + n_e m_e \approx n(m_i + m_e) \approx n m_i. \tag{3.6a}$$

$$\text{charge density} \qquad \sigma = (n_i - n_e)e. \tag{3.6b}$$

$$\text{mass velocity} \qquad \mathbf{v} = \frac{(n_i m_i \mathbf{v}_i + n_e m_e \mathbf{v}_e)}{\rho} \approx \frac{(m_i \mathbf{v}_i + m_e \mathbf{v}_e)}{(m_i + m_e)}. \tag{3.6c}$$

$$\text{current density} \qquad \mathbf{J} = e(n_i \mathbf{v}_i - n_e \mathbf{v}_e) \approx ne(\mathbf{v}_i - \mathbf{v}_e). \tag{3.6d}$$

$$\text{pressure tensor} \qquad \mathcal{P} = \mathcal{P}_i + \mathcal{P}_e. \tag{3.6e}$$

Note that:

$$\mathbf{v} \approx \mathbf{v}_i + \frac{m_e}{m_i}\mathbf{v}_e, \tag{3.7a}$$

$$\mathbf{v}_i \approx \mathbf{v} + \frac{m_e}{m_i}\frac{\mathbf{J}}{ne}, \tag{3.7b}$$

$$\mathbf{v}_e \approx \mathbf{v} - \frac{\mathbf{J}}{ne}. \tag{3.7c}$$

Four equations can be derived from the two-fluid model equations (3.4).

1) Continuity equation

Adding together the two form of equation (3.4a) for electrons and ion, using the single fluid variables of equations (3.6) the single-fluid continuity equation is obtained:

$$\frac{\partial \rho}{\partial t} + \nabla \cdot (\rho \mathbf{v}) = 0. \tag{3.8}$$

2) Momentum equation

Adding together the two equations of motion (3.4b) and performing the proper substitutions:

$$\rho \left(\frac{\partial \mathbf{v}}{\partial t} + \mathbf{v} \cdot \nabla \mathbf{v} \right) = \mathbf{J} \times \mathbf{B} - \nabla \cdot \mathcal{P}, \tag{3.9}$$

where (referring to the cartesian components of velocity):

$$\nabla \cdot \mathcal{P}|_k = \frac{\partial \mathcal{P}_{\alpha\beta}}{\partial x_\beta} \mathbf{e}_k. \tag{3.10}$$

The term $-\nabla \cdot \mathcal{P}$ includes forces associated with scalar pressure and tangential shear forces. It can be separated into diagonal (pressure forces) and off-diagonal (viscous forces) parts, $\mathcal{P} = p\mathcal{J} + \pi$.
A possible form for the off-diagonal part of $\mathcal{P}$ is (see for example [Choudhuri, 1998]) :

$$\pi_{\alpha\beta} = -\mu \left(\frac{\partial v_\alpha}{\partial x_\beta} + \frac{\partial v_\beta}{\partial x_\alpha} - \frac{2}{3} \nabla \cdot \mathbf{v} \delta_{\alpha\beta} \right). \tag{3.11}$$

This form is valid for any force between the particles forming the plasma (and thus controlling the collisions) as long as the force falls off faster than Coulomb force increasing separation. The quantity μ is called coefficient of viscosity. The *kinematic viscosity coefficient* $\nu = \mu/\rho$ is mostly used. Assuming a uniform viscosity coefficient μ the term $\nabla \cdot \mathcal{P}$ in equation (3.9) becomes, after some algebra:

$$\begin{aligned} \nabla \cdot \mathcal{P} &= \nabla p + \nabla \cdot \pi = \nabla p + \frac{\partial \pi_{\alpha\beta}}{\partial x_\beta} \mathbf{e}_k \\ &= \nabla p - \mu \nabla^2 \mathbf{v} - \frac{1}{3} \mu \frac{\partial}{\partial x_\alpha} (\nabla \cdot \mathbf{v}) \, \mathbf{e}_\alpha. \end{aligned} \tag{3.12}$$

The term involving $\nabla \cdot \mathbf{v}$ in equation (3.12) is neglected (for simplicity) and the final version of the momentum equation is given by:

$$\rho \left(\frac{\partial \mathbf{v}}{\partial t} + \mathbf{v} \cdot \nabla \mathbf{v} \right) = \mathbf{J} \times \mathbf{B} - \nabla p + \mu \nabla^2 \mathbf{v}. \tag{3.13}$$

3) Energy equation

Equation (3.4c) becomes, in its single fluid formulation:

$$\frac{3}{2}\left(\frac{\partial T}{\partial t}+\mathbf{v}\cdot\nabla T\right)+p\nabla\cdot\mathbf{v}+\pi:\nabla\mathbf{v}+\nabla\cdot\mathbf{q}=Q \tag{3.14}$$

Performing an ordering procedure on equations (3.4c) for electrons and ions, as done in [Fitzpatrick], shows that the terms associated to viscous heat conductivity ($\pi:\nabla\mathbf{v}$), with energy sources and sinks (Q) and with the thermal conductivity ($\nabla\cdot\mathbf{q}$) have a minor role. Those terms must be considered in all energy transport related studies. Deleting the negligible terms the equation can be reduced to:

$$\frac{3}{2}\left(\frac{\partial T}{\partial t}+\mathbf{v}\cdot\nabla T\right)+p\nabla\cdot\mathbf{v}=0 \tag{3.15}$$

that is easily turned, using (3.8) and $p=nT$, into the adiabatic law:

$$\frac{d}{dt}\left(\frac{p}{\rho^{\gamma}}\right)=0,\qquad \gamma=\frac{5}{3}. \tag{3.16}$$

4) Ohm's law

Ohm's law can be derived rewriting the electrons equation of motion (3.4b) using the single fluid variables of equations (3.6), neglecting the viscous term and electron inertia entirely. The equation becomes:

$$\mathbf{E}+\mathbf{v}\times\mathbf{B}=\frac{\mathbf{J}\times\mathbf{B}-\nabla p_e}{en}+\eta\mathbf{J}. \tag{3.17}$$

The term containing $\mathbf{J}\times\mathbf{B}$ is called *Hall term* (and is related to such an effect), while the term containing p_e is called *electron pressure term*. The quantity η is called *resistivity* and will be discussed in section 3.2.3. More extended version of the Ohm equation can be obtained retaining the inertia term, see [Fitzpatrick; Bittencourt, 2004].

3.2.3 Resistivity and viscosity

The derivation of equation (3.17) led to the definition of the resistivity η of the plasma treated as a single fluid. The algebra leading to Ohm's law tells us that resistivity has the following form:

$$\eta=\frac{m_e\nu_{ei}}{ne^2}. \tag{3.18}$$

This relation can also be derived on a physical ground. The change of momentum due to collisions was treated, in equation (3.4b), through a simplified term of the kind:

$$\mathbf{P}_{ei} = m_e n \nu_{ei} (\mathbf{v}_e - \mathbf{v}_i)$$

Since the collisions are Coulomb collisions the momentum change originated by them has to be proportional to e^2, to the density of ions and electrons $n_i n_e = n^2$ and to the relative velocity between electrons and ions. So we can write:

$$\mathbf{P}_{ei} = \eta e^2 n^2 (\mathbf{v}_e - \mathbf{v}_i),$$

η representing a constant of proportionality. Comparing the two forms of $\mathbf{P}_{ei}$ the *resistivity of the plasma* can be defined as in equation (3.18). It is important to note that the electron-ion collision frequency ν_{ei} has a strong dependence on temperature: the derivation of ν_{ei} assuming Coulomb collisions lead to a general form of η given by the following equation:

$$\eta \propto m_e^{1/2} Z T_e^{-3/2} \log(\Lambda), \tag{3.19}$$

where Z is the effective atomic number of the plasma and $\log(\Lambda)$ is the Coulomb logarithm [Spitzer and Härm, 1953].
The kinematic viscosity coefficient ν was defined after equation (3.11). The form there proposed for the off diagonal part of the pressure tensor $\mathcal{P}$ is needed to close the equations (3.4): those equations are in fact *incomplete*, as many quantities like the viscosity tensor π and the heat flux density $\mathbf{q}$ are *unknown* until a form of the collision operator in Boltzmann equation is given. A careful closure of the plasma fluid equations has been performed by Braginskii [Braginskii, 1965]. Treating the case of a collisional magnetized plasma led to a viscosity tensor described as a sum of five tensors, of which the *parallel viscosity* tensor is the dominant one. The results obtained by Braginskii show that an expression for the viscosity coefficient can be given by:

$$\mu \approx n T_i \tau_i, \tag{3.20}$$

where τ_i is the ions collision time, that describes the time scale for the thermalization of ions with electrons. On a physical ground it can be said that viscosity in the single fluid model viscosity describes momentum diffusion and is determined by ions, which possess nearly all the momentum on a plasma due to their higher masses. Viscosity is often enhanced by other sources: possible viscous effects can be given considering neoclassical effects (neoclassical toroidal viscosity) or considering the role of microturbulence in plasmas. All these effects are labelled *anomalous viscosity* and can be important in the

description of plasma viscosity.

3.3 Extended MHD model

The following equations represent the *extended magnetohydrodynamic model*:

$$\frac{\partial \rho}{\partial t} + \nabla \cdot (\rho \mathbf{v}) = 0, \tag{3.21a}$$

$$\rho \left(\frac{\partial \mathbf{v}}{\partial t} + \mathbf{v} \cdot \nabla \mathbf{v} \right) = \mathbf{J} \times \mathbf{B} - \nabla p + \mu \nabla^2 \mathbf{v}, \tag{3.21b}$$

$$\frac{3}{2} \left(\frac{\partial T}{\partial t} + \mathbf{v} \cdot \nabla T \right) + p \nabla \cdot \mathbf{v} + \pi : \nabla \mathbf{v} + \nabla \cdot \mathbf{q} = Q, \tag{3.21c}$$

$$\mathbf{E} + \mathbf{v} \times \mathbf{B} = \frac{\mathbf{J} \times \mathbf{B} - \nabla p_e}{en} + \eta \mathbf{J}, \tag{3.21d}$$

$$\epsilon_0 \nabla \cdot \mathbf{E} = \sigma \approx 0, \tag{3.21e}$$

$$\nabla \times \mathbf{E} = -\frac{\partial \mathbf{B}}{\partial t}, \tag{3.21f}$$

$$\nabla \cdot \mathbf{B} = 0, \tag{3.21g}$$

$$\nabla \times \mathbf{B} = \mu_0 \mathbf{J}. \tag{3.21h}$$

3.4 Visco-resistive MHD model

The main difference between the extended and the visco-resistive MHD model is in the adopted form of Ohm equation. A simple estimate of the relative importance of the $\mathbf{J} \times \mathbf{B}$ and ∇p_e terms compared to the $\mathbf{v} \times \mathbf{B}$ term shows that $JB/(envB) \approx p/(aenvB) \approx \rho_i / L \ll 1$, and can therefore be neglected.
Pressure is often neglected, which is a reasonable assumption at low β value. The following equations represent the *visco-resistive magnetohydrodynamic model*:

$$\frac{\partial \rho}{\partial t} + \nabla \cdot (\rho \mathbf{v}) = 0, \tag{3.22a}$$

$$\rho \left(\frac{\partial \mathbf{v}}{\partial t} + \mathbf{v} \cdot \nabla \mathbf{v} \right) = \mathbf{J} \times \mathbf{B} + \mu \nabla^2 \mathbf{v}, \tag{3.22b}$$

$$\mathbf{E} + \mathbf{v} \times \mathbf{B} = \eta \mathbf{J}, \tag{3.22c}$$

$$\nabla \times \mathbf{E} = -\frac{\partial \mathbf{B}}{\partial t}, \tag{3.22d}$$

$$\nabla \cdot \mathbf{B} = 0, \tag{3.22e}$$

$$\nabla \times \mathbf{B} = \mu_0 \mathbf{J}. \tag{3.22f}$$

3.5 MHD equilibrium

In the following sections some dynamical considerations will be performed, on the basis of the visco-resistive MHD model equations described in section 3.4. In this section the MHD equilibrium state will be considered in both the ideal ($\eta = \nu = 0$) case and in a resistive case ($\eta \neq 0$).

3.5.1 Ideal MHD equilibrium

The MHD model allows the study of the features of a magnetic field in which magnetic forces maintain the plasma in an equilibrium state, i.e. compensate the tendency of the plasma to expand. In this section an ideal plasma is considered, $\eta = \nu = 0$ will be imposed in equations (3.22). A one-dimensional ($\partial/\partial\theta = \partial/\partial z = 0$) and stationary ($\partial/\partial t = 0$) equilibrium will be studied. Under these hypothesis the model reduces to:

$$\mathbf{J} \times \mathbf{B} = \nabla p \tag{3.23a}$$

$$\nabla \times \mathbf{B} = \mu_0 \mathbf{J} \tag{3.23b}$$

$$\nabla \cdot \mathbf{B} = 0 \tag{3.23c}$$

$$\nabla \times \mathbf{E} = 0 \tag{3.23d}$$

$$\mathbf{E} + \mathbf{v} \times \mathbf{B} = 0. \tag{3.23e}$$

Two important relation can be derived from equation (3.23a). The first is $\mathbf{B} \cdot \nabla p = 0$ and the second is the analogous relation for the current $\mathbf{J} \cdot \nabla p = 0$. This relations imply that both the magnetic field and the current density have to lie, as long as the system is in an equilibrium state, on a surface that is perpendicular to the pressure gradient. It is thus possible to define some surfaces, labelled by different values of pressure, called *magnetic surfaces*. From the mathematical point of view this definition can be converted in a function, called *flux function* Ψ, that describes the surfaces with constant magnetic flux $\mathbf{B} \cdot \nabla\Psi = 0$. It is demonstrated in section 5.3 that if a magnetic field possesses a symmetry in a particular direction, say u, a good flux function is the covariant component of the vector potential $\mathbf{A}$ in that direction, namely $\Psi = A_u$.

3.5.2 Resistive MHD equilibrium

In the framework of visco-resistive MHD the resistive MHD equilibria obey to equations (3.23) adding Ohm's law (3.22c).
The equilibrium configuration here analyzed is called one-dimensional ohmic equilibrium (cylindrical geometry and axisymmetry are assumed). This means $\frac{\partial}{\partial\theta} = \frac{\partial}{\partial z} = 0$ and, using (3.22e), $B_r = 0$. If the assumption of negligible kinetic pressure is performed

($p = 0$) three equations remain:

$$\mathbf{J} \times \mathbf{B} = \nabla p \tag{3.24a}$$

$$\nabla \cdot \mathbf{B} = 0 \tag{3.24b}$$

$$\nabla \times \mathbf{B} = \mathbf{J} \tag{3.24c}$$

$$\mathbf{E} + \mathbf{v} \times \mathbf{B} = \eta \mathbf{J}. \tag{3.24d}$$

The solution of this model, imposing a constant axial electric field $E_z = E_0$ and neglecting pressure (this last hypothesis is used to capture the basic RFP physics), leads to two equation [Delzanno et al., 2008]:

$$B_\theta(r) = B_\theta(0) + \frac{1}{r}\int_0^r \frac{E_0}{\eta}\frac{B_z^2}{B_z^2 + B_\theta^2} r dr \tag{3.25a}$$

$$B_z(r) = B_z(0) \exp\Big[- \int_0^r \frac{E_0}{\eta}\frac{B_\theta}{B_z^2 + B_\theta^2} dr \Big]. \tag{3.25b}$$

These two equations can be solved numerically imposing $B_z(0) = 1$, $B_\theta(0) = 0$ starting from an hypothesis on the solution and iterating until convergence to a proper solution is obtained.

3.6 MHD instabilities

A further application of the MHD model consists on the study of the macroscopic stability properties of equilibrium configurations. The main macroscopic plasma instabilities, described by the MHD model, are widely studied in [Freidberg, 2007], [Biskamp, 1992], [Wesson, 1997], while here few informations will be given.
MHD instabilities are ultimately limiting fusion devices operational space, either because their onset in dangerous for the configuration equilibrium and can lead to disruptions, or because their occurrence enhances plasma transport. The main distinction, that allows the definition of two main classes of instabilities, is the one between *ideal* instabilities and *resistive* instabilities. Ideal instabilities are ruled by a peculiar feature of the ideal MHD model, the so called *frozen-in-field-line theorem*, that establishes that the magnetic field flux across an arbitrary closed surface is conserved while this surface moves with the fluid. Considering a generic flux tube this implies that the magnetic field lines are bonded to follow the plasma motion or, differently written, that two fluid elements connected by a field line at a certain time will always be connected. This prevents any change of the magnetic topology and limits the effects of ideal instabilities, as magnetic field line can not be broken and reconnected. The ideal instabilities are characterized by a growth rate given by the Alfvèn frequency $\gamma \propto \tau_A^{-1}$. The effect of

resistivity is to allow the decoupling of magnetic field lines and plasma. Magnetic field can diffuse and magnetic topology can change through the *magnetic reconnection process*. Generally resistive instabilities have a minor growth rate than the ideal ones.
Instabilities can be further divided in *external* or *internal*. This distinction depends on the behaviour of the surface that separates plasma and empty space under the action of the perturbation. External modes cause a motion on the plasma surface that has to be avoided to preserve the integrity of the confinement chamber. Internal modes on the contrary do not involve any plasma surface motion.
Instabilities can also be characterized on the basis on the forces that induce the perturbation: the main distinction is between *pressure driven* instabilities and *current driven* instabilities. The former, caused by the thermal energy available, are internal modes that set a limit to the maximum attainable β while the latter are caused by gradients of the parallel current, are called *kink modes* in the ideal case and *tearing modes* in the resistive one. Current driven modes are dangerous in tokamak, since they can induce a disruptive mode during plasma ramp-up when the current rise rate exceeds a certain value. They are dangerous in the RFP as well. Resistive Wall Modes (RWM) can destroy plasma equilibrium and end the discharge. Resistive kink- tearing modes can lock to a certain position of the wall and enhance dramatically plasma-wall interaction. Pressure driven modes are very dangerous in tokamaks, an ultimate limit to β_N (defined in 1.3.1) being set by ideal kink modes and RWM. Actually a softer β_N limit is set by Neoclassical Tearing Modes (NTMs) which reduce plasma confinement.
MHD also describes the possible stabilizing effects: the production of a perturbed magnetic field component perpendicular to the equilibrium one, i.e. magnetic field line bending, is a stabilizing action, together with good magnetic curvature, when the centre of curvature of magnetic field lines is in the opposite direction to the pressure gradient. Figure 3.1 shows the main instabilities limiting the operational space of a typical tokamak machine, as a function of β_N and of q_{min}, the value of the safety factor profile at the center of the tokamak. This figure shows the variety of instabilities of MHD origin and will constitute a link in describing some of them (ideal kink, tearing modes, RWMs).
All kind of instabilities have an infinite spectrum of possible modes that in the case of circular and large aspect-ratio machines cans take the form $\exp i(m\theta - n\phi)$, with m, n poloidal and toroidal wave number. Each mode can be described by its wave numbers.

3.6.1 Ideal kink instability

The methodology that gives the best explanation for the onset of the ideal kink instability is the use of the energy principle, based on the concept that any allowable pertur-

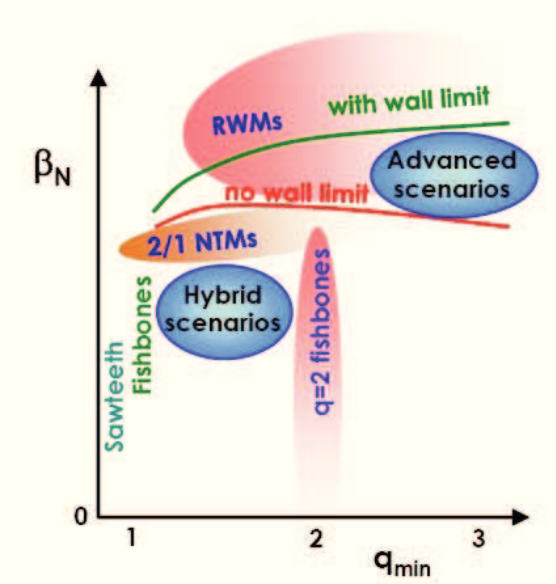

Figure 3.1: Cartoon of the various instabilities that can be found in the operational space of a tokamak as a function of the central q value and of β_N. The sawteeth is believed to be originated by the presence of a $q = 1$ rational surface in the plasma: the reason why such a surface is extremely dangerous will be explained in section 3.6.1. Tearing modes are of fundamental importance both in tokamak (Neoclassical Tearing Modes, NTMs) and in the RFP (a saturated resistive-kink tearing mode gives the helical symmetry to the configuration); they will be described in section 3.6.2. Resistive Wall Modes will be described in section 3.6.3. Picture taken from [Baruzzo, 2011].

bation of an equilibrium state that lowers the potential energy is unstable. Ideal MHD will be considered and the equations will be linearized (only first order contributions of the perturbations to the equilibrium will be considered). An adiabatic energy equation will be considered.

A displacement $\boldsymbol{\xi}$ from an ideal MHD equilibrium corresponds to a total energy change given by:

$$\delta W = -\frac{1}{2}\int dV \boldsymbol{\xi}\cdot\mathbf{F}, \tag{3.26}$$

with $\mathbf{F}$ representing a density of force given by (neglecting second order quantities):

$$\mathbf{F} = \mathbf{J}_1\times\mathbf{B}_0 + \mathbf{J}_0\times\mathbf{B}_1 - \nabla p_1, \tag{3.27}$$

with the subscript 0 and 1 referring to equilibrium and perturbation quantities. Some algebra and the use of ideal MHD equations leads to:

$$\delta W = \frac{1}{2}\int dV \left(\gamma p_0 (\nabla\cdot\boldsymbol{\xi})^2 + (\boldsymbol{\xi}\cdot\nabla p_0)\nabla\cdot\boldsymbol{\xi} + \frac{\mathbf{B}_1^2}{\mu_0} - \mathbf{J}_0\cdot(\mathbf{B_1}\times\boldsymbol{\xi})\right) + \int_{vac} dV \frac{\mathbf{B}_{vac}^2}{2\mu_0} \tag{3.28}$$

This general equation can be used to describe many configurations: the simplest case is the one of a large aspect-ratio tokamak with low β. A simple form of δW can be obtained assuming a tokamak-like ordering of the magnetic field. The reader is referred to [Wesson, 1997] for the exact calculation and assumptions. The result is given, very schematically, by:

$$\delta W = C\left(\int_0^a (rdr\,\text{positive terms}) + \left[\frac{2}{q_a}\left(\frac{n}{m}-\frac{1}{q_a}\right) + (1+m\lambda)\left(\frac{n}{m}-\frac{1}{q_a}\right)^2\right] a^2\xi_a^2\right), \tag{3.29}$$

where $r = a$ represent the position of the plasma surface and λ is a positive factor that describe the position of the wall (at $r = b$). It is clear that if a conducting wall is present at $r = a$ then $\xi_a = 0$ and the mode is stable, as $\delta W > 0$ is always true (perturbation disadvantaged). A negative energy variation can be obtained if $nq_a < m$, the lowest m modes being the most favoured.
Looking at equation (3.29) and keeping in mind the considerations made a first clue as to why the *Kruskal-Shafranov* limit for stability

$$q(r) > 1 \tag{3.30}$$

exist can be given. For sure it has to be $q_a > 1$, not to destabilize the ideal kink mode with $m = 1, n = 1$, that has the highest growth rate of all. The inclusion of resistivity in the model leads to the conclusion that if the condition $nq = m$ is verified inside the plasma a resistive instability develops, the one with $m = 1, n = 1$ having the higher growth rate. That is the reason why equation (3.30) should always be verified. In tokamak operation the ideal kink stability condition is applied trying to avoid the destabilization of the detrimental ideal kink modes with low poloidal wave number. Present scenarios for ITER operations are based on the condition $q_a > 3$.

3.6.2 Tearing mode instability

The behaviour of the resistive instability called *tearing mode* is governed by the current density profile (and by its gradients) [Goldston and Rutherford, 1995; Biskamp, 1992]. The mode causes the formation of a magnetic field lines' configuration called *magnetic island*, possible because of the magnetic reconnection process.

The linear theory of the tearing mode (that solves a linearized form of the MHD equations) consists in the perturbation of an equilibrium magnetic configuration and in the solution of two different sets of equations: one for the region next to the radial position in which the instability occurs and where the effect of the resistivity must be taken into account; the other in the region far from the instability initial position, where ideal MHD can be used. The two solutions that are obtained have to be connected in the boundary between the two regions: this process leads to the determination of the growth rate of the tearing mode. In the main studied models it is found:

$$\gamma \propto \tau_R^{-\frac{3}{5}} \tau_A^{-\frac{2}{5}}, \tag{3.31}$$

The linear theory of the tearing mode fails when the perturbation grows over the spatial scale on which resistivity is taken into account, nullifying the validity of the linearization process. The growth of the mode leads to the exhaustion of the sources of magnetic energy destabilizing the perturbation, causing the saturation of the mode.

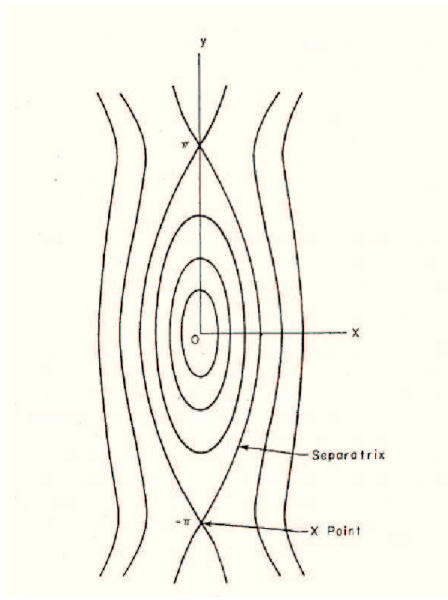

Figure 3.2: Magnetic field line configuration of a magnetic island produced by a resistive tearing perturbation. This figure refers to a simple configuration called *plasma current slab*, characterized by a thick sheet of current directed parallel to the surface of the slab. The effect of resistivity is to reconnect the field lines that initially are all in the $\hat{y}$ direction.

Why tearing modes resonate at rational values of q

A more quantitative point of view can be obtained using a derivation that makes use of the ideas at the basis of the energy principle. As pointed out before, the growth rate of resistive instabilities are sufficiently slow that inertial effects are negligible over most of the plasma. Resistivity can be considered negligible over most of the plasma (and thus the motion can be analyzed using ideal MHD) apart from a thin layer where the actual instability is initiated (resonance region). The physical-algebraic steps include taking the curl of equation (3.27), neglecting inertia, considering the usual form of the perturbations $\exp i(m\theta - n\phi)$, using $q = \frac{rB_\phi}{R_0 B_\theta}$, a tokamak-like ordering for the fields. The equation obtained after these steps can be integrated in the whole plasma volume, in order to obtain the energy contribution for each term. The following expression, representing the integration of the toroidal component of the equation, is obtained [Wesson,

1997]:

$$\int_{r_1}^{r_2} drr \left[B_{\theta 1}^2 + B_{r1}^2 + \frac{dj_\phi/dr}{\frac{B_\theta}{\mu_0}\left(1 - \frac{nq}{m}\right)} \psi^2 \right] = \left(r\psi \frac{d\psi}{dr} \right) \Bigg|_{r1}^{r2} \tag{3.32}$$

The first two terms represent the stabilizing contribution due to magnetic field line bending and the third represents the destabilizing effect due to current gradients: that is why tearing modes are labelled as *current driven modes* and this gives a hint at why tearing modes grow where $q = m/n$. In fact equation (3.32) has a singularity at the resonant surface $r = r_s$ where $q = m/n$: in a layer around this position a separate analysis taking into account resistivity is needed.

Linear stability theory

The solutions of equation (3.32) in the outer region (not taking into account resistivity) and in the inner region have to be matched at the boundary of the layer. As the equation is linear the only significant parameter in this procedure is the quantity called derivative jump:

$$\Delta' = \frac{\psi'}{\psi} \Bigg|_{r=r_s-\varepsilon}^{r=r_s+\varepsilon} \quad \varepsilon \to 0. \tag{3.33}$$

In the inner region the solution of a system formed by Ohm's law and the equation of motion leads to an analytical expression of the derivative jump Δ'_{in}. Imposing $\Delta'_{in} = \Delta'$ leads to the following expression for the growth rate of the mode:

$$\gamma \propto \left(\eta^{3/5} \left(\frac{q'}{q} \right)^{2/5} \right) \Delta'^{4/5}, \tag{3.34}$$

or, as a function of Alfvèn and resistive times as:

$$\gamma \tau_A \propto S^{-3/5} \left(n \frac{a}{R_0} \frac{aq'}{q} \right)^{2/5} (a\Delta')^{4/5}. \tag{3.35}$$

The solution of equation (3.32) allows the determination of the stability properties of tearing modes, as the quantity Δ' can be calculated (if $\Delta' = 0$ marginal stability is achieved, if $\Delta' > 0$ the mode is unstable). A detailed analysis, performed in [Wesson, 1997], gives two main informations. The first is that for sufficiently large m values the tearing modes are stable, depending on the current profile. The second is that the presence of a conducting wall only helps in the stabilization of tearing modes with resonance surfaces sufficiently close to the plasma edge while it is ininfluent on those with resonances far from it.

Nonlinear theory

The linear stability theory here briefly exposed gives only an incomplete description of the behaviour of the mode, as nonlinear effects become important in the very early stages of development of the instability. A first important effect occurs when the magnetic island created by magnetic field lines reconnection exceeds the width of the resistive layer. This slows the mode growth from exponential to algebraic [Rutherford, 1973]. The second effect occurs when the island size becomes so big that the behaviour of the mode is dominated by the gross geometry: this leads to the vanishing of the source of magnetic energy driving the instability and thus to the saturation of the mode [White, 1986; Arcis et al., 2007; Escande and Ottaviani, 2004].

3.6.3 Resistive Wall Modes

Resistive Wall Modes are a form of ideal kink instability: their peculiar name is due to the behaviour they have in presence of passive structures with a finite resistivity placed near the plasma surface. The eddy currents circulating in these structures can balance the magnetic field due to the instability and reduce the growth rate of the ideal mode down to the time scale given by the magnetic field penetration through the resistive wall. This slowdown is fundamental because it allows an efficient control strategy [Paccagnella et al., 2006].
In tokamaks the RWMs are characterized by one or more toroidal Fourier's components, the main one having $n = 1$ and a rich spectrum of poloidal mode numbers $m = 2, 3, 4$ especially. In RFPs RWMs were observed in experiments after a new generation of machines with a thin stabilizing shell were built. The lower magnetic field penetration time allowed RWMs growth: the modes have a $m = 1$ structure with several toroidal wave numbers unstable at the same time. In experiments these modes grow to saturation, producing a large magnetic chaos. For this reason many stabilization techniques were studied. *Passive stabilization techniques* involve the creation of a plasma rotation using the Neutral Beam Injector to transmit angular momentum to the plasma. Theory in fact suggests that plasma toroidal rotation can be effective in stabilizing the RWM, provided the rotation achieved to be larger than a critical value. *Active stabilization techniques* use feedback stabilization at the plasma boundary by active coils that cancel spurious components of the field at the plasma edge, essentially producing a magnetic field opposite to the one of the mode. Active control is routinely applied in the RFX-mod experiment, where the possibility to simultaneously control a wide spectrum of MHD has been widely demonstrated [Paccagnella et al., 2006]. It is also possible to control the growth of a single RWM: this possibility was explored on RFX-mod in a dedicated experimental campaign, described in chapter 10, decided after the

result presented in this thesis, in particular the ones described in chapter 7. This experimentation is based on the idea that the presence of a single helical perturbation to the axisymmetric equilibrium does not create magnetic chaos.

4

3D magnetohydrodynamic: SPECYL and PIXIE3D

SPECYL [Cappello and Biskamp, 1996] numerically integrates the equations of the visco-resistive MHD model in cylindrical geometry $\mathbf{r} = (r, \theta, z)$, under some assumptions.
Firstly the mass density ρ is considered uniform and stationary $\rho(\mathbf{r}, t) = \rho_0$.
Secondly the equations are solved in the vanishing β limit, assumption valid for the present value of kinetic pressure in experiments $\beta \approx 1\%$.
The model equations, in normalized form, are given by:

$$\frac{\partial \mathbf{v}}{\partial t} + \mathbf{v} \cdot \nabla \mathbf{v} = \mathbf{J} \times \mathbf{B} + \nu \nabla^2 \mathbf{v}, \tag{4.1a}$$

$$\frac{\partial \mathbf{B}}{\partial t} = \nabla \times (\mathbf{v} \times \mathbf{B}) - \nabla \times \eta \mathbf{J}, \tag{4.1b}$$

$$\nabla \times \mathbf{B} = \mathbf{J}, \tag{4.1c}$$

$$\nabla \cdot \mathbf{B} = 0. \tag{4.1d}$$

PIXIE3D [Chacón, 2004, 2008b,a] is a recently developed, fully implicit, finite-volume code. It numerically integrates a more complete form of the compressible visco-resistive MHD model (or a simplified version of the extended MHD model, without the Hall term in Ohm's law (3.17)).
The model equations, in normalized form, are given by:

$$\frac{\partial \rho}{\partial t} + \nabla \cdot (\rho \mathbf{v} - D \nabla \rho) = 0, \tag{4.2a}$$

$$\nabla \times \mathbf{E} = -\frac{\partial \mathbf{B}}{\partial t}, \tag{4.2b}$$

$$\mathbf{E} + \mathbf{v} \times \mathbf{B} = \eta \mathbf{J}, \tag{4.2c}$$

$$\nabla \times \mathbf{B} = \mu_0 \mathbf{J}, \tag{4.2d}$$

$$\rho \left(\frac{\partial \mathbf{v}}{\partial t} + \mathbf{v} \cdot \nabla \mathbf{v} \right) = \mathbf{J} \times \mathbf{B} - \nabla p + \rho \nu \nabla^2 \mathbf{v}, \tag{4.2e}$$

$$\frac{3}{2} \left(\frac{\partial T}{\partial t} + \mathbf{v} \cdot \nabla T \right) + p \nabla \cdot \mathbf{v} + \pi : \nabla \mathbf{v} + \nabla \cdot \mathbf{q} = Q, \tag{4.2f}$$

$$\nabla \cdot \mathbf{B} = 0. \tag{4.2g}$$

Outline of the chapter. In this chapter the SPECYL and the PIXIE3D codes will be described respectively in section 4.1 and in section 4.2. In detail the reference quantities for the normalization of the MHD equations will be described. Then the treatment of the dissipative parameters will be tackled. For each code the numerical approach and the used boundary conditions will be described in dedicated sections.
In section 4.3 the nonlinear verification process between the two codes will be briefly described and used as occasion to show the result of a set of MHD simulations on both the tokamak and RFP configurations.

4.1 SPECYL

4.1.1 Normalization and dissipative parameters

SPECYL solves equations (4.1). Every physical quantity is normalized to reference quantities related to the system under study.
Velocity is normalized to the Alfvèn velocity, that describes the propagation of MHD waves in the system. Alfvèn velocity is defined as $v_A = \frac{B}{\sqrt{\mu_o \rho}}$.
Lengths are normalized to the plasma radius a.
Times are normalized to the Alfvèn time $\tau_A = \frac{a}{v_A}$.
Magnetic field is normalized to the magnetic field at $r = 0$ and $t = 0$, B_0.
Density is normalized to a reference density, ρ_0.
Using these unities the resistivity η and the viscosity ν become adimensional parame-

ters. In particular resistivity corresponds to the inverse Lundquist number:

$$\eta = \frac{\tau_A}{\tau_R} = S^{-1} = \frac{\eta_0}{\mu_0 v_A a}. \tag{4.3}$$

Viscosity corresponds to the inverse magnetic Reynolds number:

$$\nu = \frac{\tau_A}{\tau_V} = R^{-1} = \frac{\nu_0}{v_A a}. \tag{4.4}$$

τ_R and τ_V represent the resistive and viscous time scale, respectively.
In SPECYL viscosity and resistivity do not depend on time and thus are not evolved self-consistently. Their radial profile is given by:

$$\eta(\mathbf{r}) = \eta_0 \left(1 + a r^b\right), \tag{4.5a}$$

$$\nu(\mathbf{r}) = \nu_0 \left(1 + c r^d\right). \tag{4.5b}$$

When not differently specified, in the SPECYL simulations presented in this thesis it was usually chosen: $a = 20$, $b = 10$, $c = 0$. An interesting feature of the equations emerges applying a further rescaling of time and velocities given by:

$$t \to \tilde{t} = \sqrt{\frac{\eta}{\nu}} t, \qquad \mathbf{v} \to \tilde{\mathbf{v}} = \sqrt{\frac{\nu}{\eta}} \mathbf{v} \tag{4.6}$$

equations (4.1) are thus shown to depend, when the inertia term of equation (4.7a) is negligible, only on the product of viscosity and resistivity, given by the Hartmann number $H = (\eta\nu)^{-1/2}$.

$$P^{-1} \left(\frac{\partial \tilde{\mathbf{v}}}{\partial \tilde{t}} + \tilde{\mathbf{v}} \cdot \nabla \tilde{\mathbf{v}} \right) = \mathbf{J} \times \mathbf{B} + H^{-1} \nabla^2 \tilde{\mathbf{v}}, \tag{4.7a}$$

$$\frac{\partial \mathbf{B}}{\partial \tilde{t}} = \nabla \times (\tilde{\mathbf{v}} \times \mathbf{B}) - H^{-1} \nabla \times \mathbf{J}, \tag{4.7b}$$

$$\nabla \times \mathbf{B} = \mathbf{J}, \tag{4.7c}$$

$$\nabla \cdot \mathbf{B} = 0. \tag{4.7d}$$

This property turns out to be of fundamental importance on the study of the RFP dynamics.

4.1.2 Numerical approach

The equations are solved in cylindrical geometry. Periodic boundary conditions are used for the poloidal and axial coordinates $\theta \in [0 : 2\pi], z \in [0 : 2\pi R_0]$ (R_0 is the aspect ratio of the rectified torus), thus allowing a spectral approach in the poloidal and axial direction.
The generical physical quantity $\mathbf{Q}(\mathbf{r}, t) = \mathbf{Q}(r, \theta, z, t)$ can be expressed as:

$$\mathbf{Q}(r, \theta, z, t) = \sum_{m=-M}^{M} \sum_{n=-N}^{N} \mathbf{Q}_{m,n}(r, t) \exp i \left(m\theta + \tfrac{nz}{R_0} \right). \tag{4.8}$$

The different harmonics must fulfil the reality condition, as $\mathbf{Q}$ is a physical quantity:

$$Q_{-m,-n} = Q^*_{m,n}. \tag{4.9}$$

The spectral approach consist in the Fourier-transformation of equations (4.1). A set of non linear partial differential equations with r and t as independent variables have to be solved (θ and z are ruled out thanks to the Fourier transformation and are recovered in the post-processing process when performing an anti-Fourier transform to obtain the spatial behaviour of the physical quantities). A fundamental input of the code are the quantities M and N of equation (4.8). This choice is performed considering the features of RFP plasmas. In particular the most instable MHD modes are the ones that resonate with the safety factor profile in the vicinity of the axis. It can be shown that the zero order value of the safety factor at $r = 0$ is given by $q_0 = a/(2R_0)$. Considering an aspect ratio of 4, similar to the one of the RFX-mod experiment, one of the most instable mode should be the $m = 1, n = -8$) mode. The non-linear terms in the MHD equations tend

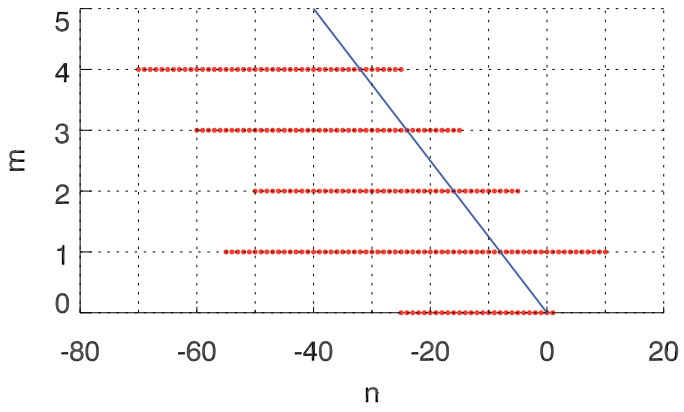

Figure 4.1: Spectrum of the calculated mode in a typical SPECYL simulation of an RFP plasma. The blue line represent the helicity $h = m/n = 8$ line.

to couple MHD modes in a 'preferential cone' centred around the $m/n = 1/8$ value. The corresponding choice of the MHD spectrum used by all the simulations showed in this thesis reflects this analysis and is shown in figure 4.1.
The radial discretization of the system of differential equation is performed through the use of two staggered meshes with a finite difference scheme.
The time advancement scheme is of the predictor-corrector type: the predictor step uses an explicit algorithm to calculate the magnetic field at $t^{n+1/2} = t^n + \frac{\Delta t}{2}$ neglecting dissipation terms. In the corrector step, used to evolve the velocity field at t^{n+1} solving equation (4.1a), dissipation terms are treated implicitly.
Physical quantities described by equation (4.8) can also be allowed to have a random phase Φ. The choice performed in all the simulations presented in this thesis is to start with the velocity and magnetic field in quadrature phase. It can be demonstrated that this initial condition is conserved during all the dynamical evolution. Consistent memory usage savings are achieved through this choice.

4.1.3 Boundary conditions

The boundary condition chosen in typical SPECYL simulations is the *ideal shell* one, meaning that both the electrical and the magnetic field must be zero inside the conductor. In particular the boundary condition is usually given as $B_r^{m,n}(a) = 0 \quad \forall\, m, n$, $E_\theta^{m,n} = 0 \quad \forall\, m, n$ and $E_z = E_0$ being a constant (externally imposed) electric field.
As for the velocity field the imposed boundary condition is the *no slip* boundary condition: $v_\theta(a) = v_z = 0$. Ohm's law can then be used to obtain the tangential components of the magnetic field and the radial component of the velocity for all the modes. In principle this condition should be enforced for all the MHD modes, in practice only the radial velocity component boundary is forced only for the axisymmetric mode.
A wide set of simulations presented in this thesis has been performed considering *helical boundary conditions* also called *magnetic perturbations* (MPs), namely imposing a non-zero radial electric field on an arbitrary mode $(\tilde{m}, \tilde{n}) \in \mathbb{Z}$, i.e. $B_r^{\tilde{m},\tilde{n}} = c$. Sometimes a negative value for the constant c can be chosen. It will not be indicated as it only corresponds to adding a π phase to the Fourier transform of the selected MHD mode and because a dedicated set of MHD simulations show that the phase does not influence the MHD dynamics.

4.1.4 Initial equilibrium

SPECYL initial equilibrium is called ohmic one-dimensional equilibrium. It is calculated solving the equilibrium visco-resistive MHD model. An axisymmetric configuration will be calculated, meaning $\frac{\partial}{\partial \theta} = 0$ and $\frac{\partial}{\partial z} = 0$. The relevant equations are:

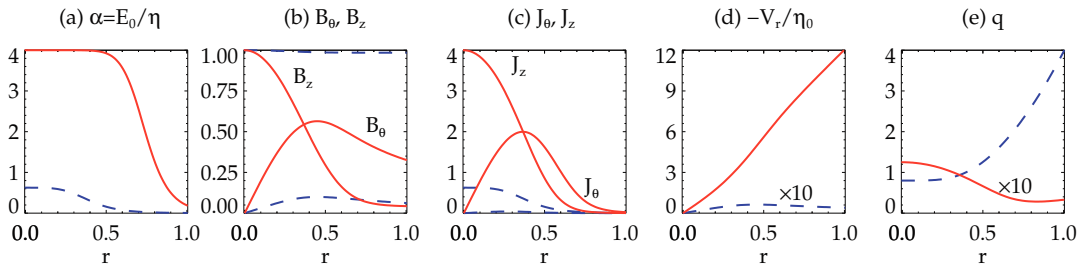

Figure 4.2: Initial equilibrium radial profiles for some significant quantities. RFP profiles are colored in red, tokamak profiles are colored in blue. The two equilibria can be obtained solving the equations in 3.5.2. In the specific case it was used $E_0/\eta(r=0)=4$ for the RFP and $E_0/\eta(r=0)=0.625$ for the tokamak.

$$\mathbf{J}\times\mathbf{B}=0, \tag{4.10a}$$

$$\nabla\times\mathbf{B}=\mathbf{J}, \tag{4.10b}$$

$$\nabla\cdot\mathbf{B}=0, \tag{4.10c}$$

$$\mathbf{E}+\mathbf{v}\times\mathbf{B}=\eta\mathbf{J}. \tag{4.10d}$$

Considering an axial electric field $\mathbf{E}=E_0\mathbf{e}_z$ the equations (4.10) are solved imposing $B_z(r=0)=1$ and $B_\theta(r=0)=0$. After the equilibrium fields computation it is possible to obtain a value of the pinch parameter Θ that will be used to classify the different simulations together with the Lundquist and Prandtl numbers. The numerical computation of this equilibrium is described in section 3.5.2. The radial profiles for some interesting quantities are shown in figure 4.2.

4.2 PIXIE3D

4.2.1 Normalization and dissipative parameters

The normalized form of the equations is such that, as in 4.1.1, all quantities are adimensional and η and ν are the reciprocals of the Lundquist number S and of the Reynolds number R, respectively.
In PIXIE3D viscosity and resistivity are treated in a manner similar to SPECYL code; their spatial behaviour can be given on a 3D mesh, and can not be changed during the dynamical evolution, though there are plans to relax this constraint.

4.2.2 Numerical approach

PIXIE3D uses a finite volume scheme for the spatial discretization of equations (4.2) [Chacón, 2004]. Fluid equations are solved by PIXIE3D in their conservative form, which is more suitable for a finite volume approach. This assures conservation of physical quantities with a great precision.
The equations are discretized on a logical uniform and rectangular grid. A proper change of coordinate function $\mathbf{x} = \mathbf{x}\left(u^1, u^2, u^3\right)$ allows the mapping into the physical space. This generalized curvilinear formulation makes the code applicable to different geometries, in particular the ones interesting in the magnetic fusion field, namely the cylindrical and the toroidal ones.
The temporal discretization scheme employed is a fully implicit second order Crank-Nicolson (5.11). A set of nonlinear algebraic equation is obtained uses a Newton-Krylov method for its solution.
The code is parallel, with excellent scalability properties [Chacón, 2008b].

4.2.3 Boundary conditions

PIXIE3D implements, for the velocity field, a no slip boundary condition resulting in a radial velocity given by:

$$v_r = \frac{(E_0 \mathbf{e}_z \times \mathbf{B}) \cdot \mathbf{e}_r}{B^2}, \tag{4.11}$$

while the tangential component of the magnetic field is given by:

$$\mathbf{J}_t = \frac{E_0 B_z}{\eta B^2} \mathbf{B}_t. \tag{4.12}$$

The radial component of the magnetic field equal to zero.

Table 4.1: Run parameters for the three selected cases used to describe the nonlinear verification benchmark between SPECYL and PIXIE3D. From the left column: configuration studied, dimensionality, Lundquist number S, Prandtl number P, n mode of the MHD modes initially perturbed to trigger the nonlinear dynamics. The complete study is presented in [Bonfiglio et al., 2010].

Configuration	Dimensionality	S	P	perturbed modes
a) RFP	2D	$3 \cdot 10^4$	300	$n = -8$
b) tokamak snake	2D	$3 \cdot 10^4$	30	$n = -1$
b) tokamak sawtooth	2D	10^5	30	$n = -1$
c) RFP	3D	$3 \cdot 10^4$	100	$\|n\| = 8, 9, 10$

4.3 Nonlinear verification of SPECYL and PIXIE3D

The codes SPECYL and PIXIE3D have undergone to a cross-benchmark (nonlinear verification) process. The codes have been compared in their common limit of application (the compressible visco-resistive MHD model with constant density approximation). The result showed excellent agreement in all the studied regimes [Bonfiglio et al., 2010]. Initial equilibrium (the one described in section 4.1.4) and boundary conditions were uniformed.

Three cases will be briefly discusses that show the agreement of the two codes in describing the MHD dynamics of both the RFP and tokamak configurations. The main features of the cases are shown in table 4.1.

The figures 4.3 and 4.5 show the MHD modes dynamics in the three cases listed in table 4.1.

In particular the temporal evolution of the magnetic energy of the most important modes will be shown in two different colour, red for SPECYL and black for PIXIE3D. The very good agreement was obtained looking for the optimal resolution both in space (resolution of the grid used to compute the physical quantities) and in time (time step employed). The main result of the benchmark is that the two codes agree in all the dynamical regimes that result from the visco-resistive MHD model, provided enough spatial resolution is provided for the finite-volume code PIXIE3D. The power of the fully implicit integration scheme of PIXIE3D was also proved, as excellent agreement was found using time steps much larger than the ones used by SPECYL.

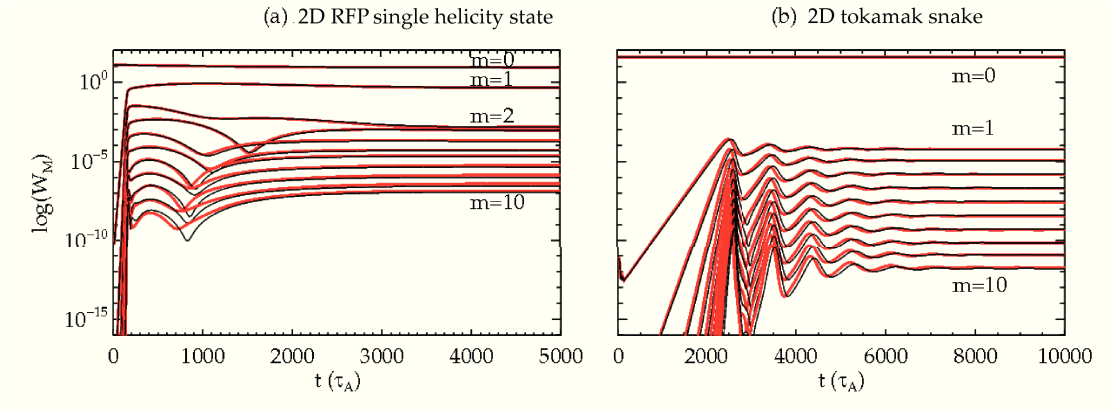

Figure 4.3: Time evolution of the magnetic energy of the most important MHD modes in a 2D SH RFP simulation and in a 2D tokamak simulation that presents a snake-like behaviour of the modes. The two codes agree very well.

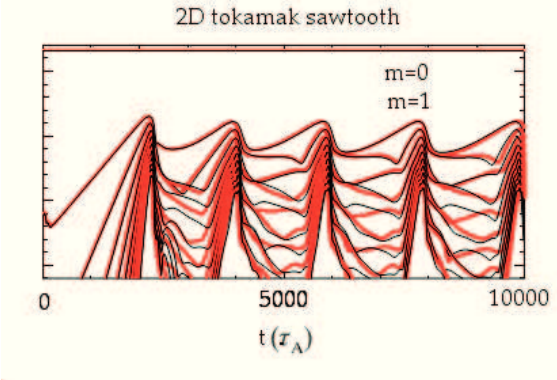

Figure 4.4: Time evolution of the magnetic energy of the most important MHD modes in a 2D tokamak simulation where a typical sawtooth behaviour of the MHD modes can be seen.

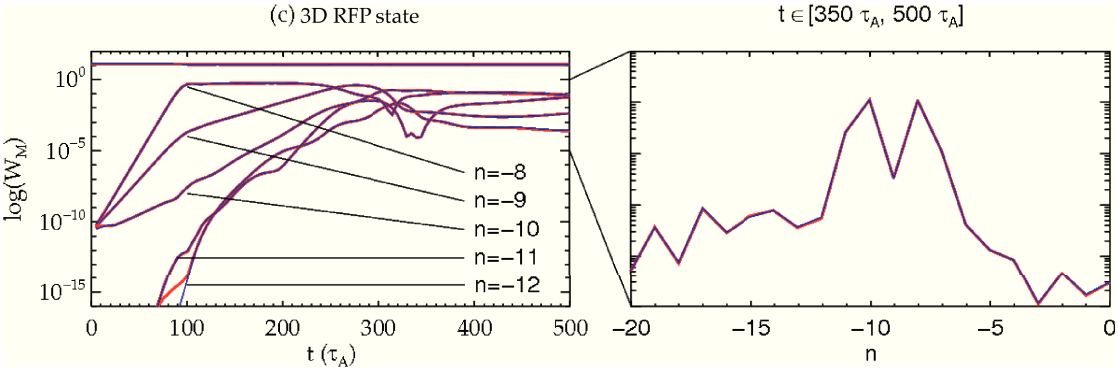

Figure 4.5: Time evolution of the magnetic energy of the most important MHD modes in a 3D RFP simulation. Again SPECYL and PIXIE3D agree very well.

5

Field line tracing: NEMATO

The study of the magnetic field's topology is of fundamental importance in the field of controlled thermonuclear fusion.
Depending on the features of the magnetic field there are two ways to determine its topology.
If the magnetic field possesses a symmetry, namely there is a coordinate system in which one or two ignorable coordinates exist, the study of magnetic topology can be performed *analytically*. This means that it is always possible to find a so called *flux function* ψ that define the existence of *magnetic surfaces*. Magnetic surfaces are surfaces whose normal is always perpendicular to the magnetic field, so that $\mathbf{B} \cdot \nabla\psi = 0$.
An important case of 1D symmetry is the axis-symmetry of basic tokamak configurations: the presence of a strong toroidal component of the magnetic field makes the various physical quantities depend only on the distance from the magnetic axis. A second important case is the 2D helical symmetry that can describe the QSH state of the reversed-field pinch configuration: here the two coordinates are represented by a radial coordinate that can be thought as a distance from the helical axis and an helical angle that describes the position on the helix.
If the magnetic field does not possess any symmetry the calculation of magnetic topology rely on the use of *numerical techniques*. The most used technique consists on the calculation of the spatial trajectory of many magnetic field line: the evaluation of their intersection with one or more surfaces, called *Poincarè surfaces*, allows to detect the presence of a definite topology and of *magnetic surfaces* or its absence. This last case is typical when magnetic field lines assume a *chaotic* behaviour.
Outline of the chapter. This chapter tackles the geometrical and numerical methods involved in the study of the NEMATO code. In section 5.1 the geometrical methods

for the solution of the magnetic field line equations will be introduced. In section 5.2 the numerical scheme of NEMATOwill be explained, while in the final section 5.3 the verification of the code against simple analytical cases will be proposed.

5.1 The magnetic field lines' equation

Magnetic field lines are curves in the three dimensional space that are everywhere tangential to the magnetic field vector $\mathbf{B}$.
The magnetic field line equation is given by:

$$\frac{d\mathbf{x}}{d\tau} = \mathbf{B}(\mathbf{x}). \tag{5.1}$$

The quantity τ does not represent a *physical time* and the magnetic field $\mathbf{B}(\mathbf{x})$ does not depend on the physical time. Equation 5.1 is then a system of ordinary autonomous differential equations. In the following topological analysis only fixed-time configurations will be analyzed.

5.1.1 Geometrical properties of the magnetic field lines' equation

The study of a system of ordinary autonomous differential equation like:

$$\frac{dx}{dt} = F(x), \qquad x \in \mathbb{R}^n, \qquad F \in \mathbb{R}^n \tag{5.2}$$

makes use of the tools from the study of dynamical systems.
An important quantity is the map $\Phi^t(x)$ of the vector field $F(x)$, defined as the value at the time t of the solution of 5.2 that has x as starting condition.
The set $\{\Phi^t(x), x \in \mathbb{R}^n\}$ is called *flux map* of the vector field $F(x)$. Consider a closed surface S_0 in the n-dimensional space. Under the action of the vector field $F(x)$ the evolution of the points inside the volume enclosed by S_0 has some interesting properties, that depend on the vector field features.

Preservation of the volume of the solutions

The following theorem shows how the volume of a set of initial conditions A varies under the action of the vector field $F(x)$.

Theorem 2 (Volume of the solutions) *Let $A \in \mathbb{R}^n$ be a measurable set. Then the volume*

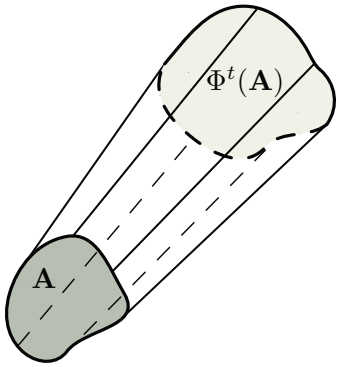

Figure 5.1: Pictorial visualization of the evolution of the set **A** under the vector field $F(x)$, that lead, after a time t to the set $\Phi^t(A)$

.

Vol($\Phi^t(A)$) varies in time according to:

$$\frac{d}{dt}Vol\big(\Phi^t(A)\big) = \int_{\Phi^t(A)} \nabla \cdot F(x) dV. \tag{5.3}$$

where

$$\nabla \cdot F(x) = \sum_{i=1}^{n} \frac{\partial F_i(x)}{\partial x_i}.$$

The demonstration of this theorem can be found in [Veranda, 2009] and uses the following lemma, that also defines the quantity $\mathrm{Vol}\big(\Phi^t(A)\big)$.

Theorem 3 (Lemma) *Let J^t the jacobian matrix of the map Φ^t,*

$$J^t_{ij}(x) = \frac{\partial \Phi^t_i(x)}{\partial x_j}. \tag{5.4}$$

Then the following identity is valid for a generic function $f(x)$:

$$\int_{\Phi^t(A)} f(x) dx_1 \dots dx_n = \int_A f\big(\Phi^t(x')\big) det J^t(x') dx_1^{'} \dots dx_n^{'}. \tag{5.5}$$

Equation 5.5 can be used with $f = 1$ to obtain:

$$\mathrm{Vol}\big(\Phi^t(A)\big) = \int_A \mathrm{det} J^t(x) dV, \tag{5.6}$$

and

$$\mathrm{Vol}\big(\Phi^0(A)\big) = \int_A dV. \tag{5.7}$$

where it has been used the fact that $detJ^0(x) = 1$.
What is important now is that equation 5.3 allows the classification of dynamical sys-

tems according to the value of their divergence. In particular if $\nabla \cdot F(x) = 0$ the system is *conservative*, while the case $\nabla \cdot F(x) < 0$ corresponds to *dissipative* systems.
Equation 5.1 is an example of a *conservative* system: equation 5.3 does not allow any variation of the volume of the solutions. Phenomena like the convergence of different magnetic field lines to a fixed point are impossible, as it must be in the case of a solenoidal field. A rigorous numerical treatment of equation 5.1 requires the use of exactly volume-preserving integrators, whose role is fundamental especially if the orbits are integrated for a long time.

Volume preserving integrators

Two main features are requested to a numerical integrator of equation 5.1 when the magnetic field $\mathbf{B}(\mathbf{x})$ is known on a grid.
The first is that the integrator must conserve the volume
The second is that the process to obtain the value of the field $\mathbf{B}(\mathbf{x})$ in points out of the grid must preserve its solenoidality.
One of the techniques used to fulfil the two stated conditions is to use high order (not necessarily volume preserving) integrators for the equations and high order interpolation functions to find the value of the field in points off the grid. Equations 5.6 and 5.7 state that the conservation of the volume

$$\frac{d}{dt}\text{Vol}(\Phi^t(A)) = 0 \tag{5.8}$$

is valid if and only if

$$i\text{det}J^t(x) = \text{det}\left(\frac{\partial \Phi_i^t(x)}{\partial x_j}\right) = 1. \tag{5.9}$$

5.2 NEMATO numerical scheme

Let

$$x^{n+1} = \Phi^t[x^n] \tag{5.10}$$

be the map that numerically evolves the system from a discrete time *n* to the time *n+1*. NEMATO [Finn and Chacón, 2005] uses a Crank-Nicolson time stepping scheme that is exactly volume preserving in a two dimensional space. The numerical scheme is implicit and its time discretization is given by:

$$x_i^{n+1} = x_i^n + hF_i\left(\frac{x_k^n + x_k^{n+1}}{2}\right), \tag{5.11}$$

where h is the integration time step, $x_i^n = x_i(t)$ and $x_i^{n+1} = x_i(t+h)$. An implicit summation on the components of the component k of the field F is present. It comes from the fact that the field F depends in general on all the components of the function x. The element J_{ij} of the jacobian matrix is given by:

$$J_{ij} = \delta_{ij} + h\frac{\partial}{\partial x_j}\Big[F_i\Big(\frac{x_k^n + x_k^{n+1}}{2}\Big)\Big], \tag{5.12}$$

$$= \delta_{ij} + \frac{h}{2}(F_{ij} + (FJ)_{ij}) \tag{5.13}$$

this last equality being valid only in 2D. In matrix form and indicating with $\mathbb{I}$ the identity matrix:

$$\mathbb{J} = \frac{\mathbb{I} + \frac{h}{2}\mathbb{G}}{\mathbb{I} - \frac{h}{2}\mathbb{G}}, \tag{5.14}$$

where $G_{ij} = \frac{\partial F_i}{\partial x_j}$. The quantity det$\mathbb{J}$ is thus calculated as:

$$\text{det}\mathbb{J} = \frac{1 + \frac{h}{2}\text{Tr}\mathbb{G} + \frac{h^2}{4}\text{det}\mathbb{G}}{1 - \frac{h}{2}\text{Tr}\mathbb{G} + \frac{h^2}{4}\text{det}\mathbb{G}}. \tag{5.15}$$

The fact that $\nabla \cdot F = \text{Tr}\mathbb{G} = 0$ implies that

$$\text{det}\mathbb{J} = 1 \tag{5.16}$$

5.2.1 Grid creation

NEMATO uses input data from a rectangular, three dimensional grid. A great importance is given to the magnetic field solenoidality preservation, both in the grid's points and outside them. The following procedure allows solenoidality preservation: the first step consist on the calculation of the vector potential $\mathbf{A}$ on the grid, by integration of $\mathbf{B} = \nabla \times \mathbf{A}$. Once $\mathbf{A}$ is obtained, a polynomial interpolation allows to *analytically* calculate a solenoidal magnetic field in every point of the domain. This is necessary in order to exploit at its best the volume-preserving Crank-Nicholson algorithm.

5.2.2 Use of the volume preserving Crank-Nicolson algorithm

The problem of the determination of the magnetic field line is a three dimensional problem, while in section 5.2 a two dimensional volume preserving numerical scheme was presented. A procedure to split one 3D problem in two 2D problems will be now presented. The magnetic field $\mathbf{B}$, written in terms of the vector potential $\mathbf{A}$, can be decom-

posed in three parts:

$$\mathbf{B}_1 = \nabla A_x \times \hat{\mathbf{e}}_x, \quad \mathbf{B}_2 = \nabla A_y \times \hat{\mathbf{e}}_y, \quad \mathbf{B}_3 = \nabla A_z \times \hat{\mathbf{e}}_z, \tag{5.17}$$

the three $\mathbf{B}_i$ being bidimensional, solenoidal and such that:

$$\mathbf{B}_1 + \mathbf{B}_2 + \mathbf{B}_3 = \mathbf{B}. \tag{5.18}$$

The problem of the integration of equation (5.1) in the three dimensional space is thus divided into three two-dimensional problems:

$$\frac{d\mathbf{x}}{d\tau} = \mathbf{B}_1(\mathbf{x}), \quad \frac{d\mathbf{x}}{d\tau} = \mathbf{B}_2(\mathbf{x}), \quad \frac{d\mathbf{x}}{d\tau} = \mathbf{B}_3(\mathbf{x}), \tag{5.19}$$

that can be reduced to two through a proper gauge transformation.

5.3 NEMATO verification

To verificate a code means to prove the correctness of the employed algorithm in reproducing a physical system whose features are already known with other methods.
In this section the case of 2D helically symmetric MHD simulations of RFP plasmas is analyzed as a verification example. Other verification cases of NEMATO can be found in [Bonfiglio et al., 2010].
One way to face the study of the topology of the 2D helically symmetric magnetic surfaces is the study of a scalar function, the helical flux function $\chi(r, u)$ (u being a second, non ignorable coordinate). The helical flux function expression can be derived from its definition: $\mathbf{B} \cdot \nabla\chi = 0$, meaning that the magnetic field is always tangential to the constant χ surfaces (the so called *flux surfaces*).
The second way consists in the calculation, with NEMATO, of the magnetic surfaces.
The verification consists in the comparison between the magnetic surfaces calculated by NEMATO and the flux surfaces obtained from the helical flux function χ.

ROAD 1: determination of the helical flux function χ

Let us consider a magnetic field $\mathbf{B}(\mathbf{r})$ in a three dimensional space with a curvilinear coordinate system whose coordinates are labelled as $u^i = (u^1, u^2, u^3)$.
Let us suppose that the system has a symmetry, i.e. $\frac{\partial}{\partial u^3} = 0$.
The magnetic field can be written using the vector potential $\mathbf{A}(\mathbf{r})$ as:

$$\mathbf{B} = \nabla \times \mathbf{A} = \frac{\epsilon^{ijk}}{J} \frac{\partial A_j}{\partial u^i} \mathbf{e}_k, \tag{5.20}$$

where ϵ^{ijk} represents the Levi-Civita tensor, J the jacobian of the coordinate transformation, A_j the covariant component of the vector potential and $\mathbf{e}_k$ is the covariant basis vector.
Imposing the relation

$$\mathbf{B} \cdot \nabla \chi = 0 \tag{5.21}$$

choosing a gauge $A_1 = 0$ and remembering that $\frac{\partial}{\partial u^3} = 0$ it is found that

$$\frac{\partial A_3}{\partial u^2}\frac{\partial \chi}{\partial u^1} - \frac{\partial A_3}{\partial u^1}\frac{\partial \chi}{\partial u^2} = 0, \tag{5.22}$$

meaning that the equality is satisfied if

$$\chi = A_3 = \mathbf{A} \cdot \mathbf{e}_3. \tag{5.23}$$

In helical geometry the helical flux function is given by the third covariant component of the vector potential, that will be indicated as A_{3h}. The next step is the determination of the helical flux function in cylindrical geometry, using the transformation law of vector between different geometries. Indicating with A_{ih} the covariant components of the vector potential in helical geometry and with A_{ic} the covariant components of the vector potential in cylindrical geometry the transformation law can be written as [D'haeseleer et al., 1991]:

$$A_{ic} = A_{ih}\frac{\partial u^{ih}}{\partial u^{ic}}. \tag{5.24}$$

The helical geometry is defined by the three coordinates $u^{ih} = (\rho, u, l)$, while the cylindrical one is defined by $u^{ic} = (r, \theta, z)$. The quantity ρ represents a radial coordinate, u represents a helical angle and the third coordinate l is ignorable in the case of helical symmetry under analysis. The coordinates of the helical geometry can be written in terms of the cylindrical coordinates as $\rho = r$, $u = m\theta + \frac{n}{R_0}z$ and $l = z$. Other possible choices are possible, in particular for the ignorable coordinate.
This identification allows to transform the helical flux function in helical geometry to cylindrical geometry using equation (5.24).
Simple calculations show that:

$$\chi = A_{3h} = A_{3c} - \frac{n}{mR_0}A_{2c}, \tag{5.25}$$

that, in terms of the *physical* cylindrical components of the vector potential $(\tilde{A}_r, \tilde{A}_\theta, \tilde{A}_z)$ the helical flux function (multiplied by m) is given by:

$$\chi = m\tilde{A}_z - \frac{n}{R_0}r\tilde{A}_\theta. \tag{5.26}$$

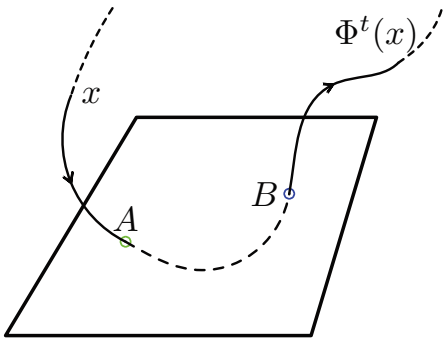

Figure 5.2: Intuitive definition of Poincarè plot.

ROAD 2: determination of the magnetic surfaces from a 2D field line tracing simulation in cylindrical geometry

Conserved magnetic surfaces are surfaces in a 3D space where magnetic field lines lie in their spatial evolution. Their presence can be evidenced by calculating the field lines of a magnetic field. If the magnetic field possesses a symmetry the intersection of a magnetic field line with a surface (a so called *Poincarè plot*) builds a surface with zero area, see figure 5.2. The quality of the result depends on the features of the field line tracing code and of the input data for the magnetic field. Two features are important:

1. the algorithm used to solve the magnetic field lines' equation, which should be volume-preserving, see 5.1.1;

2. the numerical data of the magnetic field have to be sufficiently resolved to allow a correct interpolation in points off the grid.

RESULTS

The helically symmetric magnetic field here used is obtained by a 2D MHD simulation with the SPECYLcode [Cappello and Biskamp, 1996].
Data from SPECYLare given to NEMATO with a resolution of $r = 101, \theta = 256, z = 2048$ points in the three directions, a resolution sufficient for NEMATO to calculate accurately the magnetic field lines (see [Veranda, 2009]) for a resolution study). The magnetic field line spatial behaviour has been analyzed both in a $z = 0$ and $\theta = 0$ Poincarè surface of section, see figure 5.3.
The surfaces defined by the helical flux function χ have been intersected with the same plane. NEMATO magnetic surfaces are coincident with the levels of the helical flux function as can be seen in figure 5.4.

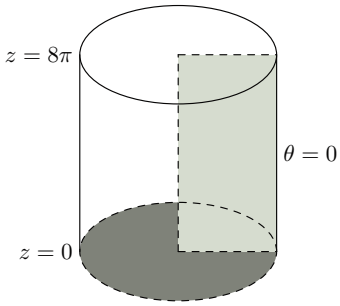

Figure 5.3: Most used Poincarè surfaces of section, respectively $\theta = 0$ and $z = 0$.

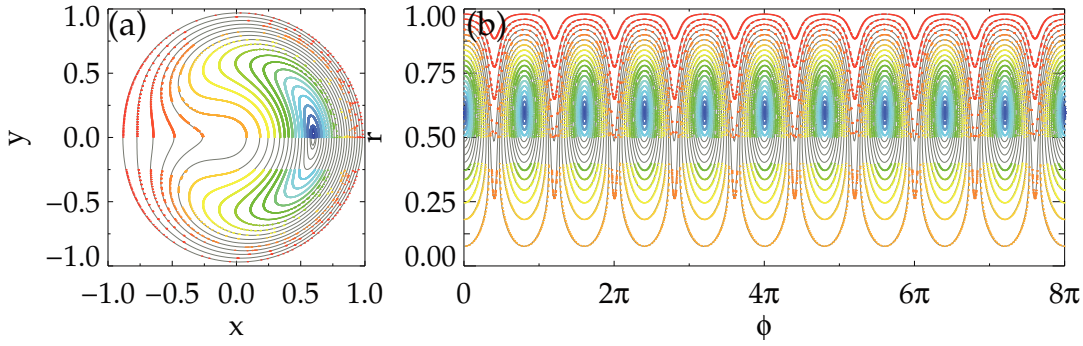

Figure 5.4: Validation of NEMATO against helical RFP configurations provided by SPECYLcode. Poincarè map in the $z = 0$ and $\theta = 0$ plane (colored dots) are compared with the helical flux function χ (black contour levels). Results are obtained with a grid resolution of $100 \times 256 \times 2048$ radial $\times$ azimuthal $\times$ axial points. To make the comparison easier a fraction of the area of the plots shows only the helical flux function contours.

III

Modelling results

6

Magnetic chaos healing by separatrix expulsion

Hamiltonian dynamics demonstrates that the resilience to chaos of a (hamiltonian) system increases when its corresponding separatrix orbit vanishes.
This universal behaviour takes a particular form in the case of magnetic chaos healing in the RFP. The separatrix that can be individuated in this case is a magnetic surface associated with the growth of a magnetic island on top of an axisymmetrix magnetic field corresponding to an unstable equilibrium.
Experimental observations show the presence of a dominant magnetic perturbation, recognized both from experimental measurement and numerical simulations. Furthermore it shows the absence of the separatrix of the dominant mode and the presence of a helical topology of the magnetic surfaces [Lorenzini et al., 2009], with expected positive effects on the confinement of particles and energy. Thermal measurements indicating a helical symmetry characterized by enhanced confinement are indeed performed in various RFP experiments [Martin et al., 2003].
In this thesis the work performed in [Escande et al., 2000c] is confirmed and extended: a systematic analysis of the condition that lead to magnetic chaos healing is operated, analyzing data from various MHD simulations performed with the SPECYL code.
In this chapter two paradigmatic SPECYL MHD simulation of the RFP configuration will be shown. The first represents a clear example of the role of the separatrix expulsion of the dominant mode in chaos healing. A second simulation will show how the role of the dominant mode can be influenced by secondary modes' presence.
Outline of the chapter. This chapter deals with two MHD simulations that present the phenomenon of the magnetic field dominant mode's *separatrix expulsion*. The first simulation (in section 6.1) describes the effect of the *separatrix disappearance* on various magnetic field-related quantities: helical flux function, helical q-profile, topology of the

magnetic field line, secondary modes. The helical flux function of the dominant mode and the helical safety factor profile will constitute the keys to analyze the role of the dominant mode (section 6.1.1 and 6.1.2). The study of magnetic topology will give a hint on the role of secondary modes (sections 6.1.3 and 6.1.4).
The second simulation (in section 6.2) shows a further example of separatrix expulsion and will be described in a similar way.
In the end, some summarizing remarks will be proposed in section 6.3.

6.1 A first paradigmatic case: the role of dominant mode

The study of chaos healing in the RFP is performed, from the numerical point of view, via 3D SPECYL MHD simulations. In particular the simulation under consideration aims at modelling the transition that leads from a MH to a QSH state. The work presented in this section is based on material published in [Bonfiglio et al., 2010].
A full spectrum of MHD modes with $0 \leqslant m \leqslant 4$, shown in 4.1, has been considered and the initial axisymmetric equilibrium has been perturbed by two helical perturbations, namely the $m = 1$ MHD modes with $n = -9$ and $n = -10$. The Lundquist and Prandtl number are set to $S = 3 \cdot 10^4$ and $P = 10^3$, resulting in a Hartmann number $H \approx 10^3$. A spontaneous SH state is then expected at the end of the simulation (see section 2.3).
Some details of the MHD simulation are reported in figure 6.1, where various quantities that will be defined in this chapter, like the *helical safety factor* (section 6.1.2) are shown. The $n = -9$ mode, the most unstable between the two perturbed modes, is the dominant mode in the second part of the linear growth phase and at the beginning of the saturation phase. The nonlinear dynamics makes the $n = -10$ mode the dominant after $t = 2000\,\tau_A$; together with the exponential decay of the secondary modes the system is brought to a final $n = -10$ SH equilibrium configuration. In the previous sentences the words *dominant mode* should be read in an intuitive sense: a more precise definition can involve quantitative considerations about the magnetic energy associated with the single MHD mode: dominant mode is the mode, different from the axisymmetric $(0, 0)$ mode, with the higher magnetic energy.

The separatrix expulsion process will be described using data from the simulation presented in this section. The process has effect on many quantities: *helical flux function topology*, *helical q profile*, *magnetic field topology*. This effects will be described in the following sections.

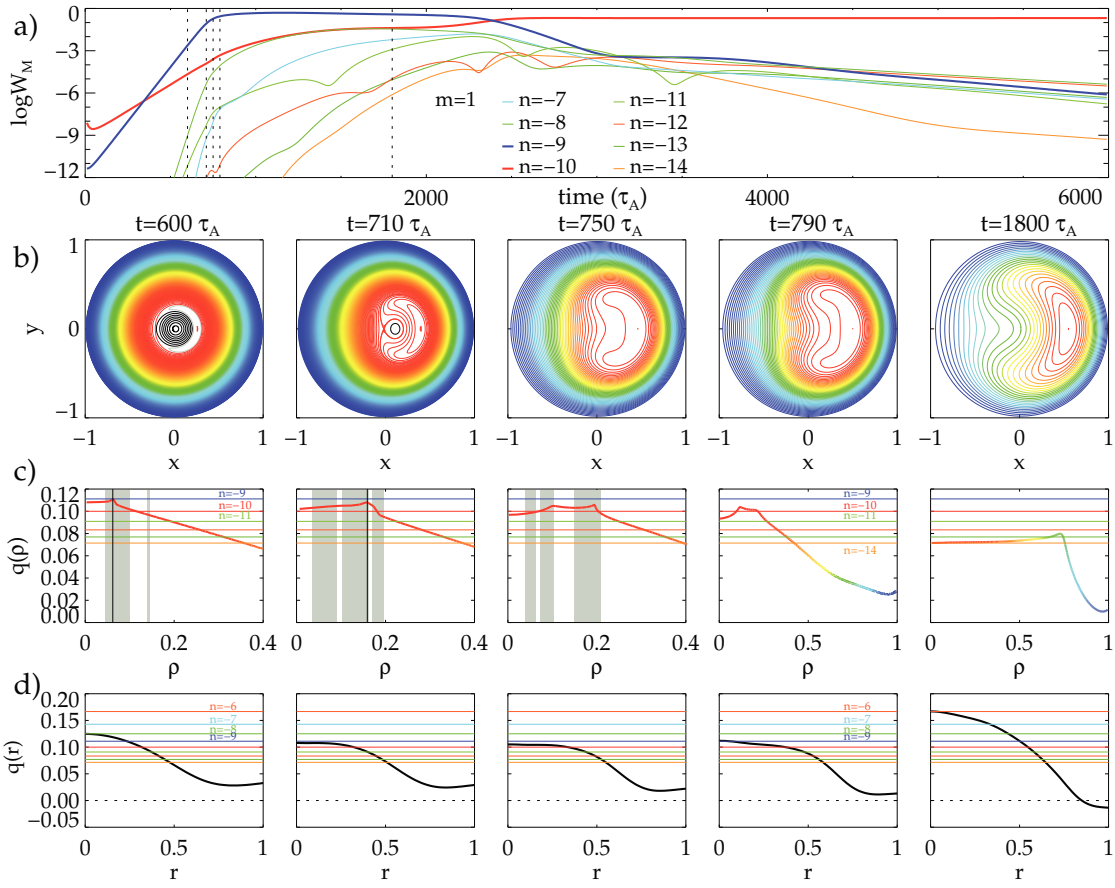

Figure 6.1: The temporal evolution of the magnetic energy of the $m = 1$ modes is reported in panel (a). The simulation times chosen for the analysis with NEMATO are marked with dashed vertical lines. For these times the contour level of the helical flux function χ are reported on the second row. In the third row the helical q-profile is plotted as a function of the effective radius ρ. Both χ and $q(\rho)$ are computed assuming a $n = -9$ helical symmetry. The color of the flux surfaces in panel (b) refer to their ρ values, which is also evidenced in panel (c). The ρ_{sep} value corresponding to the separatrix is marked in panel (c) with a black vertical line, while shaded vertical bands refer to chaotic regions in the Poincaré plots of figure 6.3. The rational values from $1/14$ to $1/9$ are shown in panel (c) with the same color employed in panel (a). Fourth row, panel (d), shows the radial profile of the axisymmetric safety factor, $q(r)$.

6.1.1 Evolution of the helical flux function topology

The contour level of the helical flux function are plotted in figure 6.1(b) for various selected times. The first two snapshots are characterized by the DAx magnetic topology (section 2.4.2), characterized by the presence of two magnetic axes, separated by the magnetic separatrix. Few Alfvén times before $t = 750\,\tau_A$ the topological transition to the SHAx state occurs (section 2.4.2), characterized by the disappearance of the

magnetic separatrix.The magnetic island O point remains the only magnetic axis of the system. The MHD dynamical evolution of the magnetic field has the effect of achieving a topological transition. The separatrix expulsion process can thus be considered as the final stage of the process of growth of a helical perturbation that non-linearly becomes the dominant in the broad spectrum of MHD instabilities.

6.1.2 Evolution of the helical q-profile

Some details of the helical q profile, $q(\rho)$ defined in section 2.2.2, shown in figure 6.1(c), have to be noticed to understand the effect of separatrix expulsion during the dynamics.
Firstly, when there is a separatrix, $q(\rho) \rightarrow 1/9$ at the separatrix (that is marked with a black vertical line in row c)). Secondly, q(ρ=0) decreases in time and a secondary maximum of q appears inside the separatrix, see $t = 750\,\tau_A$ shortly after separatrix expulsion that is modifying the helical equilibrium. The presence of secondary maximum creates regions of reversed shear s ($s = d(\ln q)/d\rho$) which will be shown to be regions of good local magnetic confinement. Later in time the complete establishment of a helical equilibrium results, at $t = 1800\,\tau_A$, in a much lower and flat in the core q profile, which still possesses a wide region of reversed shear.

6.1.3 Evolution of the magnetic field topology

In this section the topology of the magnetic field will be analyzed: its evolution during the separatrix expulsion gives a hint of the level of magnetic stochasticity related transport, because, differently from the helical flux function, the determination of magnetic topology involves the magnetic field in its entirety.
The magnetic field topology has been computed by NEMATO at the selected simulation times highlighted in figure 6.1. The corresponding Poincaré plots on the $z = 0$ and $\theta = 0$ surfaces are reported in figure 6.3 (the digital version of the thesis is preferable to appreciate the details of the magnetic structures).
At $t = 600\,\tau_A$, the $n = -9$ and $n = -10$ islands (the reason why resistive-kink tearing modes $m = 1$ and $n = -9, -10$ create a magnetic island are explained in section 3.6.2) produced by the two perturbed modes are clearly visible along the z direction in the $\theta = 0$ plane, with the $n = -10$ chain distorted by the $n = -9$ helical perturbation. By overplotting the $n = -10$ conserved surfaces on the $n = -9$ helical flux surfaces of figure 6.3(a), it could be shown that they lie on the helical flux surface with $q(\chi) = 1/10$. As it is possible to notice the two separatrices overlap and magnetic chaos develops in the region between the two islands and, in particular, inside the separatrix of the $n = -9$ mode.

This is in agreement with a *naïve application* of the Chirikov overlap criterion that can be stated as: *the larger the amplitude and the number of Fourier components, the more chaotic the dynamics*. However, different cases will be shown in this thesis where the simple Chirikov criterion application does not give any clue on the underlying magnetic topology.

The magnetic surfaces close to the cylindrical axis remain perfectly conserved, as well as those located in the outer region. Secondary islands due to the beat of the two main islands are also visible inside the chaotic sea. As for the $n = -10$ island, the effective radial position of the secondary islands with respect to the helical axis correspond to helical flux surfaces with rational q values.

At $t = 710\,\tau_A$, when the strongly deformed $n = -10$ island is quite narrow but still visible just outside the $n = -9$ separatrix, a broad chaotic region is observed between the remnant conserved surfaces around the helical axis and those around the helically displaced cylindrical axis. However, a region with conserved surfaces appears in the middle of the chaotic region. The ρ position of the conserved layer corresponds to the region with negative magnetic shear, as marked by means of an unshaded band in figure 6.1(c). The extent of the conserved layer increases in time with the deepening of the q hollow.

In the meantime the separatrix expulsion occurs, which is seen by the disappearance of the helical axis at $t = 750\,\tau_A$. At this time the conserved layer is rather large. Again, it turns out to be located in the $\mathrm{d}q/\mathrm{d}\rho \leqslant 0$ region of the q profile. Since $q(0)$ is above $1/10$ a $(1, -10)$ island appears inside the chaotic region at the $q = 1/10$ resonant surface close to the helical axis. Conserved surfaces corresponding to the original $n = -10$ island are not found at this time.

At $t = 790\,\tau_A$, when the separatrix is well expulsed, chaos is strongly reduced in the whole domain. It only survives at the separatrix of the outer $n = -10$ island, which reappears with a rather elongated shape at this time. The chaos healing effect is robust and lasts for a long time, even if the amplitude of the secondary modes is increasing.

At $t = 1800\,\tau_A$, for example, well defined magnetic surfaces are still observed in the whole domain, either closed around the helical axis or in the form of secondary islands, now with $n = -14$ due to the lower q profile.

6.1.4 The role of secondary modes

The role of secondary modes will be analyzed studying two parameters, secondary modes being all the MHD modes different from the dominant one. The two parameters are: their absolute amplitude, defined in equation (6.1), and their relative amplitude

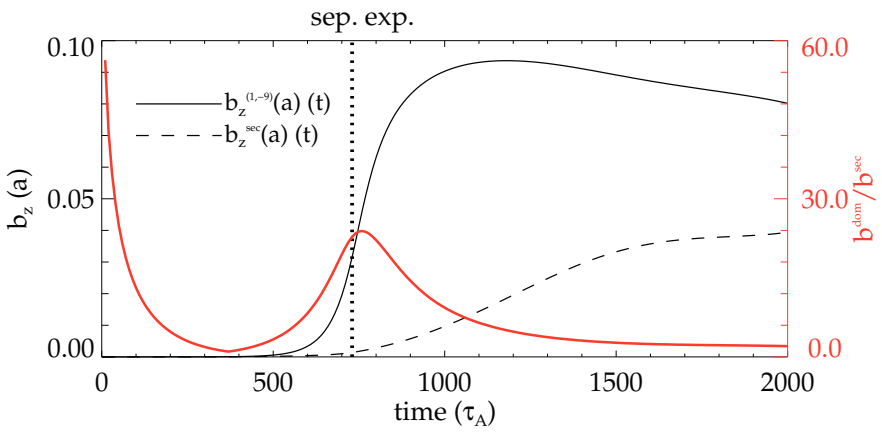

Figure 6.2: Temporal evolution of the axial component of the magnetic field associated with the dominant MHD mode at the edge $b_z^{1,-9}(a)$ is plotted with a continuous black line. The temporal evolution of the $m = 1$ secondary modes, calculated using equation (6.1), is plotted with a dashed black line. The thick red line represents the ratio between dominant and secondary modes (right axis). The vertical dotted line represents the separatrix expulsion time.

with respect to the dominant one.

$$b_z^{m=1,sec}(a) = \sqrt{\sum_{n=-20, n\neq n_{dom}}^{n=-5} \left(b_z^{1,n}\right)^2} \tag{6.1}$$

Both these parameters are plotted, as a function of time, in figure 6.2, on the same time interval analyzed in figure 6.1.

The total amplitude of the secondaries grows during the whole time slice under analysis: this does not prevent magnetic chaos to vanish.

On the contrary the ratio between dominant and secondary modes magnetic field has an oscillating behaviour, as it raises soon after the separatrix expulsion (when magnetic chaos diminishes) and drops in the final part of the simulation (when the magnetic chaos still diminishes). This parameter thus can not be used to describe the level of magnetic chaos. In this slice of simulation clearly the biggest influence on the level of stochasticity is given by the establishment of a helical symmetry of the magnetic field, constraining the secondary modes to a *secondary* role. Another interesting case, with more interesting implications in terms of role of secondary modes, will be widely explored in chapter 7.

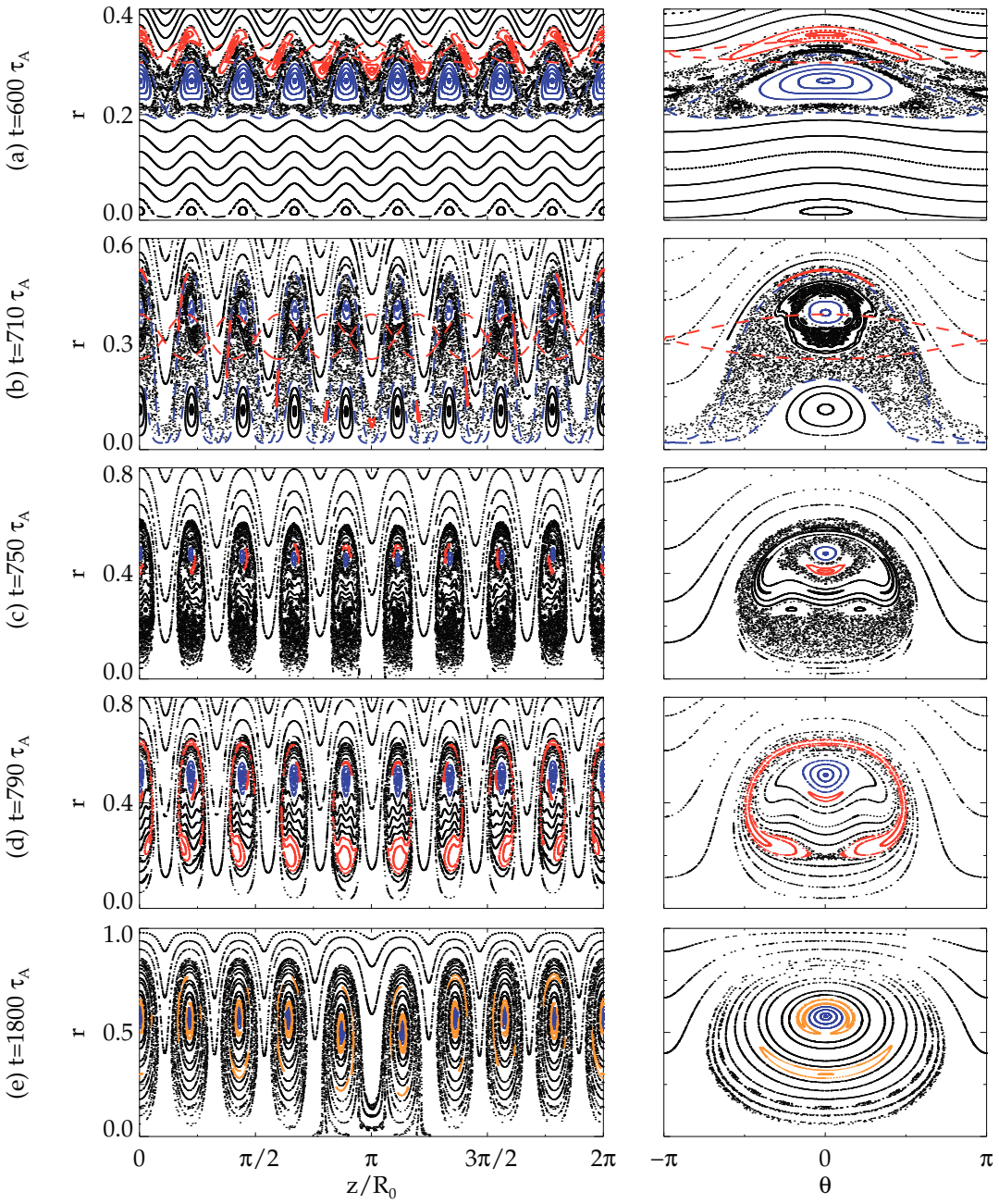

Figure 6.3: NEMATO simulations for the study of chaos healing in the RFP. Poincaré maps on the $\theta = 0$ plane (first column) and on the $z = 0$ plane (second column) are reported in panels (a-e) for the selected simulation times. Conserved surfaces corresponding to the region close to the $n = -9$ helical axis and to the $n = -10$ magnetic island are shown in blue and red, respectively. The same colors are used in the first two times for dashed curves marking the magnetic separatrices of the two modes, computed from the related helical flux functions. In the last figure the orange color is used to evidence the $n = 14$ structure.

6.2 A second paradigmatic case: the subtle role of secondary modes

A second, further example of chaos healing after the dominant mode's separatrix expulsion can be given considering the final part of a SPECYL MHD simulation whose initial frame will constitute the core of chapter 7.
As in the simulation described in 6.1, a full spectrum of MHD modes with $0 \leqslant m \leqslant 4$ has been considered. In this case the initial axisymmetric equilibrium has been perturbed by three helical perturbations, namely the $m = 1$ MHD modes with $n = -8$, $n = -9$ and $n = -10$. The adimensional dissipation parameters are the same of the previous MHD simulation, and in fact the MHD dynamic ends with the same $h = 10$ spontaneous SH state. More details of the MHD simulation are reported in section 4.3 and in figure 6.4.
The $n = -8$ marginally non-resonant with respect to the axisymmetric q-profile ($q(r = 0) = 1/8$) is the most unstable MHD mode and rapidly grows to create a QSH phase lasting in the interval $[0 : 1600]\,\tau_A$. The fact that such a marginally non-resonant mode had such a high growth rate was verified also through linear stability analysis performed using the CMR-F code [Wang and Guo, 2011], analyzing the features of the axisymmetric equilibrium. After a MH phase in the interval $[1600 : 1800]\,\tau_A$ a spontaneous $h = 10$ QSH phase is recovered, as in the previous simulation.

6.2.1 Evolution of the helical flux function topology

The evolution of the helical flux function topology, calculated assuming the helicity of the dominant mode $h = 10$, is shown in figure 6.4b. The separatrix expulsion occurs between $t = 2300\,\tau_A$ and $t = 2400\,\tau_A$. Before $t = 2300\,\tau_A$ the area occupied by the original axisymmetric topology (flux surfaces colored in black) is very small indicating a state marginally close to separatrix-expulsion. Later on a simple helical topology is obtained.

6.2.2 Evolution of the helical q-profile

The helical q-profile exhibits a less peculiar behaviour than in the case described in section 6.1.2; this may be due to the fact that the dynamics is quasi-stationary in the time interval under analysis. Its temporal evolution at five relevant times is described in figure 6.4c). The only relevant change is the disappearence of the separatrix (located around $\rho \approx 0.7$) between $t = 2300\,\tau_A$ and $t = 2400\,\tau_A$. After the separatrix expulsion a *separatrix ghost* is clearly visible in the helical-q profile, as a absolute maximum positioned around $\rho \approx 0.7$. Note that the value of the core q_h profile falls below the $1/14$ value in the continuation of the dynamical evolution of the system. The role of helical

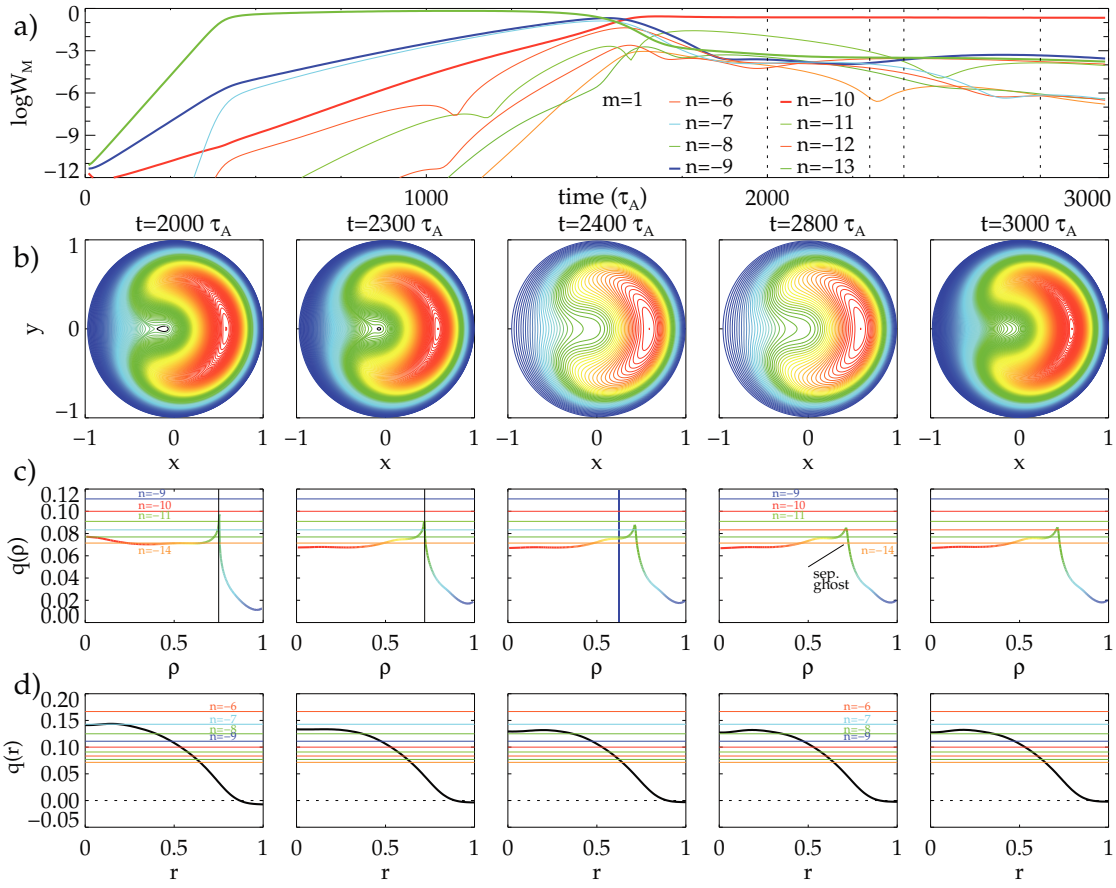

Figure 6.4: The temporal evolution of the magnetic energy of the $m = 1$ modes is reported in panel (a). The simulation times chosen for the analysis with NEMATO are marked with dashed vertical lines. For these times the contour level of the helical flux function χ are reported on the second row. In the third row the helical q-profile is plotted as a function of the effective radius ρ. Both χ and $q(\rho)$ are computed assuming $n = -10$ helical symmetry. The colors of the flux surfaces in panel (b) refer to their ρ values, which is also evidenced in panel (c). The ρ_{sep} value corresponding to the separatrix is marked in panel (c) with a black vertical line. The rational values from $1/14$ to $1/9$ are shown in panel (c) with the same color employed in panel (a). Fourth row, panel (d), shows the radial profile of the axisymmetric safety factor, $q(r)$.

safety factor profile seems to be weakened in this case as the effective chaos diminution does not correspond to any relevant change in this quantity.

6.2.3 Evolution of the magnetic field topology

The magnetic field topology evolution is shown in figure 6.5. At $t = 2000\,\tau_A$ magnetic chaos is spread in nearly the whole domain. A $(1, -10)$ helical core with conserved surfaces is found, and conserved surfaces are present at the edge of the simulation domain.

Here the cumulated effect of the interaction between many different MHD modes and of the presence of the separatrix of the dominant mode produces magnetic chaos.
At $t = 2300\,\tau_A$ magnetic chaos is still well spread in a big part of the domain, but the helical core has grown to a relevant amplitude. The chaos healing process has started.
Soon after the separatrix expulsion, at $t = 2400\,\tau_A$, the chaos healing process is progressing: the helical core raises in area and a new set of conserved magnetic surfaces appear in the chaotic part of the Poincaré plot. Note for example the structure, highlighted in blue in figure 6.5(c): this structure corresponds to the $\chi(\rho) = 1/13$ region, that is also highlighted in blue in figure 6.4(c). The blue structure is characterized by a poloidal wave number $m = 1$ and by an axial wave number $n = 10$, as ten structures can be counted in the $\theta =$ cost surface of section. The resonance with the helical safety factor profile at $1/13$ is recovered adding its *strobing* number with respect to the Poincarè surface of section (given by 10) to the *precessing* number of the structure around the $n = -10$ helical axis (given by 3, as can be verified looking at figure 6.5(c)), see [Bonfiglio et al., 2010] for another similar case.
After $t \geqslant 2800\,\tau_A$ the chaos healing process is completed, and a SH topology with perfectly conserved magnetic surfaces is present.

6.2.4 The role of secondary modes

The ratio between dominant and secondary modes is almost constant during all the time slice taken in consideration, while the cumulated secondaries amplitude is slightly decreasing in time, as can be evaluated looking at figure 6.6. As in the previous simulation explored in section 6.1 the more important role in healing magnetic chaos seem to be given by the establishment of a helical symmetry of the field. The role of secondary modes is less important, mainly because their energy is more than two order of magnitude lower than the one of the dominant mode.
The case presented here is yet more subtle: the chaos healing phase lasts more than in the other simulation (here around $600\,\tau_A$ while in the previous case $\approx 80\,\tau_A$) and during this phase neither the dominant nor the secondaries energy significantly varies. The cause of the longer healing time may be in the slower dynamics under analysis.

6.3 Summary and remarks

The two MHD simulations described in this chapter show the onset of a Single Helicity state characterized by a helicity $h = 9$ and $h = 10$ after the process of separatrix expulsion of the dominant mode.
The dynamics described in this chapter represents an academic case of study, which helps emphasizing the different roles of the dominant mode and of the secondary

modes. This is obtained using a simplified dynamics of the magnetic field. The term *simplified dynamics* means that the dynamical evolution of the system points towards a less developed spectrum of MHD modes than the one found in more realistic cases. Figure 6.7 shows the difference between a *simplified dynamics* spectrum and a *realistic dynamics* spectrum. The simplified dynamics employed in this chapter, though representing a simpler case of study with respect to the fully developed MHD modes dynamics observed in experiment is still relevant. In fact the cases shown in this and in the next chapter allowed to draw some conclusions on the role of dominant and secondary MHD modes.

The *role of the dominant mode*, that is revealed during its separatrix expulsion, is found to be important to obtain magnetic chaos healing. The process of separatrix expulsion is confirmed as a key ingredient to heal magnetic chaos [Escande et al., 2000c]. The effectiveness of the process in influencing the topology of the magnetic field, instead, depends on the choice of the dominant mode. In fact in the framework of this high dissipation dynamics a first hierarchy can be defined as the results indicate that the $n = -9$ mode is less subject to chaos (or more resilient) than the spontaneous $n = -10$. A state is *resilient* if magnetic chaos does not emerge, or emerge weakly, despite low amplitude difference between dominant and secondary modes. The study of dynamically similar states characterized by the achievement of a QSH state built upon the $n = -8$ MHD mode (see chapter 7) show that the latter state can be even more resilient to magnetic chaos.

The *role of the secondary modes* seems of minor importance in the two simulation cases shown here. Nevertheless it will emerge in its importance in further simulations, shown in chapter 7 and 9, simulations characterized by a more developed spectrum of MHD modes.

As a further remark new tools for understanding the role of the *helical symmetry* of the system are being built. The tools are based on the analysis of the configuration treating the MHD modes different from the dominant one as perturbations to a helical equilibrium, introducing helical flux coordinates for the system (for a definition of flux coordinates see [D'haeseleer et al., 1991]) and associating to each *cylindrical* mode a corresponding spectrum of *helical* modes that resonate with the quantity q_h (see section 6.1.2). Promising preliminary results are achieved in the analysis of the first paradigmatic case, described in section 6.1. This work is ongoing with the theory group at Consorzio RFX.

A last remark on the simplified dynamics must be done. The fact that it is different, under some aspects like the quasi-periodical crashes observed in RFX-mod, from the observation prevents the results here presented from being easily generalized. In any

case a list of the parameters of the model that can be changed to obtain more realistic simulation cases can be formulated and it includes the choice of the adimensional parameters S and P ruling dissipation and the radial profile of resistivity and viscosity [Sätherblom et al., 1996]. Furthermore dynamics can be influenced by the choice of boundary conditions, as here an ideal wall is employed. It can be influenced by the choice of the initial equilibrium (the one described in section 4.1.4 is used in this thesis). These parameters need to be adjusted to deal with a closer comparison with experimental findings: this adjustment will be presented in chapter 8.

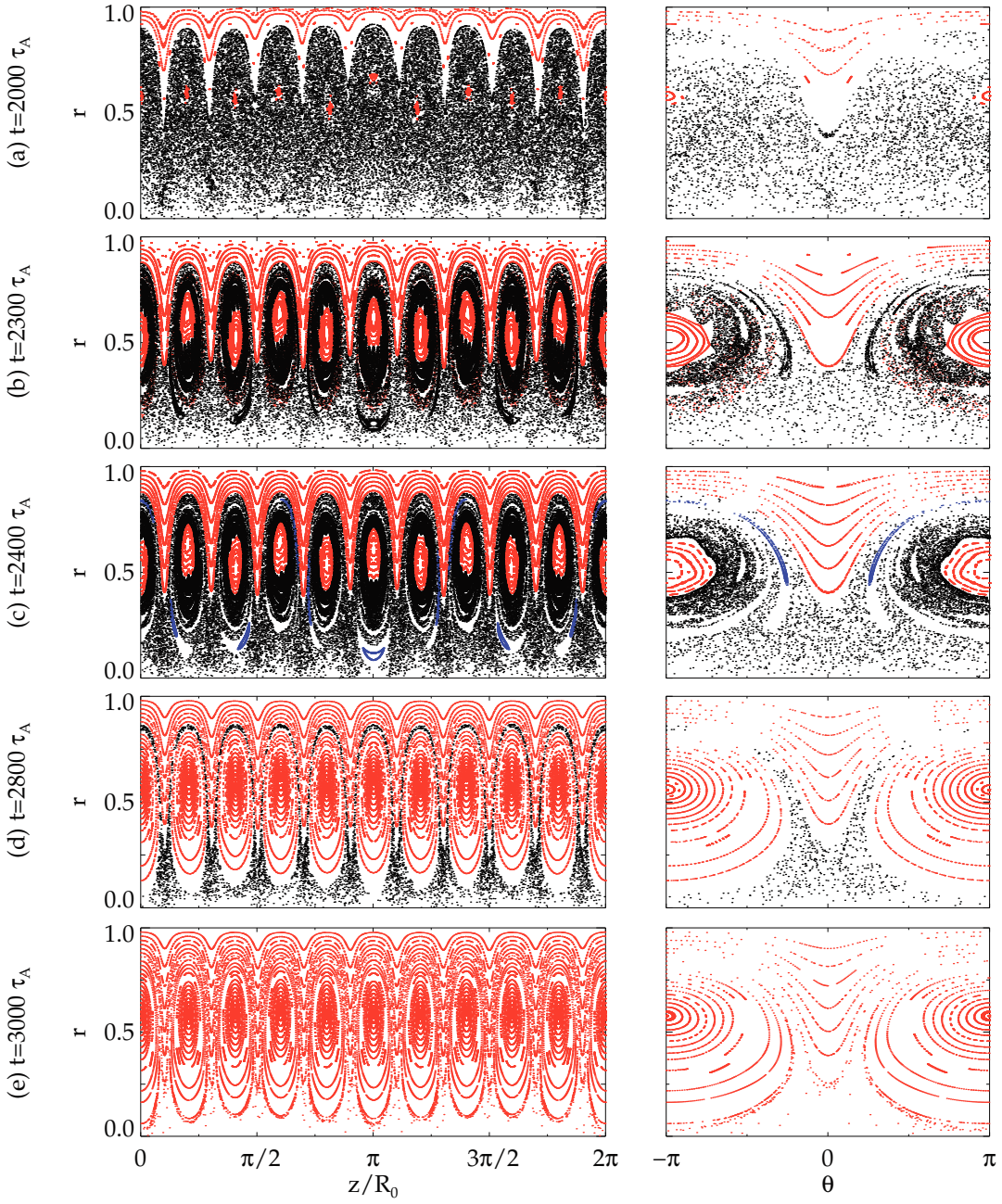

Figure 6.5: NEMATO simulations for the study of chaos healing in the RFP. Poincaré maps on the $\theta = 0$ plane (first column) and on the $z = 0$ plane (second column) are reported in panels (a-e) for the selected simulation times. Conserved surfaces corresponding to the region close to the $n = -9$ helical axis are shown in blue. Conserved surfaces related to the $n = -10$ magnetic island and to the edge are shown in red.

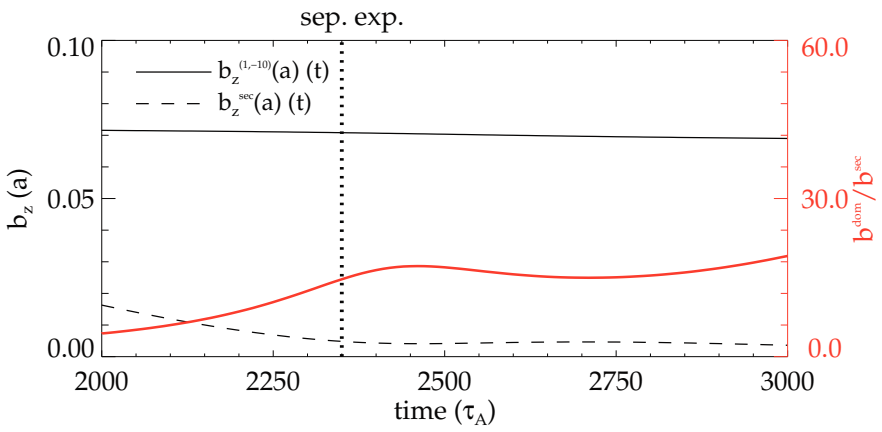

Figure 6.6: Temporal evolution of the axial component of the magnetic field corresponding to the dominant MHD mode at the edge $b_z^{1,-10}(a)$ is plotted with a continuous black line. The temporal evolution of the $m = 1$ secondary modes, calculated as in figure 6.2, plotted with a dashed black line. The thick red line represents the ratio between dominant and secondary modes.

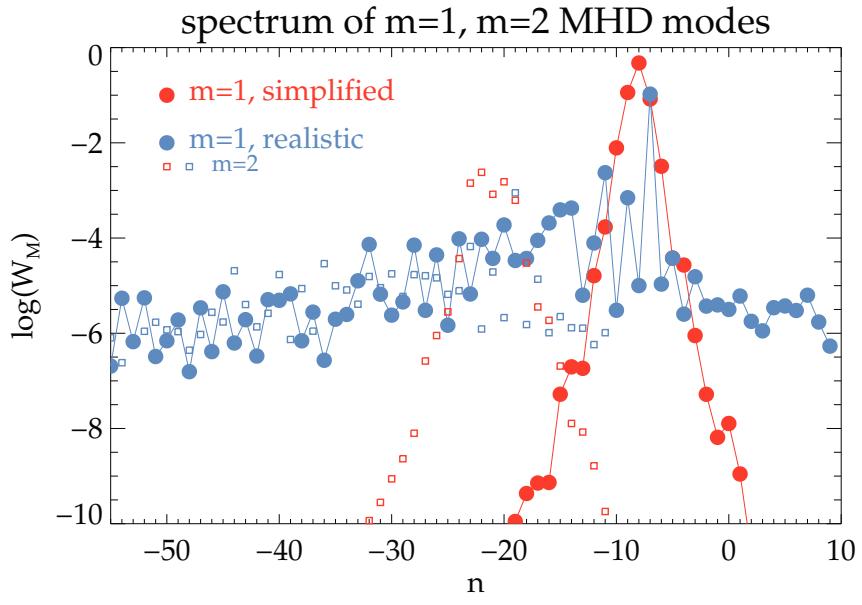

Figure 6.7: In blue a simplified spectrum is shown, corresponding to the final time instant of the simulation whose evolution is shown in figure 6.1. In red a realistic spectrum is shown, corresponding to the simulation shown in figure 8.14.

7

Magnetic chaos resilience in helical RFP states

In the class of MHD simulations described by a relatively high visco-resistive dissipation a peculiar case is the one of a QSH state built upon a mode that is non-resonant with respect to the safety factor profile. This case has been compared with the *usual* QSH built upon a resonant MHD mode. The main difference is that no magnetic island is associated with the mode and thus no magnetic separatrix is present on the magnetic flux surfaces topology from the beginning: thus an initial seed of magnetic chaos is removed. The results shown in this chapter are not easily generalizable, as the dynamics is different from the experimental one under some important aspects. For example, a SH state is spontaneously obtained at the end of the simulation: this does not usually happen in the experiments, if not temporarily (as a reference the typical RFX-mod discharge at medium plasma current is pictured in figure 10.2). Nevertheless the study provided an interesting insight in the magnetic field properties and an important input to the exploration of stimulated QSH states in the RFP (see chapters 8 and 9).

Outline of the chapter. This chapter deals with the dynamical and topological analysis of the MHD simulation described in section 7.1. In section 7.2 the evolution of the helical q-profile is shown. A perfect magnetic order is observed, in section 7.3, in time instants characterized by perturbation to the helical equilibrium whose cumulated amplitude is comparable with the amplitude of the equilibrium itself. The rest of the chapter deals with the research of the causes of such a magnetic order. Two main hypothesis can be formulated to explain this behaviour. The first states that a helical equilibrium is the fundamental ingredient to obtain magnetic order. The second states that the level of perturbations to the helical equilibrium is still the most influential parameter to take into account, and that their reduction or correct shaping is fundamental to achieve order. The two hypothesis are explored in sections 7.4 and 7.5: although

the correct explanation to this behaviour is probably in the middle between the two hypothesis, the data shown indicate that the second hypothesis is the more relevant one. In section 7.5 a new kind of simulation is presented, that used MP (section 4.1.3) to sustain a selected QSH state.
A summary and remarks section can be found in 7.6. Some of these results can be found in [Verandaet al., 2011].

7.1 Helical states built upon a non-resonant MHD mode

The SPECYL simulation that will provide the basis for the study of the dynamics of the magnetic field in the case of QSH states built upon non-resonant MHD modes has already been described in section 6.2, where its final part was analyzed. In this chapter its initial part, up to $1600\,\tau_A$, will be analyzed. Some important details of the simulation, like the magnetic energy and the safety factor profile evolution in time, can be found in figure 7.1.

This simulation is important because its initial part may schematically represent the final stage of discharge formation when achieving the toroidal magnetic field reversal. Furthermore the most interesting feature is that a long lasting phase, of almost $1000\,\tau_A$, characterized by a dominant $(1,-8)$ mode is found during which the ratio between dominant mode and secondary intensity has values, in particular for $t \geqslant 1000\,\tau_A$, comparable with the experimental one and with the previous simulations described in chapter 6. Between $t = 1300\,\tau_A$ and $t = 1400\,\tau_A$ for example the energy difference between the $(1,-8)$ and the $(1,-9)$ mode is around $\log W_M^{1,-8} - \log W_M^{1,-9} = 1$, resulting in a ratio of about 4 between the corresponding magnetic field, similarly to what happens in the RFX-mod experiment at high current [Piovesan et al., 2009]. A temporal trend for the quantity

$$\Delta \log W_M = \log W_M^{1,-8} - \log W_M^{\text{dom sec}}$$

is reported in table 7.1 ($\log W_M^{\text{dom sec}}$ represents the energy of the most important secondary mode), together with a corresponding plot showing the relative intensity between the dominant mode and the cumulated secondary modes' amplitude in figure 7.2.

7.2 Evolution of the helical q-profile: a monotonic q-profile

The helical safety factor (section 6.1.2), shown in figure 7.1, is calculated assuming that the underlying helical equilibrium has a helicity $h = 8$, because the $(1,-8)$ MHD mode is the dominant until $t \approx 1500\,\tau_A$: after that the calculation of the profile with this he-

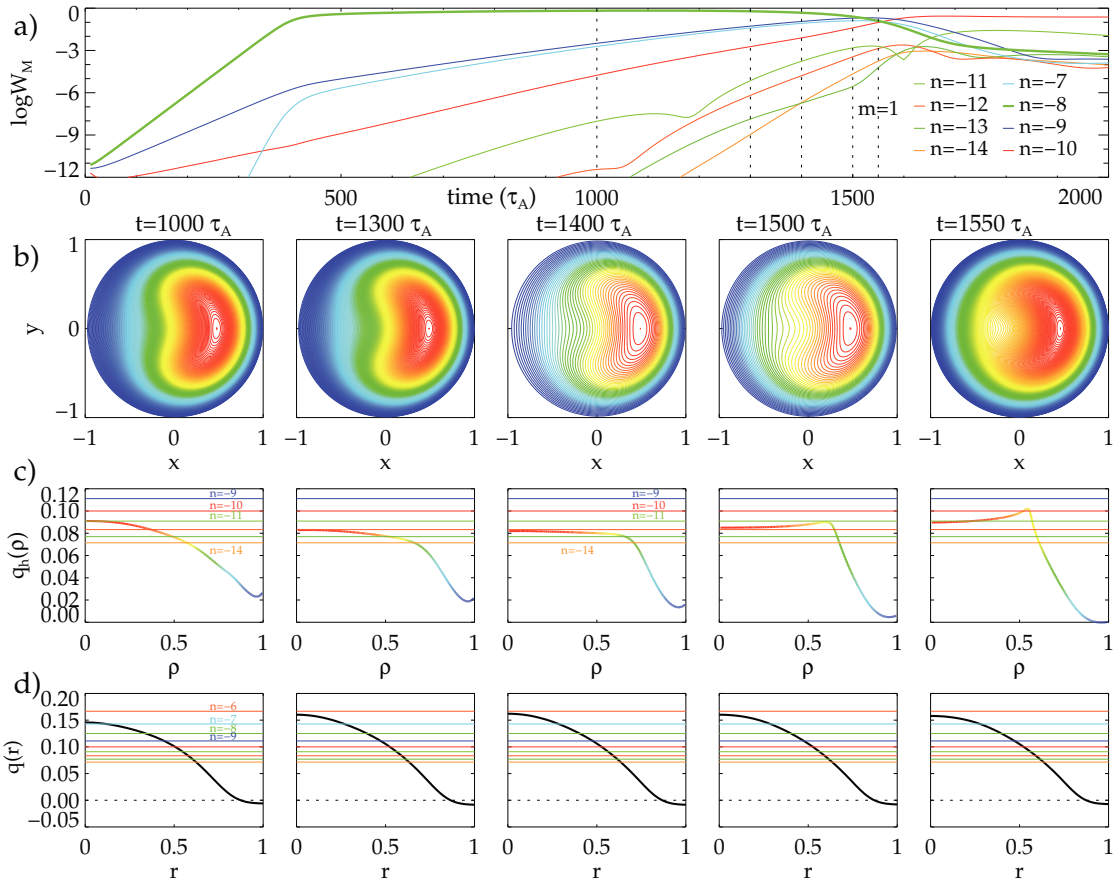

Figure 7.1: The temporal evolution of the magnetic energy of the $m = 1$ modes is reported in panel (a). The simulation times chosen for the analysis with NEMATO are marked with dashed vertical lines. For these times the contour level of the helical flux function χ are reported on the second row (b). In the third row the helical q-profile is plotted as a function of the effective radius ρ. Both χ and $q(\rho)$ are computed assuming a $n = -8$ helical symmetry. The color of the flux surfaces in panel (b) refer to their ρ values, which is also evidenced in panel (c). The rational values from $1/14$ to $1/9$ are shown in panel (c) with the same color employed in panel (a). Fourth row, panel (d), shows the radial profile of the axisymmetric safety factor, $q(r)$.

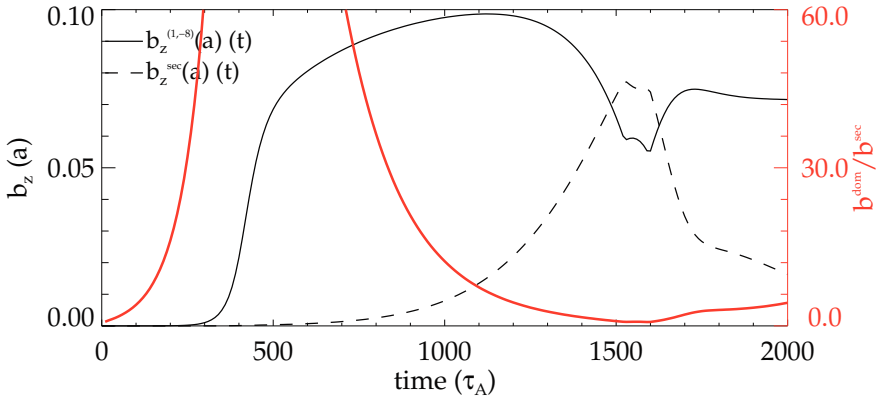

Figure 7.2: Temporal evolution of the dominant magnetic field at the edge $b_z^{1,-8}(a)$ is plotted with a continuous black line. The temporal evolution of the $m = 1$ secondary modes, calculated as in figure 6.2, plotted with a dashed black line. The thick red line represents the ratio between dominant and secondary modes.

licity is meaningless, since no clearly dominant helical mode can be recognized in the dynamics of the magnetic field.

The peculiar feature of the helical safety factor in the time instants analyzed is that it is always monotonically decreasing with respect to ρ, differently from the profiles analyzed in section 6.1.2 and 6.2.2 that exhibit a more manifold behaviour: this implies that no resonance is touched twice by the profile, avoiding the possibility to give rise to magnetic structures associated with the same MHD mode in two different radial positions. The monotonic behaviour of the helical safety factor profile associated with non-resonant MHD modes is also confirmed by other works, see [Gobbin et al., 2011]. The role of profile's flatness and of its "distance" from the resonant values on chaos formation and healing is widely discussed for example in [Nasi and Firpo, 2009; Firpo and Constantinescu, 2011]. The helical q evolution starts from a central value $q_h(a) \geqslant 1/11$ (at $t = 1000\,\tau_A$) that gradually decrease to the value $q_h(a) \approx 1/13$ at the final time in which the $(1, -8)$ is the dominant: this implies that, as time increases, a number of important resonances is no more touched, reducing the possibility for the configuration to develop resistive kink-tearing perturbations to the helical state. Another important feature of the helical safety factor profile in this dynamical situation is that after $t = 1300\,\tau_A$ it is flat in the core ($\rho \leqslant 0.5$) of the domain. This can be considered a positive fact since resistive MHD instabilities do not develop in the core region, which is available to accommodate a wide helical core. All these considerations are somewhat reflected in the topology of the magnetic field, discussed in the next section 7.3. It is interesting to note that no evolution of the axisymmetric safety factor profile is recovered in the analyzed time slice, as can be seen from figure 7.1d).

7.3 Evolution of the magnetic field topology: good magnetic order

The magnetic field topology, in the five time instants highlighted in figure 7.1, is characterized by a surprisingly high level of magnetic order. Even though this could be foreseen for the initial time instants of the simulation ($t \leqslant 1200\,\tau_A$) the level of magnetic order, and of *resilience* to magnetic chaos, in this part of the simulation is not expected. The energy difference between the dominant and the most important secondary mode is listed in table 7.1, while figure 7.3 shows the Poincarè plots at the five time instants, both in a $\theta = cost$ and $z = cost$ plane.

Table 7.1: Energy difference between the dominant $(1, -8)$ MHD mode and the most important secondary mode $(1, -9)$, $\Delta \log W_M$. For $t \geqslant 1500$ the energy difference is vanishing.

Time (τ_A)	$\Delta \log W_M$	b_r^{dom}/b_r^{sec}
1000	2.30	14.10
1300	1.10	3.55
1400	0.62	2.04
1500	0.10	1.12
1550	-0.20	0.79

The analysis of the magnetic field line topology starts at $t = 1000\,\tau_A$, when it is similar to the helical flux surfaces' one (apart from minor changes due to the weak secondary modes), and is characterized by a helical deformation of the plasma column. The lack of a resonance of the $(1, -8)$ mode inside the plasma implies that the topological changes associated with the magnetic island formation are prevented; only a simple kinking of the plasma column is observed (similar to what happens with ideal kink modes, see section 3.6.1). Perfect magnetic order is obtained, as is expected in a quasi-2D system (section 5.3).

At $t = 1300\,\tau_A$ the topological configuration is similar to the previous time instant, again perfectly conserved magnetic surfaces are recovered by NEMATO. The only difference is on the helical q profile, whose on-axis values is below the resonance $1/11$, as can be seen from figure 7.1 panel c).

The $t = 1400\,\tau_A$ case is what we call *resilient case*: we define a state *resilient* if magnetic chaos does not emerge despite low energy difference between dominant and secondary modes. The resilient case is particularly interesting because a perfect magnetic order is recovered despite the energy difference between modes is strongly reduced and is lower than in most of the experimental cases. Such a high level of perturbation to the helical plasma column can be usually very dangerous for the order of magnetic field topology. NEMATO nevertheless recovers perfectly ordered states, and the effect of the

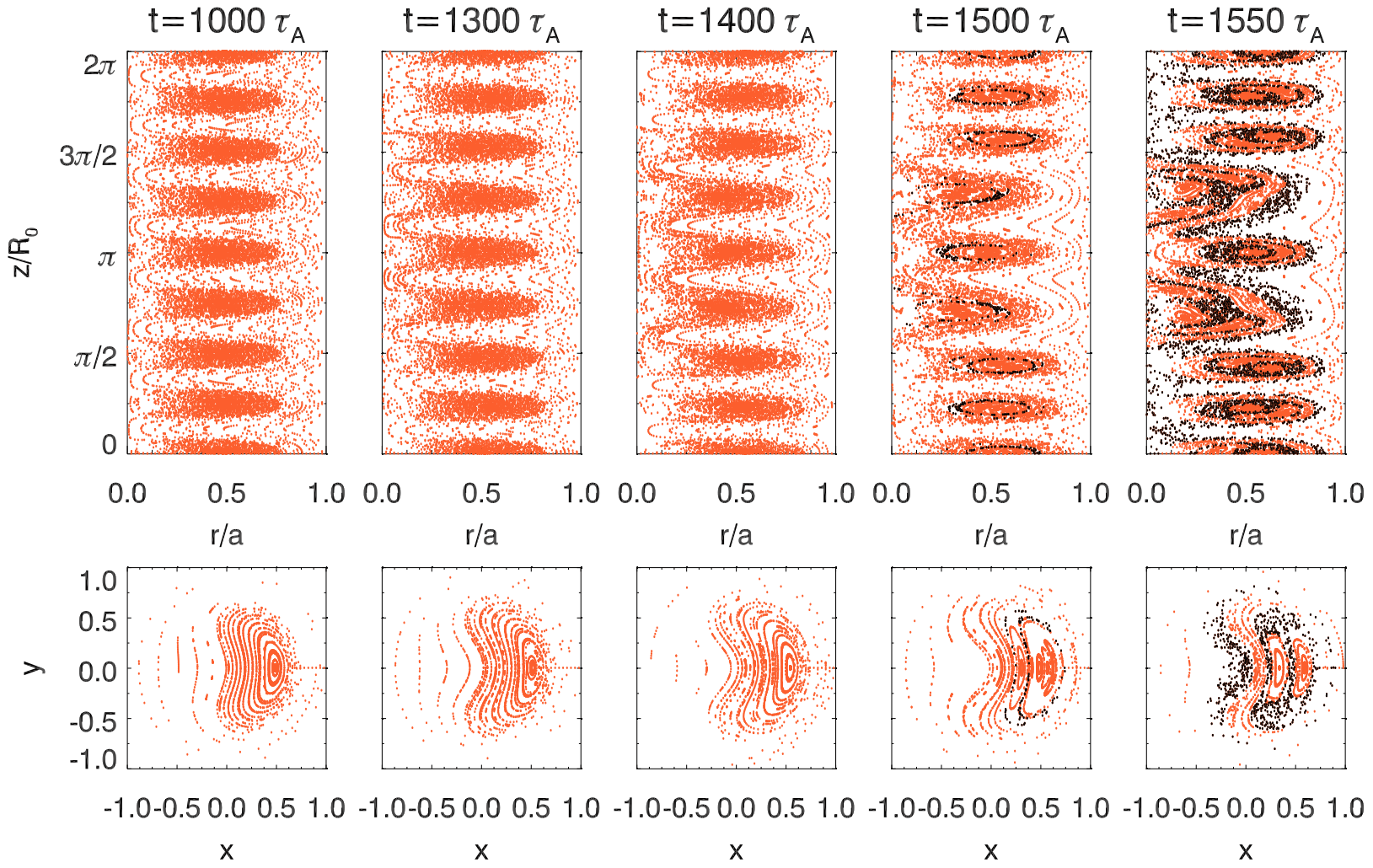

Figure 7.3: NEMATO simulations of the selected times in figure 7.1. Poincaré maps on the $\theta = 0$ plane (first column) and on the $z = 0$ plane (second column) are reported for the selected simulation times. Conserved surfaces are shown in orange. Stochastic magnetic field lines are marked in black.

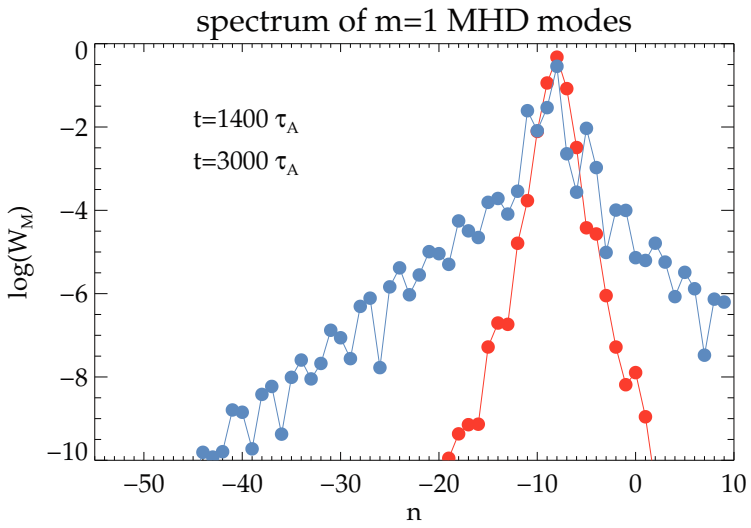

Figure 7.4: Spectrum of the $m = 1$ MHD modes for two different cases: in red the spectrum corresponding to $t = 1400\,\tau_A$ of the simulation described in figure 7.1; in blue the spectrum corresponding to $t = 3000\,\tau_A$ of the simulation in figure 7.10. Note the much faster decay of the spectrum of the resilient case as n is farther from the dominant $(1, -8)$ mode.

secondary modes is not directly observable in the Poincarè plot (the effects can be seen indirectly simply confronting the magnetic surfaces with the helical flux surfaces: the radial position of the magnetic surfaces' O point is displaced from the flux function's one). The possible explanation for this behaviour has already been introduced in section 7.2 and are related to the q_h radial profile, that is flat in the core and whose on-axis value has dropped below the resonance $1/12$ (excluding dangerous MHD activity from developing). A further explanation can be given considering the spectrum of MHD modes that are active. The spectrum of $m = 1$ MHD modes, whose role in determining the dynamics is much greater than the $m \geqslant 2$ modes, is peaked on the dominant and has a fast exponential decay as long as the toroidal wave number n departs from the value -8. The $m = 1$ spectrum is shown in figure 7.4, together with a spectrum from a different simulation presented in section 7.5: note that this spectrum has a faster decay with n, that is not usually the case in the completely developed MHD dynamics of QSH or MH state. A more complete analysis of the magnetic spectrum role is presented in section 7.4.

The Poincarè plot at $t = 1500\,\tau_A$ shows the onset of a weak magnetic chaos, associated with the breaking of the helical symmetry due to the $(1, -8)$ mode. Continuing with the parallel analysis of the helical safety factor profile figure 7.1 shows that the profile is now non monotonic, with a maximum at around $\rho \approx 0.6$. The edge of the domain continues to be characterized by good magnetic surfaces.

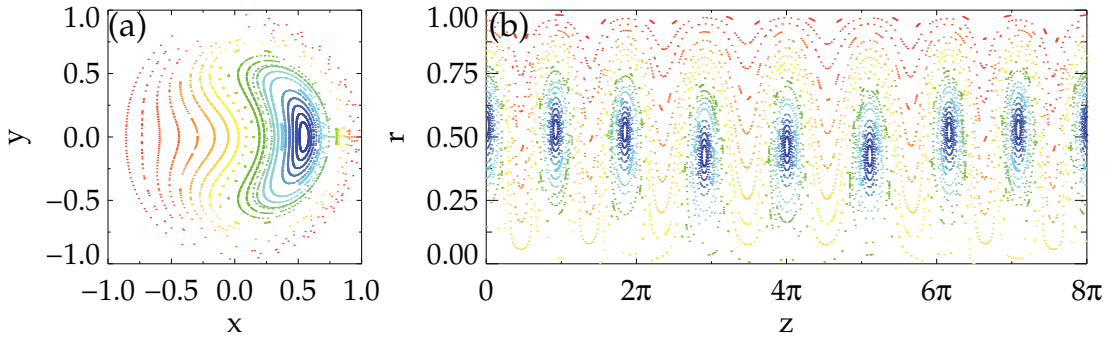

Figure 7.5: Details of the magnetic topology, $t = 1400\,\tau_A$ of figure 7.1. On the left the $z = 0$ Poincarè plot is reported while on the right the $\theta = 0$ is shown.

The last chosen time instant, $t = 1550\,\tau_A$, is no more dominated by the $(1, -8)$ MHD mode: the magnetic configuration is a multiple helicity (MH) one. Despite this the magnetic topology is still strongly influenced by the previous $h = 8$ helical deformation, as a chain of eight structures can still be noticed in the chaotic bath.

7.4 The counter-intuitive behaviour of secondary modes

This section deals with the analysis of the causes of the magnetic order recovered in the case shown in figure 7.5. As it was stated in the previous section 7.3 two main hypothesis can be advanced to explain this non-conventional behaviour: an important role of the helical safety factor profile (that will be partially ruled out in the next section 7.5.2) and the role of the spectrum of MHD modes.
Dealing with the spectrum of MHD modes stresses the power of using a spectral method to solve the MHD equations (SPECYL code), as *test magnetic fields* can be created simply by removing some modes from the Fourier antitransform or by changing their features, like radial profiles or phase. This possibility has been used to deeply analyze the magnetic field. The indication coming from the analysis here presented is that order may come from a non fully developed spectrum of magnetic perturbations to the helical equilibrium [Verandaet al., 2012].

7.4.1 Playing with the field - part 1

This section aims at exploring the role of the main MHD perturbations in defining the resilient case topological features. The magnetic field obtained at $t = 1400\,\tau_A$ of the simulation described in figure 7.1 has been manipulated, exploiting the spectral formulation of SPECYL. For simplicity only poloidal wave number $m \leqslant 2$ have been analyzed, as the intensity of the higher m components of the field is much lower than the one considered. In this section a significant selection of cases is presented: the

topological analysis is performed with the NEMATO code. The results of the topological analysis are predictable in some cases (for example case `a)`) while they present a somehow unexpected behaviour in others (for example cases `b)`, `c)` and `d)`).

`a)` Removal of the dominant mode.

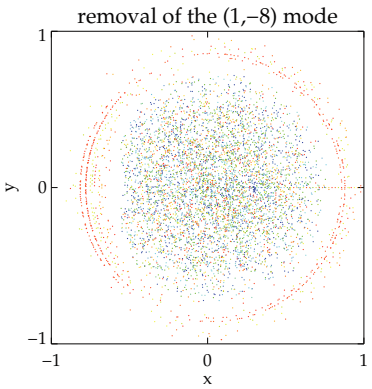

Figure 7.6: Test magnetic field `a)`: removal of the dominant mode. Chaos is completely widespread.

The test magnetic field used is the same of the resilient case without the dominant $(1, -8)$ mode. The Poincarè plot evidences a completely widespread chaos of the field lines. This is an *expected* case, since removing the mode that builds up the helical symmetry is expected to leave only the secondary modes, most of which are resonant modes with magnetic islands overlapping and producing chaos (see also Cappello et al. [2011]. A necessary, but not sufficient, condition for the presence of conserved magnetic surfaces characterized by an helical symmetry is thus the presence of a dominant MHD mode.

`b)` Removal of the $(1, -7)$ secondary mode.

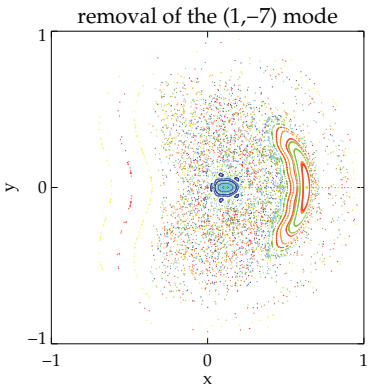

Figure 7.7: Test magnetic field `b)`: removal of the most important secondary mode. Chaos is completely widespread.

The test magnetic field used here is the same of the resilient case without the secondary $(1, -7)$ mode. The Poincarè plot evidences a wide region characterized by stochastic field lines, surrounding the helical core with a $n = 8$ winding. The edge is not influenced by the removal of the $(1, -7)$ mode. This is an *unexpected* case, that shows us how the chaos resilience evidenced in figure 7.5 is based on an interplay between magnetic modes that seems to be rather fragile, as simply removing a secondary mode causes big changes in the topology.

c) Phase flip on the dominant mode.

This test magnetic field is created changing the phase of the dominant $(1, -8)$ mode by adding a π value to the argument of equation (4.8). The main change in the magnetic topology is the rotation of π of the O-point of the magnetic structure associated with the dominant mode, while a bath of stochasticity appears, as in the previous cases. This is an *unexpected* case and it seems to indicate that the structure of the secondary modes in the resilient case is "shaped" in a way that reduces the possibility of destructive interaction between them. The formation of magnetic chaos does not depend on the particular value of the added phase, as some trials were performed with other values, like $\sqrt{2}$.

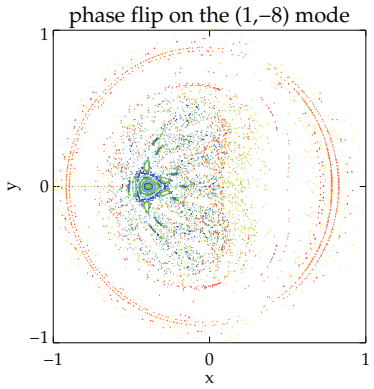

Figure 7.8: Test magnetic field `c)`: phase of π on the dominant mode. Magnetic chaos is created.

d) Phase flip on the $(1, -7)$ secondary mode.

This test magnetic field is created changing the phase of the secondary $(1, -7)$ mode by adding a π phase. Simply changing the phase value of a secondary mode (though of one of the most important) destroys almost completely the magnetic order. A small helical structure is present only in the core of the domain, in the position of the O point of the resilient case. This is an *unexpected* case telling, together with case `b)`, that a necessary condition for the presence of conserved magnetic surfaces seems to be a "good" (in a sense that is not specified) behaviour of the secondary modes.

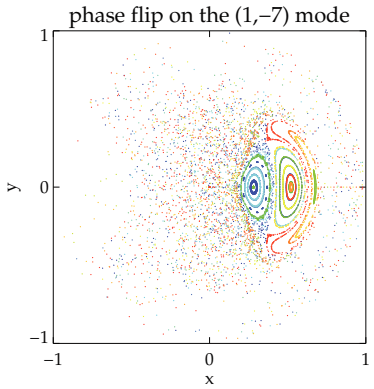

Figure 7.9: Test magnetic field `d)`: phase of π on the most important secondary mode. Magnetic chaos is created.

The fundamental role of the geometry

It is important to stress the fact that cases `b)`, `c)` and `d)` are *unexpected* considering a simple application of the Chirikov criterion (the larger the amplitude and the number of Fourier components, the more chaotic the dynamics). The role of the geometry enters when the magnetic field is no more axisymmetric: in such a case Fourier analysis of the field in cylindrical geometry is suitable to describe the perturbations to the axisymmetric equilibrium. Cylindrical geometry is no more suitable when the magnetic field has a strong 2D helical symmetry, as is the case in the resilient case. Fourier analysis should be carried out in helical geometry: a single Fourier component of the field in helical geometry can results in a wide spectrum of Fourier components in cylindrical geometry. In this view the removal of a single mode in cylindrical geometry may result in the addition of many modes in the helical one. The passage to such a new geometry, that requires the introduction of flux coordinates (see [D'haeseleer et al., 1991]), is an ongoing work. Indeed this path seems to be the correct one to describe the role of secondary modes' spectrum in determining the stochasticity of the magnetic field.

7.5 A new simulation case: magnetic perturbations to sustain the non-resonant QSH case

Figure 7.1 shows that the QSH built upon a non-resonant MHD mode is just a transient phase towards the establishment of a $n = -10$ SH state. The simulation shown in this section exploits one of the main results of this thesis: sufficiently strong externally applied magnetic perturbations (MP) can drive an RFP plasma to a desired QSH state. This property, which will be discussed in detail in chapter 8, has been used to sustain the $n = -8$ QSH state further, using helical boundary conditions, described in 4.1.3. Leaving all the comments on the use of MPs to the following chapter 8, figure 7.10 shows the resulting simulation (this simulation will be called *forced* simulation in the rest of the chapter). At $t = 1000\,\tau_A$ a magnetic perturbation with helicity $(1, -8)$ and intensity $\frac{b_r^{1,-8}(a)}{B_\theta(a)} = 20\%$ is applied at the edge of the simulation domain, $r = a$. The adimensional visco-resistive parameters are unchanged with respect to the previous case. The resulting dynamics is governed by an always dominant $(1, -8)$ mode, while the cumulated amplitude of the secondary has a value similar to the one that was encountered in the study of the resilient case (the specific MP's intensity here presented achieves this result). A plot is shown in figure 7.11. The main difference is represented by a more developed $m = 1$ spectrum (this is valid also for $m = 0$ modes), as can be seen in figure 7.4. This is an effect of the nonlinear dynamics, which creates a tail in the spectrum at toroidal wave number farther from the dominant mode.
The helical safety factor profile is shown for two time instants in figure 7.10 and the

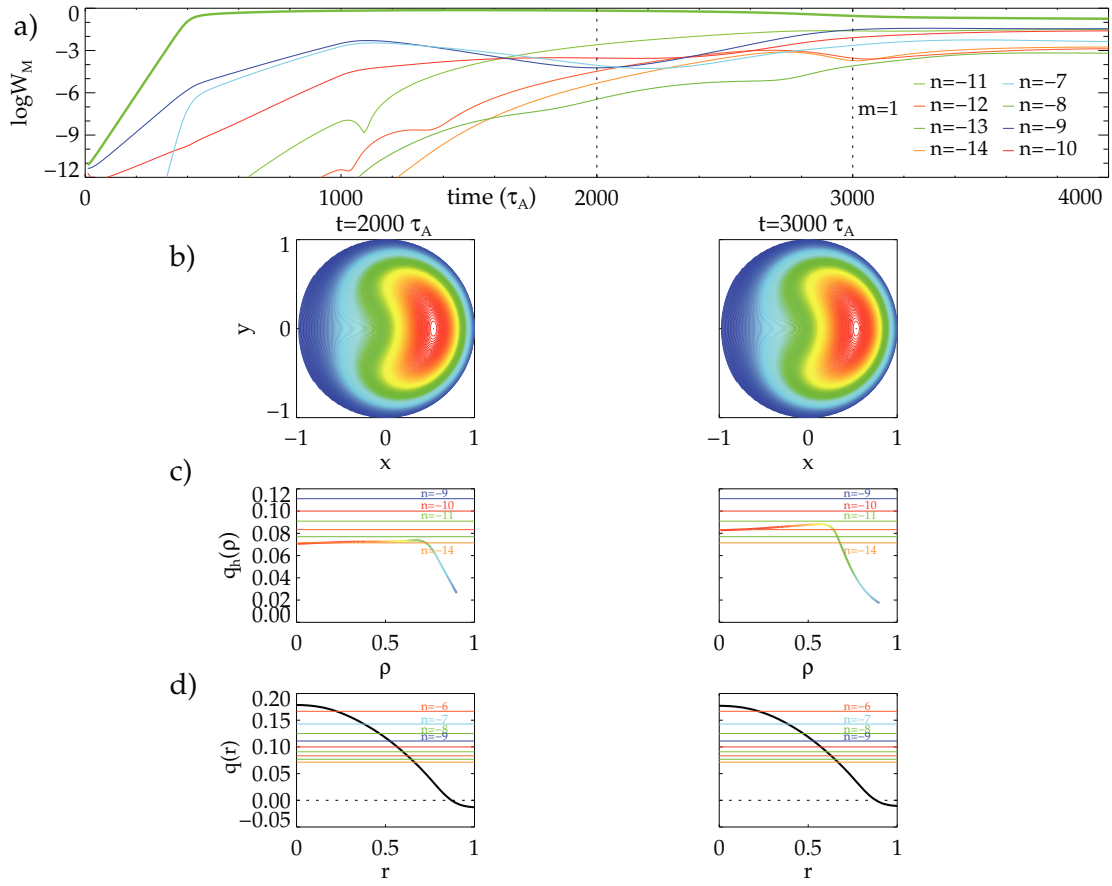

Figure 7.10: The temporal evolution of the magnetic energy of the $m = 1$ modes is reported in panel (a). Remark: a helical magnetic perturbation at the edge is applied from $t = 1000\,\tau_A$ on. The simulation times chosen for the analysis with NEMATO are marked with dashed vertical lines. For these times the contour level of the helical flux function χ are reported on the second row (b). In the third row the helical q-profile is plotted as a function of the effective radius ρ. Both χ and $q(\rho)$ are computed assuming a $n = -8$ helical symmetry. The color of the flux surfaces in panel (b) refer to their ρ values, which is also evidenced in panel (c). The rational values from $1/14$ to $1/9$ are shown in panel (c) with the same color employed in panel (a). Fourth row, panel (d), shows the radial profile of the axisymmetric safety factor, $q(r)$.

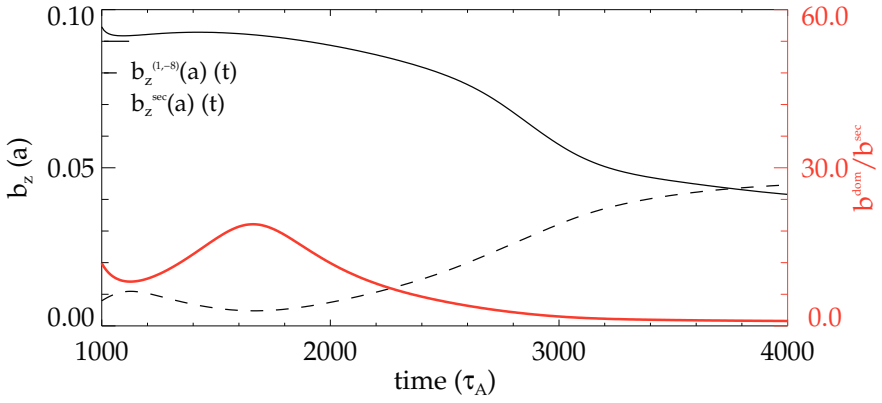

Figure 7.11: Temporal evolution of the dominant magnetic field at the edge $b_z^{1,-8}(a)$ is plotted with a continuous black line. The temporal evolution of the $m = 1$ secondary modes, calculated as in figure 6.2, plotted with a dashed black line. The thick red line represents the ratio between dominant and secondary modes.

corresponding magnetic field topology is shown in figure 7.12.

Table 7.2: Energy difference between the dominant $(1, -8)$ MHD mode and the most important secondary mode, $\Delta \log W_M$ for the two time instants highlighted in figure 7.10.

Time (τ_A)	$\Delta \log W_M$	b_r^{dom}/b_r^{sec}
1000	2.30	14.1
2000	3.30	44.7
3000	0.90	2.8

The behaviour of magnetic topology in the two cases is easily explained in terms of secondary modes' intensity. At $t = 2000\,\tau_A$ a big energy difference between dominant and secondary modes (see table 7.2) results in a perfectly ordered 2D magnetic topology, while at $t = 3000\,\tau_A$ an almost completely developed magnetic chaos is recovered, despite the energy difference is larger than in the resilient case.
The dynamics recovered in this MHD simulation can give further hints on the role of the helical safety factor profile and of the secondary modes: in particular section 7.5.1 will reinforce the indication that the features of secondary mode are determinant for the magnetic topology and section 7.5.2 will discuss the role of the helical safety factor that emerges from this simulation.

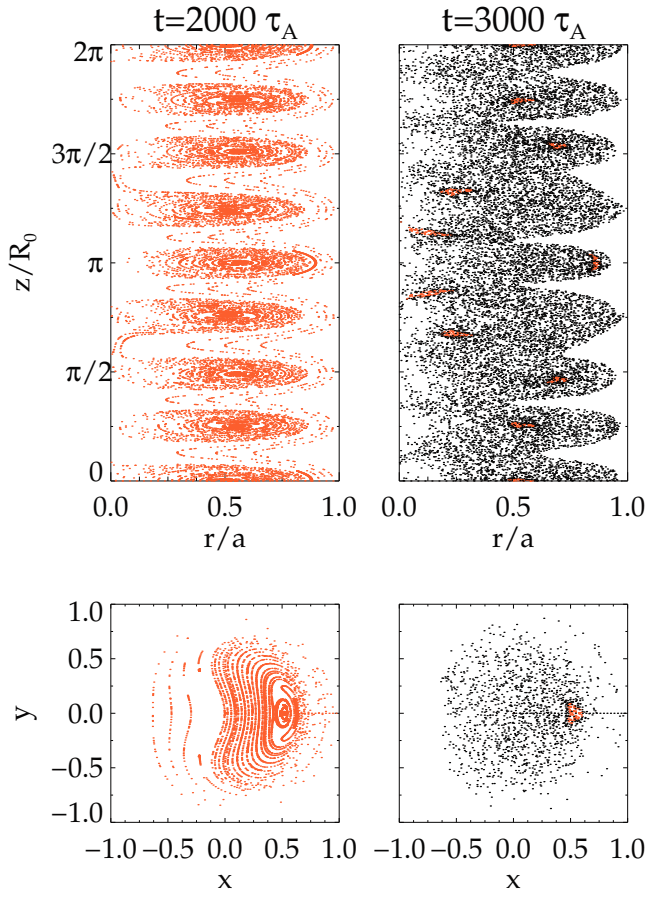

Figure 7.12: NEMATO simulations of the selected times in figure 7.10. Poincaré maps on the $\theta = 0$ plane (first row) and on the $z = 0$ plane (second row) are reported for the selected simulation times. Conserved surfaces are shown in orange. Magnetic structures related to secondary modes are shown in blue. Stochastic magnetic field lines are marked in black.

7.5.1 Playing with the field - part 2

To assess whether the main player in determining magnetic order or chaos is represented by a strong helical equilibrium or by the level of secondary perturbations, an *hybrid* magnetic field was considered. The helical equilibrium of the so called resilient case, constituted by all the modes obeying the relation $(m, n) \in \{m, n \,|\, n = -8m\}$, has been used as helical 2D equilibrium to create two test magnetic fields whose detailed features are written in table 7.3. Again only $m \leqslant 2$ modes were considered.
The Poincarè plots corresponding to the magnetic fields described in table 7.3 are reported in figure 7.13.
The magnetic field built with the secondary corresponding to the more developed mag-

Table 7.3: MHD modes used to create the two magnetic fields originating the Poincarè plots of figure 7.13.

Helical equilibrium from	Secondary modes with $m = 0, 1, 2$ from	Chaos (y/n)
$t = 1400\,\tau_A$ of fig. 7.1	$t = 1400\,\tau_A$ of fig. 7.1	a) no
$t = 1400\,\tau_A$ of fig. 7.1	$t = 3000\,\tau_A$ of fig. 7.10	b) yes
$t = 3000\,\tau_A$ of fig. 7.10	$t = 1400\,\tau_A$ of fig. 7.1	c) no

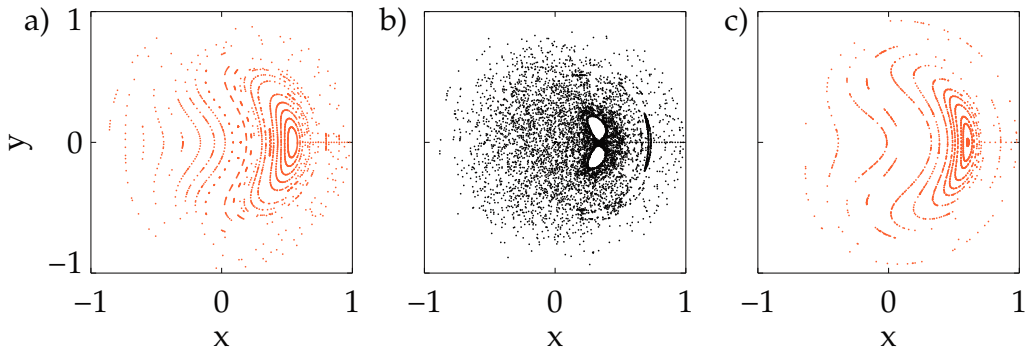

Figure 7.13: Poincaré plots on the $z = 0$ plane are reported for the selected test-magnetic field described in table 7.3. Conserved surfaces are shown in orange. Magnetic structures related to secondary modes are shown in blue. Stochastic magnetic field lines are marked in black.

netic spectrum in figure 7.4 results in an almost completely developed magnetic chaos, differently from the (reduced, as only modes with $m \leqslant 2$ were considered) resilient case. The first conclusion that can be drawn is that the role of a more developed spectrum of secondary modes is more important than the role of a strong helical equilibrium.

7.5.2 The role of helical safety factor profile

Many simulations similar to the one described in section 7.5 were performed to recover an helical safety factor both monotonic and flat in the core. In no case it was possible to recover both these positive features simultaneously. The helical safety factor profiles for the time instants $t = 2000\,\tau_A$ and $t = 3000\,\tau_A$ of figure 7.10 presents the two features separately: $t = 2000\,\tau_A$ presents a flat in the core profile, but the relevance of the profile is reduced because of the low level of secondary modes. At $t = 3000\,\tau_A$ the profile is less flat and intersects more resonances in the core. The relevance of this profile is reduced because secondary modes are very high in this instant and magnetic chaos is well spread.

The main conclusion from this section is that the role of the helical safety factor seems to be less relevant than the role of secondary modes' intensity, even though a possible

relation between these two key factor seems probable: a wider spectrum of secondary modes may be able to influence deeply the underlying helical equilibrium, a modification that results in a q_h profile that is not able to be both flat in the core and monotonically decreasing.

7.6 Summary and remarks

A set of MHD simulations (presented in this and in the previous chapter) characterized by a simplified MHD dynamics has been analyzed from the dynamical and topological point of view.
The obtained results are difficult to interpret if the process of dominant mode separatrix expulsion is taken as the only key to understand the state of order or chaos of the magnetic field. Despite chaos is always present when a separatrix is present (both cases in chapter 6), it can be also present when the separatrix is absent (simulation in section 7.5).
The cumulated amplitude of the perturbations to the helical equilibrium might be a good tool to order the results, as when a broader spectrum of perturbations is present magnetic stochasticity is active (simulations in section 7.5 and also in section 6.2). On the other hand this point of view still does not explain the fact that a level of perturbations with amplitude comparable to the equilibrium one can result in ordered magnetic surfaces (*resilient case*, simulation in 7.1).
These results seem to be contradictory and it is believed that the study of the system has to be tackled using the more correct helical geometry. This may explain why the *cylindrical perturbations* in the resilient case do not actually perturb the *helical equilibrium* (as would be the case employing a simple Chirikov-like vision). These geometrical studies are ongoing. The main conclusion that can be formulated about the peculiar/not understood resilient case is that it is based on a rather fragile interplay between the MHD modes that may be understood using the correct helical tools.

The main result of this chapter is that the role of the spectrum of perturbations to the helical equilibrium is fundamental in determining the magnetic topology features (apart from the resilient case) and that the expulsion of the separatrix of the dominant mode is a necessary (but not sufficient) condition for magnetic chaos healing).
The understanding of what happens during the magnetic field dynamics in the RFP can now be tackled considering more realistic cases, that use the key ingredient introduced in section 7.5, namely the use of radial edge magnetic perturbations to obtain QSH states. The results, in terms of MHD dynamics and topology will be described in chapters 8 and 9.

8

Magnetic perturbations to stimulate helical states

This chapter reports an extensive numerical study, performed with the SPECYL code, which considers the effect on MHD dynamics of helical magnetic boundary conditions, i.e. a finite value of the radial magnetic field of a selected harmonic at the edge (from here on called *magnetic perturbation*, MP).
It is shown that the plasma can be driven to a selected QSH state starting from both spontaneous QSH and MH regimes. In particular, a high enough MP can force a QSH helical self-organization with a helicity different from the spontaneous one. Moreover, MH states can be stimulated into QSH states with a selected helicity. A threshold in the amplitude of MP is observed above which it is able to influence the system.
This chapter thus presents a wide simulation study that represents a novel result and a key contribution to achieve a closer comparison between 3D MHD simulations and experiment.
Outline of the chapter. The simulations reported in this chapter study the effect of MP on the dynamics of the RFP. For the sake of clarity the study has been divided in three parts, characterized by a different value of the dissipation parameters and thus by a different MHD dynamics (see section 2.3). Section 8.1 shows the effect of magnetic perturbations on simulation with low H, characterized by a simplified dynamics already analyzed in chapter 7 and 6, that spontaneously ends in a SH regime. Section 8.2 is focused on the simulations with higher H whose spontaneous dynamics is a MH one: this simulations represent a more realistic case. A further section 8.3 shows the results that constitute the core of the results presented in this thesis, namely the agreement with experimental observations, achieved at high H. Figure 8.1 shows how the visco-resistive parameters were chosen in the $S - P$ plane. For each point in the plot many MHD simulations have been performed changing the helicity and the amplitude of the

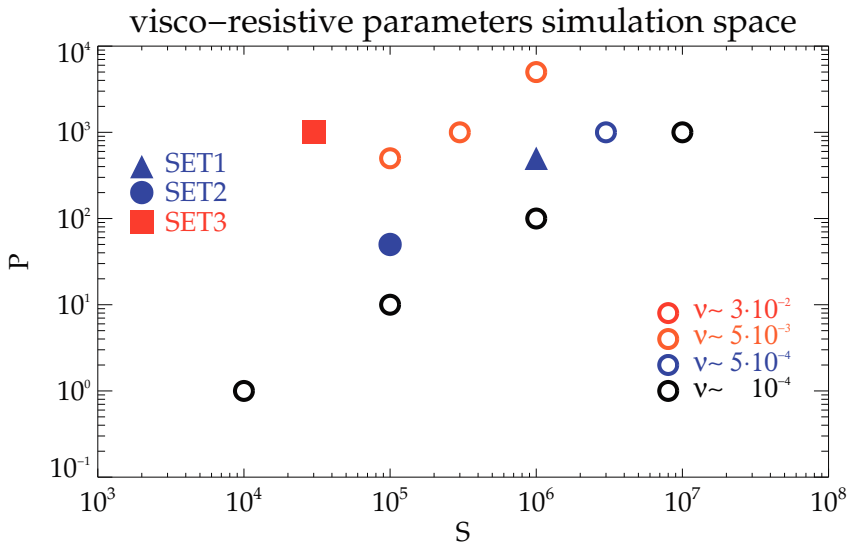

Figure 8.1: Visco-resistive parameters space. Each point in the plot corresponds to a unique couple of (S, P) and thus to a unique (η, ν). Each point may represent multiple simulations (characterized by different Magnetic Perturbations (MP) applied). The filled symbols indicate the visco-resistive parameters corresponding to the three sets of simulations presented in this chapter.

Table 8.1: Range of variation of the parameters changed during the simulation study. As for the visco-resistive parameters see a graphic visualization in figure 8.1.

Parameters	n^{MP}	MP	S	P
Values	$m = 1$ $-5 < n < -8$	from 0% to 10% of $B_\theta(a)$	from 10^4 to 10^6	from 10^0 to $5 \cdot 10^3$

MP.

A summary and remarks section can be found in 8.4.

In this chapter four parameters change: the Lundquist number (S), the Prandtl number (P), the helicity of the MP (n^{MP}), the intensity of the MP normalized to the magnetic field at the edge, (MP). Their range of variation is described in table 8.1.

8.1 Effect of magnetic perturbations on spontaneous QSH regimes (high dissipation)

A first set, Set1, of simulations characterized by spontaneous QSH dynamics is obtained using: $S = 3 \cdot 10^4$, $P = 10^3$ (i.e., $H = 950$), as summarized in table 8.2. Figure 8.2 shows the spontaneous dynamics with ideal shell, i.e. *without* helical MP. This is the same simulation that provides the basis for the analysis performed in chapter 7.

As it was previously described, the unstable initial ohmic equilibrium is perturbed by a subset of five MHD modes with $m = 1, -10 \leqslant n \leqslant -5$, triggering the non-linear RFP dynamics. Figure 8.2 shows also the temporal behaviour (rather stationary) of the reversal parameter $F = B_z(a)/\langle B_\theta(a)\rangle$, the pinch parameter Θ, and the radial profiles of the (axisymmetric) safety factor and the magnetic field components of the dominant mode at selected times.

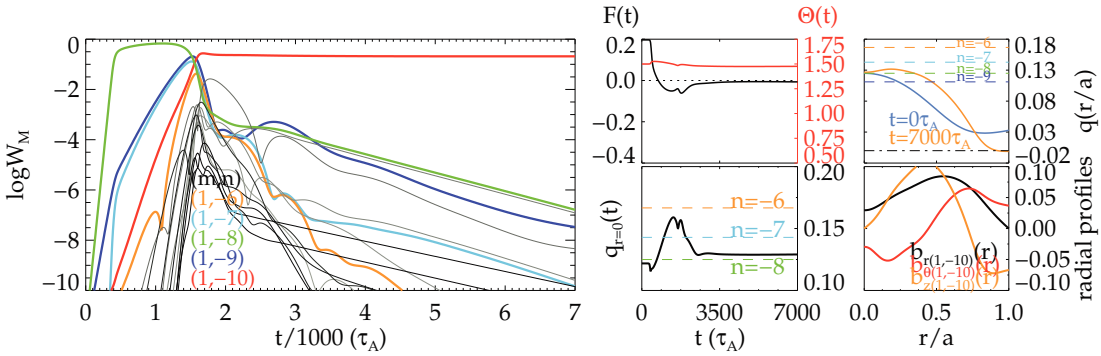

Figure 8.2: MHD simulation without MP. (*Left*) Time evolution of the magnetic energy of the most important $m = 1$ MHD modes. (*Top middle*) Time evolution of the F and Θ parameter. The reversal parameter is marginally negative during the whole simulation. (*Bottom middle*) Time evolution of an average of the safety factor between $0 < r/a < 0.2$. The $(1, -8)$ MHD mode is initially marginally non resonant, and becomes resonant at $t = 600\,\tau_A$. (*Top right*) Safety factor profile at the beginning and at the end of the simulation. (*Bottom right*) Radial profile of the dominant $(1, -10)$ mode at the final time step of the simulation.

Let us first consider the effect of a helical MP applied on the $m = 1, n = -8$ mode, which is the *first resonant mode* (with respect to the safety factor profile shown in figure 8.2). Figure 8.3 shows the dynamics of the modes after the application of the MP at $t = 3000\,\tau_A$. The $m = 1$ modes dynamics shown in figure 8.3 corresponds to the MP amplitudes highlighted using bold font in table 8.2: the behavior of the $(1, -8)$ mode proves that the system can be driven to an externally stimulated QSH state, starting from a spontaneously different one, beyond a threshold in amplitude. The threshold for this configuration is $b_{r,(1,-8)}(a)/B_\theta(a) = 6.5\%$: with this MP value the $(1, -8)$ MHD mode is only marginally able to overcome the spontaneously dominant $(1, -10)$. Simulations performed using MP around 10% lead to a temporary -8 QSH state, see figure 8.4, but eventually in the end secondary modes vanishes.

The simulations shown in figures 8.2-8.5 present peculiar topological properties, widely discussed in chapter 7. The strong resilience to magnetic chaos observed especially in the initial QSH formation phase ($t \approx 1500\,\tau_A$) was analyzed both theoretically (showing that the recovered magnetic order was based on a rather fragile interplay between the MHD modes) and experimentally (see chapter 10).

Table 8.2: Set1 of simulations with magnetic perturbations applied to the spontaneous QSH state. MPs are applied starting at $t = 3000\,\tau_A$ of the simulation reported in figure 8.2. First row: helicity of the imposed MPs. Second row: MPs amplitudes (normalized to the poloidal field at the edge, that in the RFP is the biggest one); each value in this row refers to a different simulation, while digits in bold refer to the simulations shown in this chapter (as indicated in the fourth row). Third row: value of the threshold to reach a QSH state with the imposed helicity. Note that it raises going farther from the spontaneous QSH state, here $(m = 1, n = -10)$.

MP on m=1	n =-6 (second non-resonant)	n =-7 (first non-resonant)	n =-8 (first resonant)	n =-9 (second resonant)
Amplitude $b_{r,(m,n)}(a)/B_\theta(a)\,\%$	**10**,13,20,**26**	10,13	**3**,**6.5**,8,10,**13**	0.6,1.2,3.7,7,13
Threshold $b_{r,(m,n)}(a)/B_\theta(a)\,\%$	10	10	6.5	5
Figure	figure 8.5	-	figure 8.3 8.4	-

Figure 8.5 shows the effect of helical MP on the *non resonant* $(1, -6)$ MHD mode. The threshold is much higher with this MHD mode, which is non-resonant and far from the spontaneous one. In the selected cases, highlighted in bold font in table 8.2, a MP about 10% is required as a threshold, and a value of 26% is required to obtain a SH state.

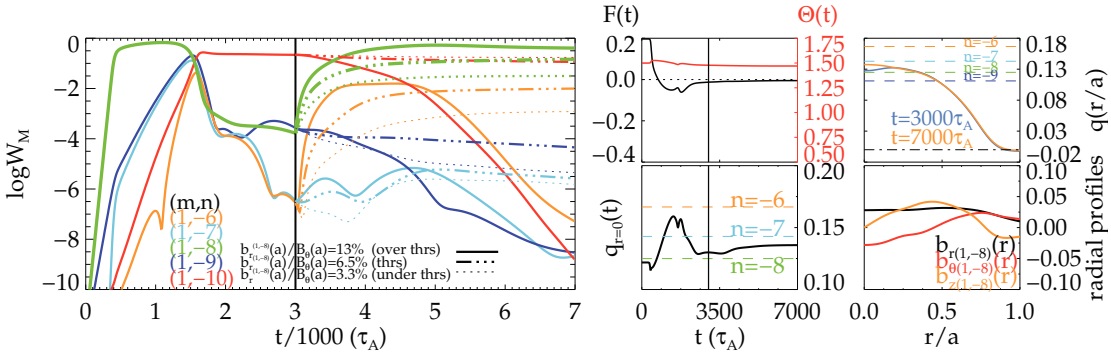

Figure 8.3: Effect of MP on the first resonant mode $(1, -8)$. Same quantities as in figure 8.2. References are applied after $t = 3000\,\tau_A$ with three different amplitudes $(3.3\%, 6.5\%, 13\%)$. With amplitudes under the threshold of 6.5% the $(1, -10)$ mode remains dominant. Smaller frames show data from the over-threshold (MP=13%) MHD simulation.

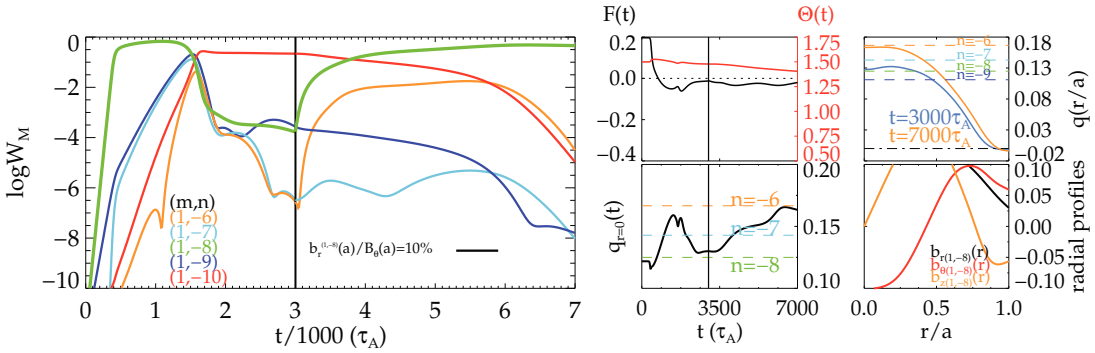

Figure 8.4: Effect of MP on the first resonant mode $(1, -8)$. Same quantities as in figure 8.2. References are applied after $t = 3000\,\tau_A$ with amplitude 10%. Until $t \approx 6000\,\tau_A$ the system is in a QSH state.

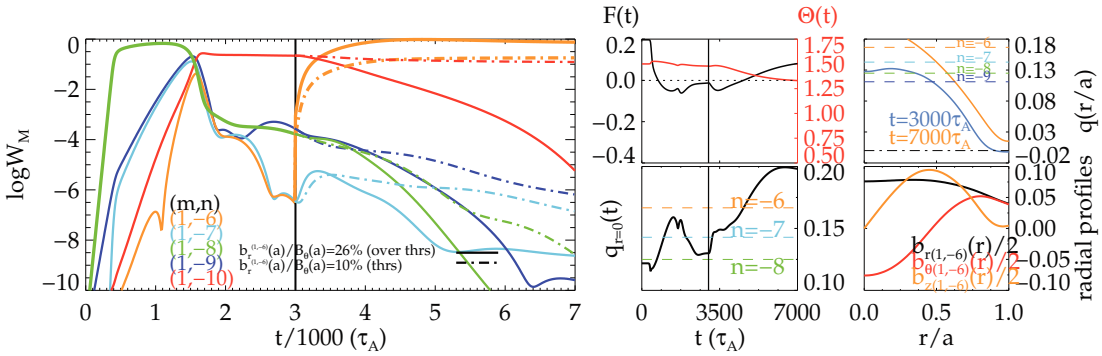

Figure 8.5: Effect of MP on the second non-resonant mode $(1, -6)$, which is farther from the spontaneous one. Same quantities as in figure 8.2. Here the simulation with $b_{r,(m,n)}(a)/B_\theta(a) = 10\%$ represents the threshold condition. Smaller frames showing data from the over threshold (MP=26%) MHD simulation.

8.1.1 Threshold dependence on perturbation's periodicity

Table 8.3: Dependence of the MP's threshold to obtain a QSH state on the MP's toroidal wave number n. $m = 1$ for all the MPs.

MP on $m = 1$ $n =$	Threshold value $b^{(1,n)}_{r,thresh}/B_\theta(a)$ %
-4	10%
-5	10%
-6	10%
-7	10%
-8	6.5%
-9	5.0%
-10	-
-11	2.0%
-12	3.5%
-14	8.0%
-16	>13%

Figure 8.6: Dependence of the threshold on the toroidal wave number of the MPs.

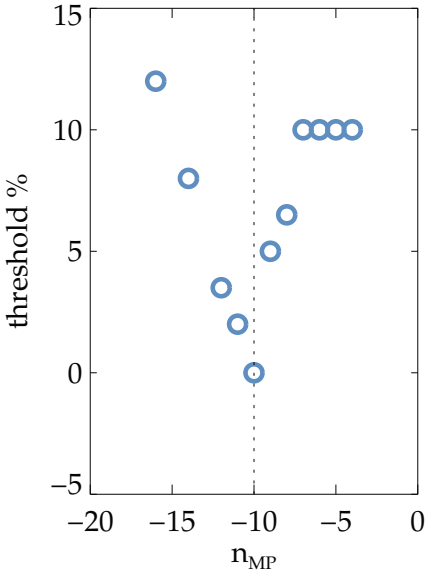

An extensive study on the dependence of the level of external MP needed to drive the system to an externally selected QSH state has been performed considering a set of simulation at $S = 3 \cdot 10^4$ and $P = 10^3$. Magnetic perturbations of different intensities were imposed on a wide range of $m = 1$ MHD modes with $-4 \leqslant n \leqslant -16$. This was done to determine the threshold, that is expected to have a minimum at the spontaneous mode $(1, -10)$ and to grow as toroidal wave numbers farther from the spontaneous are considered. Table 8.2 synthesizes the recovered thresholds, that obey to the expected behaviour written in the previous sentence.

8.2 Effect of magnetic perturbations on MH regimes (medium dissipation)

A wide set of simulations, Set2, ranging from $H = 10^4$ to $H = 10^5$, has also been performed starting from MH regimes, as summarized in table 8.4. The main visco-resistive parameters vary in the range $S \in [10^4 : 10^5]$ and $P \in [10^0 : 10^3]$. Three meaningful cases, characterized by the visco-resistive parameters $S = 10^5$, $P = 10$, ($H \sim 3 \cdot 10^4$) are presented here.

The first case, figure 8.7, shows the spontaneous dynamics. It is characterized by typical

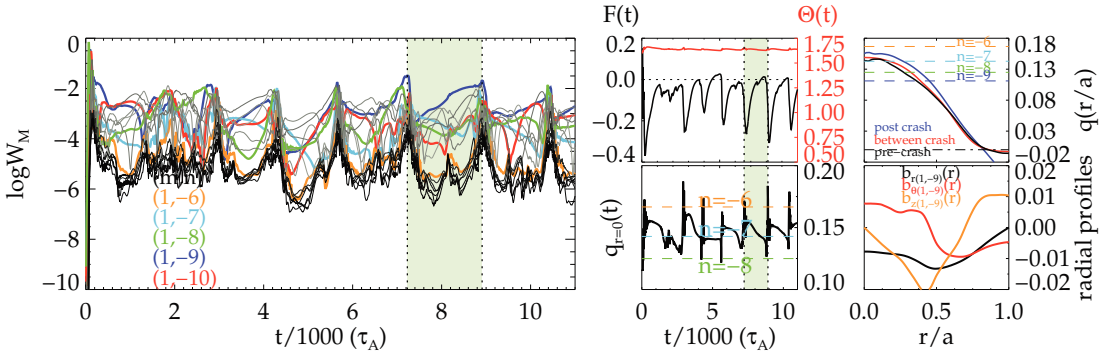

Figure 8.7: MHD simulation at high H without MP. Same quantities as in figure 8.2. (*Top right*) Safety factor profile at the beginning, in the middle and at the end of the highlighted cycle. (*Bottom right*) Average magnetic radial profile of the $(1, -9)$ mode at the end of the cycle, when it dominates.

nearly-periodic relaxation events [Cappello and Biskamp, 1996] (with a period around $2000\,\tau_A$) associated with a sudden fall of the energy of the modes. The oscillatory behavior of the F and Θ parameters is also observed. This is a typical MH dynamics case, discussed in the past in numerical studies (see for example [Cappello and Biskamp, 1996; Cappello, 2004] and references therein and [Paccagnella et al., 2007; King et al., 2012]) and experimentally observed at low plasma currents ($I_P < 1$ MA, see [Zuin et al., 2009] for a MH experimental example in RFX-mod). It can be noted from figure 8.7 that, although temporary QSH states are present (highlighted temporal frame) they don't have the experimentally observed persistence (at high plasma current) in terms of dominant MHD mode helicity and relative amplitude [Piovesan et al., 2009; Chapman et al., 2012].

The next two sample simulations show the effect of helical MPs applied to such MH regimes, according to the choices shown in table 8.4.

Figure 8.8 and 8.9 show the dynamics of the most important m=1 MHD modes when helical MPs are applied to the first non-resonant mode ($n = -6$) and to the first resonant mode ($n = -7$). The MP amplitudes (see table 8.4) are well above the threshold to obtain a long lasting QSH dominated by the selected MP. Indeed, it is possible to estimate (other simulations not shown here have been performed) a threshold value around 2%. This shows that a lower amplitude of helical MP is required to set up a QSH state from the MH state than from a SH one.

Several conclusions can be drawn from these simulations. Long lasting QSH regimes can be obtained from both simulations. The dominant mode is modulated in amplitude and sometimes drops to temporary MH spectra (the energy of the dominant mode drops to values comparable to that of secondary modes). A strict correlation with the reversal parameter (F) cycle can be observed, while the amplitude of the dominant

Table 8.4: Set2 of simulations with magnetic perturbations applied to the spontaneous MH state. MPs are imposed from the beginning of the simulations. First row: helicity of the imposed MPs. Second row: MPs amplitudes; each value in this row refers to a different simulation, while digits in bold refer to the simulations shown in this chapter. Third row: estimate of the threshold to reach a QSH state with the imposed helicity. The negative sign on the MP in the $n = -6$ case means that a negative value of the radial magnetic field was imposed at the boundary. This corresponds to a phase shift of π in the phase of the mode. This phase shift does not influence the dynamic, as it was verified with dedicated simulations.

MP on m=1	n =-6 (first non-resonant)	n =-7 (first resonant)
Amplitude $b_{r,(m,n)}(a)/B_\theta(a)\%$	1.9,3.8,**5.7**,7.8,9.7	1.9,2.9,3.8,**5.1**,7.8
Threshold estimate $b_{r,(m,n)}(a)/B_\theta(a)\,\%$	2	3
Figure	figure 8.8	figure 8.9

mode is anticorrelated to the amplitudes of secondary modes: during the crash, its value drops when the secondary modes' energy reaches its maximum. It also appears a correlation with the secondary modes behaviour, which in turn resembles the typical spontaneous MH cycle. In particular, the drop of the dominant mode amplitude is obtained at the maximum value of the secondary modes. As for the amplitude of secondary modes, its minimum occurs around the middle between two F crashes. It is interesting to note that the correlation between F crashes and the fall of $q(r = 0)$ below the $1/7$ value in both simulations. It still remains to be clarified whether, similarly to what was proposed by Kusano and Sato in [Kusano and Sato, 1990] for standard MH relaxation events, a mechanism involving ideal stability of secondary modes could be the trigger of the dominant mode back transition.

We can incidentally note that first preliminary studies of ideal stability in 3D conditions indicate monotonically decreasing helical q profiles [Gobbin et al., 2011] to be more stable than non-monotonic ones (i.e. reversed shear profiles) [Terranova et al., 2010].

Considering the dynamics of the important physical parameters F and Θ, a quasi-periodic oscillation with period lower than the case of figure 8.7, where no MP was imposed, can be observed. Indeed, we can estimate the typical period to be about $1200\,\tau_A$ (against the previous $2000\,\tau_A$). It should be noted that the dynamics observed in these simulations resembles very closely the one observed in experimental QSH regimes, where the lowest resonant MHD mode is usually diagnosed to be the dominant mode for shallow reversal discharges. It has to be noted that, in RFX-mod, non-ideal wall effects (i.e., a radial magnetic field at the edge after feedback control [Zanca, 2009]) are

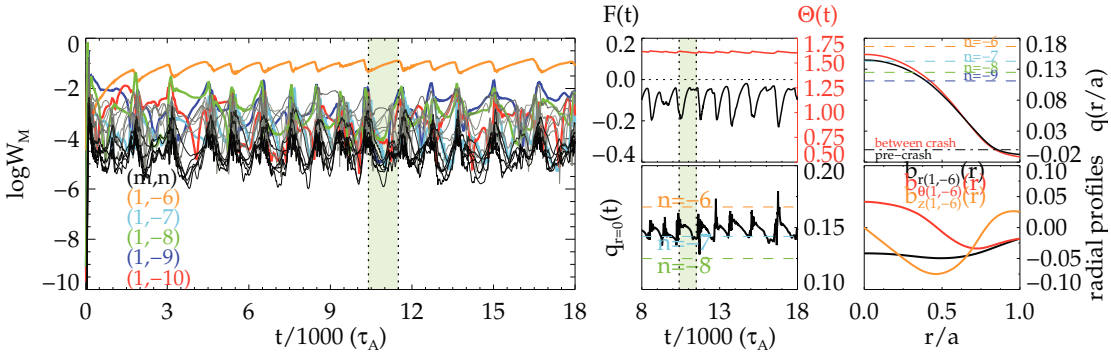

Figure 8.8: Effect of MP on the first non-resonant $(1, -6)$ mode. MPs are imposed from the beginning of the simulation. Same quantities as in figure 8.2. (*Top right*) Safety factor profile at secondary modes minimum and at the maximum (before the crash). (*Bottom right*) Average magnetic components of the dominant $(1, -6)$ mode during the highlighted cycle.

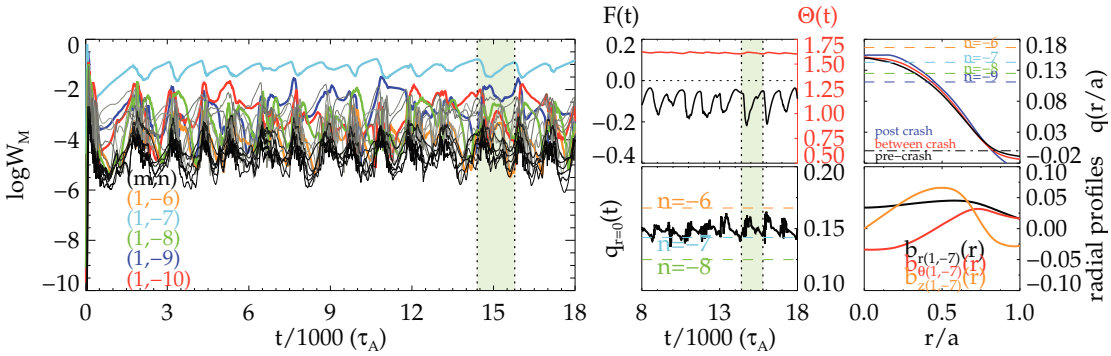

Figure 8.9: Effect of MP on the first resonant $(1, -7)$ mode. MPs are imposed from the beginning of the simulation. Same quantities as in figure 8.2. (*Top right*) Safety factor profile at the beginning, in the middle and at the end of the highlighted region. (*Bottom right*) Average magnetic components of the dominant $(1, -7)$ mode during the highlighted cycle.

routinely measured during QSH states. In particular, the experimental edge dominant mode amplitude is of the order of the ones used in present simulations at high Hartmann number. In fact, the experimental amplitude of the dominant mode at the edge is about $1 - 2\%$ with nominally zero reference value for the feedback control system and increases at most to 3% when a finite reference value is applied [Piovesan et al., 2011]. Furthermore, simulations performed imposing boundary perturbations to several MHD modes indicate that the threshold seems less dependent on the helicity of the chosen MP than in the Set1 simulations described in section 8.1.

8.3 Simulations at high dissipation parameters

A set of simulations, Set3, has been performed at a higher value of the dissipation parameters, namely $S \in [10^6 : 3 \cdot 10^6]$ and $P \in [10^2 : 5 \cdot 10^3]$. Such a level of resistivity is the lowest practically reachable with the actual version of the SPECYL code. This is due to the relatively long time required to simulate a time interval with a significant MHD dynamics: in fact, as it can be understood from equation 4.6, an interval of normalized time $\tilde{t}$ correspond to a effective time $t \propto S^{1/2}\tilde{t}$: as an example the time between two MHD crashes like the ones of figure 8.7 becomes $\sqrt{10}$ times longer passing from $S = 10^5$ to $S = 10^6$. The simulations' result shown in this section took at least a month to be obtained. A solution to this long waiting time is the parallelization of the SPECYL code.
Table 8.5 summarizes the features of the simulations performed at $S = 10^6$, $P = 10^2$.

Table 8.5: Set3 of simulations with magnetic perturbations applied to the spontaneous MH state. MPs are imposed from the beginning of the simulations. First row: helicity of the imposed MPs. Second row: MPs amplitudes; each value in this row refers to a different simulation, while digits in bold refer to the simulations shown in this chapter.

MP on m=1	n =-5 (second non-resonant)	n =-6 (first non-resonant)	n =-7 (first resonant)
Amplitude $b_{r,(m,n)}(a)/B_\theta(a)\%$	**6.1**	1.9,3.9,**6.1**,7.7,9.6	3.9,5.1,**6.1**,**9.6**
Figure	figure 8.11	figure 8.10	figure 8.13, 8.14

Four cases will be shown with a different plot style.
This new figures highlight the step performed towards a close comparison between MHD simulations and experimental measurements at RFX-mod. Consider as an example figure 8.13 and compare it with the corresponding experimental figure, 10.1. Peculiar similarities can be observed: note the typical dynamics of the dominant MHD mode with quasi-periodical crashes and the similar oscillation on the parameter F. This novel result represent a step towards a closer predictive capability of the visco-resistive MHD model and opens interesting spaces for interpretation of the experimental results and of their improvement.
Figure 8.10 shows the effect of MPs on the *first non-resonant* mode, $(1, -6)$. The dynamics is similar to the corresponding simulation shown in figure 8.8, only the MHD dynamics evolves on a much longer time-scale. The level of secondary modes is reduced with respect to the corresponding simulation at higher dissipation, according to a well known result indicating that the global level of perturbations to the equilibrium

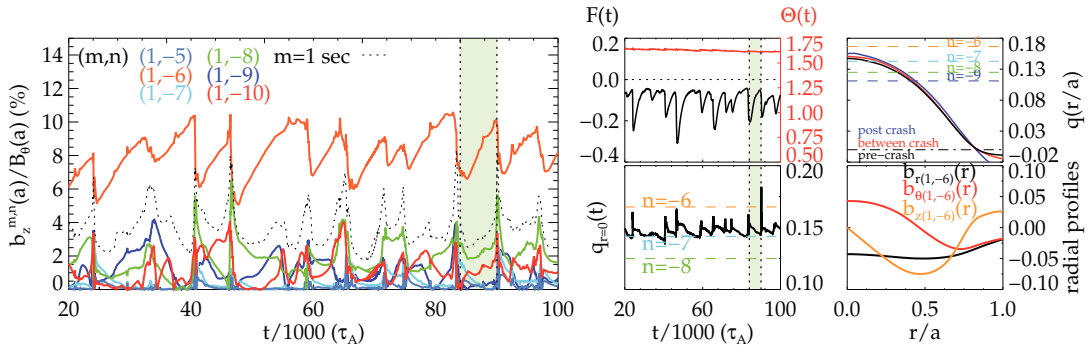

Figure 8.10: Effect of MP on the first non-resonant $(1, -6)$ mode. MPs are imposed from the beginning of the simulation. (*Left*) Time evolution of the edge axial magnetic field of the most important $m = 1$ MHD modes. (*Top middle*) Time evolution of the F and Θ parameter. (*Bottom middle*) Time evolution of an average of the safety factor (radial average between $0 < r/a < 0.2$). (*Top right*) Safety factor profile at the beginning, in the middle and at the end of the highlighted region. (*Bottom right*) Average magnetic components of the dominant $(1, -6)$ mode during the highlighted cycle.

field decreases increasing S [Cappello and Biskamp, 1996; Terranova et al., 2000]. A systematic scaling of the energy of secondary modes with the dissipation parameters will be presented in section 9.1.

Figure 8.11 shows the effect of MPs on the *second non-resonant* mode, $(1, -5)$. The dynamics, even in this "exotic" case, is very similar to the one that is shown in figure 8.13 (MP with the same intensity on the $(1, -7)$ mode) and to the one in figure 8.10 (MP with the same intensity on the $(1, -6)$ mode). This resemblance seems to indicate that no a-priori helicity can be considered the spontaneous one for an RFP-like magnetic field (at fixed aspect-ratio). The use of a sufficiently strong helical MP at the edge can stimulate the desired helicity in the magnetic field.

As a further indication consider the plot of figure 8.12. Three simulations (figures 8.10, 8.11 and 8.13) with equal parameters of the model but with different helicity of the applied MP are compared. The $(1, -7)$ MHD mode reacts more than the other two to the MP, as its amplitude averaged in time (when the system is in a QSH state defined by $N_s < 3$, see equation (9.2)) is 30% higher than the corresponding quantity for the $(1, -5)$ mode. This happens while the cumulated amplitude of secondary modes does not vary; it will be shown in chapter 9 that this quantity depends mainly on the dissipation parameters.

The problem that can be synthesized with the question *"why is the* $(1, -7)$ *mode the dominant in the RFX-mod experiment?"* is an open problem for the RFP configuration: the study presented in this chapter shows that a perturbation on the first resonant MHD mode is *favoured* by the MHD dynamics.

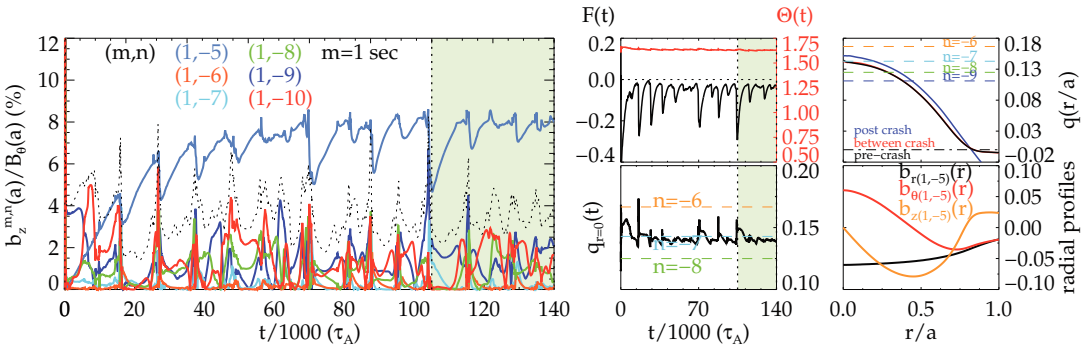

Figure 8.11: Effect of MP on the second non-resonant $(1, -5)$ mode. MPs are imposed from the beginning of the simulation. Same quantities as in figure 8.10. (*Top right*) Safety factor profile at the beginning, in the middle and at the end of the highlighted region. (*Bottom right*) Average magnetic components of the dominant $(1, -5)$ mode during the highlighted cycle.

A further dynamical transition (after the one shown by passing from a MH state to a QSH state with MHD cycles obtained through the use of MPs) can be obtained by further raising the level of MP. Above an MP level given by $b_r^{MP}/B_\theta(a) > 8\%$ the cycles in F and Θ disappear and a rather stationary behaviour of these quantities and of the energy of the MHD modes is obtained. This behaviour was found in simulations with MP imposed on the $n = -6$ and $n = -7$ modes. Two examples involving the *first resonant* mode $n = -7$ can be seen in figure 8.13 and 8.14 that represent respectively a case under this second threshold and above it.

8.4 Summary and remarks: toward a more quantitative comparison with the experiment

In this chapter we have presented a wide set of 3D MHD visco-resistive simulations applying helical Magnetic Perturbations (MP) on both spontaneous QSH and MH regimes of the RFP. The effect of resonant and internally-non-resonant helical perturbations has been considered in relation to the applied MP amplitude.

Above a certain threshold, MP boundary condition succeeds in driving the RFP to develop a global helical regime, whatever the value of viscous-resistive transport coefficients. This is a novel result which provide a key contribution in explaining experimental trends, such as the evidence that helical regimes similar to the experimental ones develop at increasing plasma currents [Piovesan et al., 2009; Chapman et al., 2012]. In particular, for MP's above-threshold values, the driven QSH may present, typically in the lower visco-resistive dissipation regime, intermittent behaviour in many physical quantities, qualitatively reproducing experimental observations. Magnetic topology studies, though performed in η and ν regimes not yet comparable to experimental con-

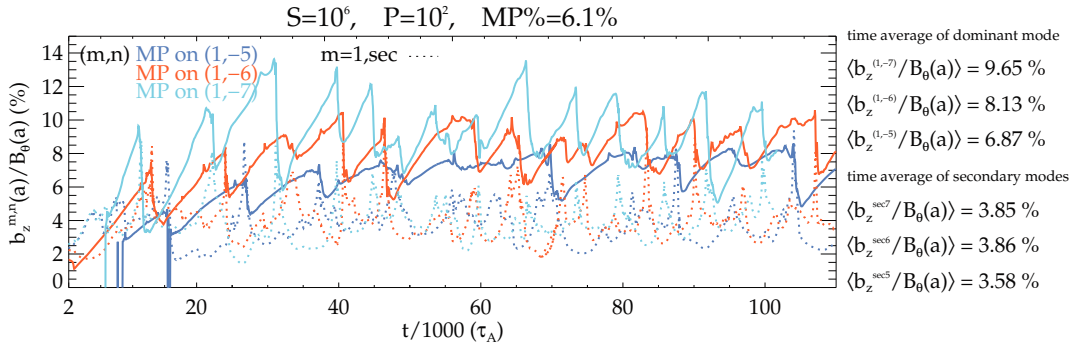

Figure 8.12: Comparison between the three simulations of figures 8.10, 8.11 and 8.13. All the parameters used during the simulations are equal apart from the helicity of the applied MP. Note the presence of a hierarchy between the dominant MHD modes: with the same external stimulation the $(1,-7)$ mode is stronger than the $(1,-6)$ that is stronger than the $(1,-5)$. The cumulated amplitude of the secondary modes does not depend on the helicity of the applied MP, instead.

ditions, are performed in chapter 9 and will show the emergence of conserved core helical surfaces, that can be linked to the appearance of wider thermal structures at the beginning of QSH rising phases.

As a final remark the MHD simulations presented in section 8.2 and 8.3 give a first indication of one of the fundamental outcomes of my PhD thesis: the combined used of helical boundary conditions and of a higher value of the dissipation parameters (higher H) allow to obtain realistic simulations of the typical RFP discharges and a quantitative agreement between the dynamics of the magnetic field from numerical simulations and experimental evidences. The material contained is being published in the *Plasma Physics and Controlled Fusion* scientific journal [Veranda et al., 2013].

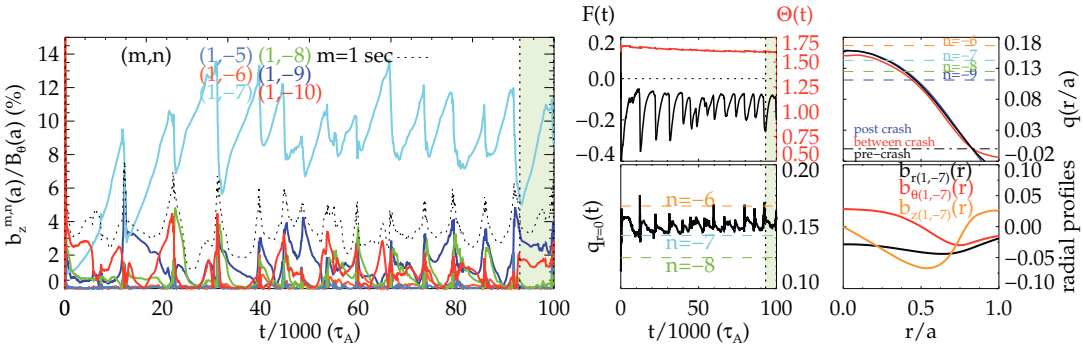

Figure 8.13: Effect of MP on the first resonant $(1,-7)$ mode, with amplitude 6.1%, see table 8.5. MPs are imposed from the beginning of the simulation. All the quantities as in figure 8.2. (*Top right*) Safety factor profile at the beginning, in the middle and at the end of the highlighted region. (*Bottom right*) Average magnetic components of the dominant $(1,-7)$ mode at the end of the highlighted time slice.

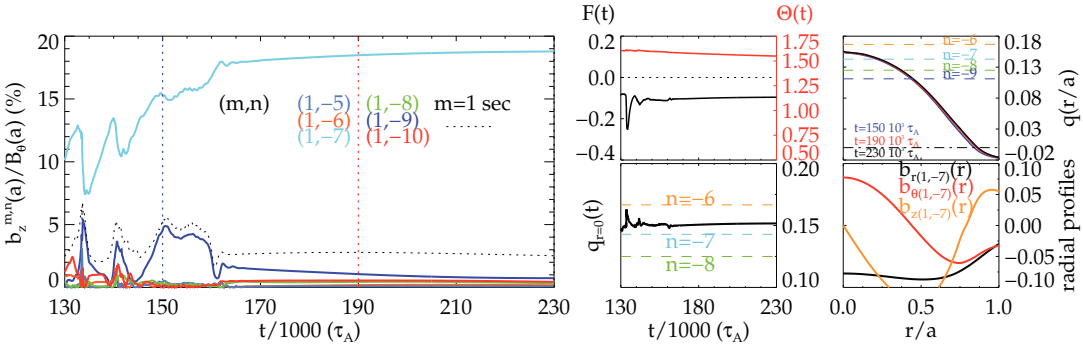

Figure 8.14: Effect of MP on the first resonant $(1,-7)$ mode, with amplitude 9.6%. MPs are imposed from the beginning of the simulation, and a partial part of the simulation is shown. Note the stationary behaviour of all the physical quantities after $t = 1.6 \cdot 10^5\,\tau_A$. All the quantities as in figure 8.2. (*Top right*) Safety factor profile at the beginning, in the middle and at the end of the highlighted region. (*Bottom right*) Average magnetic components of the dominant $(1,-7)$ mode at the end of the time slice here presented, $t = 230 \cdot 10^5\,\tau_A$.

9

Magnetic topology of RFP helical states

The simulation study reported in chapter 8 provides a numerical proof of principle that the visco-resistive MHD model, together with non-ideal wall boundary conditions on the magnetic field, can capture the skeleton of the physics that rules the behaviour of the plasma in a typical RFP experiment. The simulations reported show a qualitative resemblance with the experimental findings from various RFP devices (RFX-mod in Italy, MST in USA, RELAX in Japan, T2R in Sweden) [Martin et al., 2003].
This chapter aims at extracting some global informations from the set of simulations performed and to analyze a selected group of them from the magnetic topology point of view. The analysis shows that magnetic order is influenced by the level of perturbations to the helical equilibrium. In fact conserved structures related to the dominant helical perturbation are recovered, but at the actual level of secondary perturbation they are not able to sustain a more ordered state.
Outline of the chapter. This chapter is divided in two parts. In the first, section 9.1, a global outlook to the MHD simulations study is performed, aiming at describing the behaviour of the magnetic field against the most important parameters of the model. In the second part, section 9.2, the actual magnetic topology will be described: helical structures covering a significant volume of the domain can be found. Some general remarks will be made in section 9.3.

9.1 Behaviour of dominant and secondaries modes in simulations with MP

The three sets of MHD simulations described in chapter 8 constitute a big part of a wide set of simulations with externally imposed helical MP.
Great attention was posed in varying only some important parameters while keeping

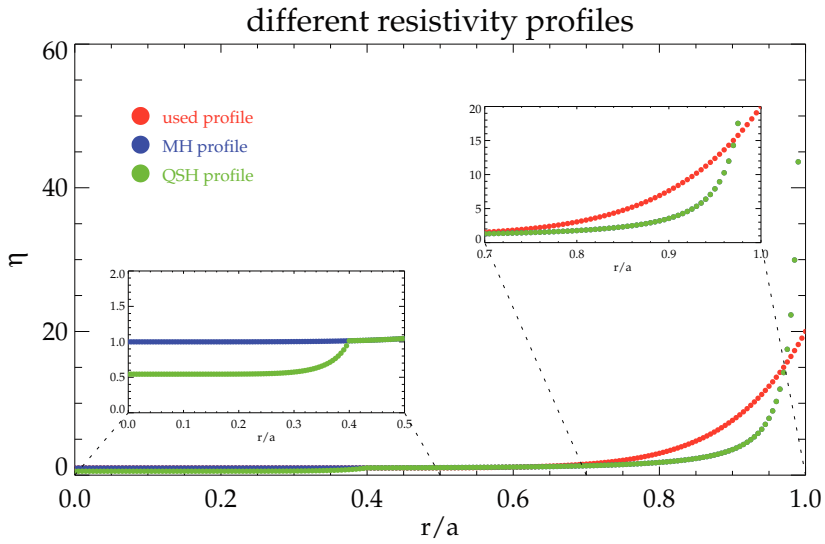

Figure 9.1: In red the radial profile of the resistivity employed in all the MHD simulations shown in this thesis is shown. In blue a MH-like profile, in green a QSH-like profile. Preliminary results indicate a reduction of the cumulated amplitude of the secondary modes of about 15% passing from the red to the blue or green profile.

others fixed, mainly the initial resistive equilibrium and the viscosity and resistivity radial profiles. Preliminary studies are ongoing to assess the influence of the latter in the MHD dynamics. It is already known that the role of the resistivity profile can be important in determining the features of the magnetic field: in particular the level of perturbations to the equilibrium state seems to depend on the shape of the resistivity profile, decreasing if resistivity is higher on the edge of the plasma [Sätherblom et al., 1996]. The resistivity profile here adopted, described in (4.5), is less peaked in the edge region than what it is considering a simple power-law expression of the temperature profile in the RFX-mod (private indications give $T \propto \left(1 - (\frac{r}{a})^{\gamma}\right)$, $\gamma \in [4-8]$ for a typical MH state). Figure 9.1 shows, in red, the radial profile of the resistivity, $\eta(r)$, employed in all the simulations shown in this thesis. Two other radial profiles are proposed, a MH-like one (calculated from the typical RFX-mod temperature profile using the law $\eta \propto T^{-3/2}$ with $\gamma = 6$) and a QSH-like one (that takes into account a higher core temperature resulting in a lower core resistivity).

In the following sections the behaviour of the dominant or of the secondary modes changing the parameters defining the simulation study will be described. The parameters and their range of variation are described in table 8.1.

9.1.1 Intensity of the dominant and secondary modes vs MP

The data presented in this section are extracted from a set of simulations with $S = 10^5$, $P = 10$, $n^{MP} = -7$. The behaviour of the dominant and of the secondary modes is studied considering their magnetic energy (proportional to b^2, b being the perturbation to the helical equilibrium). In particular the evaluation of the energy of the secondary modes was performed averaging the energy of all $m = 1$ from $n = -25$ to $n = 5$. Other estimation are possible, in particular the one described in section 9.1.3 is the one used to analyze data from RFX-mod experiment; in this case there was no need of quantitative estimates and this simple estimate is sufficient. Moreover the energy of secondary modes is a *global* indication of their amplitude, as an energy indication involves a volume integral of the modes eigenfunctions.

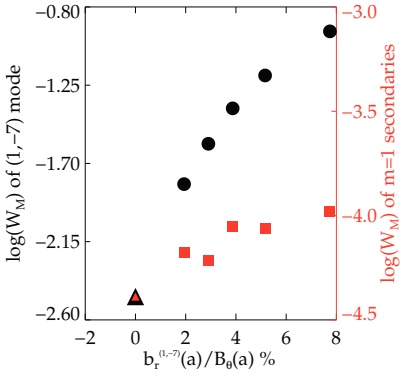

Figure 9.2: Dependence of dominant and secondary modes energy on the amplitude of the MPs on $(1, -7)$ mode for the set simulations.

The behaviour of the system under MP of different intensities can be understood by looking at figure 9.2, where different amplitudes of MPs imposed on the $(1, -7)$ mode (from 0% to 8%) are studied. The figure shows that the value of the energy of the dominant increases strongly with the amplitude of the MPs and that the energy of the secondary modes is rather independent thereof. This explain the reason of the presence of a threshold in the quantity MP. In fact to obtain a QSH state there has to be a clearly dominant MHD mode, as it happens for $MP \gtrsim 2\%$.

9.1.2 Intensity of the dominant and secondary modes vs MP and $\mathrm{n^{MP}}$

The data presented in this section are extracted from a set of simulations with $S = 10^5$, $P = 10$. Five more simulations with $n^{MP} = -6$ are added to the set studied in the previous section 9.1.1 to point out the role of a MP imposed on a different MHD mode. As it can be clearly seen the new simulations, characterized by open symbols in figure 9.3, fit very well with the previous one, showing an independence of the energy of the dominant and secondary modes from the helicity of the imposed MP. This result constitutes a first hint to the general idea that the QSH states obtained after MP are dynamically (as it was seen in chapter 8) and topologically similar for helicities closer to the experimentally dominant MHD mode.

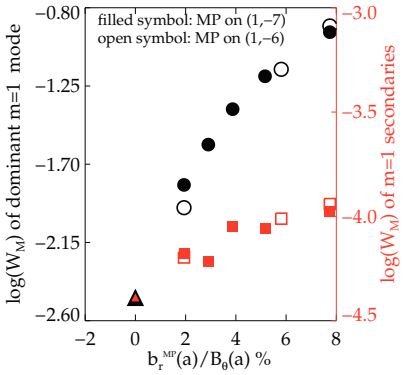

Figure 9.3: Dependence of dominant and secondary modes energy on the amplitude of the MPs on both $(1, -7)$ mode (filled symbols) and $(1, -6)$ mode (open symbols) for a set simulations at fixed S and P.

9.1.3 Amplitude of the secondary modes vs S and P

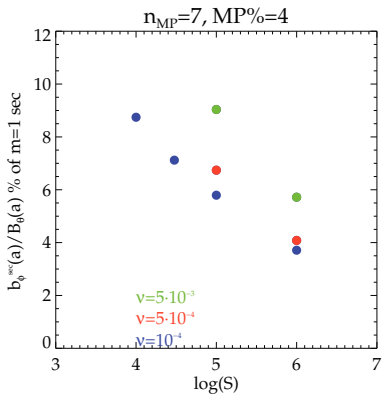

Figure 9.4: Dependence of the energy of the secondary modes on the Lundquist S and Prandtl P number for a set simulations at fixed $MP = 3.9\%$ and $n^{MP} = -7$.

Many studies can be found in the literature on the behaviour of the secondary modes with respect to the value of dissipation parameters, in the framework of the visco-resistive MHD model, see for example [Cappello and Biskamp, 1996; Terranova et al., 2000; Strauss, 1986]. These articles propose many different scaling laws of the type $b^{sec}/B \propto S^{\gamma}$ with $\gamma \in [-1/2 : -1/4]$, the specific value depending on the particular subject of the study.

Thinking of the RFP dynamics as dominated by Sweet-Parker reconnection we would expect a scaling law $b^{sec}/B \propto S^{-1/4}$ that can be corrected, taking into account the effect of viscosity, to $b^{sec}/B \propto S^{-1/4}(1+P)^{1/8}$ [Park et al., 1984; Terranova et al., 2000].

The simulations presented in this section are characterized by $n^{MP} = -7$ and $MP = 3.9\%$, while S and P varies in the range indicated in table 8.1.

The determination of the secondary modes cumulated amplitude is performed in the same way as it is performed to analyze experimental data from RFX-mod in [Piovesan et al., 2009]:

$$b_{\phi}^{m=1,sec}/B_{\theta}(a) = \sqrt{\sum_{n=-20}^{n=-8} \left(b_{\phi}^{1,n}\right)^2}/B_{\theta}(a). \tag{9.1}$$

A further constraint on the analysis is placed by the choice of calculating the intensity of the secondary modes only when the spectral index N_s, that indicates the level of single helicity, is less than 3 (this value is a convention: values below 3 generally indicate a good QSH state).

$$N_s = \left\{ \sum_{n} \left[(b_{\phi}^{1,n})^2 / \sum_{\tilde{n}} (b_{\phi}^{1,\tilde{n}})^2 \right]^2 \right\}^{-1}. \tag{9.2}$$

The results can be seen in figure 9.4. It is possible to note that secondary modes intensity decreases with the resistivity (at fixed viscosity) and with viscosity (at fixed resistivity). A global scaling can be obtained performing a multiparametric fit of the kind:

$$b_{\phi}^{sec}/B_{\theta}(a) \propto S^{\alpha}(1+P)^{\beta}. \tag{9.3}$$

From this set of simulation it is obtained $\alpha = -0.30$ and $\beta = 0.12$, that is consistent with a dynamics dominated by Sweet-Parker reconnection processes. Considering the fact the $P > 1$ in most of the simulations used to obtain the scaling the dependence can be written using other dimensionless parameters, like the Hartmann number $H = SP^{-1/2}$. The dependence can be written in the form:

$$b_\phi^{sec}/B_\theta(a) \propto S^\alpha P^\beta \propto H^{-0.31} P^{-0.04}, \tag{9.4}$$

showing that, for $P \gg 1$, the Hartmann number only rules the visco-resistive MHD dynamics (see 4.1.1 for a further corroboration of this finding).

9.1.4 Amplitude of the secondary modes vs S and P and n^{MP}

Six more simulations with $n^{MP} = -6$ are added to the set studied in the previous section 9.1.3 to point out the role of a MP imposed on a different MHD mode. In this section a slightly different criterion to determine the secondaries was used: in the previous section the average of the amplitude of the secondary modes was performed when $N_s < 3$, now it will be performed using the condition $N_s < 4.5$. This is just expected to raise the secondary modes average amplitude, as less pure QSH states will also be included in the calculation. In fact it will be shown that the scalings recovered in the previous section remain essentially unchanged. This different criterion does not modify the general behaviour of secondary modes with the dissipation parameters:

$$b_\phi^{sec}/B_\theta(a) \propto S^{-0.28}(1+P)^{0.11}. \tag{9.5}$$

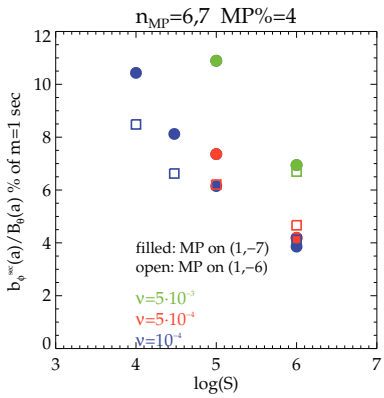

Figure 9.5: Dependence of the energy of secondary modes on the Lundquist S and Prandtl P number for two set simulations at fixed $MP = 3.9\%$ with $n^{MP} = -6, -7$. Note that the simulations with MPs on the $(1, -6)$ mode, hollow symbols, have the same level of secondaries that the ones with MPs on the $(1, -7)$ mode.

As it can be easily recognized the simulations with $n_{MP} = -6$ agree well with the corresponding simulations with $n_{MP} = -7$. This represents a further confirmation to the remark made in the summary of the previous chapter, namely that the dynamics of MHD simulations that stimulates different helicities to obtain QSH states are similar.

9.1.5 Amplitude of the $\mathrm{m} = 0$ modes vs S and P

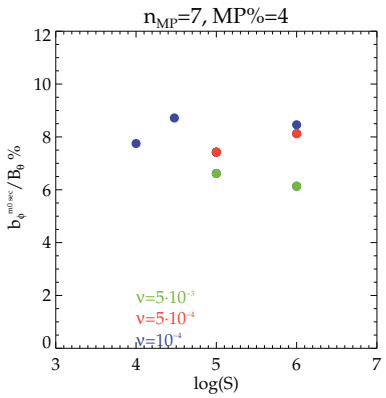

Figure 9.6: Energy of the secondary $m = 0$ MHD modes plotted against S and P (set simulations at $MP = 3.9\%$ and $n^{MP} = -7$).

It is interesting to analyze also the behaviour of the $m = 0$ MHD modes, that in the RFP are believed to have positive effects on the confinement of energy and particles, see [Spizzo et al., 2006], as they create a chain of conserved structures around the reversal radius (where the toroidal component of the magnetic field reverses). The result indicates that the intensity of the $m = 0$ modes, with $-23 \leqslant n \leqslant -1$, slightly decreases with the Lundquist number, while the role of the Prandtl number is less evident.

9.1.6 Amplitude of the dominant mode vs S and P

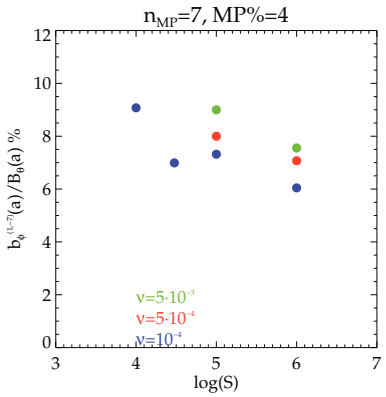

Figure 9.7: Dependence of the energy of the dominant mode on the Lundquist S and Prandtl P number for a set simulations at fixed $MP = 3.9\%$ and $n^{MP} = -7$.

In this section the same set of simulations of section 9.1.3 will be analyzed, with $n^{MP} = -7$ and $MP = 3.9\%$. The intensity of the dominant mode is evaluated calculating the intensity of the axial component of the magnetic field at the edge when the $(1, -7)$ mode is dominant. The result is synthesized in figure 9.7. The dominant mode energy is less dependent on the dissipation parameters than the secondary modes' one, as a multiparametric fit indicates:

$$b_\phi^{dom}/B_\theta(a) \propto S^{-0.11} P^{0.06}. \tag{9.6}$$

The faster decrease of secondary modes with S and P implies that better QSH states are obtained at a higher value of the dissipation parameters, as experimentally observed. This is measured by a parameter called QSH persistency, that measures the percentage of time that the plasma passes in a magnetic QSH state during a whole discharge; QSH persistency grows with S, as described in [Piovesan et al., 2009]

All the scaling presented in this section contain data that are similar to the experimental measurement performed at RFX-mod. This seems to indicate that the contemporary use of MPs and of low dissipation is the key to reinforce the visco-resistive MHD model adherence to experimental findings and its predictive capability.

9.2 Magnetic field topology in the presence of magnetic perturbations

The MHD simulations presented in sections 8.2 and 8.3 are qualitatively similar to the observed experimental behaviour in RFX-mod. They can be used to check whether there is magnetic order in such QSH states or not. The analysis will be conducted in three different cases at different values of the dissipation parameters and of the MP involved. The role of the intensity of the secondary modes will be analyzed, making a comparison with the corresponding quantity measured in the experiment RFX-mod. The data reported in [Piovesan et al., 2009] indicate (remember that no indication on the viscosity level is actually available):

$$S \approx 10^6 \longrightarrow b_z^{sec}(a)/B_\theta(a) \approx 2\%$$
$$S \approx 10^7 \longrightarrow b_z^{sec}(a)/B_\theta(a) \approx 1\%$$

while the data collected in section 9.1.3 indicate a level of secondary modes given by $b_z^{sec}(a)/B_\theta(a) \approx 4-6\%$, depending on the level of visco-resistive dissipation. This quantitative discrepancy (secondary modes in simulation are approximately three times higher that in the experiment) can be explained considering that an important role can be played by the resistivity profile [Sätherblom et al., 1996] and by extended-MHD related effect (i.e. the inclusion of a non-zero pressure) [King et al., 2012]. These studies will be addressed in the future, while in this section an "ad hoc" solution will be used: for the analysis of the magnetic topology the level of secondary modes in the magnetic field will be rescaled to the experimental value, in some selected time instants. This will allow to determine qualitatively the level of magnetic order that can be reached by the modified magnetic field.

9.2.1 A medium Hartmann number case

The first analysis deals with the simulation whose dynamics is described in figure 8.8. Figure 9.8 shows a sequence of five Poincaré plots, in the $\theta = 0$ plane, which display the evolution of the magnetic topology during the time window highlighted in figure 8.8. The main observation is that the presence of a dominant MHD mode allows for a

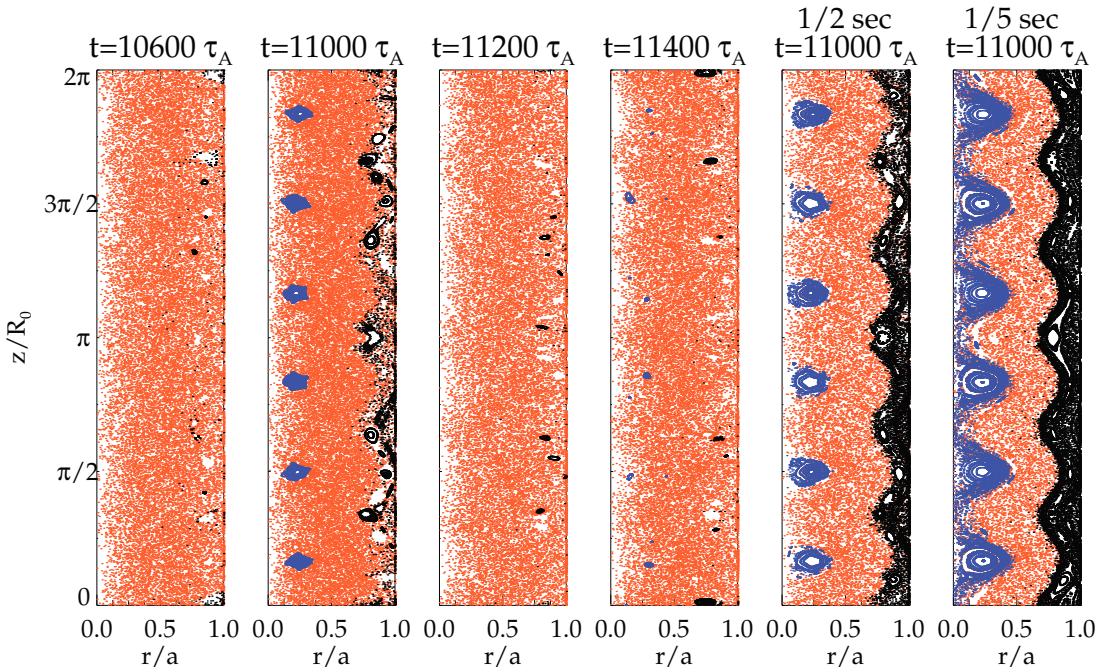

Figure 9.8: Poincaré plot in the $r-z$ plane, corresponding to the time window highlighted in figure 8.8 with MP on the $(1,-6)$ MHD mode. The plots are obtained with the volume-preserving version of NEMATO. The widest conserved structures (highlighted in blue) are present at $t = 11000\,\tau_A$, when the total energy of the secondary modes is at its lowest level (see figure 8.8). Black points refer to $m = 0$ conserved structures at the edge. As the amplitude of the secondary modes is reduced to one half or to one fifth of their original value (this last case having an intensity of secondaries similar to high current RFX-mod operations) conserved structures grow, as can be clearly seen on the last frame on the right.

conserved helical $n = -6$ core, though only temporarily and mainly during the QSH reinforcement phase subsequent to a crash, when secondary modes are small. It must be noted that the obtained QSH regime features a Single Helical Axis (SHAx), as can be proved by analyzing the helical flux function associated to the dominant helical mode (no separatrix is present). In addition to this core topological structure, a chain of $m = 0$ islands is present in the edge region, located around the toroidal magnetic field reversal surface, as is also typical in MH regimes [Spizzo et al., 2006]. We finally note that the temporary emergence of the conserved core magnetic structure in the simulated QSH shares some similarities with the *thermal* QSH structures, currently under investigation in the RFX-mod experiment [Ruzzon et al., 2012]. The determination of the magnetic topology from experimental data is an ongoing work based on the use of Newcomb's equation to reconstruct the magnetic field in the RFP from edge measurements [Zanca, 2009]. The resulting magnetic topology, calculated with other field line tracing tools,

is found to be widely chaotic (an example is reported in figure 5 of [Lorenzini et al., 2008]).
The cumulated amplitude of the secondary modes is estimated performing a temporal mean when the magnetic field is in a QSH state (i.e. when the spectral index, equation (9.2), is less than 3). Their amplitude is determined by the formula (note that it is similar to (9.1), only modes up to n=-5 are here considered):

$$b_\phi^{m=1,sec}/B_\theta(a) = \sqrt{\sum_{n=-20}^{n=-5} \left(b_\phi^{1,n}\right)^2}/B_\theta(a). \tag{9.7}$$

The result, in this case, indicates $b_z^{sec}(a)/B_\theta(a) = 5.3\%$, meaning that a reduction of the secondaries of at least five times is required to obtain a value comparable with the experimental value at $S = 10^7$. This was done in the second-last and in the last frame of figure 9.8, where secondaries where first halved and then reduced to $1/5$ of their original value. The area of the plot occupied by conserved magnetic structures clearly is larger. Given the results from the scaling shown in section 9.1.3 such amplitudes can be obtained by increasing the Lundquist number $S = \eta^{-1}$ by a factor of approximately 200 (at fixed Prandtl number, $P = \nu/\eta$). Alternatively the same effect can be obtained decreasing η by a factor of 5000, at fixed viscosity ν.

9.2.2 A high Hartmann number case

The final part of the simulation shown in figure 8.13 is analyzed from the topological point of view in figure 9.9. An estimation of the cumulated amplitude of the $m = 1$ secondaries during the whole simulation yields $b_z^{sec}(a)/B_\theta(a) \approx 4\%$. As in the case shown in figure 9.8 a helical core is able to emerge from the bath of magnetic stochasticity. The reduction to experimental-like level of perturbations (shown in the last two frames) indicates an increase of magnetic order. The second-last frame refers to the experimentally measured cumulated amplitude of secondaries at $S \approx 10^6$, $I_P \approx 0.5\,\mathrm{MA}$ (in RFX-mod) while the last one refers to $S \approx 10^7$, $I_P \approx 1.3\,\mathrm{MA}$ (the estimates are obtained from [Piovesan et al., 2009]). This last current value is similar to the one used during the experimental campaign proposed by me and the theory group at Consorzio RFX after these studies (the campaign will be described in chapter 10).

9.2.3 A second high Hartmann number case

Let now consider a case with MPs on the $(1, -5)$ MHD mode, shown in figure 8.11. The estimate of the cumulated amplitude of secondary modes gives a mean value of $b_z^{sec}(a)/B_\theta(a) = 3.6\%$, similar to the one recovered at the same Lundquist number in

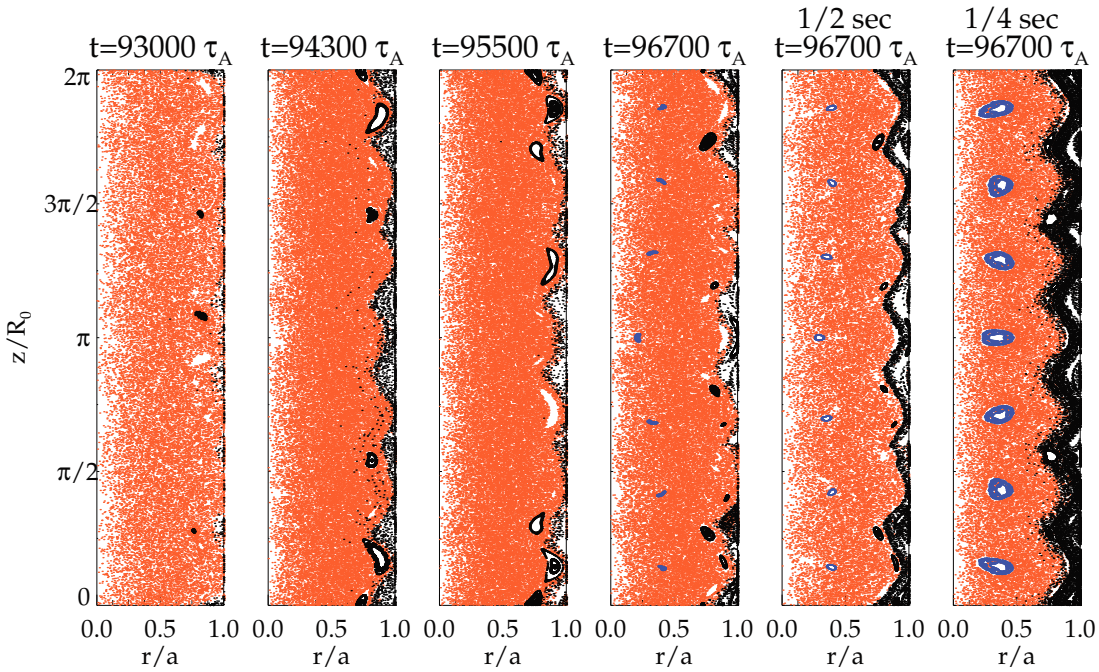

Figure 9.9: Poincaré plot in the $r-z$ plane, corresponding to the time window highlighted in figure 8.9 with MP on the $(1,-7)$ MHD mode. The plots are obtained with the volume-preserving version of NEMATO. The widest conserved structures (highlighted in blue) are present at $t = 96700\,\tau_A$, when the total energy of the secondary modes is at its lowest level (see figure 8.13). Black points refer to $m = 0$ conserved structures at the edge. The last two frames on the right show the improvement of magnetic topology when secondaries with cumulated amplitude respectively of 2% and 1% are considered.

section 9.2.2. The magnetic topology is described in figure 9.10, where the plots corresponding to the rescaled secondaries are also shown.

9.2.4 A comparison: effect of a different n^{MP}

A comparison between the three simulations of figures 8.10, 8.11 and 8.13 is performed in figure 8.12 from the dynamical point of view. All the parameters used during those simulations are equal apart from the helicity of the applied MP, n_{MP}. It was found that the first resonant $(1,-7)$ MHD mode responded more intensely to the external perturbation than the non resonant modes. The analysis from the topological point of view was performed picking a precise time instant from each simulation with the feature of having a cumulated level of secondary modes amplitude equal to 2.4%, that is near to the minimum value reached during those simulations. All the secondaries were then rescaled to the experimental-like value of 1%. The results are plotted in figure 9.11. It can be clearly seen that despite the $(1,-7)$ mode is the most reactant (in

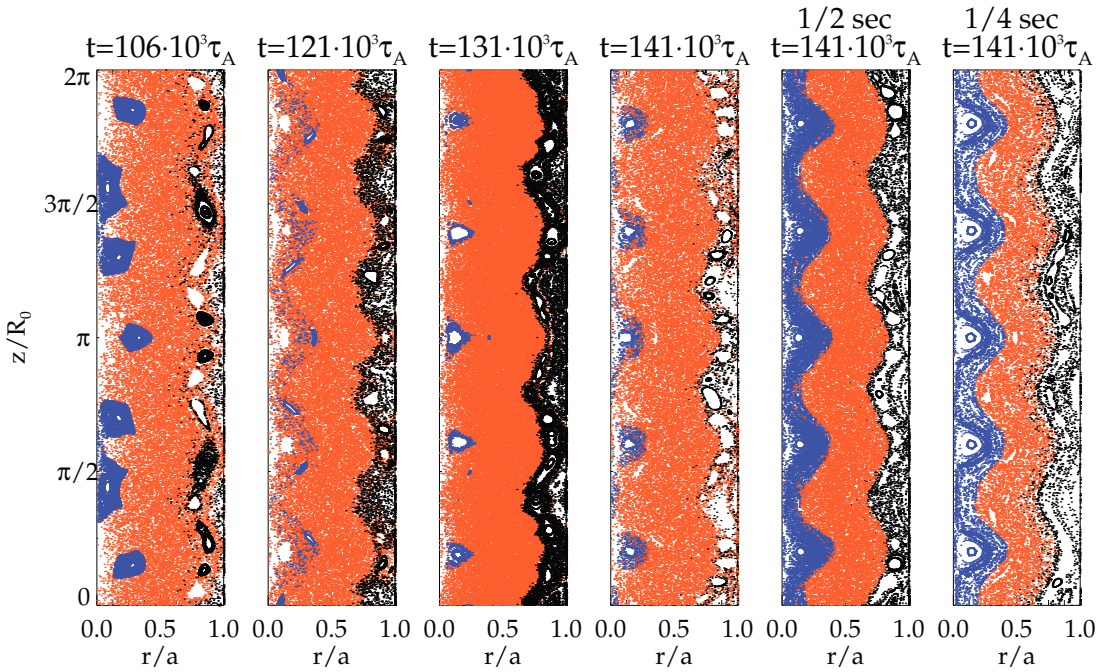

Figure 9.10: Poincaré plot in the $r-z$ plane, corresponding to the time window highlighted in figure 8.11 with MP on the $(1,-5)$ MHD mode. The plots are obtained with the volume-preserving version of NEMATO. The widest conserved structures (highlighted in blue) are present at $t = 141000\,\tau_A$, when the total energy of the secondary modes is at its lowest level (see figure 8.11). Black points refer to $m = 0$ conserved structures at the edge. The last two frames on the right show the improvement of magnetic topology when secondaries with cumulated amplitude respectively of 2% and 1% are considered.

total amplitude) to the external stimulation it also creates the lower area of conserved magnetic surfaces. This is confirmed even if the same ratio between dominant and secondary modes is artificially created in the three cases (typical experimental values for this quantity are $b_z^{dom}/b_z^{sec} \approx 6$ at $S \approx 10^7$.

9.3 Summary and remarks

The study of the magnetic field topology is of fundamental importance to assess the level of transport of particles and energy in the RFP configuration. The examples shown in this chapter indicate that the QSH states whose features resemble the experimental ones are able to sustain conserved magnetic structures, but not in the whole plasma domain. The enforcement of ordered structures seem to rely principally on a lower level of perturbations to the helical equilibrium. The analysis under the energy transport point of view is ongoing, and the preliminary quantitative result presented in the summary at the end of chapter 11 seem to indicate that the actual magnetic topology in the

experiment is similar to the one shown in this chapter.

The presence of an ordered magnetic topology is the main aim for the RFP configuration: if reached, the path toward an RFP-based reactor would be easier, as the zeroth order transport cause in actual RFP experiments would be ruled out. The challenge for the RFP configuration now is to reach a SH ohmic state in the experiment, with a higher central current and a higher confinement level than the one found in the typical experimental SHAx states.
MHD visco-resistive simulations may indicate a lower secondary cumulated amplitude considering a different treatment of some parameters. First of all dissipation has to be further reduced to experimental-like values (a reduction of more than an order of magnitude is required, at the moment limited by computing times). Secondly the effect of the resistivity's radial profile can be important, as it was previously indicated (section 9.1). The effect of a non-zero β may also be important [King et al., 2012], even though the present understanding is that zero-β simulations appear to capture the "skeleton" physics of the operating RFP devices, which quote β values around/below 0.1 in normal operations. Extended-MHD effects also (mostly taken into account in Ohm's law, (3.21d)) can be important in modifying the magnetic field dynamics.

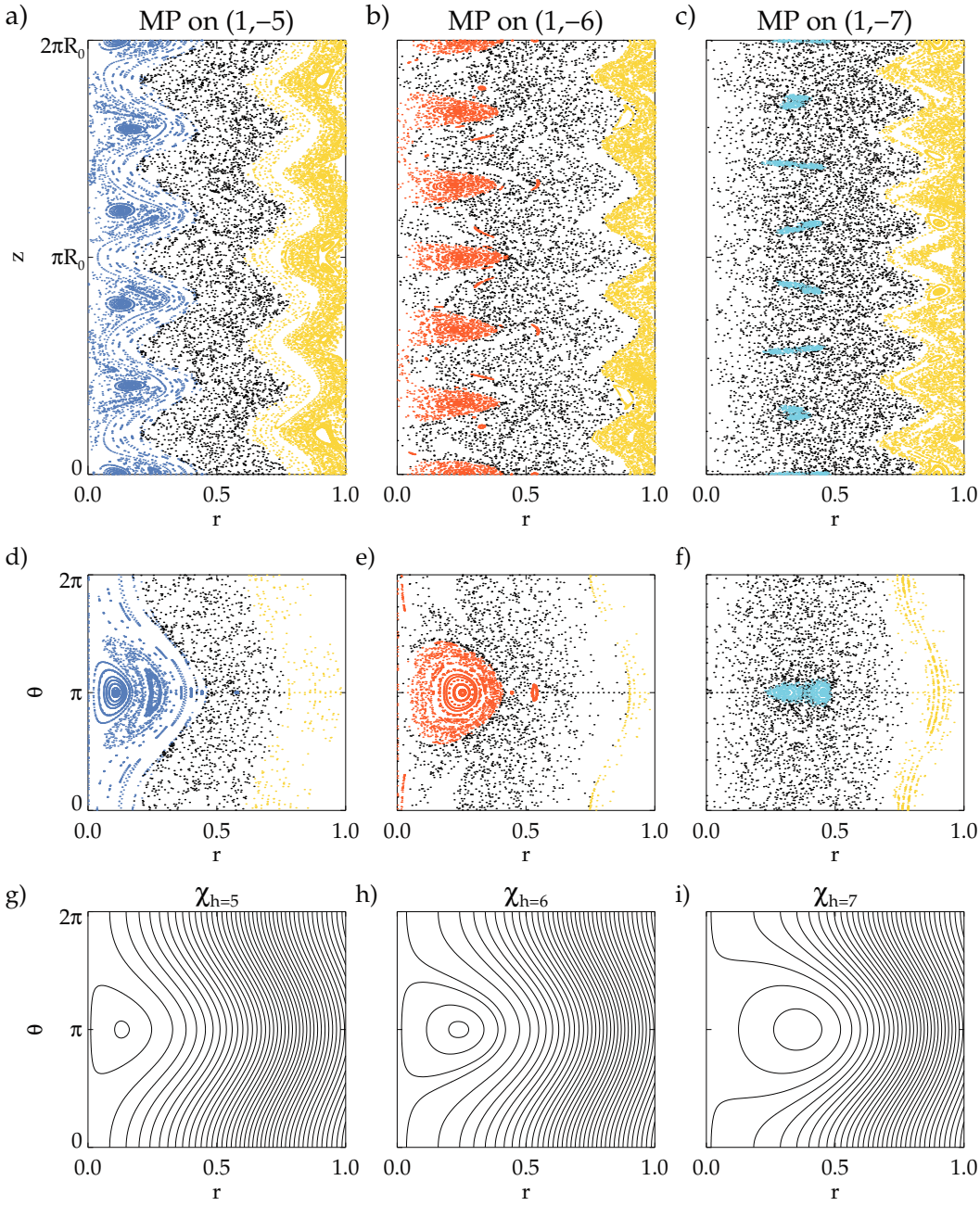

Figure 9.11: Poincarè plots in the $\theta = 0$ and $z = 0$ surfaces of section for three time instants of three MHD simulations that are different only because of the helicity of the applied MP. Note that the second non-resonant mode $(1, -5)$ creates the greater area of conserved structures. Edge conserved structures are underlined in yellow. The third row shows the helical flux function corresponding to the dominant mode of each case.

IV

Application to experimental activity

10

RFX-mod experiments motivated by the PhD work

The numerical work presented in part III motivated dedicated experiments in RFX-mod.

The main aims of the experiments are three. The first is the experimental verification of the idea that, through the use of helical boundary conditions (called Magnetic Perturbations in chapter 8 where their effect is widely analyzed) it is possible to force a QSH state with the chosen helicity. The second it to prove that this forcing happens only over a threshold in the MP's amplitude. The third and most important aim, more transport related, is to determine whether strong resilience to magnetic chaos is present in QSH states originated by the presence of a non-resonant dominant MHD mode (looking at the positive thermal effects that should be present).

The first two aims are completely achieved: as in numerical simulations above a threshold in amplitude of the helical edge magnetic field a QSH state is obtained, with the helicity of the imposed boundary condition. The third aim is connected to a thermal analysis of the experimental data that is still ongoing. Preliminary results indicate that the remarkable level of order found in the MHD simulations with a non-resonant dominant mode, presented in chapter 7 is a peculiar case. Indeed the results seem to confirm the picture of magnetic field topology found in more realistic cases and described in chapter 9.

The experimental proposal for the RFX-mod experiment that I promoted with the theory group at Consorzio RFX was technically realized by the exploitation of internal RWM modes for the stimulation of non-resonant QSH states (see section 3.6.3). The RWMs, if suitably controlled, in fact provide a way to build up helical equilibria with different toroidal periodicity n. In particular, the obtaining of $h = 6$ QSH states is attempted by performing the feedback control on the $m = 1, n = -6$ RWM mode in

such a way to keep its amplitude large enough to make this mode the dominant one in medium-to-large plasma current discharges, $I_P \gtrsim 1.2\,\mathrm{MA}$.

Outline of the chapter. This chapter describes the main aims and results of the experimental campaign proposed after the studies shown in this thesis in part III.

Section 10.1 describes the main aims of the experimental campaign. Section 10.2 describes the general details of the discharges performed at the RFX-mod experiments, with some figures to show how the aims were reached and the theories confirmed by the experimental activity.

A summary and remarks section can be found in 10.3.

10.1 Aims of the experimental proposal and main results

The experimental proposal #26 led to a series of discharges starting from November 2011, during three experimental sessions of the RFX-mod experiment. The main request to the experimental team was to feedback control the $m = 1$, $n = -6$ MHD mode (but other MHD modes were controlled, like the $(1, -5)$ and the $(1, -8)$) with clean mode control at $r = a = 0.459\,\mathrm{m}$ (see section C.1.2 for an explanation of the ideas at the basis of clean mode control). This means that a non-ideal wall boundary condition is created by the system of 192 active coils installed in the RFX-mod experiment. In particular a helical reference at the edge is imposed on the controlled MHD mode, called *reference*, whose value is of the order of some mT.

The main aims of the campaign are three and are here listed. A synthesis of the obtained results is given for each aim.

1. Prove that a magnetic QSH state can be forced to an externally selected helicity in the RFX-mod experiment.
   This aim was achieved, as magnetic measurements and reconstructions indicate that the $(1, -6)$ Resistive Wall Mode properly controlled in amplitude, becomes the dominant mode giving its helical symmetry to the magnetic field. This effect was obtained controlling also other RWMs and tearing modes (if a QSH built upon a resonant mode is chosen).

2. Prove the existence of a threshold in the value of the helical reference over which the externally controlled mode is able to become the dominant one.
   This aim was achieved. It was found, as an example, that with a reference below $8\,\mathrm{mT}$ the $(1, -6)$ mode is not able to become the dominant one as the spontaneously dominant $(1, -7)$ mode remains the dominant one. Above that threshold the $(1, -7)$ mode vanishes, and only the externally imposed MHD mode dominates.

Table 10.1: Description of the main features of the three rounds of experiments performed in the framework of the experimental proposal #26. The quantity n_G, called Greenwald density, is a quantity used in the tokamak community as a reference value for density (for densities higher than n_G violent instabilities lead to plasma disruption). It is given by $n_G = I_P/(\pi a^2)$.

Run	Date	Plasma current I_P	F	controlled $m = 1$ MHD modes	density n/n_G
1	20 sept 2011	≈ 1.2 MA	-0.03	-6	≈ 0.10
2	28 oct 2011	≈ 1.5 MA	-0.03	-5, -6, -7, -8	≈ 0.10
3	13 nov 2012	≈ 1.2 MA	-0.03	-6, -7	≈ 0.15

3. Perform a thermal characterization of the discharges, to determine whether the QSH state built upon a non-resonant mode has better confinement properties. This research is still ongoing.

10.2 Description of the experiments and analysis of a selection discharges

The proposal #26 was developed in a set of three experimental runs, for a total of three days from September 2011 and November 2012. Table 10.1 shows the parameters that were kept fixed in all the discharges of a specific run.
In this section a subset of the performed discharges, chosen between the ones that show the achievement of the aims described in section 10.1, will be described.
The typical figure, figure 10.1, will show the temporal behaviour of some interesting physical quantities. On the first row the reversal and pinch parameters, F and Θ, will be shown. On the second row the behaviour of the toroidal component of the magnetic field at the edge, for the most significant MHD modes, will be shown. The second row shows the temporal behaviour of the electron temperature on the torus' axis, while the fourth row shows the temporal evolution of the density, normalized to the Greenwald density.
Figure 10.1 shows a typical RFX-mod discharge, during which no helical boundary conditions were employed. It is possible to notice that the $m = 1$, $n = -7$ mode emerges as dominant one, though with frequent back-transitions to a MH state. The maximum temperature reached in this kind of discharges is around 800 eV and the typical density is given by $n/n_G \approx 0.15$ that is $n \approx 2 \cdot 10^{19}$ m^{-3} for $I_P \approx 1.2$ MA.
Figures 10.2 and 10.3 respectively show the application of helical boundary conditions with intensity of 6 and 8 mT on the first non-resonant $(1, -6)$ MHD mode: the two figures show that both the first and second aim listed in section 10.1 are reached.
First aim. The possibility to build a QSH state upon the non-resonant MHD mode is

proved by the discharges in figure 10.3 and 10.4. In the latter a long time interval during which the $(1, -6)$ MHD mode is dominant can be observed. It can also be noted that the behaviour of the magnetic field is rather stationary, differently from what happens in the typical discharge with the $(1, -7)$ MHD mode (this is not foreseen by MHD simulations).

Second aim. The existence of a threshold for the establishment of an externally driven QSH is proven by figures 10.2 and 10.3. In the first figure (6 mT of MP) the excited mode is not able to become the dominant, while in the second (8 mT of MP) this happens. In particular in figure 10.2 the references are applied in the time interval $[100 : 150]$ ms and the non-resonant $(1, -6)$ mode is not able to overcome the dominant $(1, -7)$ one. On the contrary figure 10.3 shows an experiment performed with references of 8 mT applied to the $(1, -6)$ mode in the time interval $[0 : 120]$ ms: this reference induces an almost complete disappearance of the usually dominant $(1, -7)$ mode, that re-emerges at $t > 120$ ms when the references are stopped.

Figure 10.5 shows the effect of MPs on the spontaneous $(1, -7)$ MHD mode: the result is that the amplitude of the back-transitions is much reduced with respect to figure 10.1. Figure 10.6 instead show the effect of the external stimulation, towards the end of the discharge, of the $(1, -5)$ mode. The mode emerges weakly, probably because the stimulation happens in a phase of fast current decay.

10.3 Summary and remarks

The experimental campaign performed using the RFX-mod experiment confirmed the main results from the numerical studies explained in part III.

It was confirmed that the use of helical boundary conditions for the magnetic field helps reaching a state closer to a helical equilibrium, with helicity that can be chosen externally.

It was also confirmed the existence of a threshold, under which the helical boundary conditions are not able to influence the system.

The experimental confirmation of the numerical findings (see chapter 8) leads to propose a vision of the RFP as a customizable helical configuration. This configuration can be driven to an externally selected quasi-helical state, with dynamical properties similar to the ones observed in spontaneous QSH states.

The analysis of the thermal data from the experiments is still ongoing: at this point there is no clear indication that the confinement properties of a non-resonant QSH state are better than the QSH spontaneously found in the RFX-mod experiment. This is in partial agreement with the magnetic topology studies presented in chapter 9.

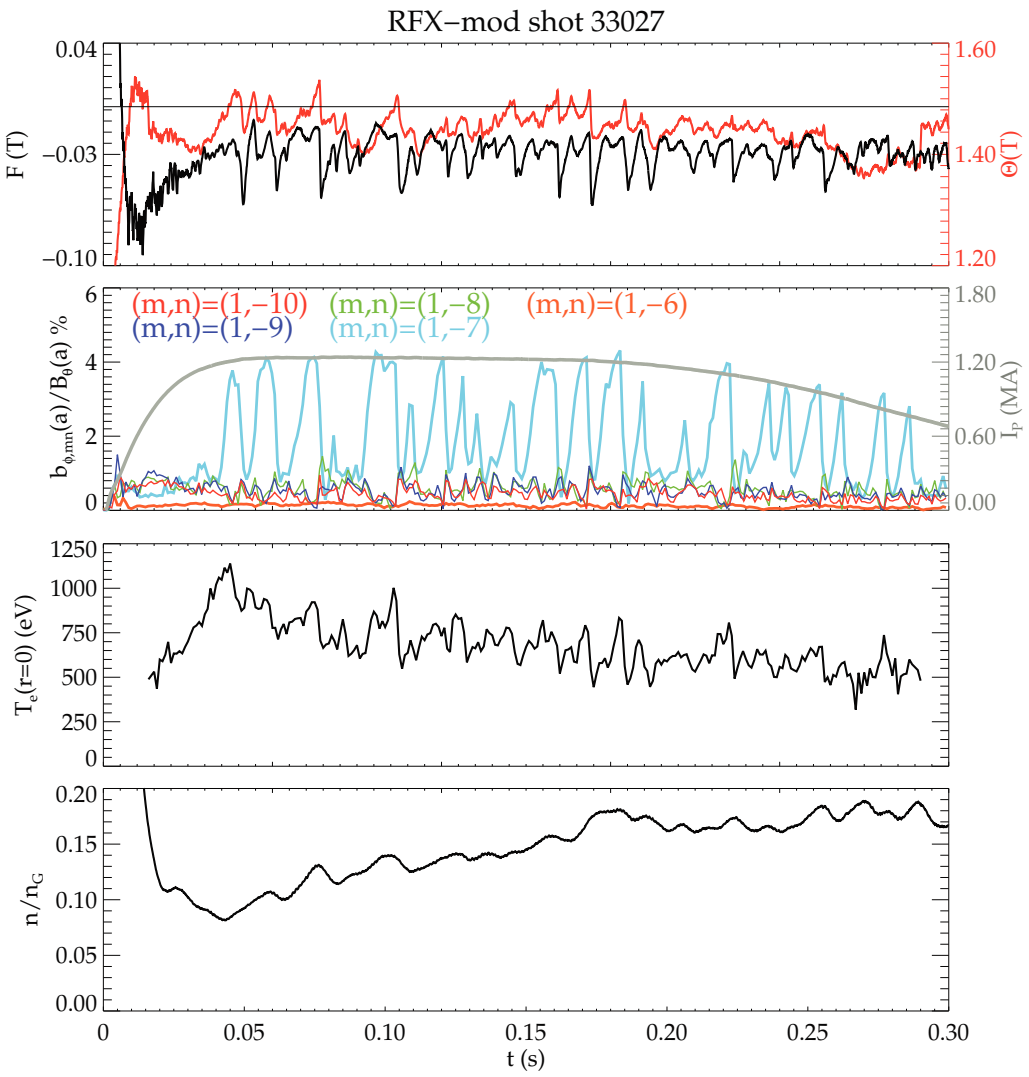

Figure 10.1: Temporal behaviour of some physical quantities for the RFX-mod shot number 33027, performed in the framework of experimental proposal #26, that represents a typical discharge at medium current. First row: temporal behaviour of the reversal parameter F and of the pinch parameter Θ. Second row: temporal behaviour of the plasma current I_P (right axis) and of the toroidal component of the magnetic field at the edge $b_{\phi,mn}(a)$, for the more important $m = 1$ MHD modes. The value is normalized to the poloidal field at the edge. Third row: temporal behaviour of the electronic temperature in axis T_e. Fourth row: temporal behaviour of the plasma density n, normalized to the Greenwald density n_G.

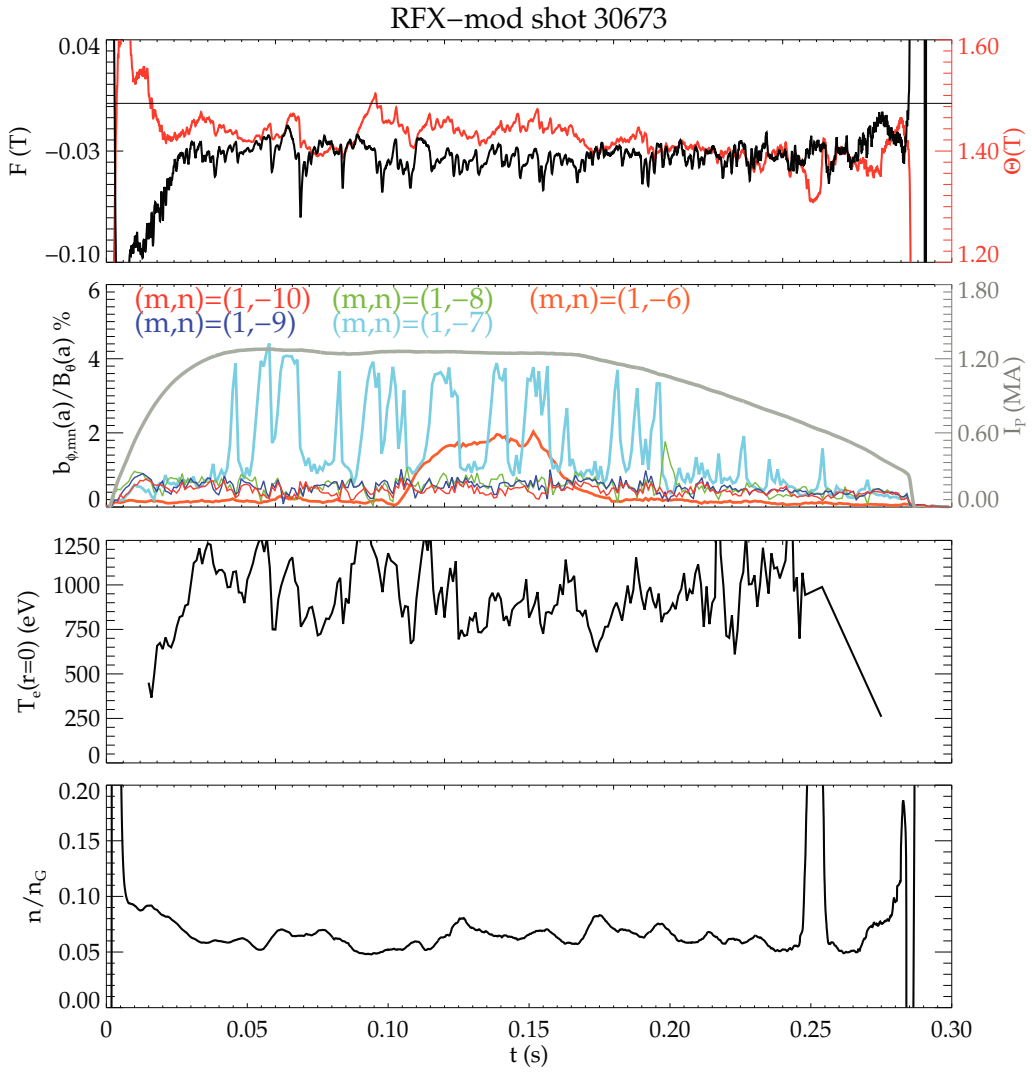

Figure 10.2: Temporal behaviour of some physical quantities for the RFX-mod shot number 30673, performed in the framework of experimental proposal #26. Physical quantities as in figure 10.1.

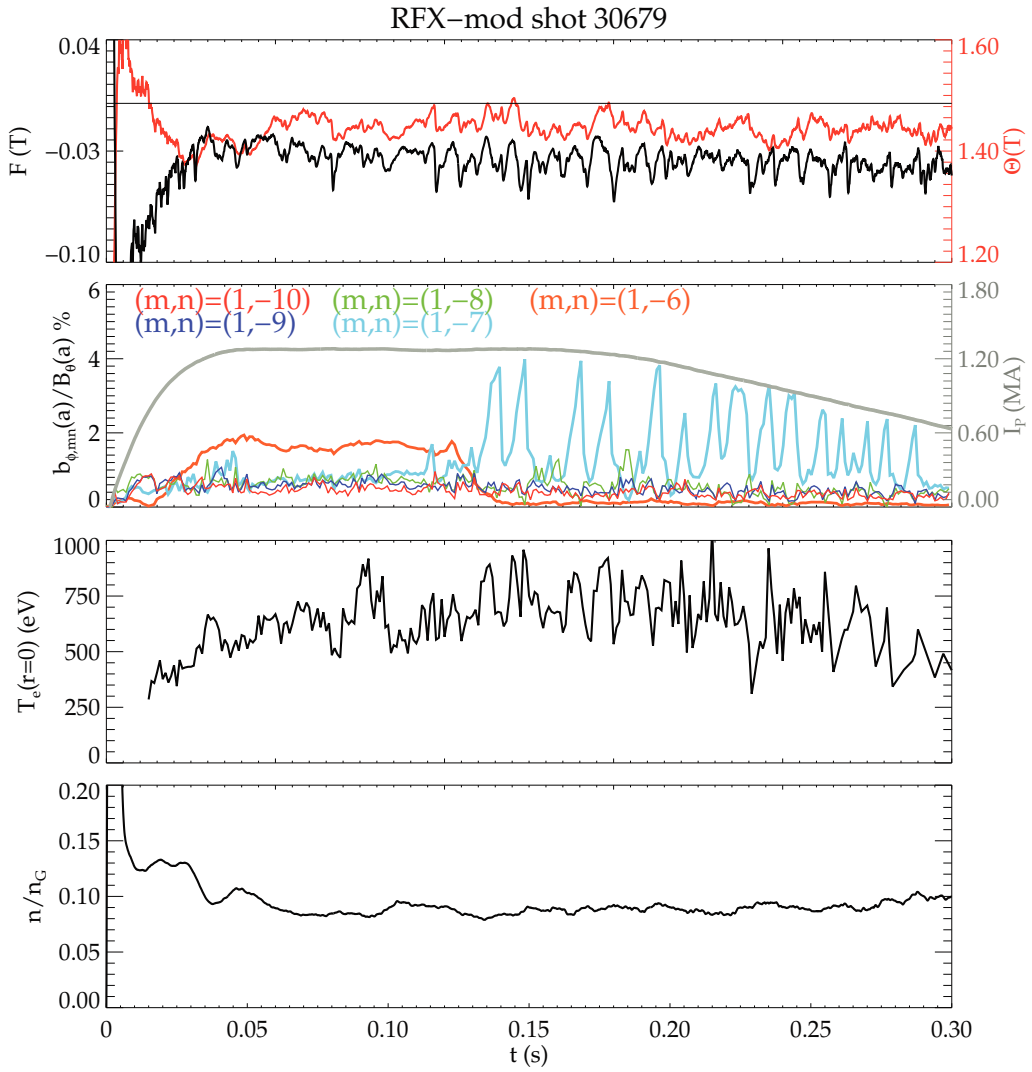

Figure 10.3: Temporal behaviour of some physical quantities for the RFX-mod shot number 30679, performed in the framework of experimental proposal #26. Physical quantities as in figure 10.1.

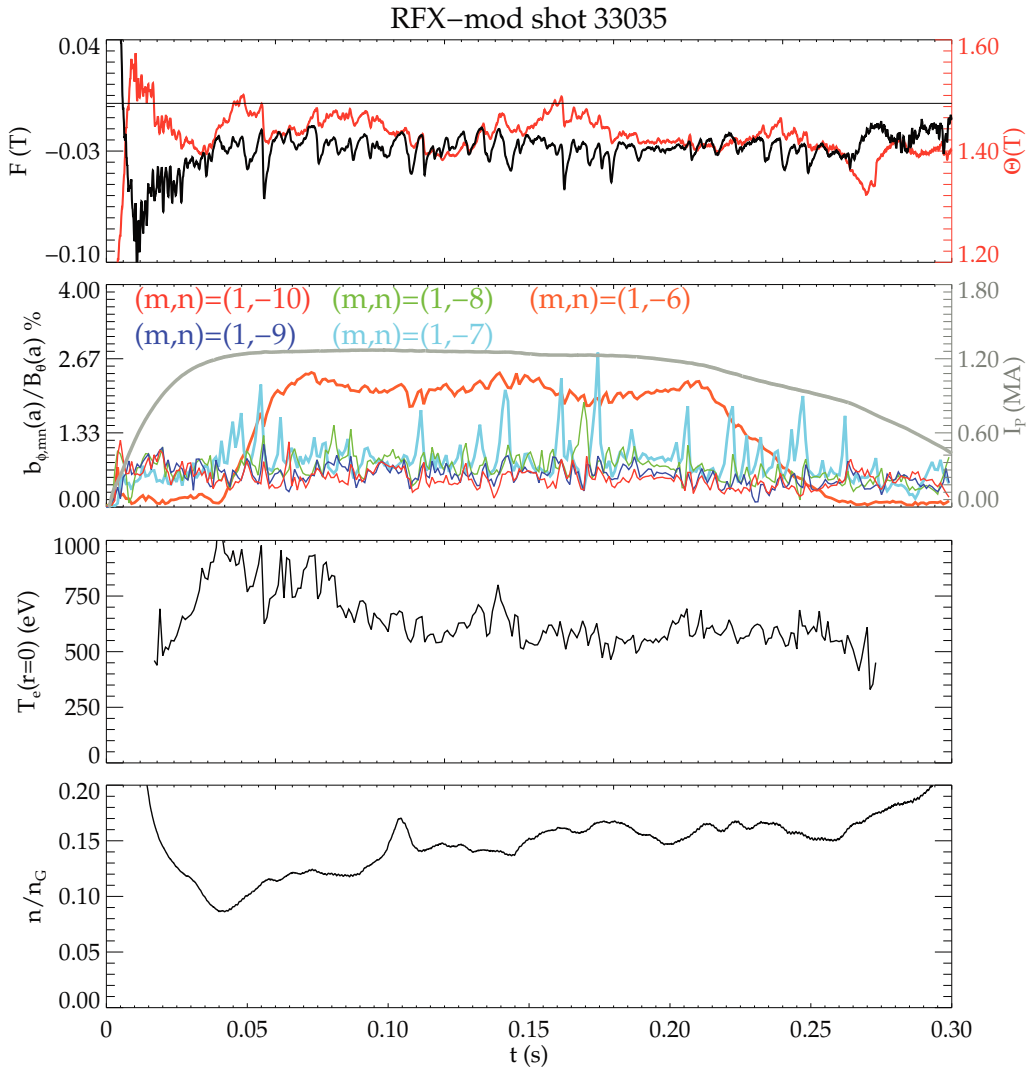

Figure 10.4: Temporal behaviour of some physical quantities for the RFX-mod shot number 33035, performed in the framework of experimental proposal #26. Physical quantities as in figure 10.1.

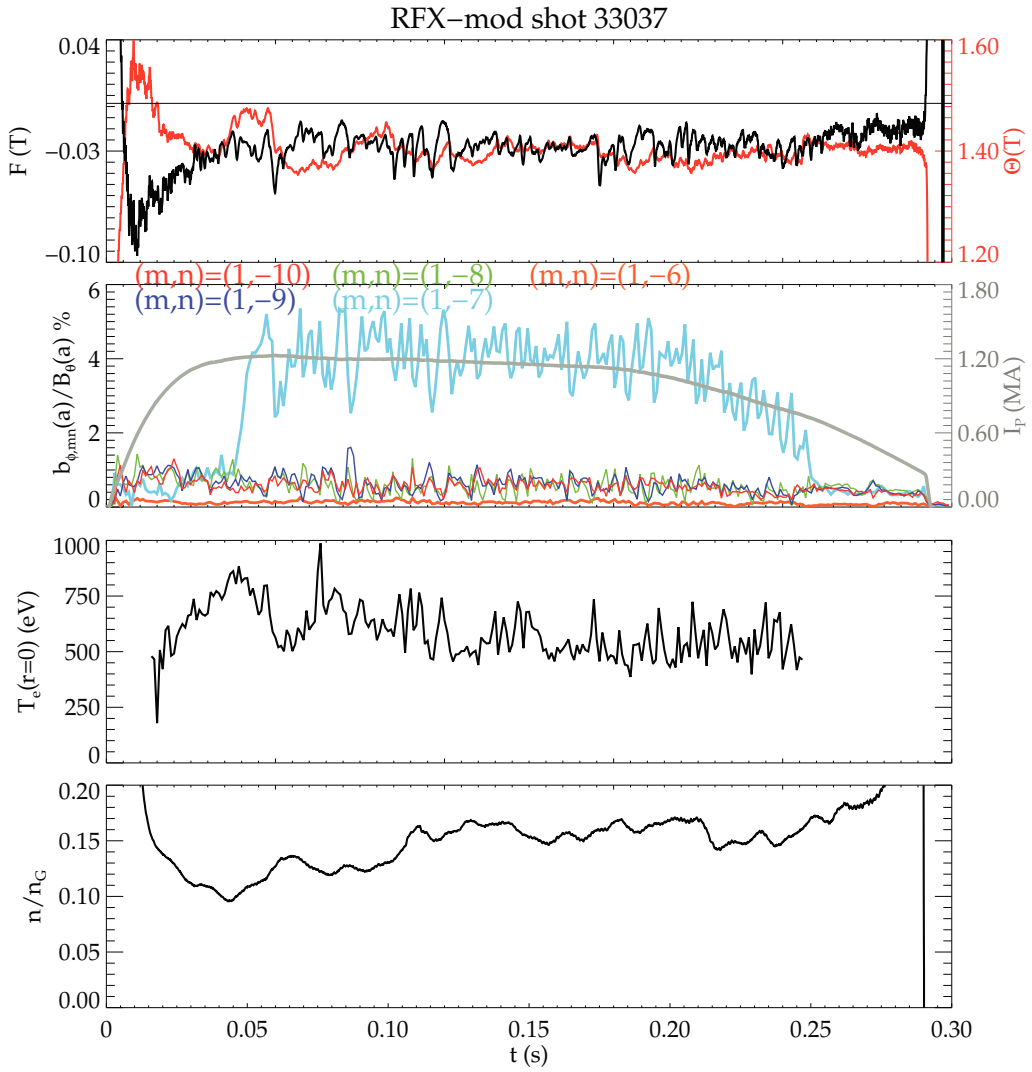

Figure 10.5: Temporal behaviour of some physical quantities for the RFX-mod shot number 33037, performed in the framework of experimental proposal #26. Physical quantities as in figure 10.1.

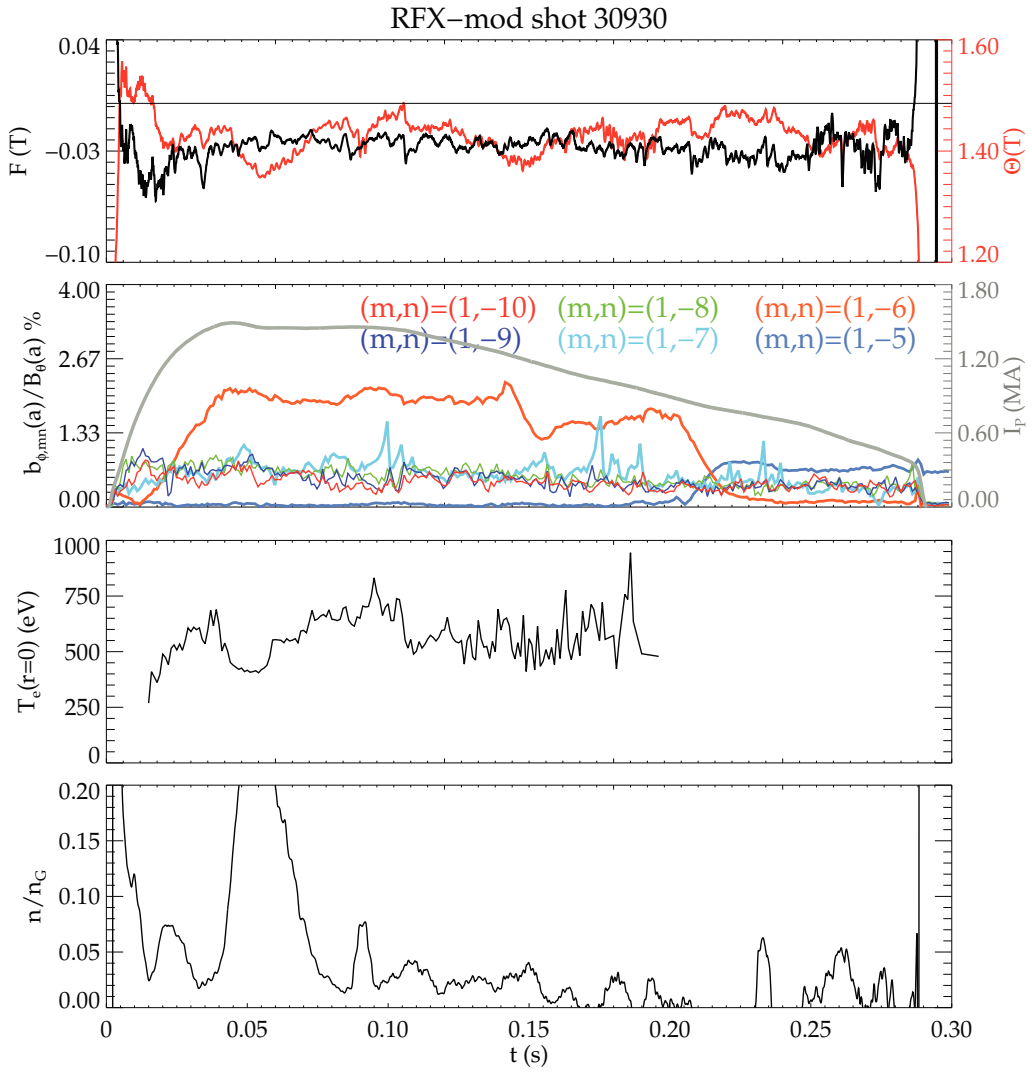

Figure 10.6: Temporal behaviour of some physical quantities for the RFX-mod shot number 30930, where the $(1, -5)$ mode was stimulated at the end of the discharge. Physical quantities as in figure 10.1.

11

Tools for transport studies of RFP and tokamak experiments

The work presented in this chapter aims at describing two applications of the tools developed for estimating the level of transport induced by the presence of a stochastic magnetic field. The tools developed to tackle stochastic-induced transport were created and used to quantitatively analyze energy transport related to magnetic field stochasticity in two experimental relevant cases regarding both the RFP and the tokamak configurations. The tools under analysis estimate the magnetic diffusion coefficient D_m for the lines of a stochastic, stationary magnetic field. The value of the diffusion coefficient is then involved in the estimate of other plasma related quantities, i.e. heat conductivity. The calculation relies on numerical integration of field lines trajectories by the field-line-tracing code NEMATO, described in chapter 5.

The first analysis presented is performed on the RFP. It deals with the study of a magnetic field whose stochasticity is caused by the presence of a wide spectrum of microtearing perturbations [Hazeltine et al., 1975; Drake et al., 1980] acting at the internal electron transport barrier observed in the RFX-mod experiment. The microtearing instabilities in the RFP were studied through the GS2 code [Kotschenreuther et al., 1995; Dorland et al., 2000] using data from experimental discharges. The main result is that the energy transport coefficient observed at the barrier is compatible with the one calculated with the tools described in this chapter. This shows that microtearing perturbation can be the responsible for the saturation of the steepness of the internal transport barrier measured in the RFX-mod experiment. The results are published in [Predebon et al., 2010; Sattin et al., 2010].

The second analysis, performed on the tokamak configuration, is the calculation of the magnetic diffusion coefficient at the edge of a tokamak plasma whose stochasticity is caused by the presence of 3D edge magnetic fields (coming both from magnetic field

errors or deliberately applied through coils). In this case the magnetic field evolution comes from the 3D MHD code PIXIE3D, described in chapter 4. The main result obtained using the tools to calculate the magnetic diffusion coefficient is that the features of plasma rotation observed in the RFX-mod experiment, used as a tokamak, can be explained by the presence of stochasticity at the plasma edge.

Outline of the chapter. The chapter is divided in four sections. The first section 11.1 is an introduction to the theoretical study of test particles transport in a stochastic magnetic field. The most important parameters that describe different transport regimes will be defined. The second section 11.2 deals with the effect of microtearing modes in the RFP configuration. The computation of the energy diffusion coefficient due to the stochastization of the magnetic field by microtearing modes is performed. The recovered value is comparable with experimental measurements, see [Predebon et al., 2010; Sattin et al., 2010]. The third part, section 11.3, deals with the study of 3D edge field in the tokamak configuration. The computation of the magnetic diffusion coefficient of the field lines of the magnetic field, that is stochastic at the edge, is used for estimating plasma rotation for different values of applied 3D edge perturbations.

A summary and remarks section can be found in 11.4.

11.1 Heat transport in a stochastic magnetic field

The problem of energy transport in the presence of a static and everywhere stochastic magnetic field is addressed considering average transport characteristics, in particular diffusion coefficients. Magnetic stochasticity leads to a random walk of magnetic field lines and to the separation of two initially close field lines (whose distance grows exponentially), two phenomena that highly influence energy transport in a plasma.

The estimation of the main diffusion coefficient, the electron thermal conductivity χ_r, is done considering the diffusion of *test particles* that follow the magnetic field lines. These particles can not be directly associable to charged particles like electrons, whose free diffusion is limited by the quasi-neutrality constraint. Instead they can be associated to thermal energy, that isn't restrained by quasi-neutrality [Isichenko, 1990]. The description of electron thermal conductivity in a stochastic field is made defining the magnetic diffusion coefficient D_m [Rosenbluth et al., 1966; Rechester and Rosenbluth, 1978; Krommes et al., 1983].

11.1.1 Definition of the magnetic field lines diffusion coefficient

The stochastic diffusion coefficient D_m in an unlimited stochastic domain is defined as:

$$D_m = \lim_{L\to\infty} F(r_0, L) \equiv \lim_{L\to\infty} \frac{1}{2}\frac{\mathrm{d}\langle (r-r_0)^2\rangle}{\mathrm{d}L} = \lim_{L\to\infty} \int_0^L \mathrm{d}L C(L) \tag{11.1}$$

with $C(L)$ the auto-correlation function and $F(L)$ the correlation function of field lines. The definition of $C(L)$ results easily from the magnetic field lines equation assuming translational independence (natural in a unlimited stochastic domain):

$$C(L) = \langle \tilde{b}_r(L)\tilde{b}_r(0)\rangle, \tag{11.2}$$

with $\tilde{b}_r$ indicate the perturbations to the magnetic field normalized to the equilibrium value of the field. In equation (11.1) r represents a radial direction, perpendicular to the equilibrium magnetic field flux surfaces, L represents the magnetic field line's arclength. The quadratic mean square displacement $\langle (r-r_0)^2\rangle$ has been introduced, which corresponds to a random walk of the field lines on a plane perpendicular to the path L along the field line. The quantity r_0 represents the initial radial position of the field lines. The average has to be intended as a spatial average over many iterates on the same plane.
The auto-correlation length L_{ac} can be defined as [Krommes et al., 1983]:

$$L_{ac} = F(r_0, \infty) = \int_0^\infty dL C(L), \tag{11.3}$$

and can be connected to a measurement of the spectral width of the magnetic field in the direction parallel to the flux surfaces of the equilibrium field. One important remark: all these definitions are based on the assumption that the perturbations to the magnetic field are not affected by the test-particles motion, defining the so-called *generalized stochastic acceleration problem*.
Let us consider again equation (11.1). We will show that it resembles a *random-walk* diffusion formula:

$$D_m = \lim_{L\to\infty} \frac{1}{2}\frac{d}{dL}\left\langle (\Delta r(L))^2 \right\rangle. \tag{11.4}$$

with $\left\langle (\Delta r(L))^2 \right\rangle$ representing the mean square of the radial displacement of the field line with respect to its initial radial position.
Consider a set of field lines taking random step of infinitesimal average magnitude Δr in radial direction; the average arc-length travelled between two successive steps is given by ΔL. After N steps the mean square distance from the starting point is $\left\langle (\Delta r(L))^2 \right\rangle = N \left\langle (\Delta R))^2 \right\rangle$ and the covered arc-length is given by $L = N\Delta L$. The

quantity $\left\langle (\Delta R))^2 \right\rangle$ represents the average squared distance performed in each step. The following definition can be adopted:

$$\left\langle (\Delta r(L))^2 \right\rangle = \frac{(\Delta R)^2 L}{\Delta L} \equiv 2D_m L, \tag{11.5}$$

obtaining a corresponding diffusion coefficient (of magnetic field lines) given by equation 11.4. The definitions given above are valid in a unlimited stochastic domain.
The definition of D_m fails in a bounded domain where $\lim_{L\to\infty} F(r_0, L) = 0$. In fact the function F takes its maximum value close to $L = 0$, vanishes for $L = L_w$ and then oscillates around zero, without reaching a diffusion regime. The length L_w is the parallel length a field line traverses to reach the boundary of the chaotic domain and then being bounced back to the center. In this process, the auto-correlation function $C(L)$ experiences a large domain of negative values, where the field trajectories are anti-correlated to one other. This means that the probability of a radial jump having an opposite sign with respect to the preceding one is larger than that of retaining the same sign. This is the definition of a *subdiffusive regime* [Sanchez et al., 2009].
When the system is subdiffusive one can rely on an approximate definition of the quadratic mean square displacement, as follows [D'Angelo and Paccagnella, 1996]

$$\langle (r - r_0)^2 \rangle \approx 2 \int_0^{L_w} d\tilde{L} F(r, \tilde{L}) = 2F(L_*)L_w \tag{11.6}$$

where $L_* \in [0, L_w]$. A reasonable definition for the diffusion coefficient is

$$D_m = \frac{\langle (r - r_0)^2 \rangle}{2L_w} = \frac{2F(L_*)L_w}{2L_w} = F(L_*) \tag{11.7}$$

where L_w is determined by the first zero of F and $L_* = L_{ac}$ by definition.

11.1.2 Parameters used to describe a stochastic magnetic field

Many different regimes can be defined characterized by different features of the radial particle diffusion in a specified static magnetic field. Four parameters, each of them characterizing some specific aspect of a stochastic magnetic field, must be defined. Without entering into the details of the definitions, which can be found in [Krommes et al., 1983], they will be simply described.
A set of spatial parameters is given by the quantity L_{ac}, auto-correlation length of the magnetic field lines (11.3), and by L_K, Kolmogorov length. The Kolmogorov length L_K describes the spatial scale of the exponential divergence of two initially close field lines in a stochastic field. A third spatial parameter is given by the mean free path

$\lambda_\nu = v_{th}/\nu$, which describes the collisionality of the system, v_{th} being the thermal velocity of the test-particles.
A temporal parameter related to the previous ones describing diffusion in a stochastic field is the correlation time τ_c, which describes the temporal scale after which a test particle can be considered decorrelated from its initial magnetic field line: a typical decorrelation mechanism is collisional diffusion. It is possible to give different estimation of τ_c depending on the scale length over which a particle can be considered decorrelated from its initial magnetic field line: possible choices are the Kolmogorov length or a length that describes the spectral width of the perturbed magnetic field in the perpendicular direction.
In the determination of the different regimes it is important the quantity $\alpha = 1/(\nu\tau_c)$, that describes the ratio between correlation and collision times. ν represent the collision frequency.
At least six different regimes can be individuated, characterized by different global values of the radial particle dispersion coefficient, which indirectly measures the test-particles thermal conductivity. These six regimes are listed in table 1 of [Krommes et al., 1983]. In the following a *collisionless* regime is selected, defined by the following inequalities between the main parameters:

$$\begin{aligned} \lambda_\nu &\gg L_{ac}, L_K, \\ \nu\tau_c &< 1, \\ \tau_c &> L_{ac}/v_{th}. \end{aligned}$$

11.1.3 The electron thermal conductivity

In terms of the magnetic diffusion coefficient D_m the electron thermal conductivity χ_r can be defined as:

$$\chi_r \equiv \frac{1}{2}\frac{d}{dL}\left\langle (\Delta r(L))^2 \right\rangle = \frac{1}{2}\frac{d}{dL}\left\langle (\Delta r(L))^2 \right\rangle \frac{dL}{dt} = D_m \frac{dL}{dt} = D_m v_{th}, \tag{11.8}$$

where v_{th} is the test particle thermal velocity (considered as an electron).
A fundamental description of the magnetic diffusion coefficient can be given considering the so-called quasi-linear limit: this limit corresponds to the case where the response of the system to a perturbation is computed as a set of independent modes, neglecting interactions between modes. At a first stage this limit is satisfied when the quantity $\langle b^2 \rangle$ describing perturbation's intensity ($b = \delta B/B$) is not too big; in other terms the quasi-linear limit can be defined as $L_{ac} \ll L_K$, describing a situation where magnetic field lines get separated in a spatial scale longer than their autocorrelation length, defining this way not too big a perturbation.

In this limit the magnetic diffusion coefficient is found to be:

$$D_m \approx b^2 L_{ac}, \tag{11.9}$$

and L_{ac} results independent from b.

11.2 Microtearing modes at the ITB of RFP plasmas

The formation of Internal Transport Barriers (ITBs) at the edge of the high temperature core in SHAx states, discovered in RFX-mod experiments [Lorenzini et al., 2009], leads to the formation of high temperature gradients, which can supply the free energy triggering microinstabilities, enhancing energy transport.
Numerical studies by means of the gyrokinetics code GS2 [Kotschenreuther et al., 1995], based on the electromagnetic nonlinear gyrokinetics equation, have been carried out to find out information about the instabilities acting in the ITBs regions, using as input data profiles (for example the electron temperature one) coming from RFX-mod experimental measurements.
These numerical investigations show that the dominant instabilities in the RFX-mod ITBs region are of microtearing kind [Hazeltine et al., 1975]. The microtearing mode (MT) is a high-wavenumber tearing mode, driven instable by electron temperature gradients, making it different from the macroscopic tearing mode (driven instable by current density gradients, see section 3.6.2). However MT mode can result in small scale magnetic islands, making it similar to its macroscopic counterpart. The result of the GS2 code indicate that in the typical experimental condition MTs are unstable over a large range of wavenumbers, their growth rate raising as the temperature gradients' characteristic length L_{Te} (proportional to the electron temperature profile's slope) and plasma β (ratio between kinetic and magnetic pressure) increases. The results show as well that in the experimental conditions different wavenumber MT perturbations forms chains of overlapping magnetic island, giving in such a way an important contribution to the stochastization of magnetic field lines in the region of ITBs, which is a necessary condition to obtain a significant energy transport caused by MT instabilities.

11.2.1 Modellization of the magnetic field

The magnetic field $\mathbf{B}(r)$ has been modelled as a sum of a macroscopic axisymmetric equilibrium magnetic field $\mathbf{B}_0(r)$ and of a perturbation part $\mathbf{b}(\mathbf{r})$. The first is modelled to copy the equilibrium field reconstructed from the data measured during discharge 23977 performed at the RFX-mod experiment (the corresponding temperature profile at $t = 64\,\text{ms}$ is plotted in figure 11.1). The perturbations are obtained using GS2's

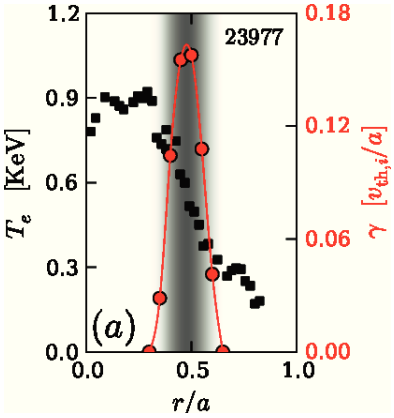

Figure 11.1: Electron temperature profiles (square symbols) for shot 23977 at $t = 64$ ms, with the growth rate of the most unstable MT mode.

results coming from the study of MT perturbations stability in the region of electron temperature gradient.

$$\mathbf{B}(\mathbf{r}) = \mathbf{B}_0(r) + \mathbf{b}(\mathbf{r}). \tag{11.10}$$

Macroscopic equilibrium

The principal aim in the description of the macroscopic equilibrium magnetic field $\mathbf{B}_0$ was that of obtaining a field whose safety factor is equal to the one used in GS2, in particular in the region where MT perturbations act.
Plasma will be described using a cylindrical coordinate system. The equilibrium magnetic field components have been calculated in cylindrical geometry and symmetry (all physical quantities depending only on r), solving the magnetostatic ideal MHD equilibrium equations; these equations are obtained from the visco-resistive MHD model neglecting viscosity and resistivity, assuming a stationary ($\frac{\partial}{\partial t} = 0$) and static ($\mathbf{v} = 0$) plasma. A further assumption is that the equilibrium is force-free, neglecting kinetic pressure with respect to the magnetic one ($p \ll B^2/2\mu_0$). Under these assumptions the MHD equations reduce to one equation:

$$\nabla \times \mathbf{B}_0(r) = \sigma(r)\mathbf{B}_0(r), \tag{11.11}$$

whose analytical solution is given in term of Bessel functions of the first kind:

$$B_{0r}(r) = 0, \quad B_{0\theta}(r) = J_1(\sigma r), \quad B_{0z}(r) = J_0(\sigma r), \qquad \sigma(r) = 2.775. \tag{11.12}$$

In figure 11.2 the radial profiles of the equilibrium field's components are shown, together with the safety factor. The radial domain where MT perturbations act (and

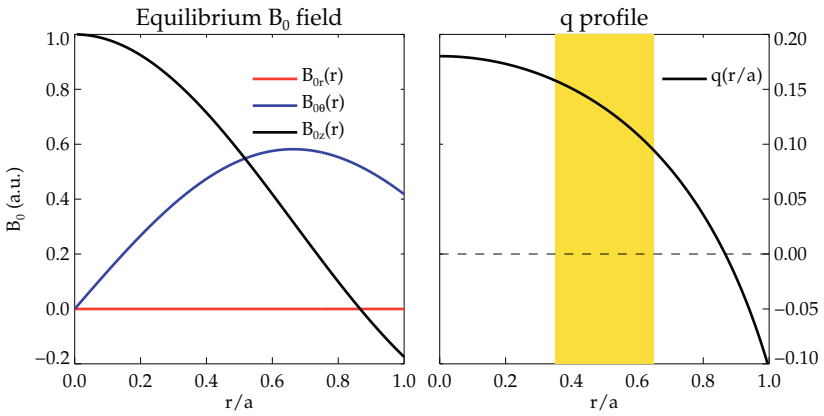

Figure 11.2: Equilibrium magnetic field's components and safety factor.

where $q(r)$ is equal to GS2's one) is underlined in yellow.

Perturbed magnetic field

The main information about magnetic field perturbations from the gyrokinetics code GS2 are of spectral type. Thus the fluctuations have been written as:

$$\mathbf{b}(\mathbf{r}) = \sum_{mn} \mathbf{b}_{mn}(r) \exp i(m\theta - nz/R_0)). \tag{11.13}$$

GS2 provided one important information about the poloidal wavenumber m which has the higher amplitude as a function of the radius. Another important information is the cumulated amplitude of the perturbations as a function of the radius. An estimation of the amplitude of magnetic field perturbation can be obtained from Drake [Drake et al., 1980]:

$$b \approx \frac{\rho_e}{L_{Te}}, \tag{11.14}$$

where ρ_e represents the electron Larmor radius and L_{Te} is the electron temperature gradient characteristic length.
These information are summarized in figure 11.3 and have been used to obtain the intensity of the different MT modes. The problem of finding a functional dependence for the three autofunctions that describe the components of the perturbed field was addressed imposing the condition:

$$\nabla \cdot \mathbf{b}_{mn}(\mathbf{r}) = 0. \tag{11.15}$$

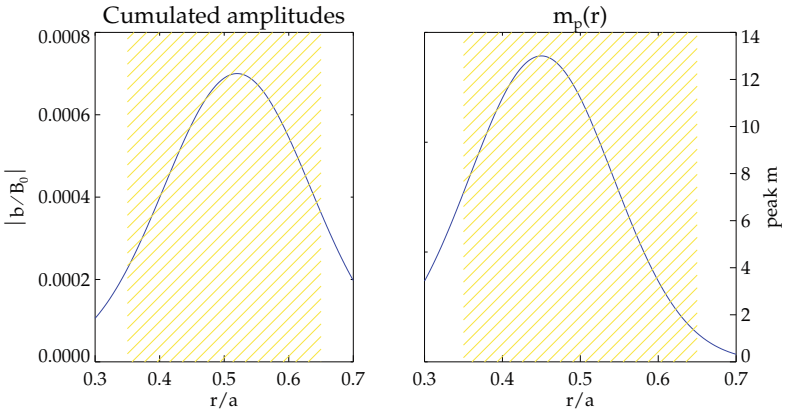

Figure 11.3: *Left:* Cumulated amplitude of magnetic fluctuations as a function of the radius. *Right:* Peak poloidal wave number m_p as a function of the radius: the corresponding axial wavenumber is obtained from the safety-factor profile in figure 11.2. The radial domain under analysis is shaded in yellow.

This condition allows the perturbed magnetic field, formed as a sum of a finite set of perturbations, to be solenoidal:

$$\nabla \cdot \mathbf{b}(\mathbf{r}) = \sum_{mn} \nabla \cdot \mathbf{b}_{mn}(\mathbf{r}) = 0. \tag{11.16}$$

The radial autofunction has thus been modelized as a Gaussian, centred at the resonance radius of the (m, n) mode, whose FWHM was imposed by data coming from GS2. The other two components were obtained imposing the solenoidality constraint, obtaining the functional forms for the autofunctions here shown:

$$b_r^{mn}(r) = A(r_{mn}, m) \cdot \exp\left[-\left(\frac{r - r_{mn}}{\alpha}\right)^2\right], \tag{11.17a}$$

$$b_\theta^{mn}(r) = A(r_{mn}, m) \cdot \exp\left[-\left(\frac{r - r_{mn}}{\alpha}\right)^2\right] \cdot \left(\frac{m}{H(r)}Q(r) - \frac{n\epsilon(r)\sigma r}{H(r)}\right), \tag{11.17b}$$

$$b_z^{mn}(r) = -A(r_{mn}, m) \cdot \exp\left[-\left(\frac{r - r_{mn}}{\alpha}\right)^2\right] \cdot \left(\frac{n\epsilon(r)}{H(r)}Q(r) + \frac{m\sigma r}{H(r)}\right). \tag{11.17c}$$

where:

$$A(r_{mn}, r) = 7 \cdot 10^{-5} \exp\left[-\left(\frac{r_{mn} - 0.52^2}{0.16}\right)\right] \cdot D(m), \tag{11.18a}$$

$$D(m) = \exp\left(-\frac{m - m_p}{\gamma^2}\right), \quad \gamma = 10, \tag{11.18b}$$

$$H(r) = m^2 + n^2 \frac{r^2}{R_0^2}, \tag{11.18c}$$

$$Q(r) = 1 - \frac{2r(r - r_{mn})}{\alpha^2}, \tag{11.18d}$$

$$\alpha = 0.012. \tag{11.18e}$$

Here r_{mn} represent the resonance radius of the (m, n) mode, obtained from the condition $m - nq(r_{mn}) = 0$, α is proportional to the FWHM of the Gaussian which describes the radial component of the perturbed field. The quantity $A(r_{mn}, m)$ represents the amplitude of the perturbed mode resonant at radius $r = r_{mn}$ and contains a factor $D(m)$ dependent on the poloidal wave number. In figure 11.4 the radial profiles of the three components are plotted for the mode $(m, n) = (13, 91)$, one of those with the higher intensity.
The constant $7 \cdot 10^{-5}$ in equation 11.18a has been chosen so that the superposition of a large number of modes determined by the GS2 results gave a cumulated effect equal to the saturated level of magnetic field perturbations provided by figure 11.3. The determination of the energy transport coefficient with respect to the variation of the perturbed magnetic field intensity has been studied considering values of the parameter ranging from the half to the decuple of the written one.
The property $\nabla \cdot \mathbf{b}(\mathbf{r}) = 0$ is verified using the autofunctions written in 11.17. In figure 11.5 the modes' amplitude is shown as function of (m, n).

Parameters which can be varied

It is possible to vary:

- the radial range where the perturbed modes resonates ($r \in [0.35 : 0.65]$ was chosen);
- their poloidal wave number range ($m \in [5 : 20]$ was chosen);
- the perturbed modes' intensity, by controlling the $A(r_{mn}, m)$ quantity;
- the parameter $D(m)$ that controls the modes' amplitude as their poloidal wave number goes farther from the peak one.

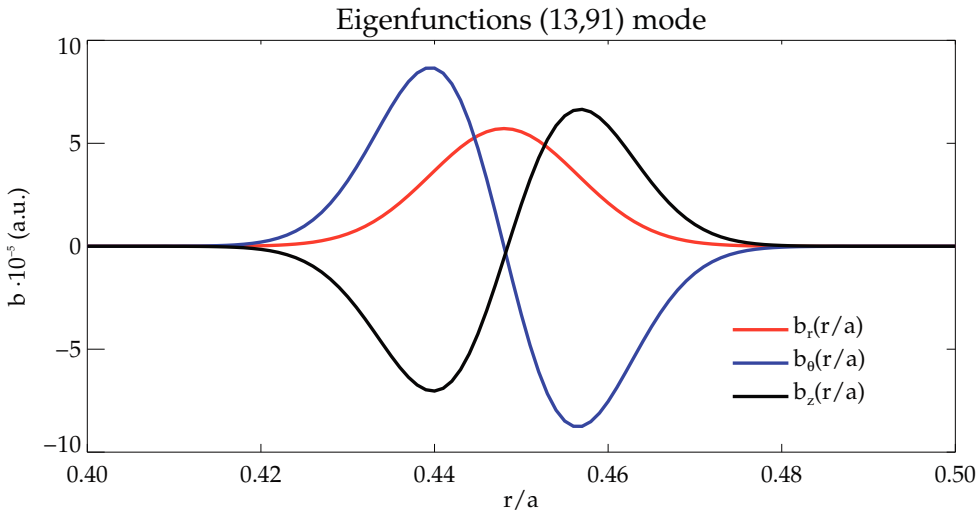

Figure 11.4: Radial profiles of the perturbed magnetic field eigenfunctions for the (13,91) microtearing mode.

11.2.2 NEMATO simulations

NEMATO (see chapter 5) has been slightly modified to accept as input the analytically magnetic field described in section 11.2.1 and to give as output the radial position of the calculated field lines at regular arc-length intervals. The code calculates the field on a mesh formed of 102 points in radial direction and 256 x 2048 points in the poloidal and axial directions, in order to have a sufficient resolution to describe the high angular periodicity MT modes. The integration scheme adopted is the solenoidal one. For each selected perturbations' intensity three different NEMATO simulations have been carried out: the first one determines the Poincarè plot of the system on a poloidal surface of section, usually placed at $\theta = 0$. The second one consists on the calculation of the spatial behaviour of 2500 magnetic field lines, whose initial points lie on a $r = cost$ surface and whose radial position was studied for an arc-length such that every line could explore in its stochastic wandering the whole region characterized by the presence of microtearing perturbations. From this simulation's data the estimation of the magnetic field lines diffusion coefficient was obtained. The third simulation consists on the calculation of the same 2500 field lines with a tighter sampling for a shorter arc-length; from this simulation the estimation of the auto-correlation length was obtained.

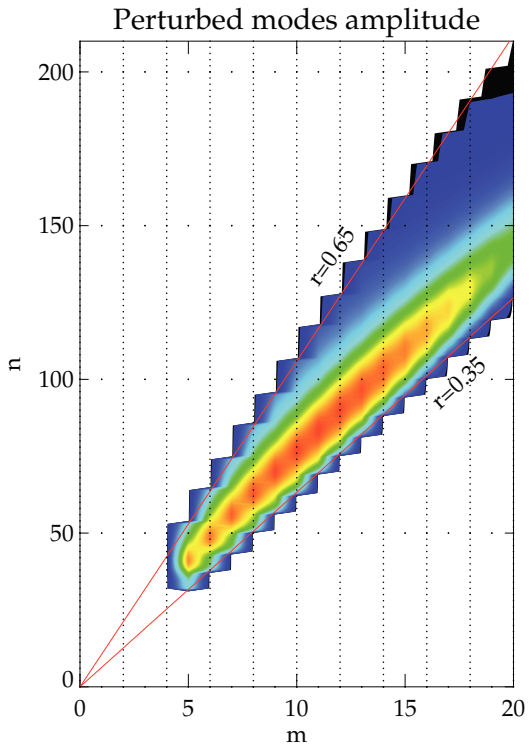

Figure 11.5: Contour plot of the microtearing modes amplitude. Amplitude is decreasing from red to blue. A total number of ≈ 850 modes has been considered in the Fourier sum defining the perturbed magnetic field.

11.2.3 Results: energy transport coefficient at the RFP internal transport barrier

The steps undertaken to obtain the estimation of the magnetic diffusion coefficient D_m and of the auto-correlation length L_{ac} will be described. A reference case will be considered, in which the perturbations' intensity is three times the previously written ones (see equation (11.18a)). NEMATO's simulations results will be related to RFX-mod experiment by choosing the radial length normalization factor a equal to the experimental minor radius, $a = 0.459m$. As first step the Poincarè plot of the magnetic field lines is obtained by a NEMATO simulation, studying the intersection of 50 field lines with a $\theta = \pi$ surface. The result is shown in figure 11.6. The stochasticity of the magnetic field is evident, though not fully developed. Some conserved magnetic surfaces are present. In the region where MT aren't active perfectly conserved magnetic surfaces are present. As a second step another NEMATO simulation is carried out to calculate the radial square displacement of the magnetic field lines and, from its dependence on their arc-length, to estimate the magnetic diffusion coefficient, see equation (11.4). 2500 field lines, whose initial points are chosen randomly at the $r = 0.52$ surface (indicated

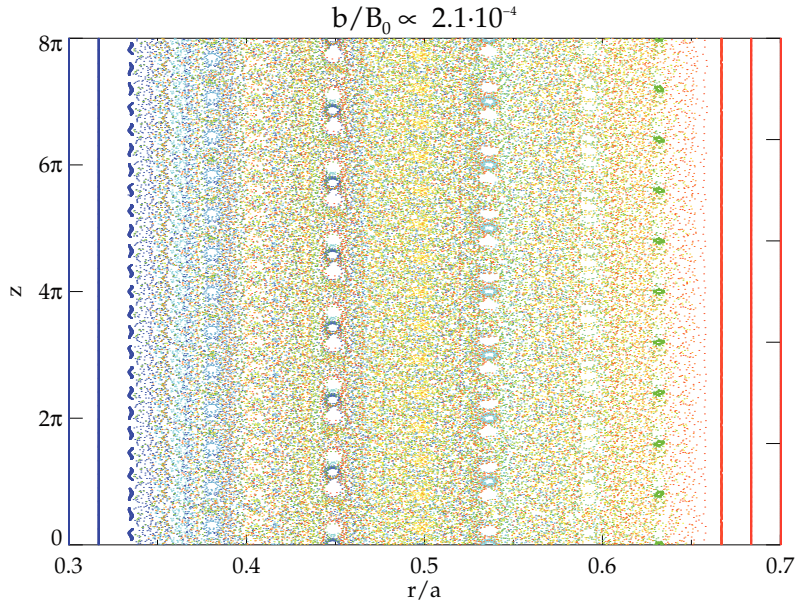

Figure 11.6: Poincarè plot, in a $\theta = \pi$ surface, of the magnetic field lines.

by red points on figure 11.6) have been calculated.
Figure 11.7a shows the complete behaviour of the $\langle(\Delta r)^2 a^2\rangle$ quantity up to an arc-length $L = 5000a$; a saturation effect can be seen because of the presence of a limited stochastic domain. Figure 11.7b shows the same behaviour in the first part of the diffusional walk, up to an arc-length $L = 200a$, from which the D_m estimation will be extracted. The third step consist on a shorter NEMATO simulation of the same 2500 field lines. From the data obtained, sampled in a tighter way than in the precedent simulation, the calculation of the auto-correlation function $C(L)$ and of its integral has been performed. In figure 11.8 the two quantities are plotted.

To confirm the forecasts of the quasi-linear limit, that predicts a linear scaling of D_m with the square of the perturbations' intensity and the constancy of L_{ac} eight different perturbations' amplitudes have been considered. The results are shown in table 11.1. The behaviours foreseen by the quasi-linear estimate were partially verified, as it was found:

$$D_m \propto b^{2 \cdot 0.67}, \tag{11.19}$$

and L_{ac} slightly decreasing with perturbations' intensity, obtaining:

$$L_{ac} \approx 2\,\mathrm{m}. \tag{11.20}$$

In figure 11.9 the calculated data are plotted. The reference case is pointed out using

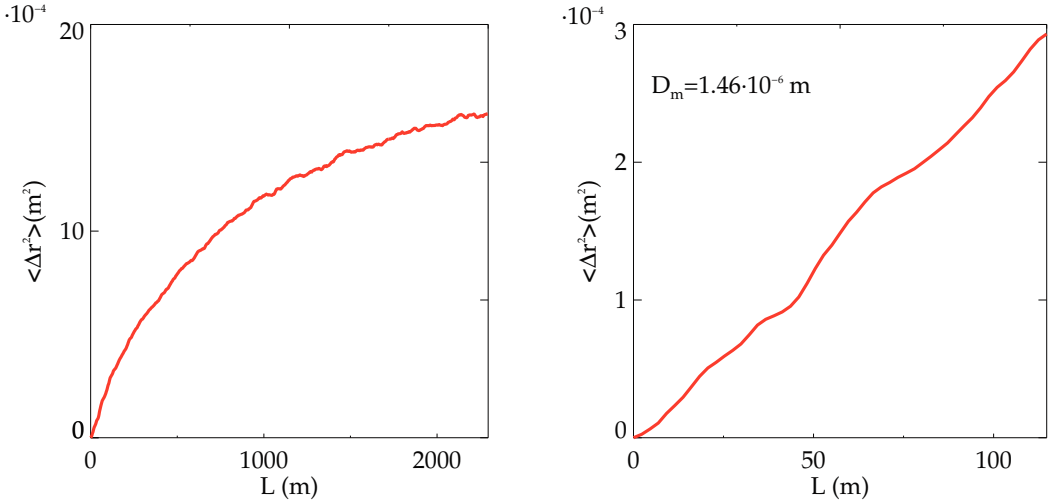

(a) Only the first part of the field lines' random walk will be used to calculate D_m, due to domain's boundary effects.

(b) The value of the magnetic diffusion coefficient was calculated as the line's slope divided by two.

Figure 11.7

Table 11.1: Magnetic diffusion coefficient and auto-correlation length for different values of magnetic perturbations

$\frac{b}{B_0} \cdot 10^{-4}$	$D_m \cdot 10^{-8}$ (m)	L_{ac} (m)
0.35	3.16	1.77
0.70	21.42	3.14
1.40	43.25	3.13
2.10	145.55	2.36
2.80	231.62	1.55
4.20	401.86	2.19
5.60	508.61	0.85
7.00	883.93	0.80

blue points, the one analyzed here with green ones and the other six considered cases are pointed by red dots.

Using the obtained value for the magnetic diffusion coefficient D_m and considering a thermal electron velocity of $v_{th,e} = 1.5 \cdot 10^7\,\mathrm{ms}^{-1}$ ($T_e \sim 1\,\mathrm{keV}$) the result is:

$$\chi_r \approx 5 : 25\,\mathrm{m}^2\mathrm{s}^{-1} \tag{11.21}$$

considering as lower limit the value of electron thermal conductivity obtained from the reference case and as upper limit the one obtained from the case with tripled amplitude,

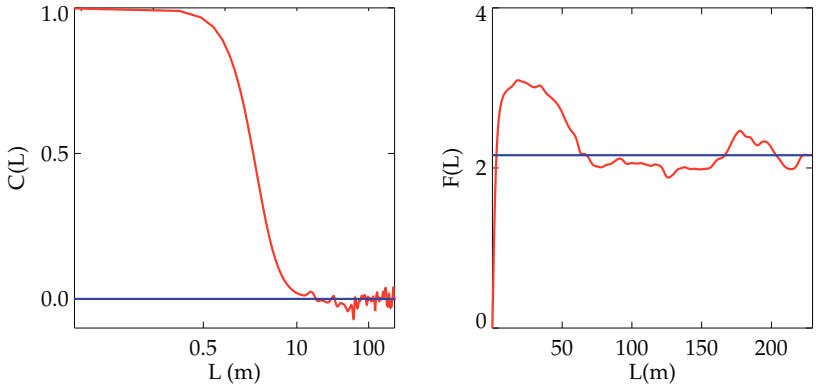

Figure 11.8: The figure on the left has a logarithmic scale, to evidence the behaviour of the autocorrelation function $C(L)$. The value of L_{ac} has been calculated as $F(L = 500 \cdot a)$.

these two being the cases where the level of magnetic perturbation was consistent with the one given by Drake (see equation 11.14).
This results turns out to be compatible to the experimental estimation of χ_r given at the barrier location by power balance analysis [Martin et al., 2009], where a value $\chi_r \approx 5 : 50\,\mathrm{m^2 s^{-1}}$ is recovered [Predebon et al., 2010].

11.3 Effect of 3D shaping in tokamak plasmas

The tools developed to study the transport due to a stochastic magnetic field, based on the definitions given in section 11.1, have been used to analyze a stochastic magnetic field of a tokamak configuration, with data coming from the 3D MHD code PIXIE3D. Many phenomena can cause the (nominally) axisymmetric field in a tokamak to become stochastic. Intrinsic magnetic field errors (coils misalignments, machine imperfections) are always present in fusion devices producing 3D fields. External 3D fields can also be deliberately applied through non-axisymmetric coils, as it happens in tokamak to suppress MHD instabilities such as RWMs [Chu and Okabayashi, 2010] and to mitigate Edge-Localized-Modes (ELMs) [Evans et al., 2006].
The effect of 3D fields on plasma rotation were addressed in a recent series of experiments performed on the RFX-mod machine (used as a tokamak). Plasma rotation has been one of the topics of major interest among the fusion community given its beneficial role on MHD stability and on improving confinement through turbulence suppression. A set of experiments performed on the RFX-mod machine (used as a tokamak) studied the effect of 3D fields on plasma rotation. The main result is that, above a threshold

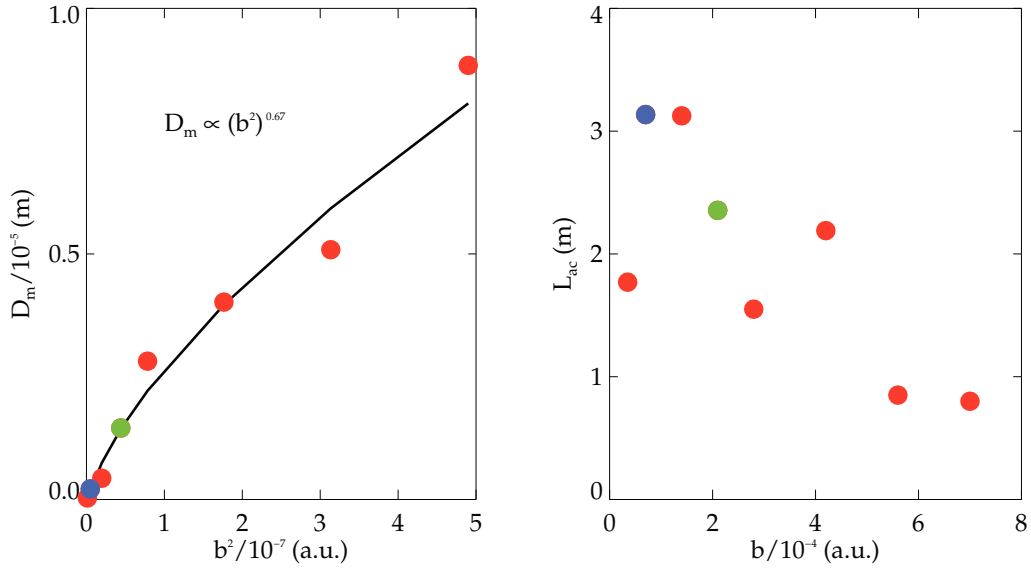

Figure 11.9: Scaling of the magnetic diffusion coefficient and of the autocorrelation length with perturbations' intensities.

in amplitude of a $m = 2$, $n = 1$ RWM, plasma rotation reverses from counter to co-I_P direction.

11.3.1 Experimental discharges

Figure 11.10 synthesizes the experimental results that inspired the PIXIE3D MHD simulation showed in section 11.3.2. The plasma experiments are characterized by the presence of a stable (in black) and an unstable (in red) $(2, 1)$ RWM, whose amplitude increases starting from $t = 0.2$ s. In the last case the mode eventually causes a disruption. It is possible to notice from panel d) that as the RWM grows the flow in toroidal direction first decelerates then reverses from counter to the same direction of the plasma current I_P. Instead the plasma rotation in presence of a stabilized RWM is constant and counter-I_P.

11.3.2 PIXIE3D MHD simulations

Visco-resistive MHD simulations performed with the code PIXIE3D (described in section 4.2) show that the plasma edge can become stochastic in the presence of a large enough 3D magnetic field.
A set of PIXIE3D simulations has been performed with dimensionless parameters given

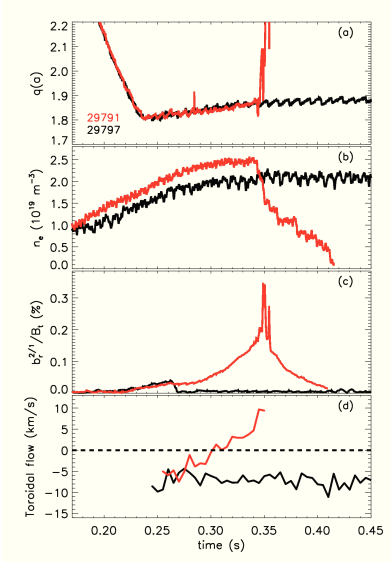

Figure 11.10: Time histories of (a) edge safety factor, (b) electron density, (c) $(2,1)$ radial magnetic field amplitude normalized to the equilibrium magnetic field at the edge and (d) toroidal flow measured from C_{VI}passive spectroscopy. Note that in the uncontrolled red case the flow reverses its direction.

by $S = 3 \cdot 10^4$ and $P = 3$, aspect ratio $R/a = 4$, initial equilibrium with $q(0) = 0.8$, $q(a) = 1.9$. The chosen current profile is given by $J_\phi = J_0(1-(r/a)^2)^\nu$, where $\upsilon = \frac{q_a}{q_0} - 1 = 1.375$. The amplitude of the $(2,1)$ MP at the ideal wall (placed at $r/a = 1.1$) has been varied. A vacuum region between the plasma boundary at $r = a$ and the wall is modelled by a region of large resistivity. Some details of two PIXIE3D MHD simulation, with no MP and MP's amplitude of 0.2% respectively, can be seen in figure 11.11 (the value of the MP is normalized to the total magnetic field at the edge).

One of the most important outcomes from this set of simulations (two important cases are shown in figure 11.11) is that the use of a helical boundary condition on the $(2,1)$ MHD mode causes a diminution of the oscillating behaviour of all the plotted quantities.

The behaviour of the core-safety factor of the simulation plotted in black represent the typical effect of a sawtooth instability. The use of MP with an amplitude of 0.2% (plotted in blue) strongly modifies the behaviour of the $(2,1)$ MHD mode, as can be seen from the second row of the figure, where the maximum of the $b_r^{2,1}$ quantity is plotted. The MP also mitigates the sawtooth behaviour of the safety factor profile and of the $(1,1)$ MHD mode. It can be demonstrated that a further growth of the value of the MP can completely heal the sawtooth behaviour, thus favouring a steady equilibrium. The results shown in figure 11.11 are at the basis of the idea proposed on the abstract,

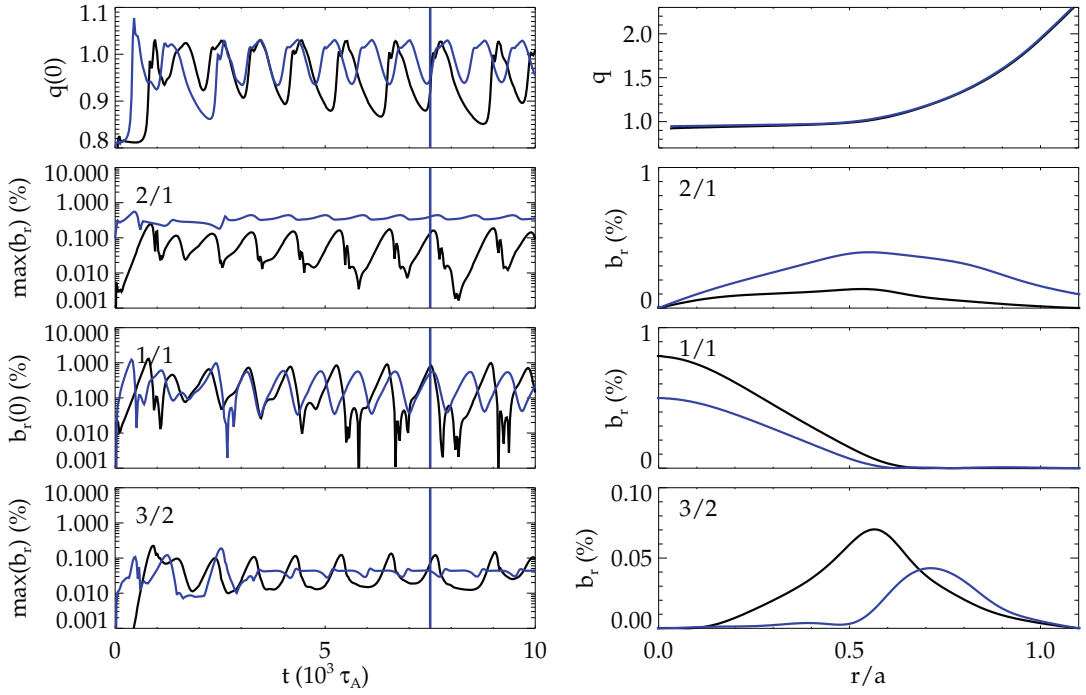

Figure 11.11: Simulations performed with MP on the $b_r^{2,1}$ MHD mode. Black lines refers to simulations with no MP, blue lines to a value of MP's amplitude equal to 0.2%. *Left column:* Time evolution of some physical quantities calculated by the PIXIE3D code. On axis safety factor $q(0)$, maximum of the $b_r^{(2,1)}$ quantity, an axis $b_r^{(1,1)}$, maximum of the $b_r^{(3,2)}$ quantity. *Right column:* Radial profile, at the colored time instant, of the safety factor profile and of the most relevant components of the magnetic field.

where it was stated that the use of MP leads to a unifying vision for the tokamak and the RFP: in fact in both the configurations a steady state behaviour can be reached using the proper helical boundary conditions.

11.3.3 NEMATO simulations

The magnetic field topology from a set of two MHD simulation with PIXIE3D is shown in figure 11.12. In panel a) a number of magnetic island chains can be observed, for example $m = 2$ structures but also $m = 3, 4$ structures. If a $(2, 1)$ MP is added the width of the corresponding island increases and chaos develops in correspondence with the partial overlap of the separatrixes of the magnetic islands related to the $(2, 1)$ and $(3, 2)$ MHD modes.

The presence of such a stochastic zone is at the origin of the formation of a current density that creates a $\mathbf{J} \times \mathbf{B}$ force that is in the co-current region, explaining the effect

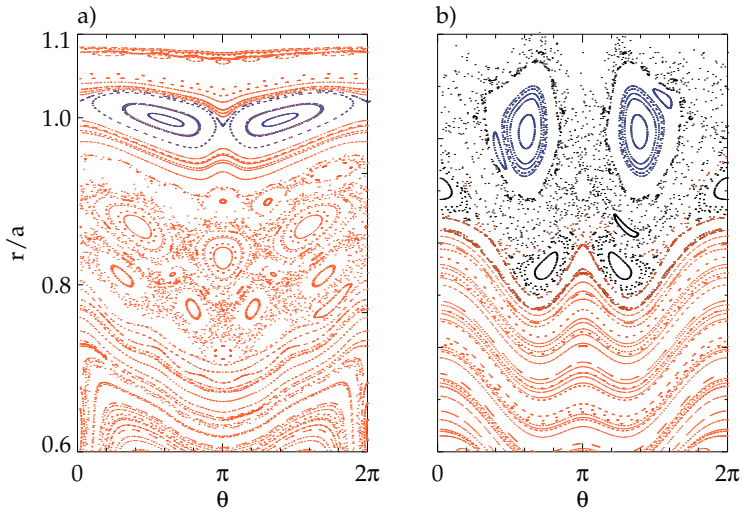

Figure 11.12: Poincaré plot of the magnetic field topology on a toroidal cross section. Panel a) refers to a simulation without 3D magnetic field, panel b) to a simulation with $b_r^{(2,1)}/B_t(a) = 0.1\%$. The $m = 2$ structures are evidenced in blue. Edge magnetic field stochasticity can be seen in black in panel b).

of magnetic edge stochasticity in plasma rotation. The relative intensity of this effect depends on the value of the magnetic field lines diffusion coefficient D_m, that can be easily calculated through the definitions given in section 11.1 and the numerical tools developed, in a similar way to the one used in section 11.2.3. The recovered values of the D_m coefficient will be listed in table 11.2.

Table 11.2: Magnetic diffusion coefficient and auto-correlation length for different values of magnetic perturbations on the $(2, 1)$ MHD mode. It displays a behaviour of the kind: $D_m \propto \left(b_r^{(2,1)}\right)^{1.6}$ (this scaling, however, is based on few MHD simulations).

$\frac{b_r^{(2,1)}}{B_t(a)}\%$	$D_m \cdot 10^{-5}$ (m)
0.05	0.7
0.10	2.2
0.20	5.7
0.30	11.2

11.4 Summary and remarks

The set of tools and definitions used to quantify the level of transport in a stochastic magnetic field can be used in many physical problems.
The most interesting is the characterization of the energy transport in the RFP configuration, where stochastic magnetic fields are routinely present. The analysis shown in this chapter describe a case of experimental interest. In this case the macroscopic tearing modes, that are the main cause of magnetic chaos, probably give a negligible contribution at the electron internal transport barrier: this allows microturbulence-related transport, usually much lower, to be revealed. It was found that if this microturbulence is of microtearing nature the value of the energy diffusion coefficient is compatible with the one reconstructed from direct experimental measurements.
The tools were also preliminarily used to assess the value of the energy diffusion coefficient in realistic RFP configurations. The data come from the MHD simulations analyzed in the chapter devoted to the study of the magnetic topology in low dissipation configurations, chapter 8 and 9. As a preliminary result, with a level of secondary modes reduced to experimental-like values, an estimation of the energy diffusion coefficient in presence of macroscopic resistive-kink tearing modes is given by $\chi_r \approx 50 : 100\,\mathrm{m}^2/s$.
A case regarding the tokamak configuration is also shown. The analysis of a field made stochastic by 3D edge magnetic field shows that the related-transport may explain the level of plasma rotation observed in the experiments.
Some additional words must be spent on the results obtained analyzing the tokamak configuration. A set of two simulations was described that used the same idea of helical boundary conditions used in chapter 8 dealing with the RFP on the tokamak. In both cases it was shown that the use of MPs allow the access to helical equilibria with interesting properties for the two configurations. For the RFP the advantage is the establishment of a quasi helical symmetry with a possibly reduced level of stochastic transport. For the tokamak the sawtooth instability can be mitigated, with positive effects in particular considering the avoidance of the sawtooth-related disruptions.
A unifying vision of the two configurations for magnetic plasma confinement can thus be proposed considering the common behaviour of the two configurations under the action of MPs.

V

Epilogue

Conclusion

The work presented in this thesis focuses on helical states achieved in the reversed-field pinch and tokamak configurations for the magnetic confinement of fusion plasmas. The work has been performed solving the 3D nonlinear visco-resistive magnetohydrodynamics model using advanced numerical modelling. The characterization of such three-dimensional states was performed following three approaches of study that can be synthesized in three main categories: *3D MHD dynamics, magnetic topology, stochastic transport*.
The results obtained during my PhD from the different approaches, described in the next three paragraphs and synthesized in the table at the end of the chapter, are deeply inter-connected and provide a further step in the path toward a qualitative and quantitative predictive capability of the numerical tools.

The most important outcome of the *dynamical studies* (part III, chapter 8) is the level of agreement achieved between the macroscopic description of the magnetic behaviour of the plasma in numerical modelling and the experimental findings from RFP devices, in particular RFX-mod. The key to obtain helical states similar to the experimental ones is the use, for the first time, of helical boundary conditions.
More in detail, the *main dynamical result* is that the combined use of magnetic perturbations on a single MHD mode (helical boundary conditions, MP) and of dissipation parameters both corresponding to realistic plasma conditions yields a dynamics of the magnetic field quantitatively similar to the experiment. The agreement can be noticed both in the behaviour of the MHD modes and of global magnetic field quantities (like the reversal parameter). MHD simulations show that a quasi-helical symmetry of the magnetic field emerges even in visco-resistive regimes where nonlinear dynamics prevents a complete symmetry and a residual spectrum of perturbations persists.
The result overcomes a seemingly contradictory result from standard MHD simulations: long lasting helical states were recovered at high visco-resistive dissipation, whereas in experiments they increasingly emerge as resistive dissipation gets lower (though the experimental determination of viscosity is still an open issue).
A *further dynamical result* is that the imposed edge MP influence the global RFP dy-

namics, providing an important indication that supports experimental reconstruction of the RFX-mod data. Furthermore Quasi Single Helicity (QSH) states characterized by an externally selected helicity can be stimulated and the obtained QSH states share similar dynamical properties. Indication from a wide simulation study show that the MHD mode that is dominant in RFX-mod seem to react more intensely to the applied MP than the other MHD modes.
This result (see chapter 8) induces to propose a vision of the RFP as a customizable helical configuration that can be driven to an externally selected quasi-helical state, with dynamics properties similar to the ones of the spontaneous QSH states.

The major outcome of *magnetic topology* studies (mostly described in part III, chapters 6,7,9) is the systematic study and characterization of the conserved core-helical structures in both simplified and realistic cases.
Topological studies were first performed considering cases with a *simplified dynamics* (chapters 6 and 7): the important role of magnetic separatrix expulsion, already emphasized in previous studies, was further confirmed. The absence of a separatrix has evident positive effects on the magnetic field lines behaviour, representing a necessary condition for magnetic chaos healing.
The role of the secondary modes perturbations to the helical symmetry was highlighted in *more realistic dynamical cases*, as described in chapter 9. It is shown that the actual level of perturbations present in both MHD simulations and experiments can produce chaotic magnetic field lines, meaning that the separatrix expulsion of the dominant mode is not a sufficient condition for magnetic chaos healing.
The results suggest that the healing of stochastic behaviour of the magnetic field should rely on two possible solutions in the contest of helical RFP. The first one is represented by an overall reduction of the residual perturbating MHD modes amplitude. This effect can be reached in states characterized by a relatively lower level of dissipations. This means, from an experimental point of view, raising the plasma current or temperature together with a choice of the optimal helical periodicity. The second and more complicated approach is represented by a suitable tailoring of the magnetic field in order to simplify its dynamics. This second option requires advanced geometrical tools to analyze the magnetic field in a correct helical geometry and an advanced control system to realize the correct configuration of the magnetic field.

The most important outcome of the work on *transport due to magnetic stochasticity* (part IV, chapter 11) is the development of a set of tools that can be used to quantitatively analyze energy transport in many different physical situations. The tools are now available for further applications.

The most relevant application addressed during the PhD is the assessment of the effect of 3D fields on both the tokamak and RFP configurations.
As for the RFP configuration the tools were applied to the study of magnetic stochasticity associated with fully 3D fields due to microtearing microturbulence at the internal transport barrier in the RFX-mod experiment. The energy transport coefficient due to microtearing turbulence predicted by gyrokinetic studies is consistent with experimental estimates of local thermal conductivity at the electron internal transport barrier in RFX-mod. As for the tokamak configuration the effect of an externally applied edge magnetic field was studied. The effects of edge 3D stochastic magnetic field are consistent with the observed reversal of toroidal rotation in tokamak plasmas studied with the RFX-mod experiment.

Table with synthesized conclusions: main outcomes and results of this PhD thesis

3D nonlinear MHD of fusion plasmas: helical regimes			
CATEGORY OF STUDIES	3D MHD DYNAMICS	MAGNETIC TOPOLOGY	STOCHASTIC TRANSPORT
PREDICTIVE CAPABILITY ACHIEVED	agreement between MHD simulations and experiments	characterization of quasi helical states obtained from realistic simulation cases	development of tools to estimate energy transport in stochastic magnetic fields
RESULTS	1) realistic simulation of RFP discharges at high current 2) key role of helical b.c. and of realistic dissipation parameters	1) role of separatrix expulsion confirmed in simplified cases 2) primary importance of perturbations reduction to heal chaos in realistic cases	first applications of transport tools to realistic cases 1) RFP microturbulence 2) tokamak stochastic edge magnetic field

Open questions and future works

This section deals with the main questions on the MHD of helical states that remain unanswered in the framework of the PhD thesis, and with the work that should be done to fill this gap. All the questions address the RFP configuration, in particular they regard the next steps to be performed in the numerical research about RFP helical states. As it was pointed out in chapter 8 the visco-resistive model with zero pressure seem to capture the basic RFP physics. Some assumptions that were made can nevertheless be improved. The role of dissipation parameters was shown to be very important in determining the MHD dynamics. More realistic radial profiles should be introduced for the resistivity dissipation while a non-flat profile for the viscosity should be used. A further step would be the to enforce a non-stationary behaviour of the resistivity profile during a typical RFP quasi periodic cycle. This can not be done self-consistently in a system where pressure is neglected. So one of the main challenge is the introduction of pressure in the equations, that would lead to a self-consistent treatment of electron energy transport and so of electron temperature profile and in turn of resistivity. The self-consistent treatment of pressure is being tackled using the 3D nonlinear MHD code PIXIE3D, that also allows the use of general curvilinear geometries (toroidal, in particular). A future work is the expansion of the visco-resistive model used in this thesis, introducing the so called *Hall term* of Ohm's law in the computation. This will allow to decouple the electronic and ionic dynamics. Another future work is the parallelization of the SPECYL code, to deal with the long computational times required to perform simulation at high values of the dissipation parameters.

More in general the RFX-mod experiment comes with some puzzling issues that numerical studies may help to solve. Up to now no clear explanation is given of the reason why the main helicity of the magnetic field is given by $h = 7$ and it is not clear even whether the $m = 1, n = -7$ is the first resonant mode with respect to the axis symmetric safety factor. The role of the aspect ratio is probably determinant, but does not completely exaplain why $(1, -7)$ is the dominant MHD mode. In fact in the RFX device, which was used before RFX-mod and which had the same aspect ratio, the dominant helicity was $h = 8$. Another issue, common to both experiment and MHD simulations is the ultimate reason of the observed quasi-periodical crashes.

VI

Appendixes

A

Numerical verification of ORBIT and NEMATO codes for magnetic topology diagnosis

We present the results of a benchmark study involving the ORBIT and NEMATO codes. The two codes have been used to compare the magnetic structure in a reversed-field pinch, where conserved magnetic structures/islands appear both in the core (dominated by $m = 1$ modes) and in the edge (dominated by $m = 0$ modes). As input, a snapshot of a 3D nonlinear MHD visco-resistive simulation (produced by the SPECYL code), has been used. The first test is given by the reconstruction via Poincarè surface of section plot of an island generated by a single mode. The benchmark between the codes has then been extended to a more complex configuration with chaotic magnetic field, using as input a fully 3D multiple mode RFP condition, characterized by the typical chain of edge magnetic islands providing a transport barrier. Finally, a quantitative benchmark has been performed, using the same 3D input, by estimating the correlation length of the magnetic field line in a bounded stochastic domain. The conclusion is that both codes yield consistent Poincarè plot structure on the one hand, and very good quantitative agreement in correlation length estimate. This gives confidence to the application of both codes to magnetic topology in the RFX-mod device, for which they are used routinely, as well as for a generic fusion device. The content of this appendix will be the subject of a dedicated paper, submitted to the *Physics of Plasmas* scientifical journal, written in collaboration with G. Ciaccio, D. Bonfiglio, S. Cappello, L. Chacón, G. Spizzo, R.B. White.

Outline of the chapter. In this chapter the benchmark verification of the ORBIT and NEMATO codes in their common application to topology reconstruction is addressed. The ORBIT code will be described in section A.1. The qualitative comparison between the codes has been successfully performed in 2D configuration and then extended to

a fully 3D configuration, by comparing the Poincaré plots, as described in section A.2. Finally, the correlation length of field lines in a stochastic bounded domain was evaluated, in order to produce a quantitative comparison between the two codes, shown in section A.3.
The conclusions are drawn in section A.4.

A.1 The ORBIT code

A.1.1 Hamiltonian of field lines

The code ORBIT uses the Hamiltonian formalism to describe the motion of a test-particle in an electromagnetic field. The guiding center Hamiltonian is

$$H = \rho_{\|} B^2/2 + \mu B + \Phi \tag{A.1}$$

where $\rho_{\|} = v_{\|}/B$ is the normalized parallel velocity, μ the magnetic momentum, Φ the electric potential. The canonical coordinates are θ and ζ, the canonical momenta $P_\theta = \psi + \rho_{\|} I$ and $P_\zeta = \rho_{\|} g - \psi_p$ where I and g are the equilibrium magnetic field components (poloidal and toroidal, respectively), in covariant representation. The particle location is given by the poloidal flux coordinate, ψ_p, and $\rho_{\|}$, so it is more convenient to advance these variables rather than the canonical momenta.
It can be shown that, in the limit of low kinetic energy of the particle ($\rho_{\|} \to 0$), the guiding center canonical equations [White, 2006] collapse to the usual Hamiltonian formulation of field lines, in the so-called "Boozer" coordinates [Boozer, 1981]. The field line Hamiltonian can be obtained in a simpler way by using the magnetic field controvariant representation

$$\mathbf{B} = \nabla\psi \times \nabla\theta - \nabla\psi_p \times \nabla\zeta \tag{A.2}$$

with θ and ζ the poloidal and toroidal angles, ψ_p and ψ the poloidal and toroidal fluxes. From the magnetic field lines definition, using the gradient of ψ given by $\nabla\psi = \partial_{\psi_p}\psi\nabla\psi_p + \partial_\theta\psi\nabla\theta + \partial_\zeta\psi\nabla\zeta$, one gets two equations in Hamiltonian form:

$$\frac{\mathrm{d}\zeta}{\mathrm{d}\theta} = \frac{\mathbf{B}\cdot\nabla\zeta}{\mathbf{B}\cdot\nabla\theta} = \frac{(\nabla\psi\times\nabla\theta)\cdot\nabla\zeta}{-(\nabla\psi_p\times\nabla\zeta)\cdot\nabla\theta} = \frac{\partial_{\psi_p}\psi(\nabla\psi_p\times\nabla\theta)\cdot\nabla\zeta}{(\nabla\psi_p\times\nabla\theta)\cdot\nabla\zeta} = \frac{\partial\psi}{\partial\psi_p} \tag{A.3a}$$

$$\frac{\mathrm{d}\psi_p}{\mathrm{d}\theta} = \frac{\mathbf{B}\cdot\nabla\psi_p}{\mathbf{B}\cdot\nabla\theta} = \frac{(\nabla\psi\times\nabla\theta)\cdot\nabla\psi_p}{-(\nabla\psi_p\times\nabla\zeta)\cdot\nabla\theta} = \frac{\partial_\zeta\psi(\nabla\zeta\times\nabla\theta)\cdot\nabla\psi_p}{-(\nabla\zeta\times\nabla\theta)\cdot\nabla\psi_p} = -\frac{\partial\psi}{\partial\zeta} \tag{A.3b}$$

with $\psi(\psi_p, \theta, \zeta)$ the Hamiltonian, ψ_p the canonical momentum, ζ the canonical coordinate, and θ the time.

The first canonical equation, (A.3a), gives simply the safety factor q:

$$\frac{\mathrm{d}\zeta}{\mathrm{d}\theta} = q = \frac{\partial\psi}{\partial\psi_p} \tag{A.4}$$

The second equation, (A.3b), is equal to $zero$ if the equilibrium $\mathbf{B}$ is not perturbed. If a perturbation term $\delta\mathbf{B}$ is added then it becomes:

$$\frac{\mathrm{d}\psi_p}{\mathrm{d}\theta} = \frac{\mathbf{B}\cdot\nabla\psi_p}{\mathbf{B}\cdot\nabla\theta} = \frac{(\mathbf{B}+\delta\mathbf{B})\cdot\nabla\psi_p}{\mathbf{B}\cdot\nabla\theta} = \mathcal{J}(\delta\mathbf{B}\cdot\nabla\psi_p) = \mathcal{J}\delta\mathbf{B}^{\psi_p} \tag{A.5}$$

$\mathcal{J}$ representing the Jacobian of the coordinate transformation from (x, y, z) to (ψ_p, θ, ζ).

A.1.2 Vector potential treatment

All tearing and Alfvén perturbations are perturbations of $\mathbf{B}$ primarily orthogonal to the original $\mathbf{B}$. The perturbation can be described as having the vector potential with gauge $\delta\mathbf{A} = \alpha\mathbf{B}$, or

$$\delta\mathbf{B} = \nabla\times\alpha\mathbf{B} \tag{A.6}$$

where α is an arbitrary scalar function which contains information about all the three components (radial, toroidal, poloidal).
Expanding in Fourier $\alpha = \sum_{m,n}\alpha_{m,n}(\psi_p)\sin(m\theta - n\zeta + \phi_{m,n})$ and developing the curl, (A.5) becomes:

$$\frac{\mathrm{d}\psi_p}{\mathrm{d}\theta} = \mathcal{J}(\nabla\times\alpha\mathbf{B})^{\psi_p} = \sum_{m,n}(mg+nI)\alpha_{m,n}(\psi)\cos(m\theta - n\zeta + \phi_{m,n}) = -\frac{\partial\psi}{\partial\zeta} \tag{A.7}$$

where I and g are the covariant components of the equilibrium field [Boozer, 1981]. Integrating separately the canonical equations:

$$\begin{cases} \frac{\partial\psi}{\partial\zeta} = -\sum_{m,n}(mg+nI)\alpha_{m,n}(\psi)\cos(m\theta - n\zeta + \phi_{m,n}) \\ \frac{\partial\psi}{\partial\psi_p} = q \end{cases} \tag{A.8}$$

and summing up the equilibrium and perturbation terms, one gets the toroidal flux:

$$\psi(\psi_p,\theta,\zeta) = \int q\mathrm{d}\psi_p + \sum_{m,n}\frac{mg+nI}{n}\alpha_{m,n}(\psi_p)\sin(m\theta - n\zeta + \phi_{m,n}) \tag{A.9}$$

We underline that the choice of the toroidal flux to be the Hamiltonian is mandatory in the RFP where $q = 0$ at the edge. We will use the toroidal flux Hamiltonian in the

$m = 0$ case, where (A.9) simplifies to

$$\psi(\psi_p, \theta, \zeta) = \int q \mathrm{d}\psi_p + \sum_n I\alpha_{0,n}(\psi_p)\sin(-n\zeta + \phi_{0,n}) \tag{A.10}$$

(A.10) clearly shows the advantage of using the scalar function α to describe perturbations, since with this choice the toroidal flux assumes the form $H = H_0 + \alpha H_1$, which is the standard form of a perturbed Hamiltonian in classical mechanics. An analogue derivation can be done taking the poloidal flux ψ_p as the Hamiltonian, and this is mostly done in the tokamak community (see e.g. equation (36) in [Boozer, 1981]). Finally, combining the fluxes as $\chi = m\psi_p - n\psi$ one can derive the helical flux function [Finn et al., 1992; Martines et al., 2011] as:

$$\chi = m\psi_p - n\int q \mathrm{d}\psi_p - \sum_{m,n}(mg + nI)\alpha_{m,n}(\psi_p)\sin(m\theta - n\zeta + \phi_{m,n}) \tag{A.11}$$

As anticipated above, the radial component of the perturbed $\delta\mathbf{B}$ is the mainly one responsible for deforming flux surfaces in presence of tearing modes. Therefore, at RFX it has been decided [Predebon et al., 2004; Gobbin et al., 2009] to match the radial component coming from (A.6) to the experimental measurement or the evaluation coming from the output of SPECYL. This in cylindrical coordinates becomes

$$b^r \equiv b^r_{orb} = (\nabla \times \alpha\mathbf{B})^r = \left(\frac{1}{r}\frac{\partial(\alpha g)}{\partial\theta} - \frac{\partial(\alpha I)}{\partial\zeta}\right) \tag{A.12}$$

It has to be mentioned that, if one calculates the curl in Boozer coordinates [Gobbin et al., 2009], then the result corresponds to a different gauge and a different α. A rapid check shows that this does not affect significantly the Poincaré in output. Inserting the Fourier expression for α, it is possible from (A.12) to get the relationship between α and the radial perturbation b^r:

$$\alpha_{m,n}(r) = \frac{b^r}{mg/r + nI} \tag{A.13}$$

Fixing the radial component of $\nabla \times \alpha\mathbf{B}$ by satisfying the condition $b^r \equiv b^r_{orb}$ automatically fixes also the other longitudinal components b^θ_{orb} and b^ζ_{orb}, given by the curl of α along the poloidal and toroidal directions.

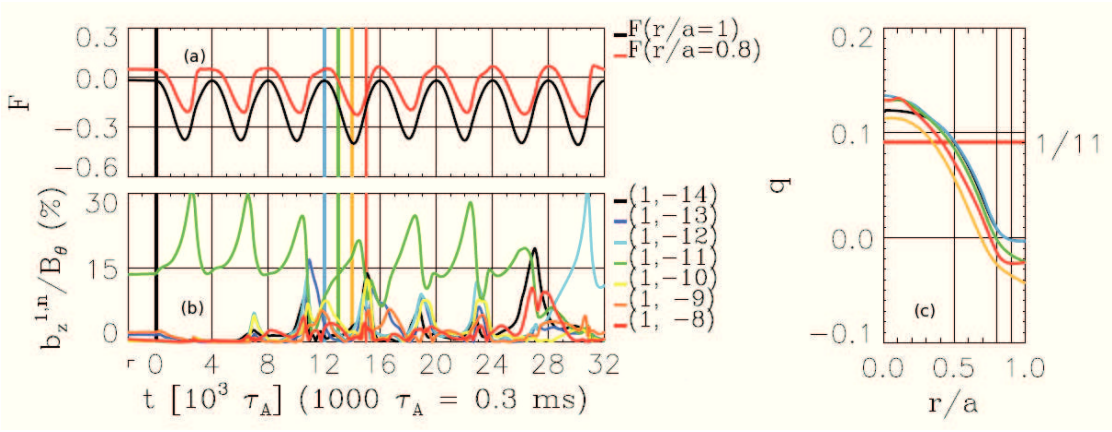

Figure A.1: OPCD SPECYL run. Time evolution of (a) q_a, (b) the radial magnetic field perturbation $m = 1$ component, (c) of the whole safety factor profile. The time instant (13500 τ_A) is chosen at half-drop of q_a, i.e. when the dominant $m = 1$ $n = 11$ mode is maximum (green vertical line).

A.2 Qualitative benchmark

A.2.1 Run used for the benchmark

The run used for the benchmark is a SPECYL OPCD (Oscillating Poloidal Current Drive) simulation (pinch parameter $\Theta = B_\theta(a)/\langle B_\phi \rangle = 1.6$, Lundquist number $S = 3 \times 10^4$, Prandtl number $P = 500$), see figure A.1. In figure A.1(a), the time evolution of the reversal parameter $F = B_\phi(a)/\langle B_\phi \rangle$ is shown. In panel (c), the temporal evolution of the whole safety factor profile is shown. SPECYL simulations show that the OPCD induces a controlled and periodic increase of the dominant kink-tearing mode ($m = 1$ $n = 11$ in SPECYL spectrum), as shown in figure A.1(b), and this is confirmed by the experiment [Cravotta et al., 2003].

In the experiment there is also a clear statistical correlation between high temperatures, obtained in the OPCD, and high amplitude of the dominant mode [Cravotta et al., 2003]. As such, OPCD is a promising way of obtaining a pulsed, quasi-stationary helical state (QSH), which can be an alternative to obtaining a long-lasting QSH state at high currents [Puiatti et al., 2011].

To select the snapshot for the benchmark, a time instant ($13500\,\tau_A$) at half-drop of q_a was chosen, i.e. when the dominant $m = 1$, $n = 11$ mode is maximum (see figure A.1(b)). The spectrum for the snapshot at $13500\,\tau_A$ ($m = 0$ and $m = 1$ modes) is shown in figure A.2(a), along with the q profile (panel (b)). The radial profiles of the kink-tearing modes, B^r components, are shown in figure A.2(c) for the $m = 0$, and in figure A.2(d) for the $m = 1$. The dominant $m = 0$ mode is the $n = 4$, while the dominant $m = 1$ is the

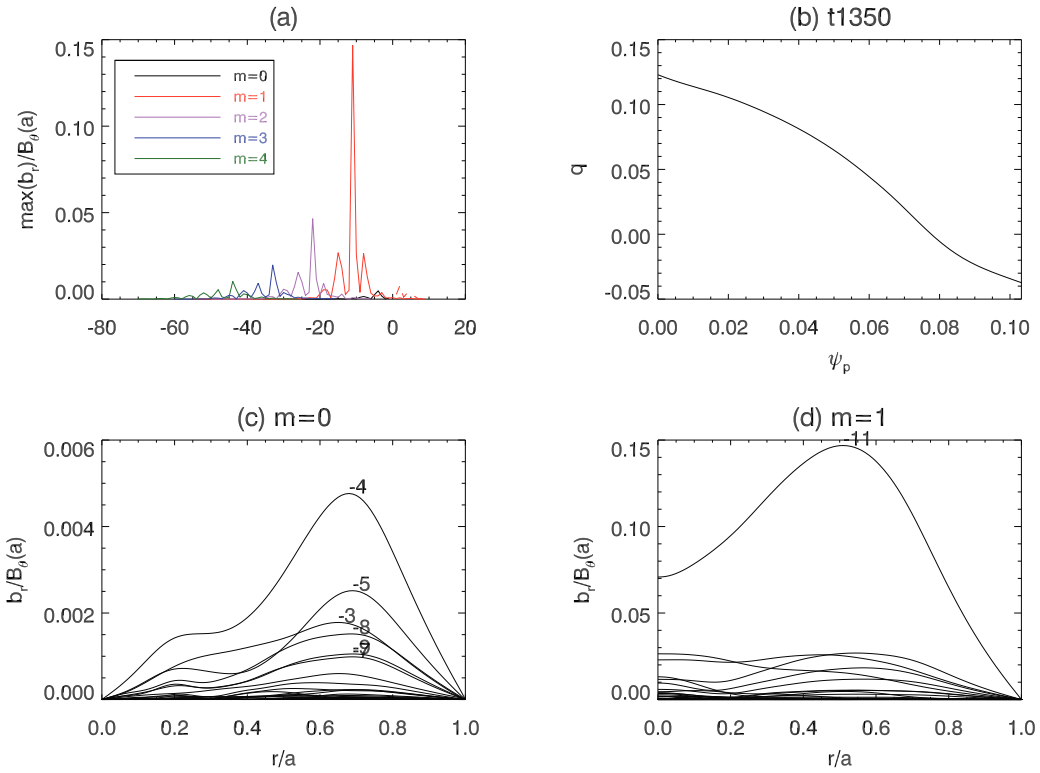

Figure A.2: (a) Spectrum for the snapshot at 13500 τ_A; (b) q profile; radial profiles of the kink-tearing modes (c) for the $m = 0$, and (d) for the $m = 1$.

$n = 11$, as already mentioned. The $m = 0$ eigenfunction is peaked at the *reversal surface*, i.e., the radius where $q = 0$, while the $m = 1$ mode has a broad peak more or less at mid-radius.

In the following sections, a qualitative benchmark of the codes will be presented. First, the comparison of the conserved flux surfaces for two cases. In the first, a single $m = 0$, $n \neq 0$ MHD mode is added to the SPECYL equilibrium field. In the second case, a $m = 1$, $n = 11$ mode is considered. In a final stage, the Poincaré plots (created by NEMATO and ORBIT) for the chaotic case, where more than one MHD mode is considered, will be compared.

A.2.2 Conserved $m = 0$ and $m = 1$ flux surfaces

In this section it is shown that the Poincaré plot made by ORBIT matches the analytical curves of a single $m = 0$ or $m = 1$ mode. Flux surfaces are calculated analytically according to (A.10) and (A.11), respectively. figure A.3 shows the comparison for the $m = 1$, $n = 11$ case. An analogue benchmark has already been published for NEMATO [Bonfiglio et al., 2010]. We conclude that comparing the analytical flux surfaces

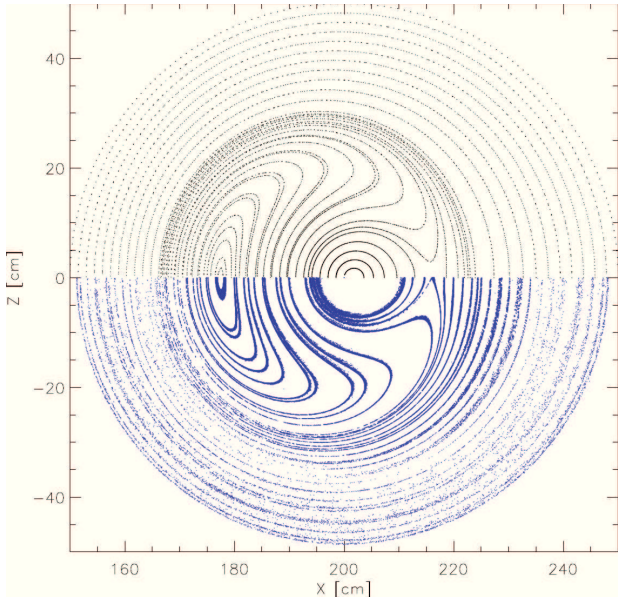

Figure A.3: Analytic flux surfaces (black) match ORBIT Poincaré plot (blue) for an $m = 1$ $n = 11$ mode.

is the same as comparing the Poincaré for a single mode.

In figure A.4, a comparison of the flux surface contours for the $m = 0$ case, $n = 1$ and $n = 1 - 25$, for ORBIT and NEMATO, respectively, is shown. In figure A.5, the same is done for the $m = 1$, $n = 11$ mode. The ORBIT and NEMATO curves match each other exactly. As a more quantitative estimate, the values of the island widths in the linear approximation is calculated (i.e., by expanding q around the unperturbed flux surface ψ_0 at the resonance, see [White, 2006]):

- $m = 0$ $n = 1$:

$$\Delta\psi_p = 4\left|\frac{\alpha_{0,1}I}{q'}\right|^{1/2} \Rightarrow \begin{cases} \Delta\psi_{p,O} = 5.214\ 10^{-3} & \text{island width for ORBIT} \\ \Delta\psi_{p,N} = 5.215\ 10^{-3} & \text{island width for NEMATO} \end{cases}$$

- $m = 1$ $n = 11$:

$$\Delta\psi = 4\left|\frac{\alpha_{1,11}(mg + nI)q(\psi_0)^2}{q'}\right|^{1/2} \Rightarrow \begin{cases} \Delta\psi_O = 6.1\ 10^{-3} & \text{island width for ORBIT} \\ \Delta\psi_N = 6.2\ 10^{-3} & \text{island width for NEMATO} \end{cases}$$

A.2.3 Poincaré plots, chaotic case

The benchmark is now extended to the full spectrum of $m = 0$ and $m = 1$ modes, by comparing the Poincaré plots directly. In this case, no analytical formulas (A.10) and

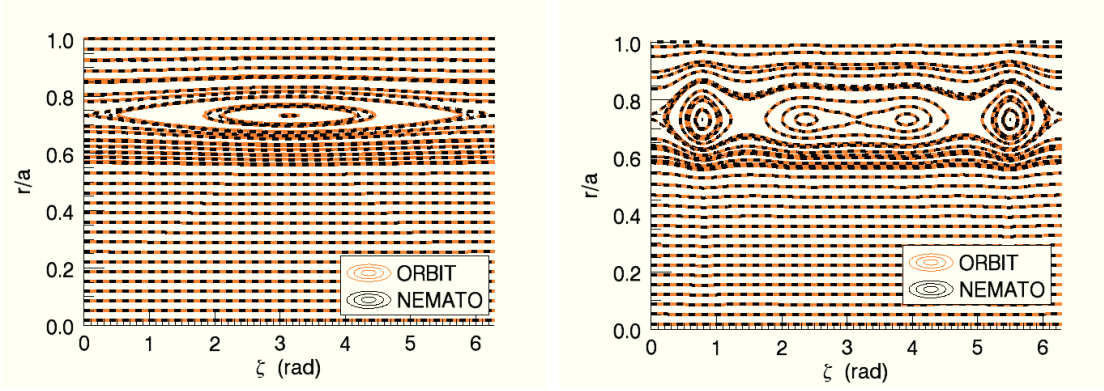

Figure A.4: Conserved flux surfaces contours for the (a) $m = 0$ $n = 1$ and (b) $m = 0$ $n = all$ modes. ORBIT (red) and NEMATO (black) curves match each other exactly.

(A.11) are available, since the non-linear interaction between different n's in the $m = 1$ spectrum causes chaos to develop in most of the spatial domain.
The plots have been generated with 52 field lines with the same initial conditions (at reversal radius, $\theta = 0$, equally spaced in ϕ), and following them for a length equivalent to 150 toroidal turns. In figure A.6, there are Poincaré with ORBIT (panel (a)), and two different plots with NEMATO: one with the α-profiles (used by ORBIT), and the other with the original SPECYL perturbations, namely, using b^{θ}_{orb} and b^{ζ}_{orb}, or b^{θ} and b^{ζ}?!?! This is done to further verify the validity of the gauge for the vector potential in ORBIT. All three plots have conserved structures with similar shape and dimension, differing just in small details. First, the test done on the gauge (panels (b) and (c)) proves that the α vector potential description of the perturbations does not modify the magnetic topology, in spite of quite different longitudinal components (see figure. A.7 and A.8). This was expected, since the radial component is the one solely responsible for tearing perturbations of the flux surfaces.
Regarding the numerical scheme (volume-preserving in NEMATO, step-size adapting in ORBIT), figure A.6 shows that there are indeed some minor differences in the plotting of secondary islands near the major conserved structures (see the differences between panel (a) and (c), at $r/a = 0.8$ and $\phi \sim -\pi/2$). These structures have a typical size $\Delta r \approx 1$ cm, comparable to the ion Larmor radius in the RFX device at plasma current $I_p = 1.2$ MA (the electron Larmor radius is of the order of few mm). Therefore, the details seen in the Poincaré plots are of minor importance in the dynamics of electrons and ions, and generally speaking on transport. But if one is interested in the description of very detailed topological structures, such as cantori and transport barriers associated

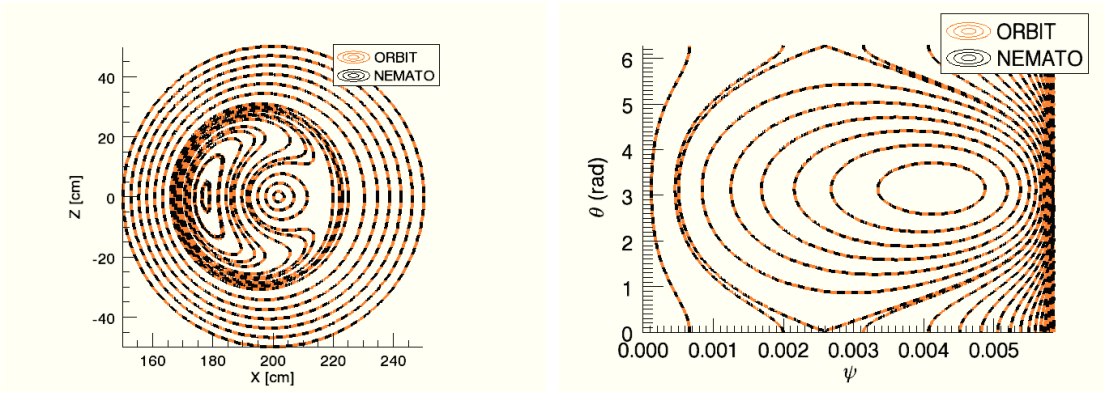

(a) **(b)**

Figure A.5: Conserved flux surfaces for the $m = 1$ $n = 11$ mode in (a) poloidal section and (b) helical section. ORBIT (red) and NEMATO (black) curves match each other exactly.

to shearless regions [del Castillo-Negrete and Morrison, 1993], NEMATO is more apt than ORBIT. This can be the case of the dynamical transition between chaos and order which takes place in the RFP.

A.3 Quantitative benchmark

In order to produce a quantitative estimate of the agreement of the two codes, the diffusion rate of the magnetic field lines through the direct evaluation of magnetic diffusivity [D'Angelo and Paccagnella, 1996] is studied. In a finite stochastic domain, as a real RFP device, a diffusive regime can be identified only locally for lengths of the order of the so-called *correlation length* of the magnetic field. We decided to use the correlation length, L_{ac} as defined in section 11.1, as parameter to be considered for the benchmark. A confirmation of the subdiffusive nature of chaos is shown in figure A.9(a): after a ballistic regime with $\langle (r - r_0)^2 \rangle \sim L^{1.8}$ and $C \approx 1$, field lines reach subdiffusion with $\langle (r - r_0)^2 \rangle \sim L^{0.3}$. It is interesting to notice that the access to the subdiffusive regime corresponds to the large negative minimum of $C(L)$, at $L \sim 0.1$ toroidal turns, namely at $L \simeq L_{ac}$. The subdiffusive nature of chaotic field lines has a counterpart in the subdiffusive nature of ion transport, as already shown elsewhere [Spizzo et al., 2007, 2009].
For the calculation of the correlation length, the codes were run with the same number of field lines (10000), initiated at $\psi_p = 0.05$ ($r \approx 33$ cm) and following them for 150 toroidal turns. The $C(L)$, $F(L)$ and $\langle (r - r_0)^2 \rangle$ curves (figure A.9 and figure A.10) show a similar behaviour.
The corresponding correlation lengths are:

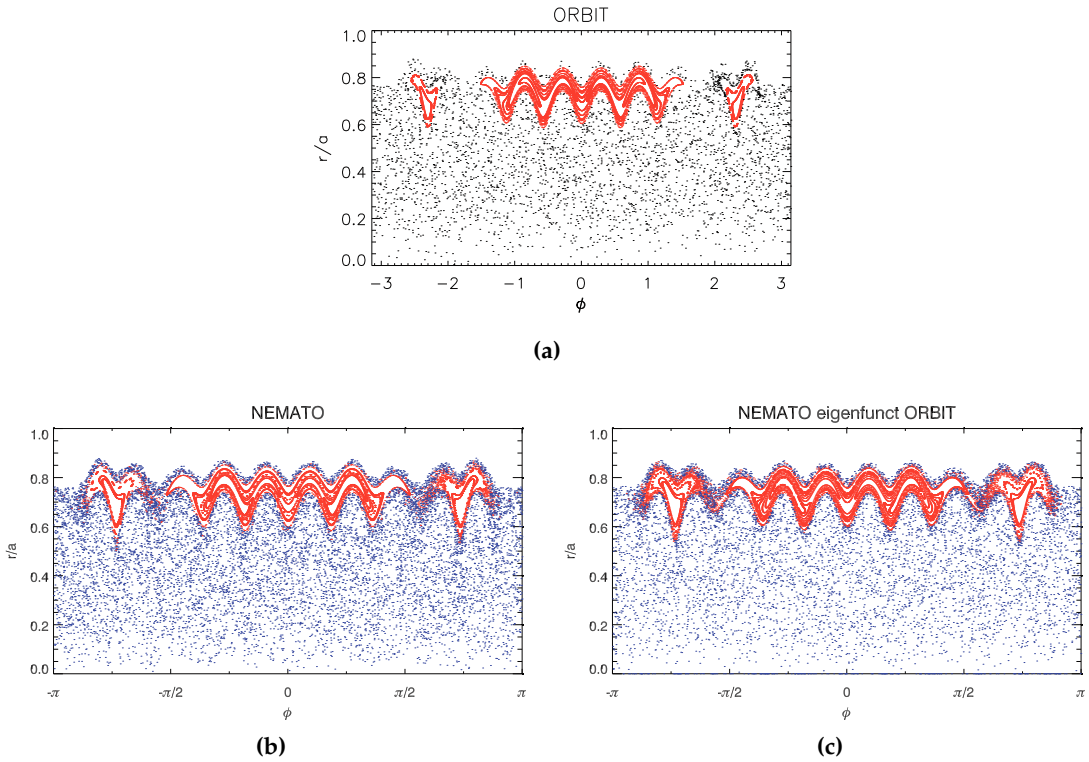

Figure A.6: Poincaré plots generated with 52 field lines with the same initial conditions (=the reversal radius), and following them for a length equivalent to 150 toroidal turns. Poincaré with ORBIT (a), and two different plots with NEMATO: one with the α-profiles (c), and the other with the original SPECYL perturbations (b). The three plots have conserved structures (red points) with similar shape and dimension, differing just in small details.

- $L_{ac} = 1.38\ m$ for ORBIT;
- $L_{ac} = 1.35\ m$ for NEMATO;

demonstrating again a very good agreement between the two codes. Despite the good correspondence of the numerical values, NEMATO shows more pronounced oscillations of $F(L)$ (and $C(L)$). In fact, in a subdiffusive system, the negative excursion of F is linked to trapping in "sticky" domains [Zaslavsky, 2002], such as the secondary islands of figure A.6b: the more numerous the secondary islands, the more pronounced the oscillations.

A.4 Conclusions

In this chapter, a benchmark between the guiding center code ORBIT and the solenoidal, field-line tracing code NEMATO has been shown. The aim of this numerical verification

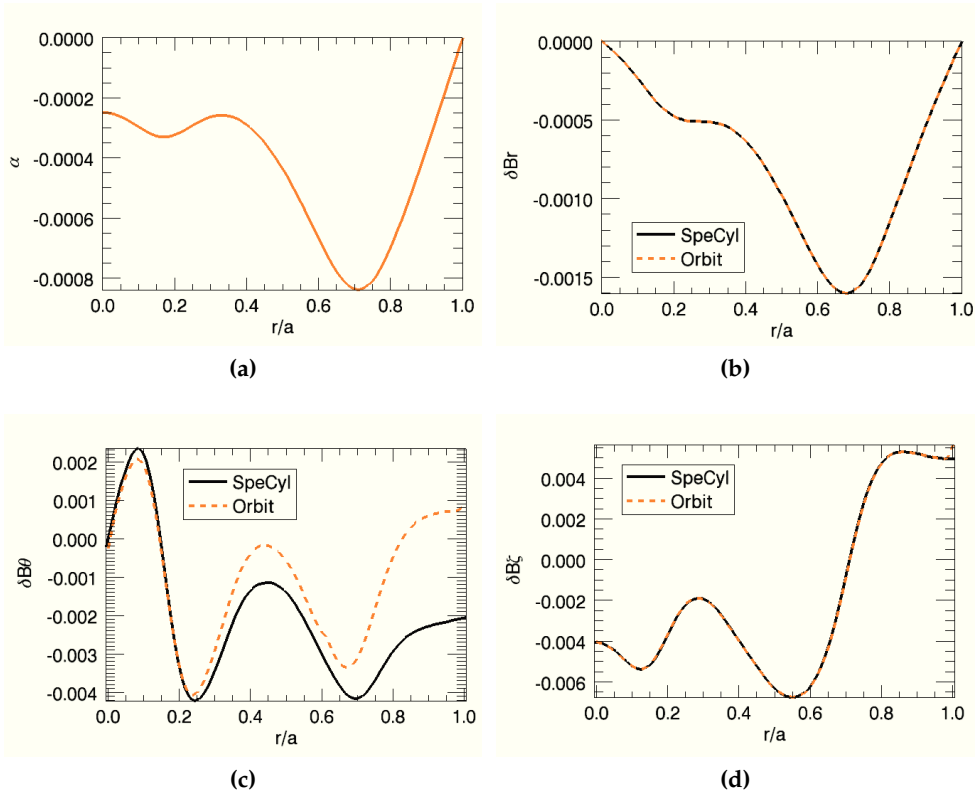

Figure A.7: α-profile and comparison of SPECYL and ORBIT perturbation component for an $m = 0\, n = 4$ mode. The ORBIT radial component matches the radial perturbation of the SPECYL run by construction (b). As expected, the α-profile is very similar to the radial perturbation (a). The ORBIT toroidal component (d) does not show a big difference from SPECYL perturbation, on the contrary of (c) the poloidal one which is the only longitudinal component for an $m = 0$ mode.

study is to assess the reconstruction of the magnetic topology in a reversed-field pinch, and to verify the validity of the gauge for the vector potential of the perturbations made in ORBIT. The benchmark can be divided into a qualitative and a quantitative test. In the first one, it has been verified that both codes give the same description of the flux surfaces when a single $m = 0$ and $m = 1$ mode is considered. Then, the comparison has been extended to the chaotic case, by direct evaluation of the Poincaré plots and with a quantitative estimate of the correlation length of field lines. The evaluation of the Poincaré plots shows a qualitative agreement in the spatial scales relevant for overall transport, while minor changes in the fine topological structure can be detected. These minor changes are not ascribed to the gauge assumption made by ORBIT on the magnetic field (which is fundamentally correct for a tearing mode), but on the different numerical scheme used for integration, namely, volume-preserving for NEMATO,

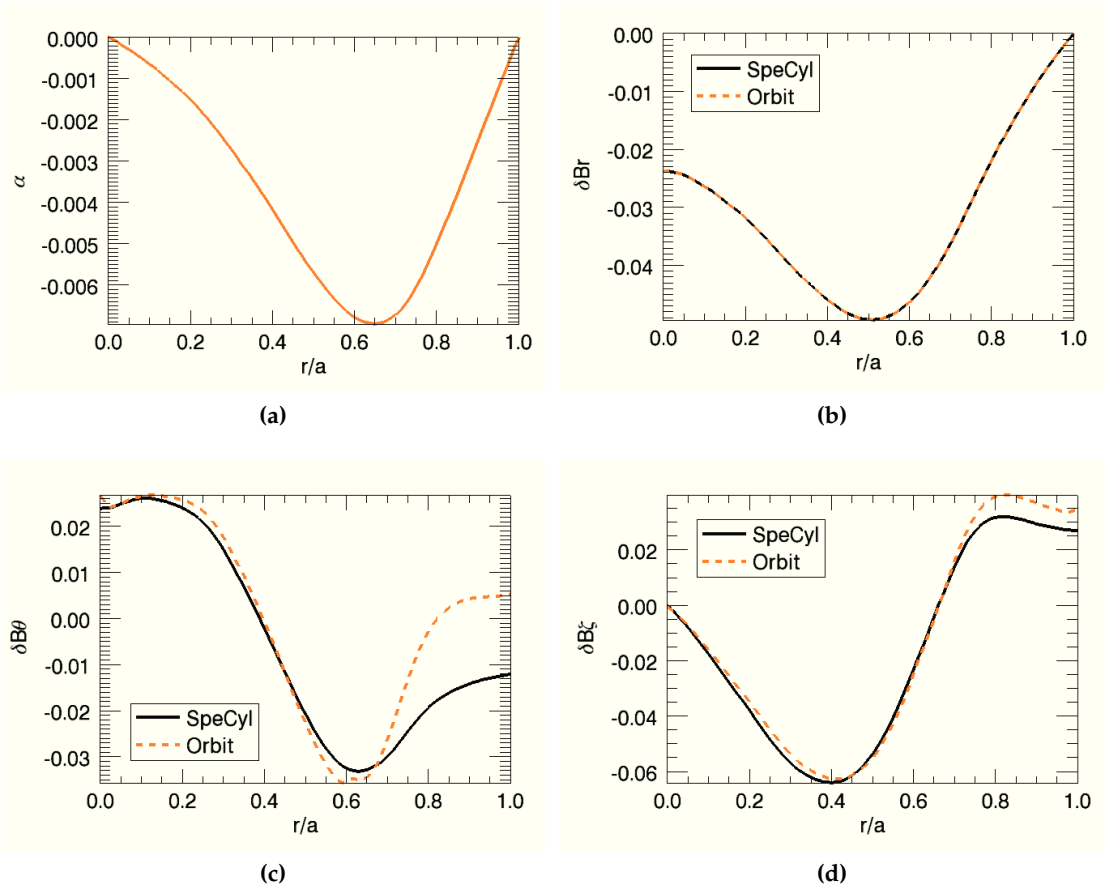

Figure A.8: α-profile and comparison of SPECYL and ORBIT perturbation component for an $m = 1$ $n = 11$ mode. The ORBIT radial component matches the radial perturbation of the SPECYL run by construction (b). As expected, the α-profile is very similar to the radial perturbation (a). However, the profiles of the longitudinal component of $(\nabla \times \alpha \vec{B})$ clearly differ from the SPECYL perturbations (c-d).

step-adapting in ORBIT. As for the quantitative test is concerned, similar results can be drawn: the main features of the chaotic system are captured in the same way by NEMATO and ORBIT, in particular, the correlation length is the same in the two codes. Small differences arise when one considers the detailed behaviour of the correlation functions, which reflects the fact that NEMATO describes better fine structures of the magnetic topology, such as secondary islands and sticky regions.

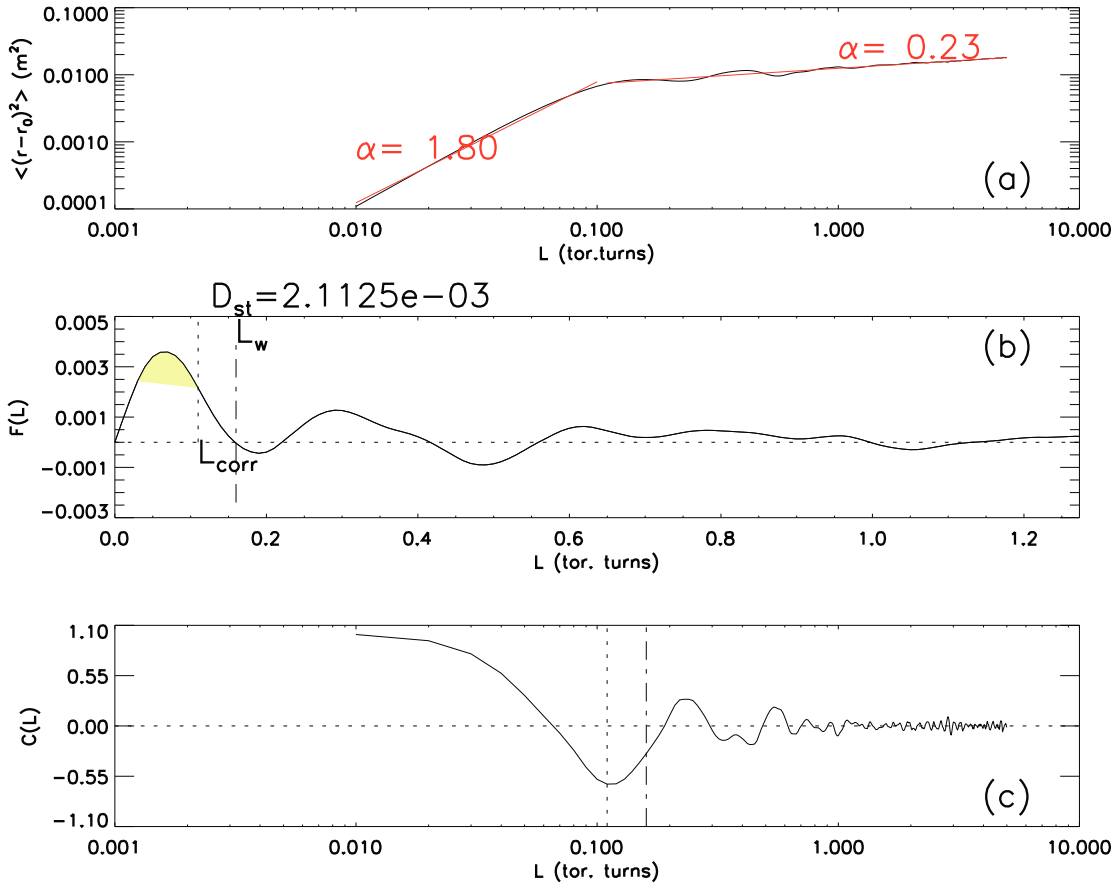

Figure A.9: The quadratic mean square displacement (a), the correlation (b) and auto-correlation (c) functions for a bounded domain from ORBIT code. Run with number of field lines (10000), initiated at $\psi_p = 0.05$ and following them for 150 toroidal turns. The function F takes its maximum value close to $L = 0$, vanishes for a $L = L_w$ and then oscillates around zero, without reaching a diffusion regime. At the same time, the auto-correlation function $C(L)$ experiences a large domain of negative values, where the field trajectories are anti-correlated one to each other. This means that the probability of a radial jump having an opposite sign with respect to the preceding one is larger than that of retaining the same sign. This fundamentally is the definition of a *subdiffusive regime*.

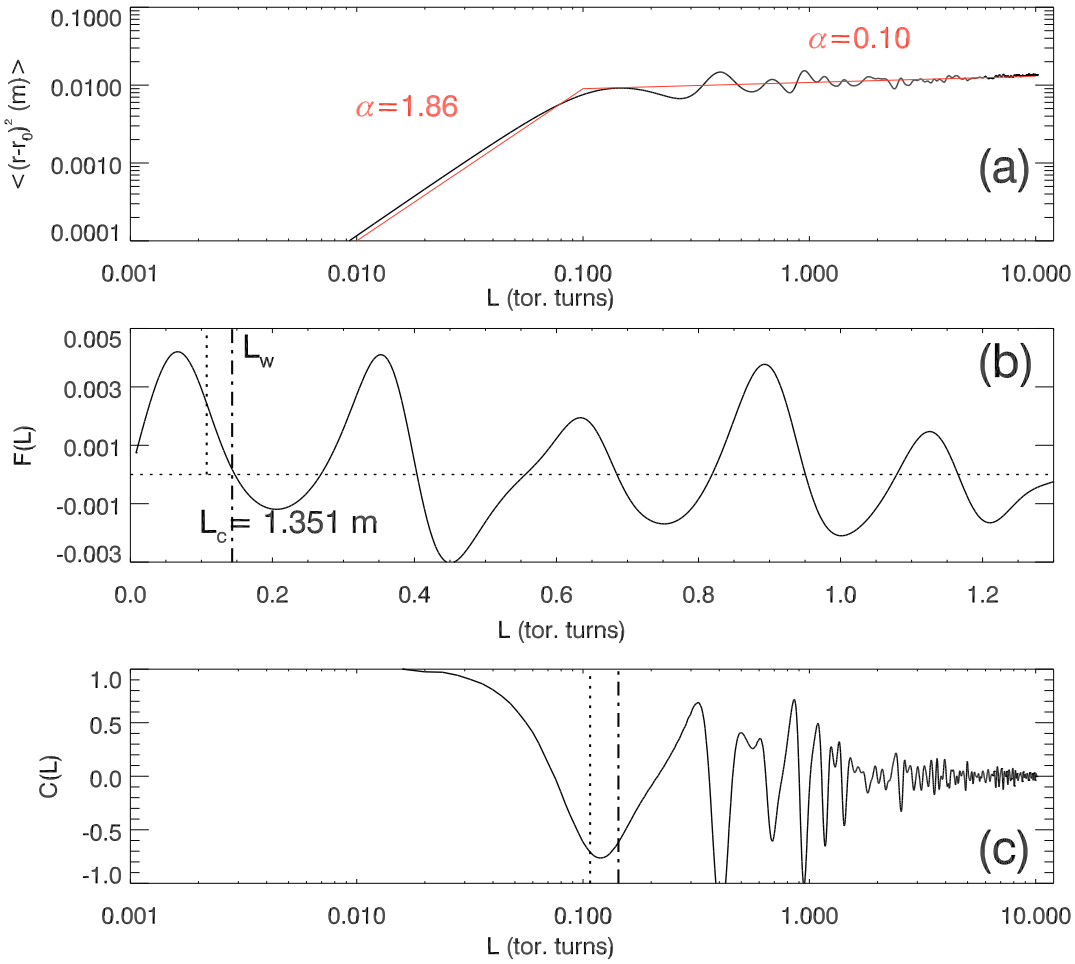

Figure A.10: The quadratic mean square displacement (a), the correlation (b) and auto-correlation (c) functions for a bounded domain from NEMATO code. Run with number of field lines (10000), initiated at $\psi_p = 0.05$ and following them for 150 toroidal turns. NEMATO finds the subdiffusive regime, though with a more oscillatory behaviour of the correlation function $F(L)$.

B

Magnetic topology reconstruction: NEMATO parallelization

The parallelization of NEMATO was performed during a one month mobility period at Oak Ridge National Laboratory, under the supervision of the creator of the code, Luis Chacón. The parallelization work was based on the initial choice of a hybrid MPI-OpenMP parallelization: this is a natural choice considering that the architecture of the computer system is constituted by the presence of interconnected symmetric multiprocessor nodes. NEMATO (that is written in Fortran) is MPI-parallelized to initially split the calculations on different nodes; inside each node the program is OpenMP-parallelized to use the available processors and save memory (as OpenMP is a shared-memory parallelization scheme). The effect of the parallelization, that involved a partial rewriting of parts of the code, is the speed up of the calculation of the magnetic field line by a factor almost equal to the number of processors employed during the execution of the program.

Outline of the chapter. This chapter deals with a brief description of the numerical work involved in the parallelization of the NEMATO code with a hybrid OpenMP-MPI approach. Section B.1 describe the features of the two approaches and the advantages of the hybrid one.

B.1 The hybrid MPI-OpenMP approach to parallelization

The problem of the calculation of a set of field line, that is the task performed by NEMATO, is a problem naturally suitable for the parallelization, since each field line can be independently traced by a single CPU as an independent process.

The parallelization of a code involves consideration about the task that the code has to perform and about the architecture of the cluster that is available (figure B.1 shows a schematic picture of a typical cluster). In particular the aim is the minimization of

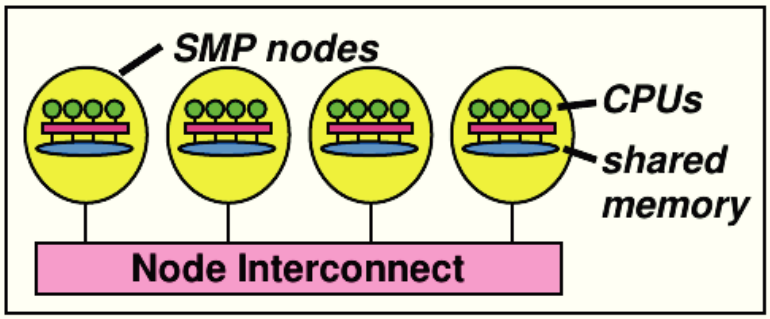

Figure B.1: A typical cluster. Different nodes, represented by yellow circles, are interconnected. Inside each node a number of CPUs is available, represented by green circles, each of them connected to a shared memory region, in blue.

some important quantities. First of all memory consumption has to be reduced: this is particularly important using the Message Passing Interface (MPI) that uses a *distributed memory* approach: each CPU involved in the calculation has its own memory, rapidly leading to memory shortage if a big amount of memory is needed by the process. Secondly load imbalances has to be reduced: this can be a problem using the Open Multiprocessing (OpenMP) approach, that uses *multithreading* to split a task between many different processes, with problems arising from the need of precise synchronization between different processes. The OpenMP approach is different from the MPI one as all the processes share the same memory (*shared memory* approach). Other important quantities to be minimized include communications between processes and duplicate calculations. Picture B.2 schematically showing the differences between the three approaches to parallelization. The hybrid MPI-OpenMP approach represents a

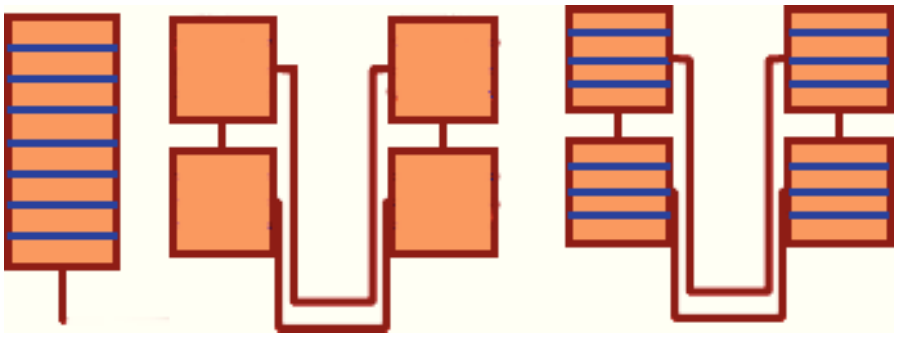

Figure B.2: From left to right the OpenMP, MPI, hybrid OpenMP-MPI approaches to parallelization are pictorially represented. Red lines indicate MPI processes, each with its own memory, that run in different nodes (that are represented by pink squares). Each node can then be used by some OpenMP processes, (represented by blue lines dividing the different CPUs present in each node).

good solution because it solves the main constraint thet is encountered in running the

code in the cluster present at Consorzio RFX in Padova, namely the limited memory present on each of the four nodes that constitute the cluster (whose features are listed in table B.1). The choice of an hybrid approach is preferable even removing the limited memory constraint, as there is little sense in replying the input data for each MPI process when a shared memory region can be used inside a single node. At the cluster of

Technical features of the cluster	
Nodes	{ra22,ra23,ra24,ra25,ra26}.igi.cnr.it
Operative System	Red Hat Enterprise Linux 5.1
RAM	{32,64,64,32,32} GB
Processors	Socket Intel(R) Xeon(R) CPU E7330
# of processors	{16,16,24,24,24}
Processors' frequency	2.40 GHZ

Table B.1: Technical features of the cluster at Consorzio RFX, in Padova, January 2013.

Consorzio RFX the limited memory did not allow to split the calculation of the magnetic field line in more than four different MPI tasks, as the code has a peak of memory usage of around 10GB for a typical resolution of the mesh on which the field is written. The first solution would be to use a simple OpenMP approach on a single node, but then the limitation would be on the number of processors that it is possible to use (the maximum number of processors available in a single node is between 16 and 24). The more natural solution is to use the hybrid approach that uses MPI between the four nodes of the cluster (creating a copy of the field informations on each node) and then to use OpenMP inside of each node sharing the informations on the field, using the same number of processor in each node. This allows the use of a maximum of 4×16 processors at a time, speeding up the time of execution of the program.

B.2 Speedup test

In parallel computing the *speedup* is a quantity that defines how much a parallel algorithm is faster than the corresponding serial one. It can be defined as:

$$S(n) = \frac{T_{1proc}}{T_{nprocs}}, \tag{B.1}$$

where T_{1proc} is the computational time with one processor, while T_{nprocs} is the computational time with n processors. It has to be noted that an ideal behaviour of the function

$S(n) = 1/n$ can not be reached as there is a part of the code that can not be parallelized. Another useful quantity is called *efficiency*, defined as:

$$E(n) = \frac{T_{1proc}}{nT_{nprocs}}, \tag{B.2}$$

with values between 0 and 1.
The test is performed considering the calculation of the Poincarè plot of figure 7.5, starting from a NEMATO input file with resolution $r = 100 \times \theta = 256 \times z = 2048$ (remember that the calculation is performed in cylindrical geometry) and asking the code to trace 512 field lines using the solenoidal algorithm up to a field lines integration time of 30000. The recovered data are listed in table B.2 and plotted in figure B.3. A figure with the corresponding efficiency is B.4.

Speedup test			
# of processors	# of nodes used	time elapsed (s)	Efficiency
1	1	23551	1.00
2	1	13672	0.86
4	1	11713	0.50
6	1	5760	0.68
8	1	6366	0.46
2	2	12929	0.91
4	2	7518	0.78
8	2	3153	0.46
12	2	6426	0.62
16	2	2461	0.60
4	4	7205	0.82
8	4	5057	0.58
16	4	2361	0.62
24	4	1719	0.54
32	4	1820	0.40

Table B.2: Speedup test data

Figure B.3 shows the expected result that employing more than one processor the total time to perform the same calculation decreases.
Figure B.4 shows the behaviour of efficiency, defined in equation (B.2). It can be noticed that the efficiency decreases from 1 to a value lower than 0.75 simply passing from a serial to a OpenMP-parallelized calculation. This seems to indicate that most of the loss in efficiency is due to the OpenMP part, as can be understood considering the fact that passing from 1 to 2 nodes or from 2 to 4 nodes does not change efficiency much.

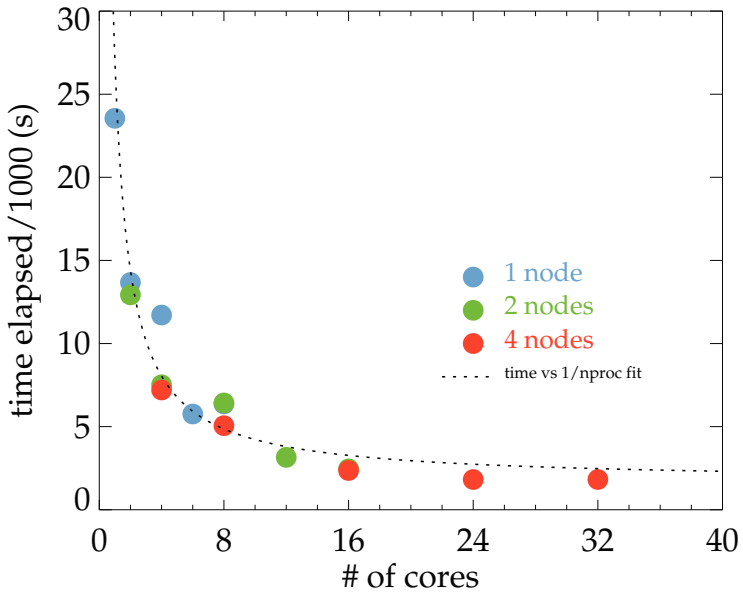

Figure B.3: Results of the speedup test. Different colors of the dots indicate the number of nodes used (this number has to be of the kind $np \in \{2^m, m \in \mathbf{N}\}$).

B.3 NEMATO scheme

This section explains in a synthetic way, through picture B.5, the main operation performed by NEMATO, indicating the parts that are parallelized.
After the definition of the initial starting point of the magnetic field lines from the input parameters the work is divided in various MPI processes on different nodes: these different processes initially spline the magnetic field $\mathbf{B}$ and, if the chosen algorithm is the solenoidal one, also integrate the vector potential $\mathbf{A}$. After this computations the main cycle on the initial points of the magnetic field lines start: this cycle is parallelized in each node using the OpenMP approach. If the magnetic field line intersect a Poincarè surface of section the intersection point is written to a file, different for each OpenMP process. The integration goes on until the maximum integration time (or the maximum arc-length of the field line) is reached. After all the field lines have been calculated the code ends.

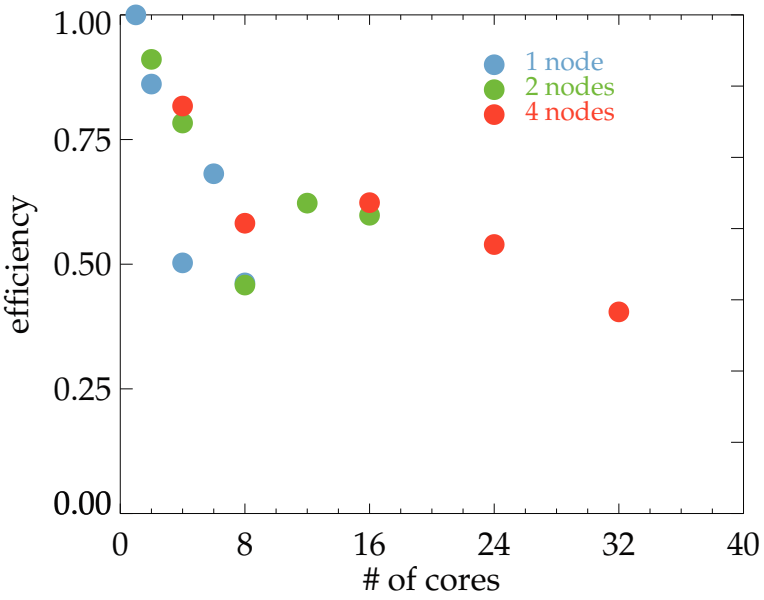

Figure B.4: Efficiency of the parallelized version of NEMATO. It can be seen that efficiency rapidly decreases passing from one to two processors inside each node. Then the reduction of efficiency is much slower.

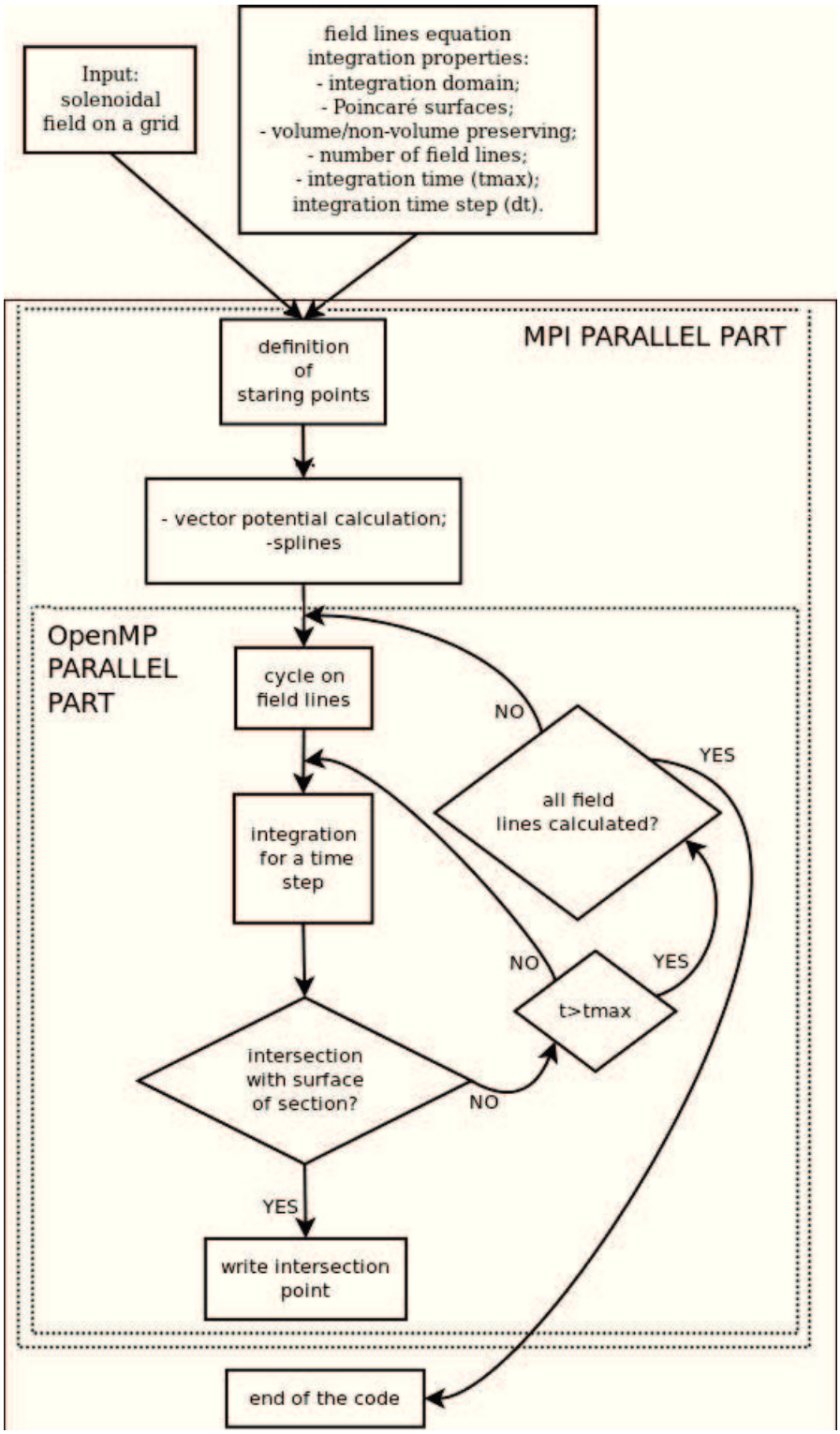

Figure B.5: Synthesis of the work of NEMATO.

C

The RFX-mod experiment

The RFX-mod device [Sonato et al., 2003] (see figure C.1) is an upgraded version of the RFX experiment [Rostagni, 1995]. Located at the Istituto Gas Ionizzati (IGI) of the italian Consiglio Nazionale delle Ricerche (CNR) in Padova, it is operational since 2004 under the management of Consorzio RFX, a research organization promoted by ENEA (Energia Nucleare Energie Alternative), CNR, INFN (Istituto Nazionale Fisica Nucleare), University of Padua, Acciaierie Venete. The RFX fusion science program is shaped to provide a contribution to ITER and its accompanying fusion program.

Outline of the chapter. This chapter describes the RFX-mod experiment, located in Padova, Italy. RFX-mod can be operated both as a RFP or as a tokamak. In section C.1 the most important features of the experiment are described. In section C.2 the diagnostics used to *look* at the plasma are analyzed.

C.1 Some features of the RFX-mod experiment

RFX-mod (Reversed Field eXperiment-modified) is the biggest magnetic confinement experiment in the world (beginning of 2013) that uses the RFP configuration. Its main geometrical and physical features are listed in table C.1.

C.1.1 RFX-mod technical components

In this section the main technical components in RFX-mod will be described.

Vacuum vessel: the toroidal chamber containing the plasma. It is an all-welded, rigid structure made of INCONEL 625, with a major radius of 1995 mm and minor radius of 475 mm.

First wall: it is the part of the machine exposed to the plasma discharge. It is composed

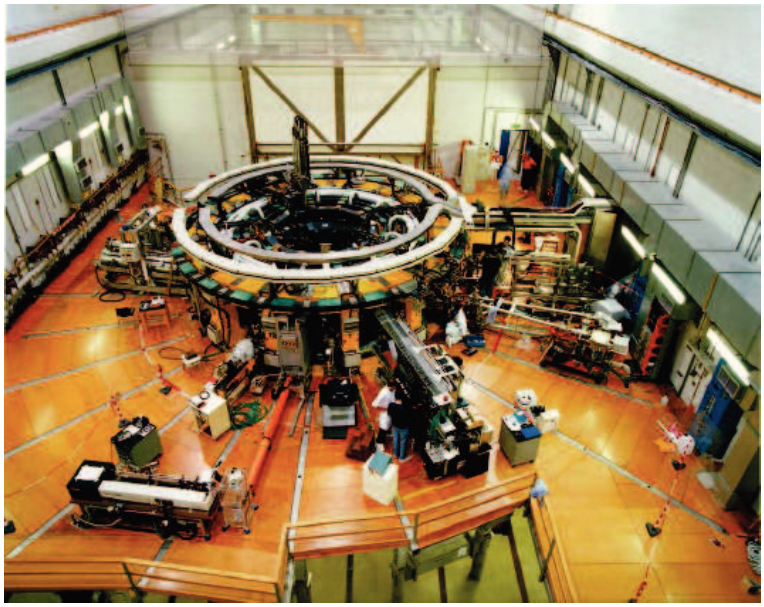

Figure C.1: Top view of the RFX-mod experiment.

by 2016 graphite tiles that covers it completely. Graphite has been chosen because it sublimates at a high temperature (for its low atomic number Z.
Stabilizing shell: it has the main purpose of stabilizing MHD ideal instabilities. It is made of copper and is 3 mm thick, located at $1.11a$ where $a = 0.51$ m is the minor radius. This shell is enclosed by a mechanical structure which bears the weight of the vacuum vessel and of the toroidal windings.
Magnetizing coils: they provide the time varying magnetic flux that induces the plasma current during the discharge. It is composed by 40 coils that can carry a maximum current of 50 kA.
Toroidal field coils: a set of 48 coils uniformly distributed along the toroidal direction, that surround the vessel and the shell. They are designed to generate the toroidal magnetic field needed to set-up and maintain the discharge (up to 0.7 T).
Field shaping coils: this set of poloidal coils is designed to generate a vertical field whose aim is to control plasma position during the discharge.
Virtual shell: this new set of saddle coils is necessary in RFX-mod in order to control the instability arising on the shell timescale. It is a set of 192 coils.
In figure C.2 you can see a scheme of the saddle coils disposition on a section of RFX-mod. An overview on the Intelligent Shell concept can be found in [Bishop, 1989] and the main results in RFX-mod obtained with the virtual shell application in [Marrelli et al., 2007].

R_0	2.00 m
a	0.50 m
I_P	$\leq$ 2.0 MA
B	$\leq$ 0.7 T
p_{vacuum}	$\sim 10^{-10}$ Pa
p_{plasma}	10^3 Pa
n_{plasma}	$5 \cdot 10^{19}$ m^{-3}
$T_{e,max}$	1.3 keV
t_{max}	0.5 s

Table C.1: Main features of the RFX-mod experiment. R_0 and a represent the major and minor radius of the torus, I_P represents the maximum achievable plasma current, B the maximum magnetic field that coils can create, p_{vacuum} is the pressure inside the vacuum chamber before plasma is created. p_{plasma} represents the typical pressure of the plasma during discharges, n_{plasma} the typical density of ion and electrons, $T_{e,max}$ is the maximum measured electronic temperature and t_{max} the maximum discharge duration.

C.1.2 Clean Mode Control

The virtual shell stabilizes MHD perturbations for time scales longer than the shell time penetration. The concept is based on the possibility to keep to zero the flux measured by each sensor loop forming the wall, as an ideal conducting wall would do. The structure of the 192 active coils constituting the virtual shell, each controlled independently from the others, is shown in figure C.2 (green coils). This scheme has been tested in RFX-mod with good results and has improved the confinement of the plasma. After a brief period of initial operations with the virtual shell it was realized that an intrinsic limitation, i.e. aliasing of the side-band harmonics generated by the discrete coils system coupled with coils with the same periodicity, did not allow further improvement. To overcome this systematic limitation, the aliased sidebands contribution (estimated from the coil currents) is subtracted from the measurements; the cleaned measurements are used as the feedback variable. More details about this procedure are reported in [Marrelli et al., 2007] and [Zanca et al., 2007].

C.2 Diagnostics in RFX-mod experiment

In RFX-mod a full set of diagnostics is capable of measuring many physical quantities, in their temporal and spatial variations. A general layout is proposed in figure C.3.

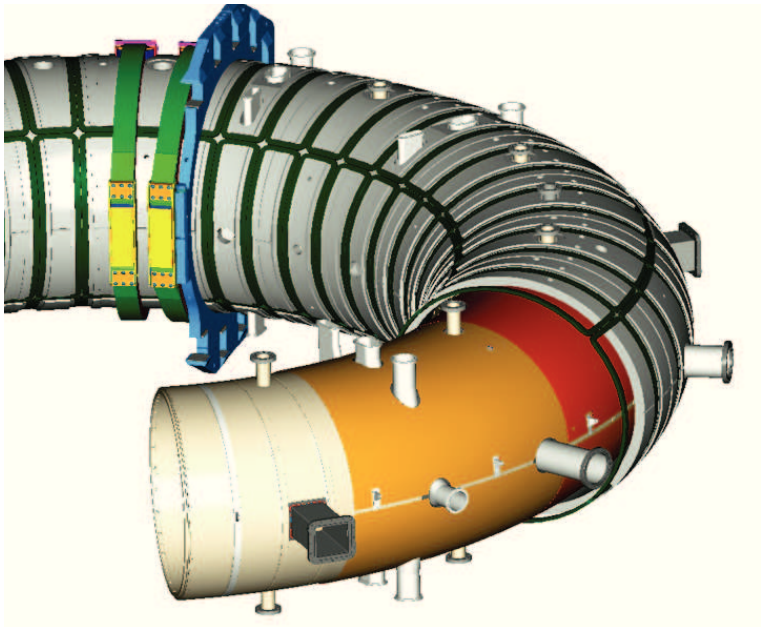

Figure C.2: Structure of the active coils in the RFX-mod experiment.

A brief description of the most important ones follows:

- a complete set of magnetic diagnostics is present: 4 Rogowski coils (measure of plasma current); 8 toroidal and 6 poloidal voltage loop coils (measure of loop voltage and toroidal flux); 196 pick-up coils, distributed along 48 toroidal directions and 4 poloidal directions, (measure toroidal and poloidal components of magnetic fields); 192 saddle probes, (measure the radial component of the field);
- a tomographic system which allows the reconstruction of total radiation losses and SXR radiation by means of 36 bolometric detectors (measure total emission of the plasma) and 78 silicon detectors (measure of soft-X rays radiation).
- a Thomson scattering diagnostic, which provides a 84 point radial profile of electronic temperature by analyzing the scattering properties of the plasma when a high power laser beam is injected;
- an interferometer, which measures the electronic density averaged along 13 lines of sight.
- spectroscopic diagnostics, which measure line intensities of radiation emitted by impurities;
- an integrated system of internal sensors (ISIS), which includes poloidal and toroidal arrays of 139 magnetic pick-up coils and 97 electrostatic (Langmuir) probes (used

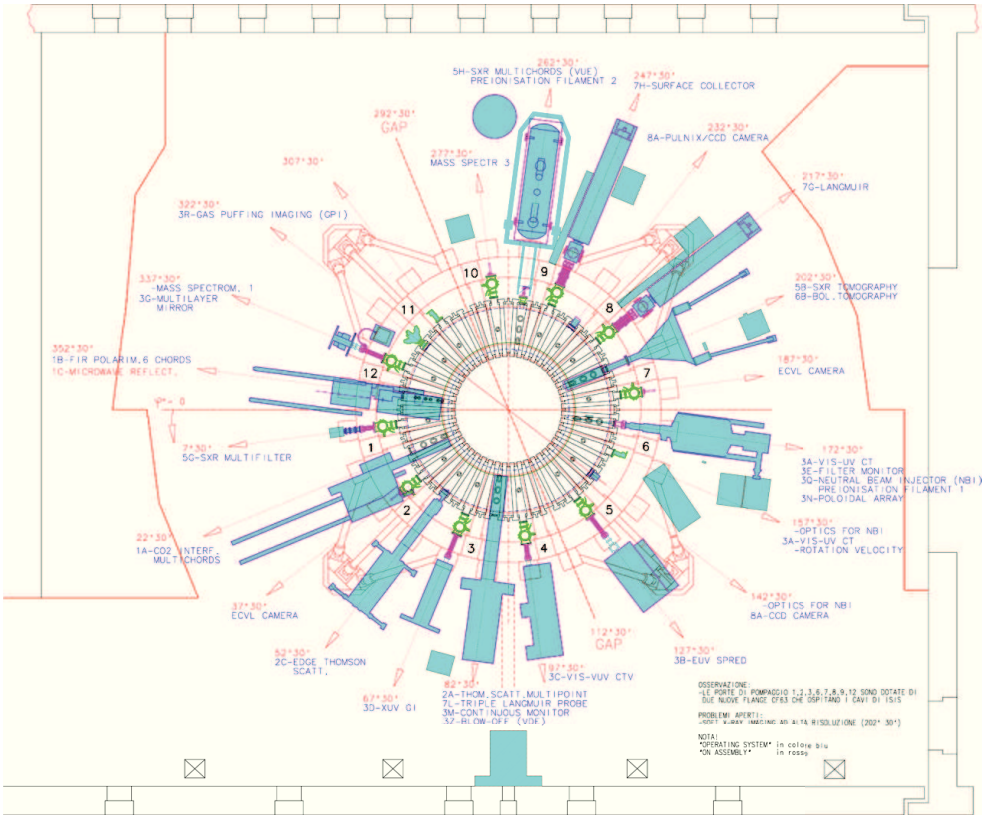

Figure C.3: Layout of the diagnostics present in the RFX-mod experiment.

to measure and correlate fluctuations of electric and magnetic fields), and 8 calorimetric sensors;

- a Soft-X Rays multifilter diagnostic, used for measuring electronic temperature at the center of the plasma; it allows a higher time resolution with respect to the Thomson scattering, but with a lower spatial resolution The data from all these diagnostics are collected during the discharge execution and are then analyzed and used as input to several numerical codes.

Aknowledgement

I wish to thank Susanna Cappello and Daniele Bonfiglio. They taught me many things during these three years. Without them this work would not have been possible.
I'd like to thank Dominique Franck Escande for some clarifying conversations about the RFP.
Susanna Daniele and Dominique pushed me to try to answer to some interesting questions about the RFP, and this is very important.
I want to thank prof. Antonio Buffa and prof. Leonardo Giudicotti for carefully reading this PhD thesis.
I also want to thank my two colleagues in this PhD, Emanuele Sartori and Alessandro Scaggion.

There are some persons, out of the fusion community, that I want to thank, for many reasons: they already know (even if I don't tell them, and this is very important too).

Bibliography

N. Arcis, D. F. Escande, and M. Ottaviani. Saturation of a tearing mode in zero-β full magnetohydrodynamics. *Physics of Plasmas*, 14(3):032308, 2007. doi: 10.1063/1.2710799. URL http://link.aip.org/link/?PHP/14/032308/1.

R. Bartiromo, A. Buffa, V. Antoni, L. Apolloni, M. Bagatin, W. Baker, F. Bellina, P. Bettini, R. Bilato, T. Bolzonella, A. Canton, S. Cappello, L. Carraro, R. Cavazzana, G. Chitarin, S. Costa, F. D'Angelo, A. De Lorenzi, G. De Pol, D. Desideri, D. Escande, P. Fiorentin, P. Franz, E. Gaio, L. Garzotti, L. Giudicotti, F. Gnesotto, D. Gregoratto, S.C. Guo, P. Innocente, A. Intravaia, A. Luchetta, G. Malesani, G. Manduchi, G. Marchiori, L. Marrelli, P. Martin, E. Martines, S. Martini, A. Maschio, A. Masiello, F. Milani, M. Moresco, A. Murari, S. Ortolani, R. Paccagnella, R. Pasqualotto, S. Peruzzo, R. Piovan, N. Pomaro, R. Pugno, M.E. Puiatti, G. Rostagni, F. Sattin, P. Scarin, G. Serianni, P.G. Sonato, E. Spada, G. Spizzo, M. Spolaore, C. Taliercio, G. Telesca, D. Terranova, V. Toigo, L. Tramontin, M. Valisa, M. Viterbo, S. Vitturi, P. Zaccaria, P. Zanca, E. Zilli, and G. Zollino. Recent progress in reversed-field pinch research in the RFX experiment. *Nuclear Fusion*, 39(11Y):1697, 1999. URL http://stacks.iop.org/0029-5515/39/i=11Y/a=309.

M. Baruzzo. *Performance limiting MHD phenomena in fusion devices: physics and active control*. PhD thesis, Joint Research Doctorate in Fusion Science and Engineering, 2011. URL http://paduaresearch.cab.unipd.it/3801/1/Baruzzo_tesi_30_1.pdf.

C.M. Bishop. An intelligent shell for the toroidal pinch. *Plasma Physics and Controlled Fusion*, 31:1179, 1989.

D. Biskamp. *Nonlinear magnetohydrodynamics*. Cambridge University Press, 1992.

J.A. Bittencourt. *Fundamentals of plasma physics*. Springer, New York, 2004.

D. Bonfiglio, L. Chacòn, and S. Cappello. Nonlinear three-dimensional verification of the SpeCyl and PIXIE3D magnetohydrodynamics codes for fusion plasmas. *Physics of Plasmas*, 17:082501, 2010. URL http://dx.doi.org/10.1063/1.3462908.

D. Bonfiglio, D.F. Escande, P. Zanca, et al. Necessary criterion for magnetic field reversal in the reversed-field pinch. *Nuclear Fusion*, 51:063016, 2011.

Allen H. Boozer. Plasma equilibrium with rational magnetic surfaces. *Physics of Fluids*, 24(11):1999–2003, 1981. doi: 10.1063/1.863297. URL http://link.aip.org/link/?PFL/24/1999/1.

S.I. Braginskii. *Transport processes in a plasma*, volume 1. Consultants Bureau, New York, 1965.

S. Cappello. Bifurcation in the MHD behaviour of a self-organizing system: the reversed-field pinch (RFP). *Plasma Physics and Controlled Fusion*, 46(12B):B313, 2004.

S. Cappello and D. Biskamp. Reconnection processes and scaling laws in reversed-field pinch magnetohydrodynamics. *Nuclear Fusion*, 36(5):571, 1996.

S. Cappello and D. F. Escande. Bifurcation in viscoresistive MHD: the Hartmann number and the reversed-field pinch. *Physical Review Letters*, 85(18):3838, 2000.

S. Cappello and R. Paccagnella. Nonlinear plasma evolution and sustainement in reversed-field pinches. *Physics of Fluids B*, 4:611, 1992.

S. Cappello, D. Bonfiglio, D. F. Escande, S. C. Guo, A. Alfier, and R. Lorenzini RFX Team. The reversed-field pinch toward magnetic order: a genuine self-organization. *AIP Conference Proceedings*, 1069(1):27–39, 2008. doi: 10.1063/1.3033714. URL http://link.aip.org/link/?APC/1069/27/1.

L. Chacón. Volume preserving integrators for solenoidal fields on a grid. *Computer Physics Communications*, 163:143, 2004.

L. Chacón. Scalable parallel implicit solvers for 3D magnetohydrodynamics. *Journal of Physics: Conference Series*, 125(1):012041, 2008a. URL http://stacks.iop.org/1742-6596/125/i=1/a=012041.

L. Chacón. An optimal, parallel, fully implicit Newton-Krylov solver for three-dimensional viscoresistive magnetohydrodynamics. *Physics of Plasmas*, 15:056103, 2008b.

B. Chapman, F. Auriemma, W. Bergerson, et al. Direct diagnosis and parametric dependence of 3D helical equilibrium in the MST RFP. In *2012 IAEA-Fusion energy conference proceedings*, number EX/P6-01, 2012.

A.R. Choudhuri. *The physics of fluids and plasmas*. Cambridge University Press, 1998.

M.S. Chu and M. Okabayashi. Stabilization of the external kink and the resistive wall mode. *Plasma Physics and Controlled Fusion*, 52(12):123001, 2010. URL http://stacks.iop.org/0741-3335/52/i=12/a=123001.

A. Cravotta, G. Spizzo, D. Terranova, T. Bolzonella, P. Franz, L. Marrelli, P. Martin, S. Martini, and S. Ortolani. A statistical analysis of pulsed poloidal current drive in the Reversed-Field eXperiment. *Physics of Plasmas*, 10(3):705–712, 2003. doi: 10.1063/1.1538594. URL http://link.aip.org/link/?PHP/10/705/1.

F. D'Angelo and R. Paccagnella. The stochastic diffusion process in reversed-field pinch. *Physics of Plasmas*, 3(6):2353–2364, 1996. doi: 10.1063/1.871919. URL http://link.aip.org/link/?PHP/3/2353/1.

Diego del Castillo-Negrete and P. J. Morrison. Chaotic transport by Rossby waves in shear flow. *Physics of Fluids A: Fluid Dynamics*, 5(4):948–965, 1993. doi: 10.1063/1.858639. URL http://link.aip.org/link/?PFA/5/948/1.

G.L. Delzanno, L. Chacón, and J.M. Finn. Electrostatic mode associated with the pinch velocity in reversed-field pinch simulations. *Physics of Plasmas*, 15:122102, 2008.

W.D. D'haeseleer, W.N.G. Hitchon, J.D. Called, and J.L. Shohet. *Flux coordinates and magnetic field structure*. Springer-Verlag, 1991.

W. Dorland, F. Jenko, M. Kotschenreuther, and B. N. Rogers. Electron temperature gradient turbulence. *Phys. Rev. Lett.*, 85:5579–5582, Dec 2000. doi: 10.1103/PhysRevLett.85.5579. URL http://link.aps.org/doi/10.1103/PhysRevLett.85.5579.

J.F. Drake, N.T. Gladd, C.S. Liu, and et.al. Microtearing modes and anomalous transport in tokamaks. *Physical Review Letters*, 44:994, 1980.

D.F. Escande and M. Ottaviani. Simple and rigorous solution for the nonlinear tearing mode. *Physics Letters A*, 323(3-4):278 – 284, 2004. ISSN 0375-9601. doi: 10.1016/j.physleta.2004.02.010. URL http://www.sciencedirect.com/science/article/pii/S0375960104001781.

D.F. Escande, S. Cappello, F. D'Angelo, P. Martin, S. Ortolani, and R. Paccagnella. Single helicity: a new paradigm for the reversed-field pinch. *Plasma Physics and Controlled Fusion*, 42:B243, 2000a.

D.F. Escande, P. Martin, S. Ortolani, A. Buffa, P. Franz, L. Marrelli, E. Martines, G. Spizzo, S. Cappello, A. Murari, R. Pasqualotto, and P. Zanca. Quasi-Single-Helicity Reversed-Field-Pinch plasmas. *Physical Review Letters*, 85(8):1662, 2000b.

D.F. Escande, R. Paccagnella, S. Cappello, C. Marchetto, and F. D'Angelo. Chaos healing by separatrix disappearance in Quasi Single Helicity states of the reversed-field pinch. *Physical Review Letters*, 85(15):3169, 2000c.

T.E. Evans, R.A. Moyer, K.H. Burrell, M.E. Fenstermacher, I. Joseph, A.W. Leonard, T.H. Osborne, G.D. Porter, M.J. Schaffer, P.B. Snyder, P.R. Thomas, and W.P. Watkins, J.G. West. Edge stability and transport control with resonant magnetic perturbations in collisionless tokamak plasmas. *Nature Physics*, 2:419, 2006. URL http://www.nature.com/nphys/journal/v2/n6/full/nphys312.html.

J.M. Finn and L. Chacón. Volume preserving integrators for solenoidal fields on a grid. *Physics of Plasmas*, 12, 2005.

J.M. Finn, R. Nebel, and C. Bathke. Single and multiple helicity ohmic states in reversed-field pinches. *Physics of Fluids B*, 4:1262, 1992.

M.-C. Firpo and D. Constantinescu. Study of the interplay between magnetic shear and resonances using hamiltonian models for the magnetic field lines. *Physics of Plasmas*, 18(3):032506, 2011. doi: 10.1063/1.3562493. URL http://link.aip.org/link/?PHP/18/032506/1.

R. Fitzpatrick. Plasma physics. http://farside.ph.utexas.edu/teaching/plasma/380.pdf.

J.P. Freidberg. *Ideal Magnetohydrodynamics*. Plenum Press, New York and London, 1987.

J.P. Freidberg. *Plasma Physics and Fusion Energy*. Cambridge University Press, 2007.

M Gobbin, L Marrelli, and R B White. Numerical studies of transport mechanisms in RFX-mod low magnetic chaos regimes. *Plasma Physics and Controlled Fusion*, 51(6): 065010 (14pp), 2009. URL http://stacks.iop.org/0741-3335/51/065010.

M. Gobbin, D. Bonfiglio, D. F. Escande, et al. Vanishing magnetic shear and electron transport barriers in the RFX-mod reversed-field pinch. *Phys. Rev. Lett.*, 106:025001, Jan 2011. doi: 10.1103/PhysRevLett.106.025001. URL http://link.aps.org/doi/10.1103/PhysRevLett.106.025001.

R.J. Goldston and P.H. Rutherford. *Introduction to Plasma Physics*. Institute of Physics Publishing, Bristol and Philadelphia, 1995.

H. Grad and H. Rubin. Hydromagnetic equilibria and force-free fields. In *Proceedings of the Second United Nation International Conference on the Peaceful uses of Atomic Energy*, volume 31, page 190, 1958.

R.D. Hazeltine, D. Dobrott, and T.S. Wang. Kinetic theory of tearing instability. *Physics of Fluids*, 18:1778, 1975.

M.B. Isichenko. Effective plasma heat conductivity in braided magnetic field. *Plasma Physics and Controlled Fusion*, 33(7):795, 1990.

J.R. King, C.R. Sovinec, and V.V. Mirnov. First-order finite-larmor-radius fluid modeling of tearing and relaxation in a plasma pinch. *Physics of Plasmas*, 19:055905, 2012.

M. Kotschenreuther, G. Rewoldt, and W.M. Tang. Comparison of initial value and eigenvalue codes for kinetic toroidal plasma instabilities. *Computer Physics Communications*, 88:128 – 140, 1995. ISSN 0010-4655. doi: 10.1016/0010-4655(95)00035-E. URL http://www.sciencedirect.com/science/article/pii/001046559500035E.

J.A. Krommes, C. Oberman, and R.G. Kleva. Plasma transport in stochastic magnetic fields. Part3. Kinetics of test particle diffusion. *Journal Plasma Physics*, 30(1):11, 1983.

K. Kusano and T. Sato. Simulation study of the self-sustainment mechanism in the reversed-field pinch configuration. *Nuclear Fusion*, 30(10):2075, 1990.

R. Lorenzini, D. Terranova, A. Alfier, P. Innocente, E. Martines, R. Pasqualotto, and P. Zanca. Single-Helical-Axis states in reversed-field-pinch plasmas. *Phys. Rev. Lett.*, 101:025005, Jul 2008. doi: 10.1103/PhysRevLett.101.025005. URL http://link.aps.org/doi/10.1103/PhysRevLett.101.025005.

R. Lorenzini, E. Martines, P. Piovesan, D. Terranova, P. Zanca, M. Zuin, A. Alfier, D. Bonfiglio, F. Bonomo, A. Canton, S. Cappello, L. Carraro, R. Cavazzana, D.F. Escande, A. Fassina, P. Franz, M. Gobbin, P. Innocente, L. Marrelli, R. Pasqualotto, M.E. Puiatti, M. Spolaore, M. Valisa, N. Vianello, and P. Martin. Self organized helical equilibria as a new paradigm for ohmically heated fusion plasmas. *Nature Physics*, 5:570, 2009.

R. Lüst and A. Schlüter. Axialsymmetrische magnetohydrodynamische gleichrewichtskonfigurationen. *Zeitschrift Naturforschung Teil A*, 12:850, oct 1957.

L. Marrelli, P. Zanca, M. Valisa, G. Marchiori, A. Alfier, F. Bonomo, M. Gobbin, P. Piovesan, D. Terranova, M. Agostini, C. Alessi, V. Antoni, L. Apolloni, F. Auriemma, O. Barana, P. Bettini, T. Bolzonella, D. Bonfiglio, M. Brombin, A. Buffa, A. Canton, S. Cappello, L. Carraro, R. Cavazzana, M. Cavinato, G. Chitarin, S. Dal Bello, A. De Lorenzi, D.F. Escande, A. Fassina, P. Franz, G. Gadani, E. Gaio,

E. Gazza, L. Giudicotti, F. Gnesotto, L. Grando, S.C. Guo, P. Innocente, R. Lorenzini, A. Luchetta, G. Malesani, G. Manduchi, D. Marcuzzi, P. Martin, S. Martini, E. Martines, A. Masiello, F. Milani, M. Moresco, A. Murari, L. Novello, S. Ortolani, R. Paccagnella, R. Pasqualotto, S. Peruzzo, R. Piovan, A. Pizzimenti, N. Pomaro, I. Predebon, M.E. Puiatti, G. Rostagni, F. Sattin, P. Scarin, G. Serianni, P. Sonato, E. Spada, A. Soppelsa, G. Spizzo, M. Spolaore, C. Taccon, C. Taliercio, V. Toigo, N. Vianello, P. Zaccaria, B. Zaniol, L. Zanotto, E. Zilli, G. Zollino, and M. Zuin. Magnetic self organization, MHD active control and confinement in RFX-mod. *Plasma Physics and Controlled Fusion*, 49(12B):B359–B369, 2007. URL `http://stacks.iop.org/0741-3335/49/B359`.

P. Martin, L. Marrelli, G. Spizzo, P. Franz, P. Piovesan, I. Predebon, T. Bolzonella, S. Cappello, A. Cravotta, D.F. Escande, L. Frassinetti, S. Ortolani, R. Paccagnella, D. Terranova, B.E. Chapman, D. Craig, S.C. Prager, J.S. Sarff, P. Brunsell, J.A. Malmberg, J. Drake, Y. Yagi, H. Koguchi, Y. Hirano, R.B. White, C. Sovinec, C. Xiao, R.A. Nebel, and D.D. Schnack. Overview of quasi-single helicity experiments in reversed-field pinches. *Nuclear Fusion*, 43(12):1855, 2003.

P. Martin, L. Apolloni, M.E. Puiatti, and et.al. Overview of RFX-mod results. *Nuclear Fusion*, 49:104019, 2009.

P. Martin, J. Adamek, P. Agostinetti, M. Agostini, A. Alfier, C. Angioni, V. Antoni, L. Apolloni, F. Auriemma, O. Barana, S. Barison, M. Baruzzo, P. Bettini, M. Boldrin, T. Bolzonella, D. Bonfiglio, F. Bonomo, A.H. Boozer, M. Brombin, J. Brotankova, A. Buffa, A. Canton, S. Cappello, L. Carraro, R. Cavazzana, M. Cavinato, L. Chacon, G. Chitarin, W.A. Cooper, S. Dal Bello, M. Dalla Palma, R. Delogu, A. De Lorenzi, G. De Masi, J.Q. Dong, M. Drevlak, D.F. Escande, F. Fantini, A. Fassina, F. Fellin, A. Ferro, S. Fiameni, A. Fiorentin, P. Franz, E. Gaio, X. Garbet, E. Gazza, L. Giudicotti, F. Gnesotto, M. Gobbin, L. Grando, S.C. Guo, Y. Hirano, S.P. Hirshman, S. Ide, V. Igochine, Y. In, P. Innocente, S. Kiyama, S.F. Liu, Y.Q. Liu, D. Lòpez Bruna, R. Lorenzini, A. Luchetta, G. Manduchi, D.K. Mansfield, G. Marchiori, D. Marcuzzi, L. Marrelli, S. Martini, G. Matsunaga, E. Martines, G. Mazzitelli, K. McCollam, S. Menmuir, F. Milani, B. Momo, M. Moresco, S. Munaretto, L. Novello, M. Okabayashi, S. Ortolani, R. Paccagnella, R. Pasqualotto, M. Pavei, G.V. Perverezev, S. Peruzzo, R. Piovan, P. Piovesan, L. Piron, A. Pizzimenti, N. Pomaro, N. Pomphrey, I. Predebon, M.E. Puiatti, V. Rigato, A. Rizzolo, G. Rostagni, G. Rubinacci, A. Ruzzon, H. Sakakita, R. Sanchez, J.S. Sarff, F. Sattin, A. Scaggion, P. Scarin, W. Schneider, G. Serianni, P. Sonato, E. Spada, A. Soppelsa, S. Spagnolo, M. Spolaore, D.A. Spong, G. Spizzo, M. Takechi, C. Taliercio, D. Terranova, V. Toigo, M. Val-

isa, M. Veranda, N. Vianello, F. Villone, Z. Wang, R.B. White, D. Yadikin, P. Zaccaria, A. Zamengo, P. Zanca, B. Zaniol, L. Zanotto, E. Zilli, G. Zollino, and M. Zuin. Overview of the RFX fusion science program. *Nuclear Fusion*, 51(9):094023, 2011. URL http://stacks.iop.org/0029-5515/51/i=9/a=094023.

E. Martines, R. Lorenzini, B. Momo, D. Terranova, P. Zanca, A. Alfier, F. Bonomo, A. Canton, A. Fassina, P. Franz, and P. Innocente. Equilibrium reconstruction for single helical axis reversed-field pinch plasmas. *Plasma Physics and Controlled Fusion*, 53(3):035015, 2011. URL http://stacks.iop.org/0741-3335/53/i=3/a=035015.

L. Nasi and M.C. Firpo. Enhanced confinement with increased extent of the low magnetic shear region in tokamak plasmas. *Plasma Physics and Controlled Fusion*, 51(4): 045006, 2009. URL http://stacks.iop.org/0741-3335/51/i=4/a=045006.

S. Ortolani and D.D. Schnack. *Magnetohydrodynamics of Plasma Relaxation*. World Scientific, Singapore, 1993.

R. Paccagnella, S. Ortolani, P. Zanca, A. Alfier, T. Bolzonella, L. Marrelli, M. E. Puiatti, G. Serianni, D. Terranova, M. Valisa, M. Agostini, L. Apolloni, F. Auriemma, F. Bonomo, A. Canton, L. Carraro, R. Cavazzana, M. Cavinato, P. Franz, E. Gazza, L. Grando, P. Innocente, R. Lorenzini, A. Luchetta, G. Manduchi, G. Marchiori, S. Martini, R. Pasqualotto, P. Piovesan, N. Pomaro, P. Scarin, G. Spizzo, M. Spolaore, C. Taliercio, N. Vianello, B. Zaniol, L. Zanotto, and M. Zuin. Active-Feedback Control of the Magnetic Boundary for Magnetohydrodynamic Stabilization of a Fusion Plasma. *Phys. Rev. Lett.*, 97:075001, Aug 2006. doi: 10.1103/PhysRevLett.97.075001. URL http://link.aps.org/doi/10.1103/PhysRevLett.97.075001.

R. Paccagnella, D. Terranova, and P. Zanca. Modelling and interpretation of MHD active control experiments in RFX-mod. *Nuclear Fusion*, 47(8):990, 2007. URL http://stacks.iop.org/0029-5515/47/i=8/a=033.

W. Park, D.A. Monticello, and R.B. White. Reconnection rates of magnetic fields including the effect of viscosity. *Physics of Fluids*, 27:137, 1984. doi: 10.1063/1.864502.

S. Pfalzner. *Introduction to inertial confinement fusion*. Taylor and Francis, first edition, 2006.

P. Piovesan, M. Zuin, A. Alfier, D. Bonfiglio, F. Bonomo, A. Canton, S. Cappello, L. Carraro, R. Cavazzana, D.F. Escande, A. Fassina, M. Gobbin, R. Lorenzini, L. Marrelli, P. Martin, E. Martines, R. Pasqualotto, M.E. Puiatti, M. Spolaore, M. Valisa,

N. Vianello, and P. Zanca. Magnetic order and confinement improvement in high-current regimes of RFX-mod with MHD feedback control. *Nuclear Fusion*, 49:085036, 2009.

P. Piovesan, D. Bonfiglio, F. Bonomo, et al. Influence of external 3D magnetic fields on helical equilibrium and plasma flow in RFX-mod. *Plasma Physics and Controlled Fusion*, 53:084005, 2011.

I. Predebon, L. Marrelli, R. B. White, and P. Martin. Particle-transport analysis in reversed-field pinch helical states. *Physical Review Letters*, 93(14):145001, 2004. doi: 10.1103/PhysRevLett.93.145001. URL http://link.aps.org/abstract/PRL/v93/e145001.

M.E. Puiatti, M. Valisa, M. Agostini, F. Auriemma, F. Bonomo, L. Carraro, A. Fassina, M. Gobbin, R. Lorenzini, B. Momo, A. Scaggion, B. Zaniol, A. Alfier, L. Apolloni, M. Baruzzo, T. Bolzonella, D. Bonfiglio, A. Canton, S. Cappello, R. Cavazzana, S. Dal Bello, G. De Masi, D.F. Escande, P. Franz, E. Gazza, S. Guo, P. Innocente, G. Marchiori, L. Marrelli, P. Martin, E. Martines, S. Martini, S. Menmuir, L. Novello, R. Paccagnella, P. Piovesan, L. Piron, I. Predebon, A. Ruzzon, F. Sattin, P. Scarin, A. Soppelsa, G. Spizzo, S. Spagnolo, M. Spolaore, D. Terranova, M. Veranda, N. Vianello, P. Zanca, L. Zanotto, and M. Zuin. Internal and external electron transport barriers in the RFX-mod reversed-field pinch. *Nuclear Fusion*, 51(7):073038, 2011. URL http://stacks.iop.org/0029-5515/51/i=7/a=073038.

A.B. Rechester and M.N. Rosenbluth. Electron heat transport in a tokamak with destroyed magnetic surfaces. *Physics Review Letters*, 40(1):38, 1978.

M.N. Rosenbluth, R.Z. Sagdeev, J.B. Taylor, and G.M. Zaslavski. Destruction of magnetic surfaces by magnetic field irregularities. *Nuclear Fusion*, 6(4):297, 1966. URL http://stacks.iop.org/0029-5515/6/i=4/a=008.

G. Rostagni. RFX: an expected step in RFP research. *Fusion Engineering and Design*, 25 (5):301, 1995.

P.H. Rutherford. Nonlinear growth of the tearing mode. *Physics of Fluids*, 16(11):1903–1908, 1973. doi: 10.1063/1.1694232. URL http://link.aip.org/link/?PFL/16/1903/1.

A. Ruzzon, A. Fassina, P. Franz, et al. Temperature profle dynamics in QSH regimes with multichord Soft X-Rays diagnostic in RFX-mod. 2012. http://ocs.ciemat.es/epsicpp2012pap/pdf/P2.023.pdf.

R. Sanchez, D. E. Newman, J.N. Leboeuf, B. A. Carreras, and V. K. Decyk. On the nature of radial transport across sheared zonal flows in electrostatic ion-temperature-gradient gyrokinetic tokamak plasma turbulence. *Physics of Plasmas*, 16(5):055905, 2009. doi: 10.1063/1.3129727. URL http://link.aip.org/link/?PHP/16/055905/1.

J.S. Sarff et al. Overview of the results from the mst reversed-field pinch experiment. *Nuclear Fusion*, to be published, 2013.

D.D. Schnack, D.C. Barnes, Z. Mikic, D.S. Harned, and E.J. Caramana. Semi-implicit magnetohydrodynamic calculations. *Journal of Computational Physics*, 70(2):330 – 354, 1987. ISSN 0021-9991. doi: 10.1016/0021-9991(87)90186-0. URL http://www.sciencedirect.com/science/article/pii/0021999187901860.

V.D. Shafranov. On magnetohydrodynamical equilibrium configurations. *Soviet Phys. JETP*, 6:545, 1958.

P. Sonato, G. Chitarin, P. Zaccaria, F. Gnesotto, S. Ortolani, A. Buffa, M. Bagatin, W.R. Baker, S. Dal Bello, P. Fiorentin, L. Grando, G. Marchiori, D. Marcuzzi, A. Masiello, S. Peruzzo, N. Pomaro, and G. Serianni. Machine modification for active MHD control in RFX. *Fusion Engineering and Design*, 66:161, 2003.

C. R. Sovinec, T. A. Gianakon, E. D. Held, S. E. Kruger, D. D. Schnack, and NIMROD Team. Nimrod: A computational laboratory for studying nonlinear fusion magnetohydrodynamics. *Physics of Plasmas*, 10(5):1727–1732, 2003. doi: 10.1063/1.1560920. URL http://link.aip.org/link/?PHP/10/1727/1.

L. Spitzer and R. Härm. Transport phenomena in a completely ionized gas. *Physical Review*, 89(5):977, 1953.

G. Spizzo, S. Cappello, A. Cravotta, D.F. Escande, I. Predebon, L. Marrelli, P. Martin, and R.B. White. Transport barriers inside the reversal surface in the chaotic regime of the reversed-field pinch. *Physical Review Letters*, 96:025001, 2006.

G. Spizzo, R. B. White, and S. Cappello. Chaos generated pinch effect in toroidal confinement devices. *Physics of Plasmas*, 14(10):102310, 2007. doi: 10.1063/1.2776907. URL http://link.aip.org/link/?PHP/14/102310/1.

G. Spizzo, R.B. White, S. Cappello, and L. Marrelli. Nonlocal transport in the reversed-field pinch. *Plasma Physics and Controlled Fusion*, 51(12):124026, 2009. URL http://stacks.iop.org/0741-3335/51/i=12/a=124026.

H. D. Stephens, D. J. Den Hartog, C. C. Hegna, and J. A. Reusch. Electron thermal transport within magnetic islands in the reversed-field pinch. *Physics of Plasmas*, 17(5): 056115, 2010. doi: 10.1063/1.3388374. URL http://link.aip.org/link/?PHP/17/056115/1.

H.R. Strauss. Finite beta in reversed field pinches. *Physics of Fluids*, 29(9):3008, 1986.

H.E. Sätherblom, S. Mazur, and P. Nordlund. Resistivity profile effects in numerical magnetohydrodynamic simulations of the reversed-field pinch. *Plasma Physics and Controlled Fusion*, 38(12):2205, 1996. URL http://stacks.iop.org/0741-3335/38/i=12/a=012.

J. B. Taylor. Relaxation and magnetic reconnection in plasmas. *Rev. Mod. Phys.*, 58:741–763, Jul 1986. doi: 10.1103/RevModPhys.58.741. URL http://link.aps.org/doi/10.1103/RevModPhys.58.741.

D. Terranova, T. Bolzonella, S. Cappello, P. Innocente, L. Marrelli, and R. Pasqualotto. Study of the scaling of magnetic fluctuations in the RFX reversed-field pinch. *Plasma Physics and Controlled Fusion*, 42(7):843, 2000. URL http://stacks.iop.org/0741-3335/42/i=7/a=307.

D. Terranova, D. Bonfiglio, A.H. Boozer, et al. A 3D approach to equilibrium, stability and transport studies in RFX-mod improved regimes. *Plasma Physics and Controlled Fusion*, 52:124023, 2010.

M. Veranda. Proprietà topologiche della transizione dal caos all'ordine magnetico nel reversed-field pinch: metodi e strumenti per la diagnosi. Master's thesis, Università degli Studi di Padova, 2009. URL https://www.igi.cnr.it/www/sites/default/files/Tesi_Veranda.pdf.

Z.R. Wang and S.C. Guo. Physical understanding of the instability spectrum and the feedback control of resistive wall modes in reversed-field pinch. *Nuclear Fusion*, 51(5): 053004, 2011. URL http://stacks.iop.org/0029-5515/51/i=5/a=053004.

J. Wesson. *Tokamaks*. Clarendon Press, Oxford, second edition, 1997.

R.B. White. Resistive reconnection. *Reviews of Modern Physics*, 58:138, 1986.

R.B. White. *The theory of toroidally confined plasmas*, page 66. Imperial College Press, 57 Shelton Street, Covent Garden, London WC2H 9HE, second edition, April 2006. ISBN 1860946399. URL http://www.icpress.co.uk/physics/p440.html.

R.C. Wolf. A stellarator reactor based on the optimization criteria of Wendelstein 7-X. *Fusion Engineering and Design*, 83(709):990 – 996, 2008. doi: 10.1016/j.fusengdes.2008.05.008. URL http://www.sciencedirect.com/science/article/pii/S0920379608001063.

P. Zanca. Avoidance of tearing modes wall-locking in a reversed-field pinch with active feedback coils. *Plasma Physics and Controlled Fusion*, 51:015006, 2009.

P. Zanca, L. Marrelli, G. Manduchi, and G. Marchiori. Beyond the intelligent shell concept: the clean-mode-control. *Nuclear Fusion*, 47(11):1425, 2007. URL http://stacks.iop.org/0029-5515/47/i=11/a=004.

G. M. Zaslavsky. Chaos, fractional kinetics, and anomalous transport. *Physics Reports*, 371(6):461 – 580, 2002. doi: DOI:10.1016/S0370-1573(02)00331-9. URL http://www.sciencedirect.com/science/article/B6TVP-46XHPB1-2/2/ebfe82357a097be85176da210bb1779a.

M. Zuin, N. Vianello, M. Spolaore, et al. Current sheets during spontaneous reconnection in a current-carrying fusion plasma. *Plasma Physics and Controlled Fusion*, 51(3):035012, 2009. URL http://stacks.iop.org/0741-3335/51/i=3/a=035012.

Publications

D. Bonfiglio, M. Veranda, S. Cappello, L. Chacón, and G. Spizzo. Magnetic chaos healing in the helical reversed-field pinch: indications from the volume-preserving field line tracing code NEMATO. *Journal of Physics: Conference Series*, 260(1):012003, 2010. URL http://stacks.iop.org/1742-6596/260/i=1/a=012003.

S. Cappello, D. Bonfiglio, D.F. Escande, S.C. Guo, I. Predebon, F. Sattin, M. Veranda, P. Zanca, C. Angioni, L. Chacón, J.Q. Dong, X. Garbet, and S.F. Liu. Equilibrium and transport for quasi-helical reversed-field pinches. *Nuclear Fusion*, 51(10):103012, 2011. URL http://stacks.iop.org/0029-5515/51/i=10/a=103012.

I. Predebon, F. Sattin, M. Veranda, D. Bonfiglio, and S. Cappello. Microtearing modes in reversed-field pinch plasmas. *Phys. Rev. Lett.*, 105:195001, Nov 2010. doi: 10.1103/PhysRevLett.105.195001. URL http://link.aps.org/doi/10.1103/PhysRevLett.105.195001.

F. Sattin, S.C. Guo, I. Predebon, S.F. Liu, X. Garbet, and M. Veranda. Microturbulence studies in RFX-mod. *Journal of Physics: Conference Series*, 260(1):012018, 2010. URL http://stacks.iop.org/1742-6596/260/i=1/a=012018.

M. Veranda , D. Bonfiglio, S. Cappello, L. Chacón, and D.F. Escande. Impact of helical boundary conditions on nonlinear 3D MHD simulations of reversed-field pinch. *Plasma Physics and Controlled Fusion*, to be published, 2013.

M. Veranda, D. Bonfiglio, and S. Cappello. Magnetic topology and flow in helical reversed-field pinch (RFP) configuration from MHD simulations. 2011. http://ocs.ciemat.es/eps2011pap/pdf/P4.028.pdf.

M. Veranda, D. Bonfiglio, S. Cappello, et al. Helical features in nonlinear 3D MHD modeling of pinch configurations. 2012. http://ocs.ciemat.es/epsicpp2012pap/pdf/P4.004.pdf.